Determination of the Critical Incipient Failure Conditions for Angular Riprap Dumped on Wide & Steep Trapezoidal Channels

by

Michael Appolus

Thesis presented in partial fulfilment of the requirements for the degree of
Master *of Engineering in the Faculty of Engineering at Stellenbosch University*

Supervisors : Mrs. Adele Bosman
: Prof. Gerrit Basson

April 2019

Declaration

By submitting this thesis electronically, I declare that the entirety of the work contained therein is my own, original work, that I am the sole author thereof (save to the extent explicitly otherwise stated), that reproduction and publication thereof by Stellenbosch University will not infringe any third-party rights and that I have not previously in its entirety or in part submitted it for obtaining any qualification.

Date: April 2019

Abstract

The main objective of this thesis was to determine the critical MN that defines the incipient failure conditions of angular riprap dumped on wide and steep trapezoidal channels. A total of 32 physical hydraulic model tests were performed in three test series. There were 7 tests performed for Test series one, 15 tests performed on Test series two and 10 tests were performed on Test series three. The tests were executed by gradually increasing flow rates over the hydraulic model to enable establishment and recording of the flow rate that induced incipience of riprap for a specific hydraulic model setup. Failure was defined as the flow rate that instigated a significant movement of riprap stones less and equal to D_{50}.

Based on the physical model tests of this thesis it was found that for the riprap on the bed of a relatively wide trapezoidal channel (bottom width to D_{50} ratio of 16 to 31) and steep bed slopes (of 0.333-0.5), the critical MN value defining the incipient failure conditions for these steep bed slopes was 0.12 with an exceedance probability of 95%. This MN value is in good agreement with Rooseboom's (1992) MN criteria of 0.12. In addition, the MN for defining the critical incipient failure condition of riprap on a 0.4 steep side bank slope was found to be 0.227, with an exceedance probability of 95%.

Based on the HEC-RAS steady state flow numerical simulations of the physical model tests series performed in this thesis, it was found that HEC-RAS overestimates the actual incipient failure MN. HEC-RAS overestimated the critical incipient failure MN of the steep bed and steep side bank by a critical factor of 1.91 and 1.35, respectively. As a result, the two factors were recommended as the MN adjustment factors (the steep bed and side bank MN must be adjusted to MN values of 0.12 and 0.227, respectively) for defining the incipient failure of a specific D_{50} rock size when using HEC-RAS steady state flow analysis.

Lastly, the applicability of the findings of this study are limited to riprap dumped in straight trapezoidal cross-sectional channels with steep beds ranging from 0.333 to 0.5 and with side bank slopes of 0.4. The scale of the hydraulic physical model used in the investigation was selected relatively large i.e. 1:15 to minimize model scale effects. The model D_{50} size was 0.038 m and 0.075 m which represent prototype stone sizes with D_{50} between 0.57 m and 1.125 m respectively. The results of the study are therefore only valid for the design of prototype D_{50} stone size between stone 0.57 m and 1.125 m. Most importantly, the bed bottom width to D_{50} ratio needs to be between 16-31.

Opsomming

Die hoofoogmerk van hierdie verhandeling is om die kritiese MN vas te stel wat die beginweieringtoetande van hoekige stortklip, gestort op breë en steil trapesoïedkanale, bepaal. Altesaam 32 fisiese hidrouliesemodeltoetse is in drie toetsreekse uitgevoer. Sewe toetse is in Toetsreeks een uitgevoer, terwyl 15 toetse in Toetsreeks twee en 10 toetse in Toetsreeks drie uitgevoer is. Die toetse is uitgevoer deur vloeitempo's geleidelik oor die hidrouliese model te verhoog om die vloeitempo, wat die begin van klipstorting in 'n spesifieke hidrouliesemodel-opset bewerkstellig, vas te tel en op te teken. Weiering is gedefinieer as die vloeitempo wat 'n beduidende beweging van stortklippe van minder as en gelyk aan D_{50} bewerkstellig het.

Gegrond op die fisiese modeltoetse in hierdie verhandeling is daar bevind dat, vir klipstorting op die bedding van 'n relatief breë trapesoïedkanaal (bodembreedte-tot-D_{50}-verhouding van 16 tot 31) en steil beddinghellings (van 0.333-0.5), die kritiese MN-waarde, wat die beginweieringtoestande vir hierdie steil beddinghellings bepaal, 0.12 is, met 'n oorskrydingswaarskynlikheid van 95%. Hierdie MN-waarde stem ooreen met Rooseboom (1992) se MN-kriteria van 0.12. Verder is daar bevind die MN vir die bepaling van die kritiese beginweieringtoestand van klipstorting op 'n 0,4-steil sywalhelling is 0.227, met 'n oorskrydingswaarskynlikheid van 95%.

Gebaseer op die HEC-RAS-program se numeriese simulasies van die bestendigetoestandvloei in die fisiese modeltoetsreeks wat vir hierdie verhandeling uitgevoer is, is daar bevind die HEC-RAS-program oorskat die werklike beginweiering-MN. Die HEC-RAS-program oorskat die kritiese beginweiering-MN van die steil bedding en die steil sywal met 'n kritiese faktor van onderskeidelik 1.91 en 1.35. Gevolglik word dié twee faktore aanbeveel as die MN-aanpassingsfaktore (die steilbedding- en sywal-MN moet tot MN-waardes van onderskeidelik 0.12 en 0.277 aangepas word) vir die bepaling van die beginweiering van 'n spesifieke D_{50}-rotsgrootte wanneer die HEC-RAS-bestendigetoestandvloeiontleding gebruik word.

Laastens is die toepaslikheid van hierdie studiebevindings beperk tot stortklip wat in reguit trapesoïeddwarssnitkanale met steil beddings, wat van 0.333 tot 0.5 wissel en met sywalhellings van 0.4, gestort word. Die skaal van die hidroulies-fisiese model wat in die studie gebruik is, is relatief groot gekies, dus 1:15 om die skaaleffekte van die model te verminder. Die model D_{50}-grootte was 0.038 m en 0.075 m, wat prototipe-klipgroottes met D_{50} tussen onderskeidelik 0.57 m en 1.125 m verteenwoordig. Die resultate van die studie is dus slegs geldig vir die ontwerp van prototipe D_{50}-klipgrootte tussen klipgrootte van 0.57 m en 1.125 m. Veral van belang is dat die beddingbodembreedte-tot-D_{50}-verhouding tussen 16-31 moet wees.

Acknowledgements

Firstly, I would like to thank God for the strength and courage that He has instilled in me through my entire tertiary studies. Most of all, I thank Him for providing me with the physical and mental strength to successfully carry on with this thesis, to shed light whenever I am in the absence of light, Isaiah 9:2 "*The people who walk in darkness will see a great LIGHT; those who live in a dark land, the LIGHT will shine on them.*"

Thanks to every person who has helped in all the prerequisite work to ensure that the research project deliverables were successfully executed. This thesis would not have been possible without the support and assistance from several individuals and entities.

Special thanks to my academic supervisors Mrs Bosman and Prof Basson for the continual guidance and noteworthy supervision through the development stages until the completion of the research project. Thanks to Mr Eddie Bosman for his insightful and helpful comments on the draft thesis review.

Most importantly, thanks to the Western Cape Department of Agriculture for the bestowed privilege of financial support and academic development while pursuing post-graduate studies.

My sincere gratitude goes to Mr Ning Ma, Mr Christiaan Visser, Mr Illiyaaz Williams and Mr Johan Niewoudt who have assisted in advising on the practicalities of building a working laboratory model and for ensuring that material was bought and delivered when required. Most importantly for promptly finding solutions to all the laboratory complications.

Thanks to my academic colleagues from the post-graduate office, for frequently sharing inspiring words of wisdom and for reviving faith when it was needed most.

I would like to acknowledge the support from AfriSam for the sponsorship with the angular graded stone for the first Test series of the tests which was critical in the laboratory study.

More gratitude goes to the supporting staff members at the Department of Civil Engineering at the University of Stellenbosch for general academic assistance, guidance and for providing an enabling and conducive environment for post-graduate students to do their research.

Ultimately, I dedicate this thesis to my supportive family, my late father who would have loved to see me progressing with the life that I have chosen to pursue. To my loving mother and my three brothers, thanks for your love and support.

Table of Contents

List of Figures

List of Tables

Acronyms and Abbreviations

AF- Adjustment Factor

CIRIA – Construction Industry Research and Information Association

CSRA - Committee of State Road Authorities

CSU – Colorado State University

CUR – CUR Building and Infrastructure

CETMEF- Centre d'Etudes Techniques Maritimes Et Fluviales

LT- Length to Thickness Ratio

MN- Movability Number

NCHRP – National Cooperative Highway Research Program

SANRAL - South African National Roads Agency

Nomenclature

Δ_s	unit weight of stone (kN/m^3)
Δ_w	unit weight of water (kN/m^3)
ΔP	change in fluid pressure (Pa)
α	Steep side bank angle (°)
α_i	The α_i is the constant associated with the D_i, Froehlich (2012).
β	Angle of steep bed slope (m/m)
C	Chezy roughness coefficient
D_i	the diameter of the particle that is larger than the percentage *i* by mass (m)
C_D	the drag coefficient of particle
D_{16}	sieve size in which is passed by 16% (by mass) of particles in the sample (m)
D_{20}	sieve size in which is passed by 20 % (by mass) of particles in the sample (m)
D_{50} / d / d_{50}	sieve size in which is passed by 50% (by mass) of particles in the sample. Also known as the median stone size / median sieve size (m)
D_{84}	sieve size in which is passed by 84 % (by mass) of particles in the sample. as the median stone size (m)
D_{85}	sieve size in which is passed by 85 % (by mass) of particles in the sample (m)
D_{90}	sieve size in which is passed by 90 % (by mass) of particles in the sample (m)
D_{100}	sieve size in which is passed by 100 % (by mass) of particles in the sample (m)
D_w	average channel water depth (m)
$\frac{du}{dy}$	velocity gradient (m/s/m)
h_e	energy head loss (m)
g	gravitational acceleration (m/s^2)

k	represents the Von Karman constant, absolute roughness parameter that represents the size of eddies near the bed.
k_s	roughness coefficient or roughness element (m)
K_s	boundary roughness length scale (in Nikuradse's theory) (m)
k_α	steep side bank slope correction factor
k_β	steep bed slope correction factor
L	characteristic length within the model and prototype (m)
m	subscripts defining the model parameters
θ_g	geometric standard deviation
$\theta/\theta*_c$	shields parameter, represents dimensionless critical shear stress
σ	surface tension (N)
p	subscripts defining the prototype parameters
p_{app}	apparent rock density (kg/m^3)
p_r	rock mass density (kg/m^3)
p_s	particle density (kg/m^3)
p_w	fluid (water) density (kg/m^3)
p_{por}	the density of porous rock (kg/m^3)
Q_i	incipient failure flow rate (m^3/s)
r	subscript referring to the ratio of the prototype to the model
R	hydraulic radius (m)
Re_*	particle Reynolds number
$Re^*{}_c$	critical particle Reynolds number.
S_0	average bed/friction slope (uniform flow conditions assumed)
S_r	the degree of saturation, the ratio of the volume of water in pores to the volume of rock pores.

u_*	the shear velocity (m/s)
$u^*{}_c$	critical shear velocity (m/s)
v_{ss}	settling velocity of a natural particle (m/s)
y_0	ordinate where the velocity is theoretically equal to zero (m)
τ_0	bed shear stress (kN/m²)
τ_c	critical shear stress (kN/m²)
φ_r	angle of repose of a particle (°)
ν	is the kinematic viscosity of water (m^2/s)
V	average velocity of flowing channel (m/s)
$V(y)$	velocity at distance y above the bed (m/s).
V_m	velocity in model (m/s)
V_p	velocity in prototype (m/s)
V_r	ratio of velocity in protype and model (m/s)
y	distance above the bed/ point of depth from the bed (m)

Chapter 1 : Introduction

This chapter provides a synopsis to the thesis research project. The introduction chapter starts with outlining an overview of the background on riprap and its applications as a river revetment design solution. Description of the applications and advantages of riprap uses were highlighted. The background section acknowledges some of the main riprap researchers who contributed to the development of riprap research. Reflections on the challenges, problems and gaps encountered in research studies related to riprap studies were described.

Following the background description, the purpose statement of the study was stipulated. Then, the main objectives of the study were outlined. The significance of this research was emphasised to ensure that the reader understands the contribution of the thesis towards the field of riprap research. Finally, the scope of the project was described, as well as all the limitations that were experienced during the execution of the research project.

1.1 Background

Catchments consist of a network of river channels which aid the conveyance of water sourced from precipitation. Safe and efficient transportation of water from catchments into ponds, dams, and estuaries can only be made possible by a network of river channels. The hydraulic flow processes that occur in a river channel conveyance system are differentiated depending on factors such as the shape of the river, roughness of the bed, and the steepness of the slope. As a result, river channels in steep channel beds and riverbanks are more susceptible to the impacts of bed and riverbank erosion due to aggressive flows of water.

Riprap is one of the direct river erosion control measures, whereby rocks of specified size, gradation and thickness are either dumped or strategically placed on riverbanks to protect erosion susceptible areas. Riprap can also be used to preserve hydraulic structures vulnerable to erosion. Hydraulic structures include levees and dam embankments exposed to overtopping flows(Najafzadeh *et al.*, 2018).

The riprap erosion protection method is attractive to engineers, environmentalists, and hydrologists because of the following reasons (California Division of Highways, 1970; Committee of State Road Authorities, 1994; Langmaak and Basson, 2015):

- Exhibits a natural and aesthetically pleasing appearance.
- Has a minimal environmental impact.

- May provide a cost-effective solution if the specified rock size is available locally.
- Riprap is relatively easy to construct and repair.
- Riprap is durable.
- Riprap is flexible and has a self-adjusting layer that does not break due to a slight adjustment of the embankment.
- Riprap is reusable; central for sustainability and the protection of natural resource design principles.

For many years, riprap has been used as a river revetment design solution. Studies on the design and construction applications of riprap are prevalent in the United States of America. Riprap-related research has been a significant stepping stone in the development of riprap design manuals and design guidelines for the (1) US Army of Corps of Engineers manual (1988), (2) US Geological Survey (1986), Hydraulic Engineering Circular 11 (1986) and (3) US Nuclear Regulation Commission (1982), as well as the CIRIA(2007) Rock Manual.

An extensive and broad range of analytic, field and laboratory research studies have been developed in the riprap study field. Previous years of research have progressively contributed to the determination of preferred rock gradation(Stevens *et al.*, 1979), riprap thickness (Frizell *et al.*,1998), length of protection (de Almeida and Martín-Vide, 2009), the most stable rock shape and angle of repose of riprap (Froehlich, 2011).

Rock size determination is of significance in riprap design because rock sizing has a direct implication on the costs of the related river revetment project. Nonetheless, to date, there is little agreement in the empirical and analytical equations that are used to determine the stable riprap median stone size. Some expressions specify stone sizes that are more conservative than other expressions. Extensive investigations have been performed on riprap research, but there remain areas for improvement.

The disagreement and inconsistency in stable riprap size determination methods may be attributed to differences in the research systematic methodological biases in riprap stability studies (Buffington and Montgomery, 1998). Furthermore, the knowledge gaps related to different hydraulic flow properties may contribute to the inconsistencies. The knowledge gaps in open channel flow hydraulics include but are not limited to the complexity of velocity and shear stress distributions, erratic rock size and shape properties, inconsistent bed roughness determination methods, complex turbulent flow phenomena, and inconsistent analytic drag coefficient determination methods.

The previously mentioned open channel flow hydraulic phenomena are complex and have been studied for an extended period in hydraulics. Nonetheless, there remain gaps in understanding, quantifying and accurately modelling the different phenomena or properties. Therefore, this leaves a

gap in the research of the subject dependant on the previously mentioned gaps as prerequisite knowledge.

Sediment transportation is a parent research field to riprap research studies. The connection between the two is the phenomenon of the incipient motion of particles under hydraulic loads. The incipient motion is generally described by hydraulic conditions where the movement of particles is initiated or the hydraulic conditions at which riprap fail or overtop. Thus, initially, researchers were more interested in the hydraulic testing of small particles under smooth flow conditions for sediment transport studies. However, riprap studies require the hydraulic testing of larger stone sizes of rock to determine overtopping flow conditions. Therefore, most riprap studies generally borrow from the results of studies of the incipient motion concept and define failure accordingly.

The stable riprap rock size is normally defined as the D_{50} median rock size that does not move when a design flood or design peak flow enters the river stream. Most of the recent riprap research has been based on the testing of stable sizes of riprap rock on channel beds with different longitudinal slopes i.e in the flow direction. These riprap studies have been based mainly on flat and gentle bed slopes armoured with round shaped stones. Furthermore, flumes used for previous studies mainly comprised a rectangular cross-section, meaning that only the bed slope stability of riprap has been frequently studied.

Even though extensive research has been conducted in riprap studies, scant research has been conducted to investigate the stability of angular riprap on steep longitudinal riverbed slopes and trapezoidal cross-sectional slopes of the riverbanks. One of the latest research developments in this regard was by Langmaak (2013) from the University of Stellenbosch. Mr Langmaak conducted a riprap stability investigation on steep longitudinal bed slopes but only executed the study in a rectangular channel cross-section. However, most river cross-sections in real life comprise of banks with mild to steep side slopes. In Langmaak's study, only the stability of riprap dumped on steep beds was studied. The stability of the riprap dumped on the side banks was not investigated.

1.2 Purpose Statement

This thesis examines the stability of purely angular riprap dumped on straight trapezoidal channels that comprise hydraulically steep longitudinal bed slopes with steep side bank slopes. The analysis was executed using Liu's(1957) stream power theory, and the MN was used as a criterion for defining incipient failure.

1.3 Objectives of the Research

The main aim of the thesis was to determine the stable hydraulic conditions of angular riprap rocks dumped on steep bed slopes and steep banks of wide trapezoidal channels. Consequently, to recommend a method that designers can apply to specify the stable D_{50} median rock size to be dumped on the steep bed and steep side bank slopes of trapezoidal channels, at a pertinent design flow rate.

To achieve the main aims of the research, it was essential that the following objectives were met:

- The execution of an extensive and comprehensive literature study to understand and assess the broad spectrum of studies that have been conducted in the riprap research field and to understand the theories underpinning riprap incipient motion studies.
- Conduct physical hydraulic model tests in a laboratory at a scale of 1:15 (model: prototype). The main reason to choose the 1:15 scale was based on the intent to minimise potential hydraulic scale effects (refer to section 2.4.3). The physical hydraulic model tests comprised of the following main variables:
    - Graded riprap with D_{50} rock sizes of 0.038 m in model scale (represented by 0.57 m in prototype scale) and D_{50} rock sizes of 0.075 m in model scale (represented by 1.125 m in prototype scale).
    - Graded riprap of the above sizes with dumped placing on three steep longitudinal slopes (0.5, 0.4 and 0.333) and one steep side bank slope (0.4). The three steep bed slopes were specifically chosen because they represent typical steep bed and steep side bank slopes in prototype scale.
- Perform the following actions with the aid of the 1:15 scaled hydraulic model:
    - Observe, measure and analyse different riprap failure behaviours and hydraulic conditions for the angular riprap in the different steep slope setups in the model study.
    - Based on the results of the study, recommend a method for determining the incipient riprap median stone size (D_{50}) for river channel banks on steep sloped trapezoidal river cross-sections as well as on steep bed slopes.

1.4 Significance of the Study

The research findings in this thesis contribute towards improving the understanding of failure modes of riprap dumped on steep bed slope and side steep side banks of trapezoidal cross-sectional channels. Given the significant variability and inconsistencies in previous research results, the findings in this thesis contribute towards the currently available database of riprap flow studies which can be utilised for future comparative studies. Engineers may use the results and conclusions of the study (within the

tested ranges and limitations as presented in **section 1.5** below) as a guideline when designing future river revetment training works as well as for the protection of hydraulic structures susceptible to erosion induced by overtopping flows.

1.5 Scope and Limitations of the Study

This thesis only investigated the stability of angular riprap rocks through a physical model study. Two different median model stone sizes (D_{50}), i.e. 0.038 m and 0.075 m were tested. A scale of 1:15 was used to represent the prototype D_{50} rock sizes of 0.57 m and 1.125 m, respectively. The stone sizes were also chosen based on the available sieving equipment at the hydraulics laboratory.

The study only tested riprap rocks laid on a limited number of steep slopes, i.e. three different bed slopes, namely 0.5, 0.4 and 0.333. The three slopes were tested in combination with one steep bank slope of 0.4. However, it should be noted that this study was susceptible to limitations which had an impact on the obtained results. Some of the main limitations were as follows:

- Temporal limitations - due to time constraints only two riprap median stone sizes were chosen for testing. The study only tested for the two median model stone sizes (D_{50}), i.e. 0.038 m and 0.075 m. A total of 32 tests were performed due to time limitations. More confidence in the results could be gained with a larger number of tests and variables.
- Spatial limitations - The flume space available in the hydraulics laboratory limited the size (and consequently the selected scale) of the model. Thus, a half symmetrical model of a trapezoidal cross-sectional channel was chosen for the model study.
- Flume visibility – there was no transparent flume available for this specific study. Thus a brick wall flume was used and perspex glass was installed in the testing region to enable observation from one side of the flume.
- Rock property irregularities- these include rock shape, size, drag coefficient and the roughness coefficient of rocks. These parameters are listed as limitations to the results of this study due to the subjective definitions and quantifying of the parameters. There is no one universal way of defining/quantifying the shape of rocks, the roughness of rocks and drag coefficient. Nonetheless, due to the similarity of model rock to prototype properties, the model rock may be anticipated to behave similarly to the prototype.

1.6 Brief Chapter Overview

Figure 1 illustrates the skeletal structure of the thesis. Succeeding **Figure 1** is a summary of each chapter in the main body of the thesis. The summary provides the reader with an overview of the critical areas that were considered in each chapter. Only the main points are highlighted in the chapter summary in **Figure 1**.

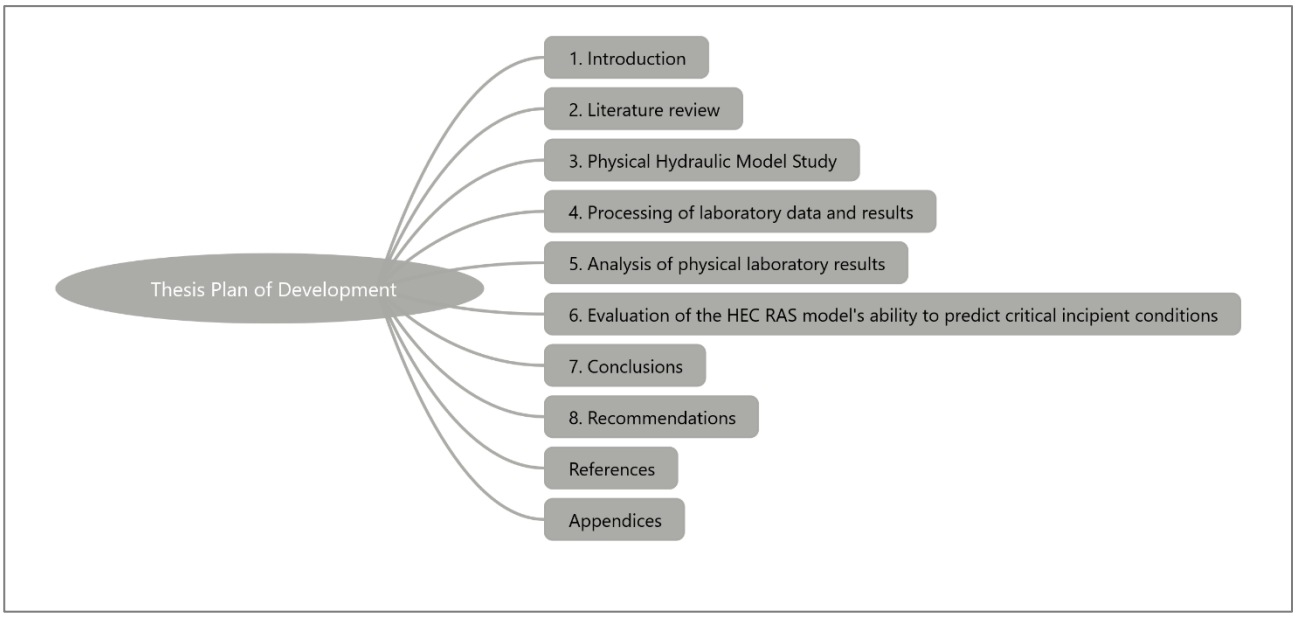

Figure 1: Thesis development plan framework

Chapter 1: Introduces the research project by highlighting the background to riprap research studies, indicating the gaps in riprap studies; provides a description of the objectives of the study; then the scope and limitations of the thesis.

Chapter 2: Reports on the main literature referred to during the study. The literature consulted, mainly reviewed the properties of riprap, failure modes of riprap, the critical theories generally used in riprap analysis and finally, a summary of the main hydraulic similarity laws relevant to scaled physical models. Lastly, a discussion on the causes and avoidance of scale effects in physical hydraulic models was presented.

Chapter 3: Provides a detailed description of the methods followed during the design and construction of the physical model. Then describes the laboratory equipment used and the laboratory procedure followed when performing the laboratory physical hydraulic model tests.

Chapter 4: Summarises the processing of the data collected in the hydraulic laboratory tests. The main data that was obtained from the model study were the failure flow rates, the channel upstream

and downstream surface water elevations, the local failure water depths and the average bed slopes in the failure regions.

Chapter 5: Describes in detail the analysis of the physical model results. The analysis provides a description of the process adopted to determine the critical incipient failure MN values for steep bed slopes as well as the steep side bank slopes.

Chapter 6: Provides a description of the evaluation performed to determine the HEC-RAS software's capability to define the critical incipient failure conditions that were observed at the laboratory. The chapter also describes how to use the recommended design tool that was developed using Microsoft Excel based on the HEC-RAS evaluation results.

Chapter 7: Conclusions are presented based on the findings from the physical model study and the analysis of the HEC-RAS simulated MN results.

Chapter 8: This chapter is divided into two parts. The first part describes recommendations based on the physical hydraulic laboratory tests and the analysis performed. The second part of the chapter provides recommendations for future research.

References: Provides a detailed list of the critical references consulted during the study.

Appendices: Appendices cross-referenced in the thesis are appended here

Chapter 2 : Literature Review

This chapter delves deep into the details of the literature that was consulted. There were myriads of research papers reporting on riprap. However, this study focused on the literature that was useful for the development of this specific study. The objectives and aims of the thesis were the main guidelines as to which literature to consult.

The main aim of the study was to determine the critical incipient failure conditions of angular riprap placed on steep straight trapezoidal channels. It was important that the hydraulic model was built in the laboratory to study the failure behaviour of the riprap. Thus, the first section of the literature review reports on the riprap properties required and critical in the design of a functional riprap protection.

This study was based on the failure modes of riprap. It was important in this study to understand riprap failure modes and for the effective design of riprap armour in practice. The failure modes knowledge assisted the researcher to design a functional riprap protection layer for the laboratory and to allow the designer to focus on the specific phenomena investigated.

An example of how critical this section was during the design of the model was when sand was initially used as the underlying material; the sand washed away, and the whole riprap slope failed. Initially, the premature failure of the slope did not allow the researcher to investigate the specific failure phenomena that were intended for this research. The model was redesigned and constructed with much more stable smaller gravel stones that provided the necessary stability on the slope.

The investigation of the incipience of riprap would not be possible without the analysis of the phenomena using a realistic hydraulic theory. Thus, the third section of the literature review reports on the main theories and hydraulic principles that have been widely implemented to analyse the incipience of riprap.

The literature study ends with a descriptive summary of the four main hydraulic similarity laws applicable in physical hydraulic models. The review of the similarity laws was critical for the study because the understanding of the relationship between the hydraulic parameters of the hydraulic model and the prototype is essential to realise the limitations of hydraulic models such as the scale effects when all the required scale laws are not fully satisfied. The hydraulic similarity scaling laws were critical to facilitate the design of a functional hydraulic model which sufficiently represents the prototype.

2.1 Riprap Properties

For a riprap layer to perform as anticipated by the designer, it is important that the properties of the riprap are considered and well thought out during the design stage. Riprap design procedures are mainly derived from empirical and theoretical analysis by different researchers. Each researcher follows a unique methodology even if the same theory may be followed in the analysis series. Application of different methodologies also means that different properties of riprap may be used in each research study. Therefore, the designer needs to keep this in mind and use the recommended riprap design methods according to the researcher's recommendations.

Regardless of the differences in the methodologies and riprap properties implemented by different researchers in different studies, there exist general recommendations as to which properties produce the best performing riprap layer. Therefore, this section reviewed the literature about all the critical properties of riprap and the recommended riprap properties currently applied in riprap design projects.

2.1.1 Riprap Size

For incipient motion studies, the riprap rock size is the most critical parameter in riprap design according to Langmaak (2013) and Abban (2007). The reason is that the particle size is the main parameter that provides the riprap rock with resistance against incipient motion induced by fluid flow forces. The mass of the rock is directly related to the particle size and density. The mass of the riprap rock contributes to the resistance against incipient motion. It is for this reason that the size of a riprap rock, of the same density, is important in riprap design.

Generally, riprap rocks can be classified as very large boulders down to large cobbles, with each rock classification corresponding to a respective size range. The classification of riprap rocks can be subjective. Thus, a widely accepted standard is preferable for classification. One such classification was provided by Simons and Senturk (1992), summarised in **Table 1**:

Table 1: Rock size classification

Median diameter rock size (m)	Classification
4 - 2	Very large boulders
2 - 1	Large boulders
1 - 0.5	Medium boulders
0.5 - 0.25	Small boulders
0.25 - 0.13	Large cobbles

Riprap rock size specification may be specified as a single rock size of diameter *D*. However, because riprap normally comprises of a grade of sizes a widely accepted method of the riprap size specification is according to the median sieve size, D_{50} of the total rock sample. The median sieve size describes the 50% (by mass) of the particles or rocks, which passes through a specified sieve diameter size, in a rock sample (CIRIA *et al.*, 2007). The standard sieve aperture type used for the previously mentioned method is the rectangular sieve opening.

2.1.2 Gradation

Riprap rock gradation refers to the nature of the distribution of different rock sizes in a pertinent sample. A riprap rock sample can be defined as well-graded, gap-graded or uniformly-graded. The well-graded riprap sample comprises a fair distribution of different sizes of rock, with small, medium and large rocks fairly represented in the sample. Whereas, a gap-graded riprap sample exhibits a significant size range of rocks that are more abundant compared to other rock sizes in the same sample. A uniformly-graded riprap rock sample comprises almost the same size range of rocks throughout the sample (NCHRP, 2006).

According to NCHRP (2006), most literature and researchers in the past agreed that the widely accepted gradation of riprap is the well-graded distribution. The reason for this is that well-graded riprap rock provides a self-healing property (CSRA, 1994), through the migration of smaller particles that fill in the gaps between the larger particles, and in so doing provides support to large rocks and decrease the possibility of failure.

However, it is apparent from the literature reviewed (Simons and Senturk (1992), Langmaark and Basson (2015), Robinson *et al.* (1998), CIRIA *et al.* (2007) and NCHRP (2006)), that there is little agreement in choosing the best gradation specification type. The reason for this may be attributed to the wide range of available grading scales. The disagreement in preference of uniform- or well-graded riprap also exacerbates the possibilities of agreement in choosing the best standard gradation type for riprap rocks.

After studies by Wittler and Abt (1990), Abt *et al.* (1988), and Maynord (1988), according to NCHRP (2006), the current views on riprap gradation are that uniformly-graded riprap rock affords greater stability for riprap. Furthermore, uniformly-graded riprap rock tends to behave rigidly due to the similar rock size distribution. However, it is also argued that uniform-riprap rock gradation tends to fail abruptly compared to well-graded riprap rock. Abrupt failure is not a desirable form of failure in engineering as it can lead to catastrophe without the provision of time in which to take precautions.

For uniform-riprap rock sizes, the uniformity of particle gradation may be calculated using the geometric standard deviation (De Almeida & Martin Vide, 2009):

$$\theta_g = \sqrt{\frac{D_{84}}{D_{16}}} \qquad \textbf{Eq. 1}$$

Whereby, D_{84} is sieve size in which is passed by 84% (by mass) of particles in the sample and similarly to D_{16} the sieve size in which is passed by 16% (by mass) of particles in the sample. Raudziki (1998) defined the condition where $\theta_g < 1.35$ for sediment particles of a sample, as uniformity. However, Raudziki (1998) expressed θ_g in terms of D_{85} and D_{15} as the input parameters of the equation, which is very similar to **Equation 1**.

Langmaak and Basson (2015) agree that the gradation of riprap is a debatable issue in which different researchers have different views on the best grading type. However, Langmaak (2013) point out that the riprap gradation recommendations by Simons and Senturk (1992) are widely used and are defined as follows:

$$D_{100} \geq 2D_{50}$$

$$D_{20} \geq 0.5D_{50}$$

$$D_{min} \geq 0.2D_{50}$$

From Simons and Senturk (1992) gradation criterion above, a distribution of small to large riprap is provided by the criteria. The grading criterion is non-uniform due to the wide grading type.

Blodgett (1986) claims that in general, the preferred riprap rock gradation is that which is (1) dense, (2) uniform, (3) durable, (4) angular, and (5) has few voids. The well-graded riprap rock has few voids due to the smaller sized rocks filling the voids between larger rocks making it is dense but non-uniform. Therefore, a riprap rock with the previous general gradation and properties is expected to afford adequate protection towards fluid flow current.

2.1.3 Density

The density of rock is one of the important properties in the hydraulic design of riprap (CIRIA *et al*., 2007). Most rocks display approximately the same density if the mineral composition of the rocks is similar. Rocks with different mineral composition generally comprise of different density; for example, sandstone, granite, and basaltic rocks all have different densities corresponding to the difference in the rocks' mineral compositions.

Construction Industry Research and Information Association (CIRIA *et al*., 2007) states that there are several different rock density definitions available. The use of each density definition depends upon the approach or application. Hence, CIRIA *et al*. (2007) recommends the use of the apparent mass density whenever designing hydraulic works. The apparent mass density is then defined as the ratio of the mass to its volume, noting that the mass of the rock may have pores. However, if there are no pores, then the apparent mass density is the mass density denoted by ρ_r. Nonetheless, ρ_{app} is the preferred denotation for hydraulic design purposes, so as not to forget to account for rock pore volume when applicable.

In hydraulic design applications, the apparent rock density can be calculated from the equation (CIRIA *et al*., 2007):

$$\rho_{app} = \rho_r(1 - \rho_{por}) + \rho_w \rho_{or} S_r \qquad \textbf{Eq. 2}$$

Where,

ρ_r = Rock mass density

ρ_{por} = Porosity of rock, ratio of rock volume to total volume (rock + pore volume).

S_r = Degree of saturation, the ratio of the volume of water in pores to the volume of rock pores.

In **Equation 2**, if there are no pores on the rock ($\rho_{por} = 0$), then $\rho_{app} = \rho_r$.

2.1.4 Settling Velocity

The settling velocity of a rock is the terminal velocity that the rock reaches when free falling through a medium of fluid (Armitage, 2002). When a riprap rock free falls in a fluid medium, the rock reaches a settling velocity, whereby the sum of the buoyant and lift force is equal to the gravitational force acting on the rock. Therefore, a riprap rock reaches dynamic equilibrium during its quiescent fall into a fluid medium (Armitage, 2002).

The settling velocity of a rock is dependent on its shape, size, surface roughness, density and the density of the flowing fluid (Sadat-Helbar *et al.*, 2009). Other possible influences on the settling velocity include the particle concentration, turbulence around the particle and the presence of rough boundaries near particles in fall conditions. The previously mentioned dependencies comprise complexities related to quantifying and measuring. Consequently, making the accurate determination of settling velocity more cumbersome.

Given that v_{ss} is the settling velocity, ρ_r is the particle density, ρ_w is the fluid (water) density, C_D is the drag coefficient of the particle, then the settling velocity of a natural particle can be defined as follows (Graf, 1971 & Raudziki, 1998):

$$v_{ss} = \sqrt{\frac{4}{3}\frac{(\rho_r - \rho_w)}{\rho_w}\frac{gD_{50}}{C_D}} \qquad \textbf{Eq. 3}$$

In **Equation 3**, the drag coefficient is the actual parameter that is mainly dependent on the particle shape. However, the shape and size of particles vary due to the erratic nature of rocks. The variation of the geometric rock properties affects the ease and accuracy to calculate the drag coefficient of irregularly shaped particles. Thus, generally, the drag coefficient is related to the particle Reynolds number, especially in the low Re* number region (Armitage, 2002). However, the drag coefficient is argued to be independent of the Reynolds particle number at high particle Reynolds number. The reasoning is based on the results of previous researchers' studies, where particles of different shapes were revealed to have a constant drag coefficient at high Re* regions for typical values in the range$10^3 < Re_* > 10^5$. The drag coefficient is related to the particle Reynolds number through the following expression, but applicable to $Re_* \leq 1$, also known as the Stokes law (Armitage, (2002) & Cheng (1997)):

$$Re_* = \frac{u*d}{v} \qquad \textbf{Eq. 4}$$

Several studies have been conducted on the settling velocities of spherical particles including irregular particles with defined shapes such as prisms, cubes and cylinders (e.g. Jimenez & Madsen (2003), Le Roux (2014)). However, no specific study was found in the literature for studying drag coefficient and settling velocities of large angular rocks.

Langmaak (2013) agrees that the primary challenge in determining the settling velocity is in determining C_D for irregularly shaped particles. Thus, Armitage (2002) recommends that the settling velocity of irregular or unusual shapes must be determined experimentally.

2.1.5 Cohesiveness

Non-cohesive sediments are generally discrete particles, which are not attached to adjacent particles by any electrochemical forces (Raudziki, 1998). Moreover, the incipient motion of a non-cohesive particle is mainly dependent on its weight. Large rocks, boulders, gravel and sandstones are referred to as non-cohesive due to their individuality, and when packed with other particles there are no adhesive forces between particles.

However, cohesive sediments are mostly found in the form of small particle sizes that are of dense coherent mass. The sediments are mostly fine in size and the electrochemical forces from the sediment's mineral composition dominate. Cohesive sediments mainly comprise small particles such as clay and silt which assume control of sediment properties (Raudziki, 1998).

Riprap rocks are mainly large rocks, which are individually packed or dumped in river protection systems. Due to their individuality, nature and high density, plus the absence of dominating electrochemical forces between rocks, it is evident that riprap rock is a non-cohesive particle. The riprap rock transportability is highly dependent on the individual weight of the rock.

2.1.6 Angle of Repose

The angle of repose, also known as the friction angle of a particle, is defined as the maximum side slope angle with respect to a horizontal plane that a particle sustains before it begins descending when placed on a slope. The angle of repose of a particle may be denoted by φ_r.

The angle of repose of a rock is mainly dependent on the particle shape, particle size and porosity (Van Rijn, 1993). In general, an increase in particle size and angularity tends to increase the angle of repose of a particle. However, an increase in the porosity of a rock sample reduces the angle of repose.

Various researchers have recommended different values for the angle of repose (e.g. Lane (1953), Van Rijn (1993) and Froehlich (2011)) . It makes logical sense to assume that the variations in the angle of repose are due to the infinite variations in the shapes of particles and the subjectivity in which different researchers characterise and quantify the shape of particles in the pertinent research studies.

In **Figure 2**, Lane (1953) produced a family of curves with relationships between the particle shape, size and estimated angle of repose for cohesionless particles.

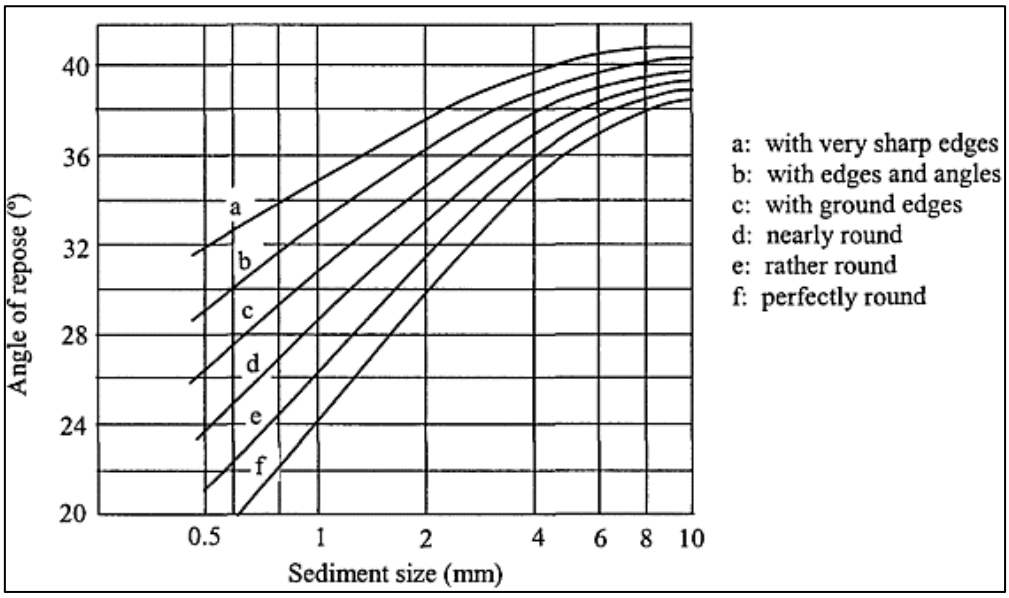

Figure 2: Sediment size and angle of repose relationship for differently shaped sediments. (extracted from Abban (2007), by Lane (1953)

Van Rijn (1993) recommended a useful table of values with the angle of repose for quarzitic sand with size ranging from approximately 1 mm up to 100 mm. However, Van Rijn (1993) only differentiated the particles into two different shape categories, rounded and angular as shown in **Table 2.**

Table 2: Angle of repose for quarzitic sand material for stable channel design (Van Rijn, 1993)

Size (D_{50})	**The angle of repose (φ_r) in degrees**	
(mm)	**Rounded**	**Angular**
< 1	30	35
5	32	37
10	35	40
50	37	42
>100	40	45

Riprap is generally in the form of packed rocks. Regardless of the thickness of the layer, riprap always has rocks in the form of a mass rather than individual rocks. Thus, it makes more sense for riprap studies to specify the angle of repose as a form of a mass.

Froehlich (2011) performed a multiple regression analysis on 74 stockpile samples of crushed angular and natural rocks. A simple expression to calculate the mass angle of repose of open-graded rock riprap was then developed and specified as follows:

$$\ln \varphi_r = 3.46 + 0.0833 I_1 + 0.188 I_2 \qquad \textbf{Eq. 5}$$

Where, φ_r is the expected mass angle of repose, I_1 and I_2 are the indicator variables defined as following:

$$I_1 = 1 \text{ for subangular and angular}, 0 \text{ for round}$$

$$I_2 = 1 \text{ for angular}, 0 \text{ for otherwise}$$

In **Equation 5**, Froehlich (2011) found that the angle of repose is not statistically significant to the difference in angular and subangular shapes.

Equation 5 was further developed by incorporating the gradation to produce **Equation 6**. As a result, **Equation 6** was found to provide a much better estimation of the mass angle of repose. Froehlich (2011) defined the equation as follows:

$$\ln \varphi_r = 3.43 + 0.0799 I_1 + 0.183 I_2 + 0.125 \ln\left(\frac{D_{85}}{D_{50}}\right) \qquad \textbf{Eq. 6}$$

Whereby, D_{85} = size of stone which are 85% finer

D_{50} = size of stone which is 50% finer

The above literature studied the angle of repose of rocks open to the atmosphere. However, riprap is generally fully or partially submerged when there is flow. It is justifiable to assume that studies with submerged riprap rock and investigation of the related mass angle of repose of rocks could be more representative. However, there was no such study found in the retrieved literature for this research.

2.1.7 Shape

The shape of a rock refers to the geometric description of the dimensions and appearance of the pertinent sediment or rock. In general, the shape of a rock is described as round, blocky, angular or platy depending on the nature of its geometric or physical appearance. The shape of a rock has a significant influence on the determination of the stability of riprap revetments. The main physical effect of stone angularity is the contribution to the increase in interlocking. As a result, the angle of repose increases as well (Froehlich, 2011). An increase in the interlocking and angle of repose, therefore, justifies the assumption of an increased stability for angular riprap.

From previous research, it can be deduced that riprap shape has a significant influence on the stability of riprap. Abt and Johnson (1991) recommended that a 40% increase in the size of round riprap rocks provides a comparable size of angular riprap rock which provides the same level of protection. However, Abt *et al.* (2008) determined that the required round-shaped rock ranges from 5% to 42% larger than angular rocks to protect the riprap slopes of 40% in similar flow conditions. Moreover, Abt *et al.* (2008) emphasised that the deviation can reach up to 70%. Therefore, it cannot be easily concluded what percentage of round rock can provide the same stability as a comparative angular rock. Nevertheless, it is apparent that angular rocks provide higher stability compared to similar sized round rocks. The increased stability may be due to the increased propensity of angular rocks to interlock with each other, therefore reducing a rock's likelihood of sliding or rolling NCHRP (2006) and Abt *et al.* (1988).

Literature has little specific guidelines or specification regarding the specific shape dimensions of angular rocks. Most literature and design guidelines usually specify that an angular rock is generally accepted for riprap design and research e.g. Brown & Clyde (1989), Keller (2005), Abt *et al.* (1989). However, NCHRP (2006) and CIRIA *et al.* (2007) have attempted to close this gap by providing comprehensive guidelines and specifications of shape descriptors that can facilitate the choice of an appropriate rock shape.

An angular riprap rock is recommended in riprap revetment design, provided the rock is not thin, platy or long, i.e. resembling a needle-like shape (NCHRP, 2006). Thus, NCHRP (2006) recommends the use of the length to thickness ratio less or equal to three, denoted as LT. The LT ratio limit of three ensures that the chosen angular rock is not platy or thin, but slightly blocky.

Another useful riprap shape descriptor is the blockiness, denoted as BL_c (%). The blockiness is the ratio of the stone volume to the orthogonal XYZ. The XYZ box dimension measurement procedure is further explained in CIRIA *et al.* (2007). The significance of specifying BLc is that it is related to the compactness and packing behaviour of the rocks when placed individually. Moreover, it is emphasised that the BLc not be correlated to the LT ratio, meaning that one cannot deduce one parameter from the other (CIRIA *et al.*, 2007). **Figure 3** shows the relation between the blockiness and shape of angular rocks, from left to right, BLc=80%, 60% and 40%.

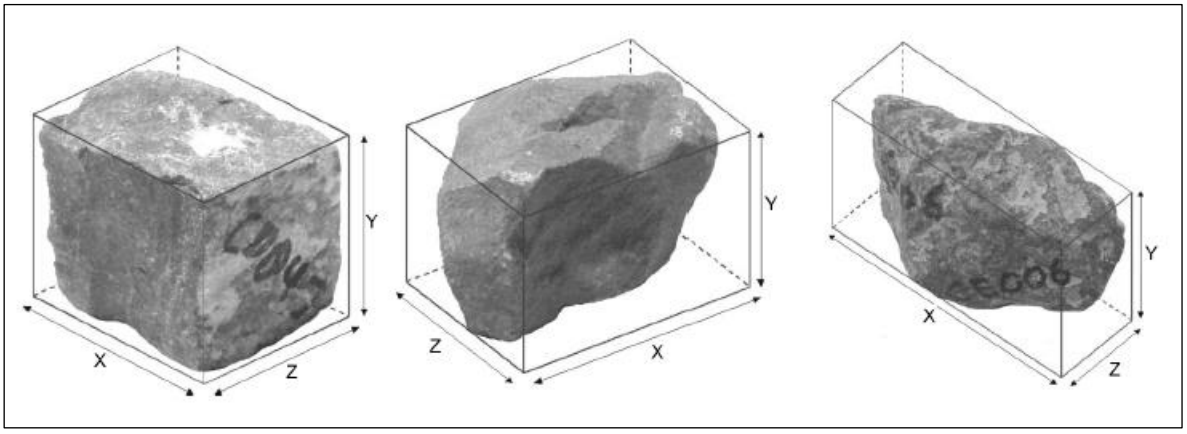

Figure 3: Illustration of the correlation between shape and blockiness of stones (CIRIA *et al.*, 2007)

2.1.8 Durability

The durability of riprap stone refers to the stone's capacity to sustain loads and impacts for the duration of its design life without degrading. Since stones are made up of minerals, they can either degrade physically or chemically (NCHRP, 2006). Determining the rock's ability to sustain its original shape and weight is vital in durability tests. Durability tests involve the testing of the rocks against stresses, such as:

- Rolling;
- Freezing;
- Thawing;
- Drying; and
- chemical resistance tests against sodium or magnesium sulphate.

NCHRP (2006) states that the stone sample needs to retain a specific minimum of its original weight after it has been subjected to different tests. After that, a pass or fail decision is made based on the riprap stone sample's performance in the tests.

2.1.9 Filter Layer

The filter layer is the underlying transitional gravel layer between the riprap and the protected underlying soil. Proper design of the filter layer is critical for non-cohesive soils because if the non-cohesive soils are eroded, then the foundation of the riprap may be compromised, thus failing the top riprap protection layer. According to Ji, *et al.* (2013) the filter layer is important due to its ability to prevent riprap subsidence which could result from the winnowing or leaching of the underlying soil that should be protected by riprap from eroding.

Smaller gravel stones are typically used as a filter layer. Alternatively, geotextile material can be installed. According to the Design of Riprap Revetment, Hydraulic Engineering Circular No.11(1989) widely known as the HEC-11, the main advantages of using geotextile filter layers are listed as follows:

- quick and easy to install;
- economical design alternative;
- high tensile strengths;
- consistent quality of material; and
- removes the time and effort spent in determining the availability of gravel sizes and quality of the filter layer.

When gravel is used as the bedding filter layer a well-known criterion is generally applied. The filter layer needs to adhere to the following criteria (CIRIA *et. al*. (2007) and HEC-11(1989):

$$\frac{D_{15(filter\ layer)}}{D_{85(protected\ layer)}} < 5 > \frac{D_{15(filter\ layer)}}{D_{15(protected\ layer)}} < 40$$

In the HEC-11(1989) it is argued that the inequality on the left-hand side of the criteria intends to prevent piping through the filter layer, the middle part of the inequality intends to provide sufficient permeability for the structural bedding layers and the right-hand side portion of the inequality ensures a uniformity criterion.

A guideline for the thickness in relation to the D_{50} of the filter layer could not be found from the two design manuals. However, HEC-11(1989) recommends that the thickness of the filter layer should be between 0.15 m to 0.38 m for a single filter layer. A double layered filter blanket must adhere to a thickness of 0.1 m to 0.2 m per layer.

Therefore, the answer to the question of whether a geotextile or gravel filter layer should be used for a specific site merely depends on the availability of the filter materials. When both filter layers materials types are available, a cost-benefit analysis may be applied to decide which solution will result in the most economical and sustainable solution. In the case where only one of the two filter types are available, then it would be wise to use the available resources in that case as it is generally expensive to transport materials from outside the local project area.

2.2 Riprap Failure Modes

To effectively study riprap incipient motion, it was inevitable that a comprehensive literature study of the failure methods was undertaken. The understanding of the failure modes facilitated the planning and design of the laboratory hydraulic model. The most cited literature about riprap failure modes was by Blodget and McConaughy (1986). There are four different riprap failure modes, as defined in the sections below, including the probable causes of each failure mode.

2.2.1 Particle Erosion

The particle erosion failure mode is described as the continuous removal of individual riprap rocks due to excessive hydraulic stresses from the flowing water. **Figure 4** shows a typical particle erosion aftermath.

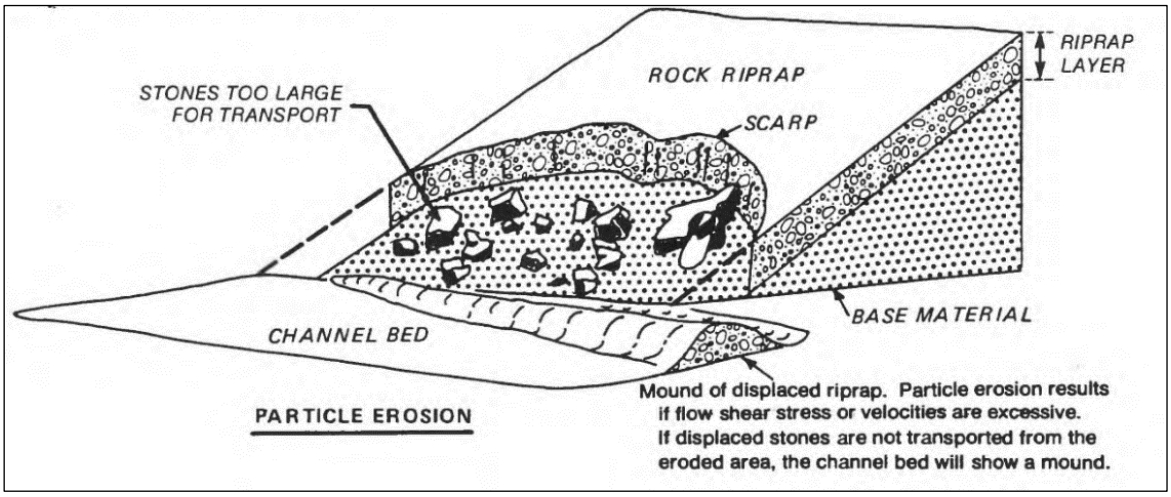

Figure 4: Particle erosion failure mode on a riprap protected side bank (Blodgett, 1986).

Factors such as flow channelisation, abrasion, ice flow, debris flow, and eddies are referred to as the initiators of particle erosion. Stone undersizing, steep side slope, improper riprap gradation and removal of stones from impact forces are possible causes of particle erosion (Blodgett,1986).

2.2.2 Translational Slide

A translational slide is a form of a catastrophic riprap failure mode where a mass of riprap material abruptly moves down the slope and leaves a fault line on a horizontal fault plane. The development of a translational slide may be seen by horizontal cracks along the channel flow direction. **Figure 5** below shows an illustration of the translational slide failure mode.

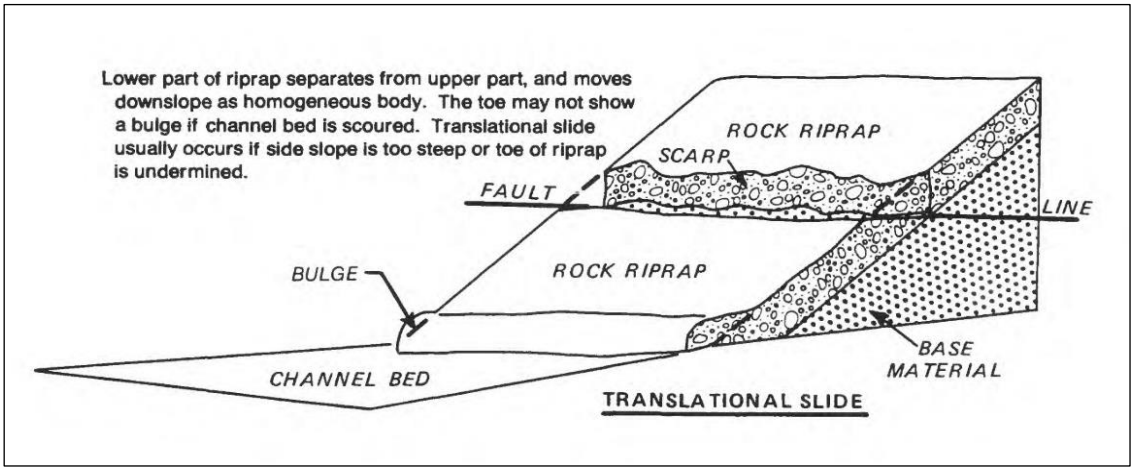

Figure 5: Translational failure mode on a riprap protected side bank (Blodgett, 1986)

The main cause of the translational slide failure mode is generally due to flows that undermine the riprap toe of the bank. The probable cause of the undermining toe material is due to the scour or erosion of particles at the toe. Possible mechanisms that can contribute to translational failure are steep bank slopes, excess pore pressure at the toe or impacts resulting in a reduction of the toe support (Blodgett,1986).

2.2.3 Modified Slump

The modified slump is the mass movement of the underlying material along an internal slip surface within the riprap thickness as shown in **Figure 6**. The base material does not fail in the modified slump failure mode.

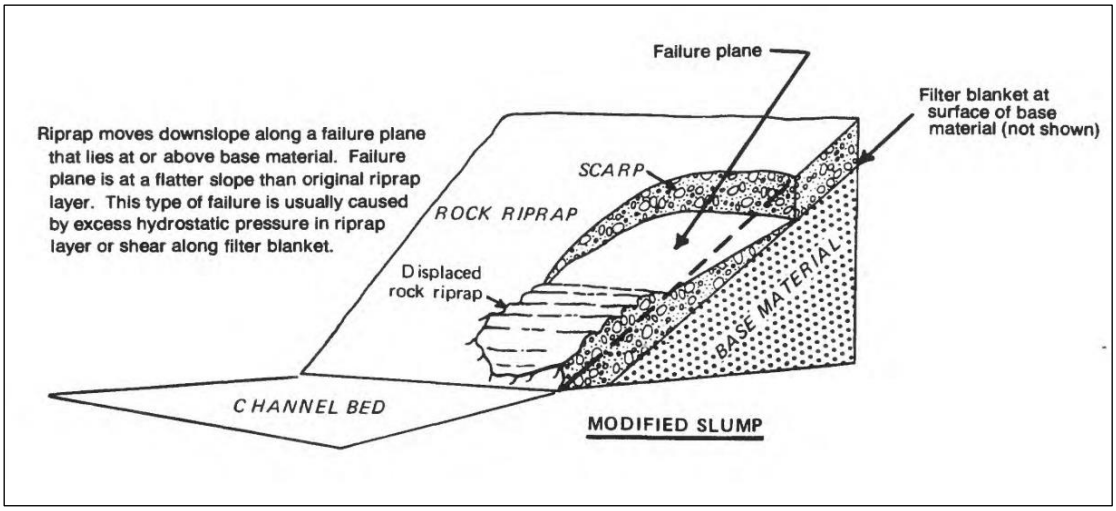

Figure 6: Modified slump failure on a riprap protected side bank (Blodgett, 1986)

Possible causes of slump failure are steep riprap slopes that are close to the angle of repose of the riprap rocks and the dislodging due to the settlement of underlying material that supports critical upslope riprap material (Blodgett,1986).

2.2.4 Slump

A slump failure mode is a form of rotational movement along a slip surface that has a predominantly concave shape. Unlike the modified slump, the slump failure mode occurs due to the failure of the base material. The base material fails because of shear failure in the underlying material. **Figure 7** shows a typical slump failure and the characteristics involved in the failure type.

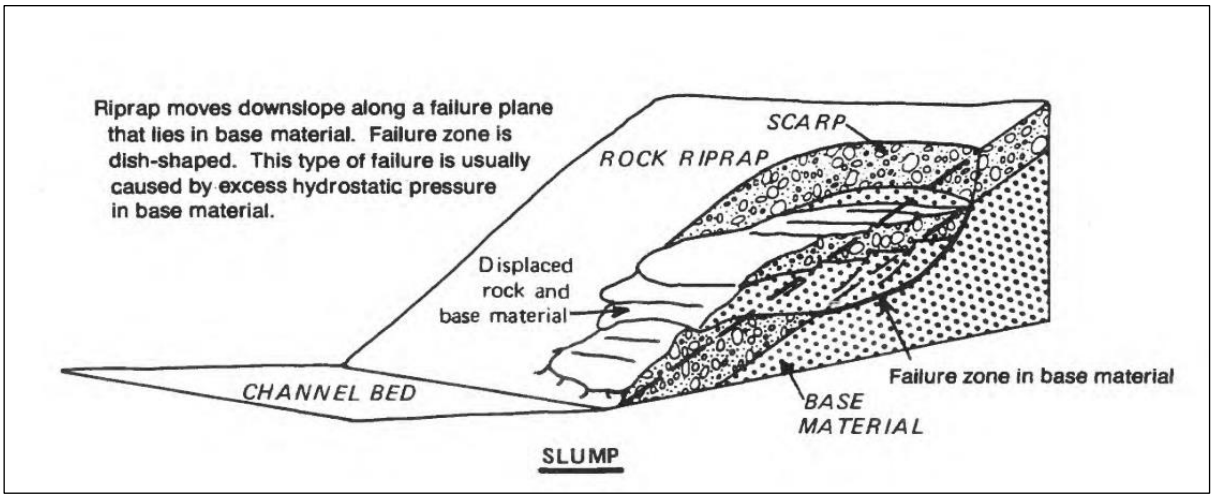

Figure 7: Slump failure on a riprap protected side bank (Blodgett, 1986).

One of the factors that initiate slump failure is the presence of excess water pressures on the underlying base material. Possible causes of slump failure may be attributed to the existence of impermeable non-homogenous base material, steep riprap slopes and excessive overburden at the top of the slope (Blodgett,1986).

From the failure modes described and illustrated by Blodgett (1986) in **Figures 4** to **7** above, the major causes of failure for riprap can be summarised as follows:

- Undersizing of the riprap median stone size.
- Placement of improperly graded riprap material.
- Improper placement or dumping of riprap.
- Underlying filter material not installed or damaged.
- Placement of riprap on very steep side slopes.
- Excessive hydrostatic pressure that leads to failure of the underlying base material.

When designing riprap, it is critical that the above failure modes and the listed causes are understood. The next section provides a summary of compensating provisions for the failure modes listed in **Figures 4 to 7**.

2.2.5 Summary of Failure Modes and the Respective Provisions

A comprehensive summary of riprap failure modes is provided in the NCHRP (2006). **Table 3** provides a summary of the failure modes, the failure mode effects on other components of the riprap system, methods to detect failure mode, and the recommended safety provisions.

Table 3: A summary of riprap failure modes, extracted from NCHRP (2006).

Failure modes	Effects on other components	Effects on the whole system	Detection methods	Compensating provisions
Translational Slide or slump (slope failure)	Disruption of armour layer	Catastrophic failure	A mound of rock at bank toe; unprotected upper bank	Reduce bank slope; use more angular or smaller rock, use a granular filter rather than geotextile.
Particle erosion (rock undersized)	Loss of armour layer, erosion of filter	Progressive failure	Rock moved downstream from the original location, exposure of filter layer	Increase rock size, modify rock gradation.
Piping or erosion beneath armour (improper filter)	Displacement of the armour layer	Progressive failure	Scalloping of the upper bank; bank cutting; voids beneath and between rocks	Use appropriate granular or geotextile filter.
Toe failure (Under designed)	Displacement or disruption of armour layer	Catastrophic failure	Slumping of rock unprotected upper bank	Increase size, thickness, depth or extent of the toe.

2.3 Incipient Motion Theories

There are various approaches adopted to study the incipient motion of particles within the sediment transportation field. The most common theoretical approaches are the shear stress-based, velocity-based, and stream power-based theories. The shear stress approach specifies the bed shear stress in which the motion of particles is instigated. The velocity approach specifies the threshold velocity as

the main parameter to define the state of particle motion at a specific velocity. Generally, Shields (1936) dimensionless shear stress parameter was used for shear stress-based studies.

Lastly, the stream power theory has gained more popularity when studying the incipient motion of riprap. This has been made possible by linking the stream power theory and using Liu's (1957) MN as a criterion to specify the point of incipience for particles. The following sections provide a review of the three main approaches which are generally adopted in incipient motion research studies.

2.3.1 Incipient Motion in Terms of Shear Stress

Within the theme of sediment incipient motion, the shear stress-based method appears to be one of the oldest. Moreover, Shields' (1936) shear stress concept of incipient motion study is claimed to be one of the most cited and popular in the study fields of sediment transport and river hydraulics (Armitage and McGahey, 2003), (Samos, 2014). Fundamental to Shields' (1936) theory is the concept of incipient motion in which particles on a loose sediment bed are at a transition from a stationary state to a state of instigation of motion due to excess hydrodynamic stresses acting on the bed particles (Siloes, 2014).

Shields (1936) is claimed to be the pioneer of the bed shear stress theory of sediment incipient motion. However, from Buffington and Montgomery (1998) it is evident that Shields' (1936) pioneering findings regarding the critical shear stress and dimensionless particle Reynold number were founded from Nukuradse's (1933) theory. Shields (1936) hypothesised his work under Nukuradse's (1933) theory, which is defined as follows:

$$Re^*_c = \frac{u^*_c K_s}{\nu} \qquad \textbf{Eq. 7}$$

Where,

u^*_c = Critical shear velocity

K_s = Boundary roughness length scale

ν = Kinematic viscosity of water

Shields (1936) introduced the D_{50} median particle grain size to replace the K_s in Nukuradse's expression. As to Shields, being a pioneer of the theory is a matter of contention for another day, but it is indisputable that Shields' (1936) shear stress theory for incipient motion has contributed significantly to the study of sediment transport and hydraulics. Engineers, geomorphologists, and stream ecologists rely on the use of the critical shear stress methods of incipient motion to solve problems pertinent to their fields of specialisation (Shvidchenko *et al.*, 2001).

According to Buffington and Montgomery (1998), from the use of dimensional analysis, Shields' (1936) findings validate that the dimensionless critical shear stress (τ^*_c) varies with the critical dimensionless particles Reynolds number (Re^*_c), defined as follows:

$$\tau^*_c = \frac{\tau_c}{(\rho_r - \rho_w) g D_{50}} \quad \textbf{Eq. 8}$$

and the critical particle Reynolds number is defined as follows:

$$Re^*_c = \frac{u^*_c D_{50}}{\nu} \quad \textbf{Eq. 9}$$

Where,

τ_c = Critical shear stress

ρ_s = Density of the particle

ρ_w = Density of water

g = Gravitational acceleration

D_{50} = Median particle grain size

ν = Kinematic viscosity of water

u^*_c = Critical shear velocity

The critical shear stress, τ_c, is related to the shear velocity, u^*_c. The two variables are interchangeable through the following equation (Buffington and Montgomery, 1998):

$$u^*_c = \sqrt{\frac{\tau_c}{\rho_w}} \quad \textbf{Eq. 10}$$

Figure 8 illustrates Shields (1936) relationship between the dimensionless critical shear stress and particle Reynolds number. The θ , also known as the Shields parameter, in the graph represents dimensionless critical shear stress, τ^*_c. The graph displays the area in which most researchers' data lies. The uppermost area illustrates the conditions in which particle movement would be initiated. The area of no movement of the particle, which is also referred to as the incipient motion state, is at the bottom of the graph, in the area written "no motion". Thus, it was earlier claimed that the shear stress-based theory for incipient motion is useful in sediment transport studies due to its potential to solve sediment incipient motion related problems.

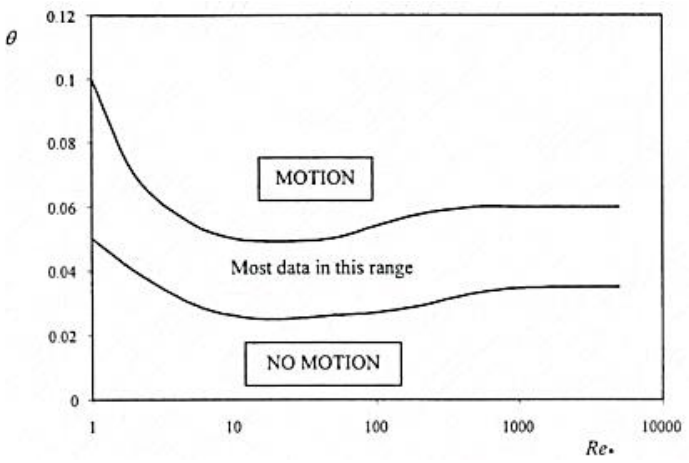

Figure 8: Shields diagram showing the relationship between dimensionless critical shear stress and the particle Reynolds number (Armitage, 2002).

The Shields diagram shows the data scatter, which is illustrated by the broadband of the data range in between the motion- and no-motion- data bands. According to Armitage & McGahey (2003), the wide variation in the data scatter is an indication of the complexity that is linked to defining the exact point of incipient motion of a particle. Buffington and Montgomery (1998) also agree that the scatter in the data of traditional Shields diagrams is a manifestation of the systematic methodological biases on the definition of the point of incipience of the particle.

However, Buffington and Montgomery (1998) argue that there are no exact values for the dimensionless critical shear stress from the gravel-bed river in rough turbulent flow, but the scatter should instead be interpreted as a band rather than an anticipated definite curve.

Concerning the spread in data scatter in the Shields diagram, Buffington (1999) claims that the scatter of τ^*_c values might be reduced through the calculation of the bed stresses with corrected channel bed roughness values. Ward (1969) also proved that the inclusion of the relative density term, defined as $(\rho_r - \rho_w)$, plays a critical factor in reducing the scatter. Buffington (1999) does agree that other factors have an influence on the scatter illustrated in Shields' (1936) traditional plot of dimensionless critical shear stress values.

Shields' dimensionless shear stress for the incipient motion approach has several limitations accompanying its application. One widely known drawback is the presence of the shear velocity on both the axes of the Shields (1936) diagram. The presence of the shear velocity in both axes results in inconveniences. One is the fact that to solve the dimensionless critical shear stress and the particle Reynolds number, an iterative process is required to be followed. Secondly, Beheshti and Atai-

Ashtiani (2008) argue that the presence of the shear velocity in both axes causes difficulties in interpretation since the shear velocity is interchangeable in **Equation 10**.

Yang (1973) also stresses the fact that in the determination of the shear stress applying **Equation 11** does not use local velocity distribution:

$$\tau_0 = \rho_w g D_w S_0 \qquad \textbf{Eq. 11}$$

Equation 11 assumes an average uniform velocity over the channel bed which is not a realistic representation. Yang (1973) emphasises the fact that lift forces play a critical role in the instigation of sediment incipient motion. However, the Shields diagram never took the lift forces into account. Yang (1973) criticises the fact that Shields only accounted for or assumed that the shear stress is the only cause of sediment transport load.

The previous critique is vital because the incipient motion of sediment particles depends on many other parameters (Buffington and Montgomery,1998), which influence the point of incipient motion of sediment particles. These include, among other things:

- sediment size;
- shape;
- density; and
- placement.

Regardless of the limitations and criticism that Shields' (1936) shear stress methods have received, the method is still used and widely applicable internationally in the fields of research, engineering and conservation of soil natural resources. One of the reasons for designers to still use this method is that it computes a conservative solution by specifying large design particles. Moreover, it is grounded on an eloquent theory of shear stress that makes other methods seem less attractive or have limitations regarding the scope of application (Buffington & Montgomery, 1998). As a result, SANRAL Road Drainage Manual (2013), CSRA (1994) and CIRIA *et al*. (2007) are among many design guidelines for riprap design which adopted the Shields shear stress theory for designing purposes.

The SANRAL (2013, pp 5-26) and CSRA (1994) cite and recommend an approach by Henderson (1966). The riprap design approach by Henderson (1966) was directly derived from the Shields diagram. The chosen value of dimensionless critical shear stress corresponds to a conservative value of 0.056, interpolated from the turbulent flow region where Re^*_c>400. The chosen value is a constant in the Shields diagram in the turbulent flow regime. Plus, at that point, it is assumed to depict the

point of incipient motion of riprap. The following derivation was used to derive the equation used to determine the median size of required riprap, based on Henderson (1966), but extracted from SANRAL (2013, pp 5-26):

$$\Theta^*_c = \frac{\tau_c}{(\rho_r - \rho_w) g D_{50}} = 0.056 \qquad \textbf{Eq. 12}$$

However, for uniform steady flow, $\tau_0 = \rho_w g D_w S_0$ **Eq. 13**

Thus, substituting the shear stress **Equation 13** into the dimensionless critical shear stress **Equation 12** results in:

$$\frac{\rho_w g D_w S_0}{(\rho_r - \rho_w) g D_{50}} = 0.056 \qquad \textbf{Eq. 14}$$

If $\rho_r = 2650 \frac{Kg}{m^3}$, then $\frac{D_w S_0}{1.65\ D_{50}} = 0.056$ **Eq. 15**

Thus, at the incipience point the stone size required to initiate movement of riprap rock is calculated using **Equation 16**:

$$D_{50} = 11 D_w S_0 \qquad \textbf{Eq. 16}$$

Where D_w is the water depth and S_o is the bed slope.

The dimensionless shear stress theory is not ultimately disputed and is supported by most researchers. The reason for this support can be attributed to the eloquent presentation of his findings with a simple dimensionless diagram that is justified by a sound and comprehensive theory (Buffington, 1999). The accuracy of Shields' data is indeed self-explanatory that there is a scatter in his findings, and thus the manifestation of a band instead of an exact curve. Consequently, Shields (1936) remains useful even to the individuals not accepting its application for solving incipient motion problems, because the theory can be used as a theoretically comprehensive and sound reference point for riprap incipience studies.

2.3.2 Incipient Motion in Terms of Velocity

Sediment incipient motion may be studied based on the velocity flow. The velocity-based concept of incipient motion is grounded on the determination of the stable riprap rock size, which would safely resist the channel flow at a specific threshold velocity. The approach is much more straightforward for application purposes, especially in designing stable channel beds. Thus, it may be more attractive to engineers during the process of designing. Armitage (2003) agrees that velocity-based approaches

are convenient to use because the channel velocity distribution is easily visualised, and the average channel velocities are relatively simple to calculate. Physical and numerical modelling methods facilitate the ease of calculating average critical velocities, according to Maynord (1986).

There have been several velocity-based incipient motion studies conducted ever since the concept of incipient motion was established. These studies provide a fundamental theoretical base for the application of velocity flow as a reasonable approach to study incipient motion. According to Armitage & McGahey (2003), Fortier and Scobey (1926) conducted one of the earliest velocity-based theory for incipient motion studies.

According to Armitage and McGahey (2003), Hjulstrom (1935) conducted a study in which the objectives were to investigate the relationship between the mean velocity and size of respective sediment at the point of incipience. The curves in **Figure 9** were developed and used as criteria of incipient motion. In **Figure 9**, three main regions were highlighted whereby erosion, transportation and sedimentation are anticipated. Erosion is the uplifting or sliding of a particle from the bed due to loss of friction. Sedimentation is the process where eroded particles land or drop onto the riverbed due to loss of energy on the streamflow. Transportation is the process whereby the flow transports an eroded particle from the bed.

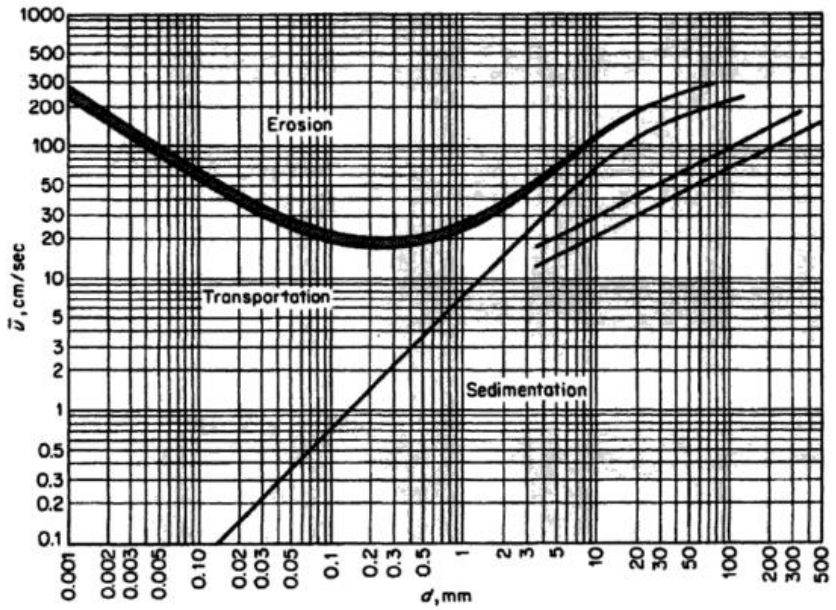

Figure 9: Erosion deposition criteria for uniform particles versus the threshold mean velocity after Hjulstrom (1935).

Isbash (1936) performed a classical velocity-based study. Isbash investigated the critical velocity, which caused dumped stones in a channel flow to become unstable and consequently to overtop. However, the main objective of Isbash's study was to be able to obtain stability conditions of round

rocks to construct dams in flowing channels (Abt & Johnson, 1991). Isbash concluded with the following relationship (Abt & Johnson, 1991):

$$V = Y\psi d^{\frac{1}{2}} \qquad \textbf{Eq.17}$$

Where:

Y = Coefficient

$$\psi = \left(2g\left(\frac{\Delta_s - \Delta_w}{\Delta_s}\right)\right)^{\frac{1}{2}}$$

Δ_s = Stone unit weight

Δ_w = Water unit weight

d = Stone size reduced to an equivalent sphere

Therefore, Isbash (1936) ended up with an equation that later permitted the design and construction of dams by the method of dumping stones in a flowing river channel while the stones remained stable against the channel flow.

By applying dimensional analysis, Maynord *et al.* (1989) also conducted a study in which the local depth-average velocity was used to determine the stable stone particle size, specifically to develop a simple riprap design method.

Armitage (2003) also lists several well-known researchers who conducted velocity flow-based incipient motion studies. The researchers comprise Shamov (1952), Levy (1956), Knoros (1958), Liu (1957), Gonchorov (1962), Zang and Wan (1963). A summary of each of the previously mentioned researchers' approaches can be found in Chien and Wan (1998).

From the above, it is evident that studies of incipient motion based on velocity flow are in abundance. However, many researchers are reluctant to use the velocity-based approach for incipient motion studies e.g. Armitage & McGahey (2003), Raudziki (1998). The main reason for their reluctance is the limited application of the velocity-based approach in incipient motion studies.

The limitation concerning the applicability of the average velocity in incipient motion studies is because the average velocity of the stream is not representative of the velocity flow conditions at the boundary. The average velocity does not affect the particle stability in the boundary. The stability of particles near the boundary is dependent on the velocity gradients near the boundary (Stoffberg, 2005).

As a result, it can be argued that a much more representative velocity that is near the riprap on the bed or bank of a channel may be much more representative of the local velocity conditions near the particle (Stoffberg, 2005). However, the main problem concerns the difficulty to accurately determine the local velocity at the vicinity of the riprap (Maynord *et al.*, 1989). Due to the unavailability of accurate methods of determining the actual local velocity near the boundary, it can be argued that the velocity approach is not an attractive method of application for incipient motion studies.

2.3.3 Incipient Motion in Terms of Stream Power Theory

The stream power approach of studying incipient motion has been introduced as a favourable alternative theoretical approach contrary to the shear stress- and velocity-based incipient motion study approaches. Previous research on the stream power approach proves that the principle of stream power has good potential in solving problems and in the development of new solutions in the study fields of incipient motion, erosion, and sediment transportation, especially in fluvial processes research.

Figure 10 shows an arbitrary stream reach in open channel flow conditions. The water is flowing through the stream at a water depth, D_w and a bed slope S_o. For the illustrated stream to keep flowing, some form of energy is required to keep the water flowing. This energy is outsourced from the potential energy of the stream as it moves along the sloped bed. The rate at which this energy is made available is known as the available stream power or preferably the input stream power, as per Rooseboom & Mulke's (1982) definition. The available stream power is mathematically defined as follows:

$$P_{available} = \rho_w g S_0 V \qquad \textbf{Eq. 18}$$

Where,

$S_0 = Energy\ Slope$

$V = average\ velocity\ of\ flowing\ stream\ section$

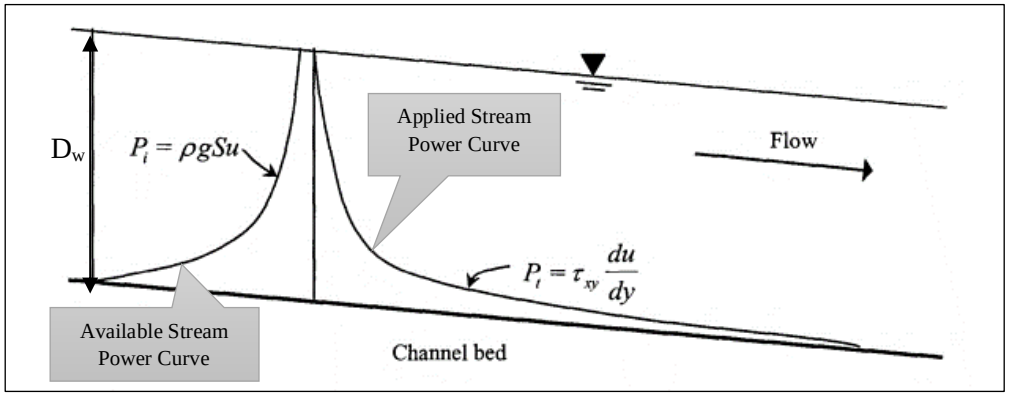

Figure 10: Showing the distribution of input and applied stream power in an arbitrary reach (Rooseboom, 1992).

As the water flows down the stream, the available stream power or potential energy is expended in the form of heat and kinetic energy. Energy is lost due to shear forces within the water particles and through the interaction of water with the bed particles. In summary, the potential energy of the flowing water is obtained from the gravitational forces, thereafter the potential energy of the flowing water is dissipated through heat and frictional interactions with the streambed (Armitage, 2002).

The rate at which the available energy of the water is dissipated in the uniform open channel flow is known as the dissipation or preferably applied stream power as per Rooseboom and Mulke's (1982) description. The applied stream power is mathematically defined as follows:

$$P_{applied} = \tau_0 \frac{du}{dy} \qquad \textbf{Eq. 19}$$

Where, $\tau_0 = bed\ shear\ stress$

$\frac{du}{dy} = velocity\ gradient$

The diagram in **Figure 10** aptly facilitates the understanding of a few fundamental concepts and principles governing the stream power variations along the reach. The stream power input curve on the left in **Figure 10**, shows a logarithmic relationship between the depth and available stream power. The logarithmic nature of the relationship emphasises the view of the velocity being at a maximum on the surface of the water and theoretically equal to zero at the bed of the streamflow.

The stream power dissipation curve on the right-hand side in **Figure 10**, demonstrates that the stream power is decreasing exponentially from top to bottom. The decrease in stream power from top to bottom is due to the shear stress being theoretically zero at the surface and at a maximum at the

bottom of the bed. Moreover, the velocity gradient and shear stress are at a maximum near the riverbed, further contributing to the high stream power dissipation at the bottom.

Three well-known laws govern hydraulic flow in the uniform open channel, namely the conservation of mass, momentum and energy laws. However, according to Rooseboom and Mulke (1982) and Rooseboom (1975), the stream power law can be defined as the fourth hydraulic law.

The stream power law states that the total input stream power is always equal to the total applied stream power. The relationship is eloquently illustrated in **Figure 10**, whereby the area enclosed by the input stream power cover equal to the area enclosed by the applied stream power. Rooseboom (1975) mathematically defined the law of conservation of stream power as follows:

$$\int_{y_0}^{D} \rho_w g S_0 V \, dy = \int_{y_0}^{D} \tau_0 \frac{du}{dy} \, dy \qquad \textbf{Eq. 20}$$

Whereby,

y_0 = is the ordinate where the velocity is theoretically equal to zero (m)

y = Distance above the bed (m)

V = Velocity at distance y above the bed (m/s)

Equation 20 illustrates the dynamic equilibrium nature of the stream power and how the stream power is never lost but conserved, similarly to mass, momentum and energy conservation. Stoffberg (2005) states that whenever there is a change on the applied stream power due to hydraulic or geometric properties of the flow, then the stream conditions always change to compensate for the induced change such that the input stream power equals the applied stream power.

According to Rooseboom (1992), the mode of flow which requires the least amount of stream power will be favoured. Therefore, this implies that fluid flow over a movable bed only applies stream power to initiate movement of the bed particles if the flow results in a decrease of the applied stream power along the bed.

The influence of the bed roughness elements relative to the viscous sublayer is critical in sediment threshold studies. The influence of bed roughness elements determines the prevailing conditions at the bed surface that influence the movement of bed material (Cunninghame, 2005). **Figure 11** physically illustrates the relationship between the depths of the viscous sublayer with respect to the height of the roughness elements, k_s (shown by the dimensional arrows in **Figure 11**).

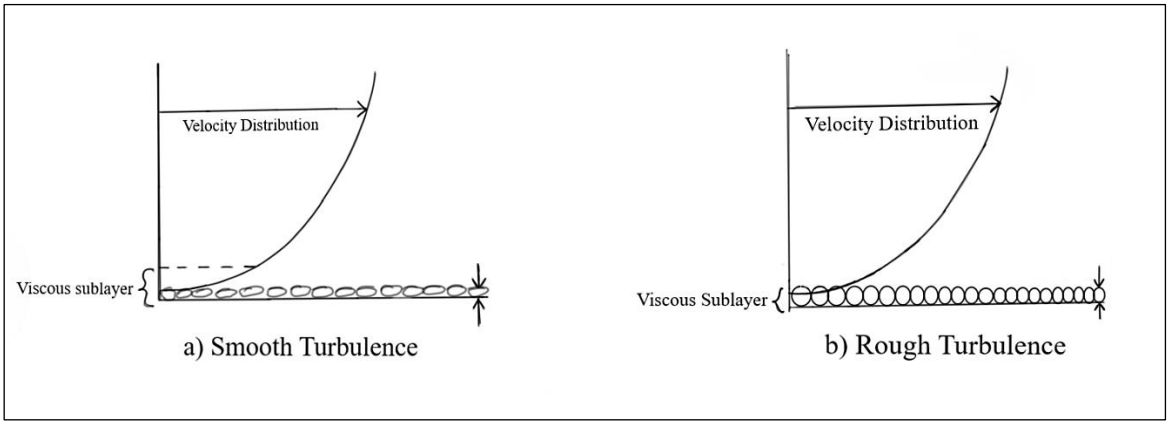

Figure 11: Showing roughness height element in relation to the viscous sublayer for smooth and rough turbulent flow.

Figure 11 (a) demonstrates a condition when laminar conditions prevail. In this case, at the bed level, the roughness element height k_s is smaller compared to the viscous sublayer. As a result, the viscous effects reduce the influence of bed roughness on the flow.

However, when turbulent flow prevails at the bed, the viscous sublayer depth reduces. Therefore, the influence of the roughness elements may become more significant than the viscous sublayer as shown in **Figure 11 (b)**. Thus, in turbulent flow conditions along the boundary, the viscosity effects are dampened and have no significant effect on the flow (Cunninghame, 2005).

Critical threshold conditions of the bed material depend on the mode of flow at the bed (Gazendam, 2005). On the other hand, the stream power applied to the bed of a channel varies according to the mode of flow along the bed. If laminar flow conditions prevail at the bed, then the laminar conditions govern the stream power at the bed. However, if rough turbulent flow prevails, the turbulent flow dynamics govern the stream power at the bed. It is critical that this distinction is recognised and models are developed accordingly.

2.3.3.1 Applied stream power: Laminar flow

When laminar conditions prevail at the bed, it is imperative that the velocity gradient is defined according to laminar flow conditions to measure the applied stream power. Thus, for uniform flow conditions, the shear stress is defined as $\tau_0 = pgD_wS_0$. Based on the shear velocity equation the shear stress is also defined as $\tau_0 = \rho u_*^2$.

The velocity gradient for laminar flow conditions can be defined as follows (Rooseboom, 1974 & 1992)

$$\frac{\partial u}{\partial y} = \frac{u_*^2}{v} \qquad \textbf{Eq. 21}$$

Therefore, $$P_{Applied(l)} = \tau_0 \frac{\partial u}{\partial y} = \rho u_*^2 . \frac{u_*^2}{v} = \frac{\rho u_*^4}{v} \qquad \textbf{Eq. 22}$$

$$P_{Applied(l)} = \frac{(pgS_0 D_w)^2}{\mu} \qquad \textbf{Eq. 23}$$

2.3.3.2 Applied Stream Power: Turbulent Flow

The difference with the laminar and the turbulent flow applied stream power is due to the definition of the velocity gradient, which describes the local velocity conditions at the bed. The velocity gradient for the turbulent flow boundaries may be defined as follows:

$$\frac{\partial u}{\partial y} = \frac{u_*}{ky} \qquad \textbf{Eq. 24}$$

Where, $k = Von\ Karman\ Constant$, absolute roughness parameter that represents the size of eddies near the bed.

$y = point\ depth\ from\ the\ bed$

As mentioned earlier, turbulent flow conditions can prevail at the bed and **Equation 25** defines the stream power over the bed, Armitage (2002):

$$P_{Applied(t)} = \tau_o \frac{\partial u}{\partial y} = \rho u_*^2 \frac{u_*}{ky} = \frac{\rho u_*^3}{ky} \qquad \textbf{Eq. 25}$$

Therefore, $$P_{Applied(t)} = \frac{\rho (g D_w S_0)^{\frac{3}{2}}}{ky} \qquad \textbf{Eq.26}$$

Equations 23 and **26** describe the applied stream power for laminar and turbulent conditions respectively. However, for particles to be entrained into the fluid flow the applied stream power needs to be higher than some arbitrary threshold stream power, defined as the required stream power. According to Armitage (2002), the power that is required to induce a resistance force for keeping a sediment particle suspended in a fluid is approximately equal to the released stream power if the particle were to be released in free fall at terminal velocity. Rooseboom (1992) defined the required stream power as follows:

$$P_{required} = (\rho_r - \rho_w) g v_{ss} \qquad \textbf{Eq. 27}$$

The ingenious implication of **Equation 27** is that the stream power required for incipient motion is dependent on the settling velocity and relative density of particles. The particle size is not directly

included in the expression but implicitly incorporated through the inclusion of the settling velocity. The settling velocity of a natural particle can be calculated from **Equation 28** Graf (1971):

$$v_{ss} = \sqrt{\frac{4}{3}\frac{(\rho_r - \rho_w)}{\rho_w}\frac{gD_{50}}{C_D}} \qquad \textbf{Eq. 28}$$

Where, $C_D = Drag\ coeffecient$

The use of average stream velocity in incipient motion studies has been identified as a critical disadvantage not only in velocity-based approaches but also in shear stress-related studies. However, many researchers agree that the boundary conditions influence the incipient motion of non-cohesive particles near the boundary. Thus the boundary velocity profile is much more representative of the flow conditions and must be used instead of the average velocity. Because of the previously mentioned fact, it has been argued that the settling velocity of a particle resembles the local flow conditions around a particle during the point of incipient motion, thus making it a suitable input parameter in representing the required stream power (Armitage,2002).

Theoretically, a particle in the streambed can only be suspended or entrained by the stream when the applied stream power is equal or exceeds the required stream power, which can be mathematically defined as (Armitage, 2002):

$$P_{Applied} \geq P_{Required} \qquad \textbf{Eq. 29}$$

However, Cunninghame (2005), points out that the movement of particles governed by **Equation 29** is not only limited to suspension. A particle can slide or roll at applied stream power lower than the input stream power. The cause is due to the stochastic nature of incipient motion, which is explained by the presence of variations in particle gradation, size, sorting, packing and orientation.

2.3.3.3. Stream Power Link with MN

MN is a dimensionless parameter used as an incipient motion criterion. MN is defined as the ratio of the shear velocity to the settling velocity i.e. $MN = \frac{u_*}{v_{ss}}$. According to the literature, Liu (1957) was the first researcher to explore the concept of the MN as a criterion for incipient motion. Liu (1957) used the MN as criteria for investigating the formation of ripples due to channel flow. Since then the approach has attracted many researchers to explore the approach further due to its potential in being a better criterion for incipient motion.

Rooseboom (1992) developed the fundamental theoretical equations that govern the behaviour of stream power principles. Rooseboom (1992) analysed the data from Grass (1970) and Yang (1973) and showed that the empirically derived MN equations for laminar and turbulent flow conditions. Rooseboom (1992) found that the theoretically derived equations that govern stream power principles agree with the empirically derived MN equations.

Figure 12 illustrates the input data and curves of researchers Rooseboom (1992), Stoffberg (2005), Yang (1973), and Armitage (2002) who have contributed towards Liu's MN criteria of incipient motion approach. The graph shows the relation between the MN and the particle Reynolds number. It can be perceived that from the Reynolds number of zero to approximately 11, the curve is nonlinear and from approximately 11 up to 10^5, the curve is approximately a constant value. The previous range of the particle Reynolds number illustrates the laminar and turbulent regions of flow respectively. An interesting observation is that for the laminar and turbulent regions, different researchers obtained different MN criteria. However, the difference in the results was relatively small. The data points being close to the curve by Rooseboom (1992) further reinforce the applicability of the theory.

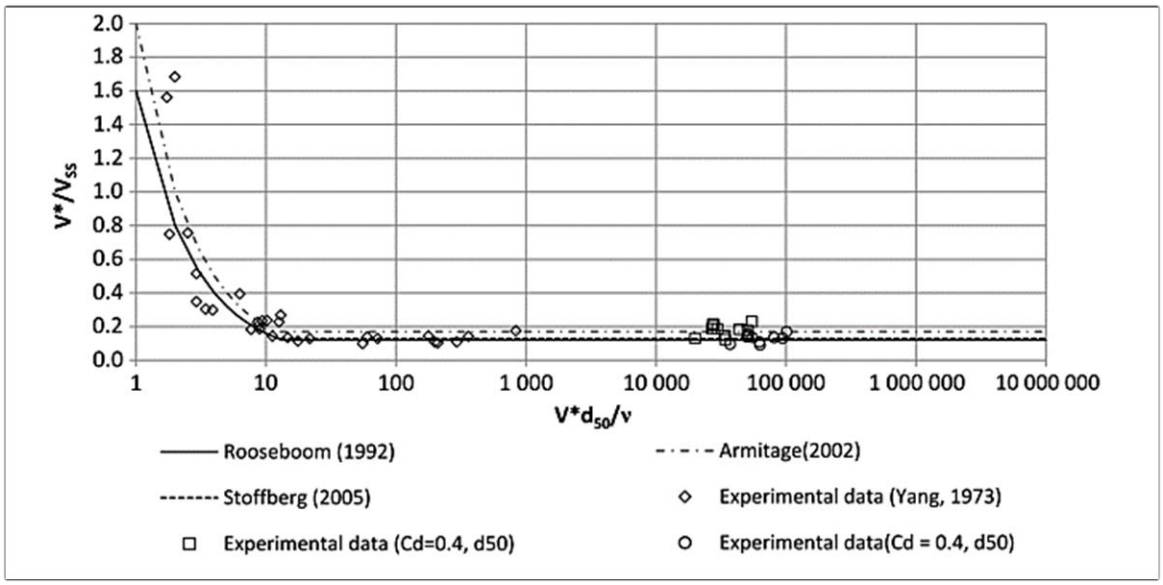

Figure 12: A graph showing the MN $\left(\frac{u_*}{v_{ss}}\right)$ criteria of incipient motion of sediment particles versus the particle Reynold number $\left(\frac{u^* D_{50}}{\nu}\right)$ (Langmaak & Basson, 2015).

Rooseboom (1992) made a significant attempt to derive the MN criteria for both laminar and turbulent flow conditions using the stream power theory as a basis. Hence, providing both analytical and empirical formulations for the study of incipient motion based on the MN criteria. From Rooseboom (1992), the MN criteria can be theoretically derived as follows:

For relatively small particles, where Re* < 1, Stokes law can be used as a reference for the drag coefficient of the particle. Therefore, it follows that the drag coefficient for small natural sediments can be estimated by:

$$C_D = \frac{32v}{V_{ss} D_{50}} \qquad \textbf{Eq. 30}$$

Substitute **Equation 30 into 28**, thereafter square each side and then rearrange to obtain:

$$V_{ss} = \frac{(p_s - p_w) g {D_{50}}^2}{24\, p_w v} \qquad \textbf{Eq. 31}$$

On the other hand, from **Equation 29** it can be deduced that the proportionality relation is:

$$P_{Required} \propto P_{Applied} \qquad \textbf{Eq. 32}$$

Therefore, the following is true if **Equation 22 and 27** are substituted into **Equation 32**:

$$(\rho_s - \rho_w) g v_{ss} \propto \frac{p u_*^4}{v} \qquad \textbf{Eq. 33}$$

Divide both sides by v_{ss}^2, then rearrange to yield the following **Equation 34**:

$$\frac{u_*^2}{V_{ss}^2} \propto \frac{\mathbf{24 v^2}}{\boldsymbol{u_*^2 D_{50}^2}} \qquad \textbf{Eq. 34}$$

Taking the square root of both sides of the equation and realising that $Re_* = \frac{u_* D_{50}}{v}$, therefore the new **Equation 35** becomes:

$$\frac{u_*}{v_{ss}} \propto \frac{4.9}{Re_*} \qquad \textbf{Eq. 35}$$

Equation 35 results in an analytical solution describing the relationship between the MN and the particle Reynolds number for laminar and uniform flow conditions for Re* < 1 of small natural sediments. As stated earlier, Rooseboom (1992) analysed incipient motion data from two researchers, namely Yang (1973) and Grass (1970) and found the following empirical relation for laminar flow conditions:

$$\frac{u_*}{v_{ss}} = \frac{1.6}{Re_*} \qquad \textbf{Eq. 36}$$

Looking at the structure of **Equations 35 and 36**, one can conclude that Rooseboom's (1992) findings effectively presented how the MN can be used to define incipient motion criteria and revealed how

the MN was linked to the stream power principle. It was expected that **Equations 35** and **36** be of similar nature but comprise of different numerators, because **Equation 35** is a theoretical equation of proportionality and only **Equation 36** is a solution equation that is based on experimental data. The reason for the different numerators in **Equation 35 and 36** is based on unknowns (drag coefficient, particle size definition and grading) involved in the hydraulic laboratory tests conducted by Grass (1970) and Yang (1973) during their studies.

As a result, Armitage (2002) recommended that it would be convenient to define the MN criterion of incipient motion in laminar boundary flow conditions as follows:

$$\frac{u_*}{v_{ss}} = \frac{\alpha_1}{Re_*} \qquad \textbf{Eq. 37}$$

Where $\alpha_1$is an empirical constant that is determined from measurements. According to Armitage (2002), α_1, is a function of the intensity of motion.

Similarly, MN derivation for the turbulent boundary conditions can be conducted. According to Chien and Wan (1998), the drag coefficient of large natural sediments in high particle Reynolds number boundaries, specifically $Re_* > 1000, C_D = 1.1$.

Substituting $C_D = 1.1$ into **Equation 28**, thereafter squaring both sides of the equation and rearrange to obtain:

$$V_{ss} = \frac{4}{3}\frac{(\rho_r - \rho_w)}{\rho_w}\frac{gD_{50}}{1.1} \qquad \textbf{Eq. 38}$$

On the other hand, substitute **Equation 25** and **27** into **Equation 32,** this yields **Equation 39**:

$$(\rho_r - \rho_w) g v_{ss} \propto \frac{p u_*^3}{ky} \qquad \textbf{Eq. 39}$$

Divide **Equation 39** by v_{ss}^3 both sides and rearrange to obtain:

$$\frac{u_*^3}{v_{ss}^3} \propto \frac{(\rho_r - \rho_w) g k y}{\rho_w V_{ss}} \qquad \textbf{Eq. 40}$$

Thereafter, substitute **Equation 38** into **Equation 40** and rearrange to obtain the following expression:

$$\frac{u_*^3}{v_{ss}^3} \propto \frac{3.3ky}{4D_{50}} \qquad \textbf{Eq. 41}$$

Finally, take the root of both sides and assume that D_{50} = y (critical value of MN), then the operation yields **Equation 42**:

$$\frac{u_*}{v_{ss}} \propto \sqrt[3]{\frac{3.3}{4}k} \qquad \textbf{Eq. 42}$$

From **Equation 42**, it is evident that for the MN under turbulent flow, at high particle Reynolds number the movability results to a constant number. For instance, at high Reynolds number the Von Karman constant, k = 0.4, and thus the theoretical solution when substituting 0.4 for the constant k in **Equation 42** results to:

$$\frac{u_*}{v_{ss}} \propto 0.69 \qquad \textbf{Eq. 43}$$

However, when Rooseboom (1992) analysed the Grass (1970) and Yang (1973) data, the constant under turbulent conditions was found to be:

$$\frac{u_*}{v_{ss}} \propto 0.12 \qquad \textbf{Eq. 44}$$

MN studies are not limited to the abovementioned researchers. Several other researchers have contributed to the database of studying incipient motion by applying the MN approach. **Table 4** comprises a list of the main researchers who have completed studies based on the MN approach to study the incipient motion of non-cohesive particles. The table illustrates the results that have been found by each investigator.

Table 4: MN criterion and the related nature of sediment motion (Cunninghame, 2005).

Reference	**Criteria**	**Nature of sediment motion**
Breusers and Raudziki (1991)	0.17<MN<0.5 0.5<MN<1.4 MN>1.4	Bed load Saltation Suspension
Julien (1995)	MN>0.2 MN>2.5	Beginning of suspension Suspended load dominates

Reference	Criteria	Nature of sediment motion
Graf (1998)	MN>0.1 MN>0.4	The beginning of load transportation The beginning of suspended load transport
Raudziki (1998)	0.17<MN<0.5 0.5<MN<1.7 MN>1.7	Bed load Saltation Suspension
Armitage and McGahey (2003)	0.12<MN<0.17 0.4<MN<0.5 MN>2.5	Sliding/rolling commences Suspension commences Suspended load dominates

From the above derivations and stream power theoretical concepts, it can be concluded that Rooseboom's (1992) MN inferences can be useful in studying incipient motion. Similarly, to Shields' (1936) shear stress method, the MN approach results are not immune to data scatter and deviations as illustrated in Table **4**. The scatter is shown by the different values found by different researchers using the same MN principle for the analysis. The investigations conducted by the researchers shown in **Table 4** show that the MN approach is a valuable theoretical approach to the studies of incipient motion.

Most importantly, it is shown that the MN has a link with the stream power and the shear stress. The link is a result of the use of shear stress equations in the theoretical derivations of the MN equations in the laminar and turbulent flow regions.

Langmaak and Basson (2015) successfully explored the extent to which the MN approach can be implemented on large riprap in steep bed slopes. The results of the study confirmed that the MN for large particle Reynolds number resulted in a constant:

$$Constant = \sqrt{k_\beta}\frac{\sqrt{gD_wS_o}}{V_{ss}} \qquad \textbf{Eq. 45}$$

Where,

k_β= Steep slope bed correction factor

$u_* = \sqrt{gD_wS_o}$ = Shear velocity

V_{ss} = Settling velocity

The MN for the study of particle incipient motion in steep beds was found to be 0.18. This value was recommended to be used for riprap design purposes in steep bed channel slopes. The MN of 0.18 for (Langmaak and Basson, 2015) study fell within the acceptable range relative to the results shown in **Figure 12**.

2.4 Hydraulic Scaling of Physical Models

It is critical that a physical model accurately simulates the hydraulic flow properties and flow behaviour of the pertinent prototype. A 100% accuracy of the model to prototype flow behaviour prediction is impossible to achieve. However, the hydraulic laws of similitude can be used to reliably predict the hydraulic flow conditions in the prototype scale based on a physical model study.

2.4.1 Hydraulic Similarity Basic Equations

For a model to behave correspondingly to the prototype the following hydraulic similarities need to apply (Chanson, 2004):

- Geometric similarity - similarity in linear dimensional lengths
- Kinematic similarity - similarity of motion
- Dynamic Similarity - similarity of forces

Geometric similarity indicates that the ratios of the prototype length to the model lengths are equal as mathematically shown in **Equation 46** (Chanson, 2004),

$$L_r = \frac{l_p}{l_m} \qquad \textbf{Eq. 46}$$

The “p” and the “m” subscripts define the prototype and model parameters respectively. The subscript r refers to the ratio of the prototype to the model. Chanson (2004), states that the length, area and volume are the main parameters in geometric similitude. Kinematic similarity infers that the ratios of the velocities in the prototype to the velocities in the model are equal, as illustrated in **Equation 47:**

$$V_r = \frac{V_p}{V_m} = \frac{(V_1)_p}{(V_2)_m} = \frac{(V_1)_p}{(V_2)_m} \qquad \textbf{Eq. 47}$$

The main parameter in kinematic similarity is the velocity. According to Bosman and Basson (2012), acceleration and velocity are regarded as the main parameters in the kinematic similarity between the prototype and the model. Finally, the dynamic similarity implies that the ratio of the forces in the prototype to the forces on the model are equal as illustrated in **Equation 48** (Chanson, 2004):

$$F_r = \frac{F_p}{F_m} = \frac{(F_1)_p}{(F_2)_m} \qquad \textbf{Eq. 48}$$

The main parameters of the dynamic similarity are the forces, stresses and pressures. The constant ratios of the previously mentioned parameters at specific points and time frames of the prototype and model imply dynamic similarity.

2.4.2 Hydraulic Similitude Laws

Four main hydraulic similitude laws govern fluid flow in the model to prototype similarities. According to Bosman and Basson (2012), the main laws of similitude are listed below:

- Froude law - Gravitational force dominant
- Reynolds Law - Fluid Viscosity dominant force
- Weber's Law – Surface Tension dominant force
- Euler's Law – Elastic forces dominant

The four laws were summarised to be used on scaling flow behaviour from hydraulic models to prototypes. The main dominant forces were linked to similarity law to guide the researcher to use the correct law when modelling hydraulic models.

2.4.2.1 Froude's Law

According to Chanson (2004) in open channel flow (river, open channels, spillways and weirs) the gravity effects are usually dominant. Thus, model to prototype similarity can be achieved by Froude similitude. Therefore, this means that the Froude number in the model and the prototype needs to be equal as shown in **Equation 49**:

$$Fr_{(m)} = Fr_{(r)} \qquad \textbf{Eq. 49}$$

The Froude number was defined as follows (Chanson.2004),

$$Fr = \frac{v}{\sqrt{gL}} \qquad \textbf{Eq. 50}$$

The parameters in the Froude number are the velocity v, gravitational accelaration g and the characteristic length L, which is normally the flow depth in open channel flows. **Table 5** provides a list of scaling ratios which can be used for scaling hydraulic parameters from model tests to prototype Chanson (2004).

Table 5: Froude Law scaling ratios

Parameter	Unit	Froude Law
Geometric properties		
Length	m	$\boldsymbol{L_r}$
Area	m^2	$\boldsymbol{L_r^2}$
Kinematic properties		
Velocity	m/s	$\boldsymbol{\sqrt{L_r}}$
Discharge per unit width	m^2/s	$\boldsymbol{L_r^{\frac{3}{2}}}$
Discharge	m^3/s	$\boldsymbol{L_r^{\frac{5}{2}}}$
Time	s	$\boldsymbol{\sqrt{L_r}}$
Dynamic Properties		
Force	N	$\boldsymbol{p_r L_r^3}$
Pressure	Pa	$\boldsymbol{p_r L_r}$
Density	Kg/m^3	$\boldsymbol{p_r}$
Dynamic Viscosity	Pas	$\boldsymbol{L_r^{\frac{3}{2}}\sqrt{p_r}}$
Surface Tension	N/m	$\boldsymbol{L_r^2}$

The Froude similitude scaling factors in **Table 5** may only be used for scaling undistorted models. Additionally, the gravitational acceleration in the model and the prototype should be the same. Lastly, it is evident from the above that the density of fluid remains the same for model and prototype given that the same fluid is used. With the above scale ratios, the researcher or engineer may confidently select model and prototype parameters given that the inertial and gravitational forces are dominant forces in the free-surface flow hydraulic systems.

2.4.2.2 Reynold's Law

Model to prototype scaling is generally performed with Reynolds number whenever the viscosity effects between the fluid and the solid boundary of an enclosed hydraulic system become dominant. The following Reynolds similitude applies in physical modelling (Chanson, 2004):

$$Re_p = Re_m \quad \textbf{Eq. 51}$$

Given that the same fluid is used in the physical model and prototype, then **Equation 51** implies (Chanson, 2004):

$$V_r = \frac{1}{L_r} \quad \textbf{Eq. 52}$$

Whenever the scale factor L_r is greater than one, then the velocity of the model must be higher than that in the prototype.

2.4.2.3 Weber's Law

Generally, when a physical hydraulic model exhibits turbulent flow and high Reynolds numbers, the surface tension may be ignored. However, surface tension effects may not be ignored when small-scale models are used for physical hydraulic modelling. Surface tension effects may be prevalent when the physical models comprise of low weir heads; air entrainment, as well as splash and spraying fluid phenomena (Weber, 1979). Chanson (2004) further states that studies involving de-aeration in shaft or bubble plums are often modelled using the Weber number scaling. According to Chanson (2004), the Weber number may be calculated using **Equation 53**:

$$We = \frac{v}{\sqrt{\frac{\sigma}{pL}}} \quad \textbf{Eq. 53}$$

Whereby v is the velocity, p is the fluid density, L is the characteristic length in the model and prototype and σ is the surface tension. According to Chanson (2004), the velocity in Weber similarity maybe scaled using $V_r = \sqrt{L_r}$.

2.4.2.4 Euler's Law

The Euler number is generally used for scaling model studies when a physical model study is comprised of an enclosed fluid flow system in which turbulence is in a fully developed state. Additionally, the viscous forces need to be insignificant compared to the inertial forces. Lastly, Euler's Law application is relevant when surface tension and gravity forces are not present. The Euler's Law in **Equation 54** illustrates that the change in pressure and the fluid velocity are the main parameters influencing the value of the dimensionless Euler number:

$$Eu = v\sqrt{\frac{p}{2}.\Delta P} \quad \textbf{Eq. 54}$$

Whereby v is the fluid velocity, p is the fluid density and ΔP is the change in fluid pressure.

2.4.3 Hydraulic Scaling Implications for Riprap Studies

Physical hydraulic models are either scaled up or down (normally down) in relation to the real-world prototype. However, for technical and economic optimisation reasons the laboratory model is generally built to be smaller than the prototype. According to Heller (2011), scale effects arise due to force ratios that are inconsistent between the hydraulic model and its pertinent prototype. The consequences of the influence of scale effects result in deviations between the upscaled model and prototype observations (Heller, 2011).

Heller (2011) argues that decreasing a model size may increase scale effects and upscaling the model size may as well result in deviations in the hydraulic parameter observations of the prototype. Thus, choosing a scale is both a technical and economic optimisation problem. As a result, physical models are normally downscaled and are consequently subjected to a degree of scale effects. To minimize the degree of scale effects on the results of a physical model the scale of the model should be made as large as is technically and economically feasible.

The following methods can be applied to achieve model-prototype similarity, to quantify or at least understand the influence of the scale effects on the hydraulic parameters being investigated (the reader is referred to Heller (2011) for an in-depth description of each of the methods):

- Inspectional analysis- similarity is achieved when both model and prototype follow a similar set of equations describing the hydrodynamic force balances.
- Dimensional analysis-similarity is achieved when each of the dimensionless parameters in the model and the prototype are quantitatively similar.
- Calibration- similarity is achieved when the model tests are executed for a prototype with observed data available, the data is generally used to calibrate the model and prototype results.
- Scale series- similarity is achieved when at least three kinematically similar models of different scales are tested in the same manner at the appropriate scale ratios.

According to Wang *et. al.* (2013) depending on the phenomena and parameters, scale effects related to employing small scale models might be corrected by means of correction parameters. This is achieved by implementing mutually-calibrated physical models and numerical models. However, it is not always possible, especially in the case where the hydraulic model being numerically modelled comprises parameters that are complex to model and quantify. For example, in this thesis, riprap is a porous media. It is physically complex to model the accurate roughness of the bed as well as the porous flow through the riprap.

Sediment transport and incipient motion studies involve the use of very small sediment particles. Wang *et. al.* (2013) argues that prototype sediment is not feasible to act as model bed material if the grain size is too fine because cohesive forces begin to emerge. According to Heller (2011), the grain median diameter in sediment transport is critical. As a result, in Heller (2011), Kobus (1980) suggests that the median grain size required to ignore the effects of cohesion in sediment transport hydraulic models should be greater than 0.0005 m (0.5mm), also the limiting median grain size was defined to be between 0.0008 m (0.8mm) by Oliverto and Hager(2005) and 0.001 m (1mm) by Schmoker and Hager(2009).

Heller (2011) and Wang *et. al.* (2013) suggest that there are common practices to deal with hydraulic model scale effects. One of the main practices of dealing with scale effects includes “avoidance”. The appropriate way to avoid significant scale effects in a Froude model requires the satisfaction of the limiting values of force ratios known as the Froude Number, Reynolds Number, Weber Number, Cauchy Number and the Euler Number.

However, rules of thumb are generally applied without doing an inspectional analysis, dimensional analysis, calibration or scale series modelling to ensure similarity in the model and prototype. Heller (2011) provides descriptive tables that can be used for applying the rule of thumbs in which the scale effects on a Froude model may be avoided. It is important to note that the rules of thumb must be applied not only based on the scale, but the investigator must look at the type of investigation executed, the hydraulic phenomenon, as well as the related prototype features to choose an appropriate scale.

From table one in Heller (2011), the limiting criteria specifically for riprap studies were not available. However, studies based on mountain rivers investigating bed morphology were referenced as generally scaled at 1:10 to 1:20 and the sediment median sizes are specified as between 0.2m to 0.9 m at slopes of up to 13%. The rule of thumb applicable to river expansion investigation were referenced as comprise a limiting criteria scale of up to 1:55 and the bed load transport was generally the investigated hydraulic phenomena.

Based on the above literature, it makes logical sense that, to avoid significant scale effects in a Froude physical hydraulic model, the chosen median riprap size needs to be large enough to ignore cohesive forces between particles as well as the model scale should range between 1:10 to 1:20, or up to 1:55. Without checking the similarity force ratios, the limiting criteria of a large scale models with large riprap median stone size investigated provides confidence that scale effects in the physical hydraulic model may be avoided in a Froude model, even though the scale effects still exist since it is impossible to obtain 100% similarity in any physical hydraulic model (Heller, 2011).

In the zones of low flow velocities where the particle Reynolds number is too small, the viscous forces become relatively large in comparison with gravitational and inertial forces (Froude scale) – the model then does not fully represent the prototype and we say scale effects influence the model results such that the model is not fully representative of the prototype in that low flow particle Reynolds number zone. In areas of high flow and consequent high turbulence, the turbulence "breaks" the viscous layers around particles/rock in the flow and then inertial and gravitational forces dominate so that the Froude scale law is then satisfied.

Based on the literature study on scale effects in Froude scaled models and specifically the statement by Heller (2011), that studies based on mountain rivers investigating bed morphology were referenced as generally scaled at 1:10 to 1:20 and the prototype sediment median sizes are specified as between 0.2 m to 0.9 m at slopes of up to 13%, it was decided to use a physical Froude scaled model (with scaling laws as per **Table 5**) of scale 1:15 to minimize scale effects and therefore to ensure that the results from the physical model study are reliable.

2.5 Literature Study Summary

This chapter reviews the critical literature for the study of the incipient motion of riprap. The first chapter investigated the literature of all the important riprap properties. These included the assessment of the literature on the size of particles, grading of riprap, rock density, the mass angle of repose for riprap, the desired shape of riprap, and the settling velocity of riprap.

From the literature, it was found that large angular rocks with a non-uniform grading are desirable for riprap design. It was also found that large angular rocks provide higher stability in the riprap layer due to the angularity of the rocks that increase the interlocking.

The settling velocity was found to be a critical parameter in the study when adopting the MN analysis approach, implying that it must be accurately determined. The settling velocity was dependent on the shape and size of the particle. However, angular rocks are irregular in shape and size. Therefore, it was required that the settling velocity of irregular shapes are accurately determined in a large laboratory settling tank rather than analytical methods.

An understanding of how and why riprap fails is critical. The review of the failure phenomena of riprap allowed the understanding of critical design parameters for designing a functional physical hydraulic model. The review of the failure modes would also facilitate the understanding of the failure types during the testing of the model for this research.

An extensive review of the literature on the theories of incipient motion was also completed. The stream power theory was found to be a useful tool in the study of incipient motion. However, shear stress-based methods are more favourable for design purposes. The velocity-based design methods are not highly reliable, and most engineers do not recommend the use of velocity-based theories due to the variations of velocity with water depth in fluid flowing channels. It was found that when the stream power theory is linked to the MN, it provides a useful tool for the studying incipient motion and for design purposes.

At the end of the literature study, a detailed description of the physical hydraulic laws applicable to different hydraulic studies was described. It was found that hydraulic similarity between the model and prototype was critical to ensure that scale effects involved are either accounted for by being avoided, compensated or corrected where possible. It was found that overlooking scale effects may result in erroneous specification of prototype hydraulic parameters. This may result in economic or catastrophic consequences in the prototype. The literature with provisions for avoiding scale effects and specifying a limiting criteria scale for Froude models was summarised at the end of the literature.

Chapter 3 : Physical Hydraulic Model Study

Based on the limitations of the physical hydraulic models due to scale effects (refer to **section 2.4.3**) a relatively large scale of 1:15 was selected to minimise scale effects so that the results obtained from the model would be a sufficiently accurate representation of prototype D_{50} rock sizes between approximately 0.5 m to 1 m. With a model scale of 1:15 D_{50} model rock sizes of 0.038m (0.57 m prototype) and 0.075 m (1.125 m prototype) were selected for the model study to determine their incipient failure conditions.

An undistorted physical hydraulic model was designed and constructed to simulate the physical hydraulic model in **Figure 13**. The physical hydraulic model study was carried out in the Department of Civil Engineering's hydraulics laboratory of the University of Stellenbosch. The test setups comprised of three main testing series, which are listed below:

- **Test series one** tested the incipient motion failure conditions of the D_{50} = 0.038 m angular riprap rock. The hydraulic tests were performed on three different steep bed slopes and one steep side bank slope.
- **Test series two** tested the incipient motion failure conditions of the D_{50} = 0.075 m angular riprap rock. The hydraulic tests were performed on three different steep bed slopes and one steep side bank slope.
- **Test series three** tested the incipient motion failure conditions of the D_{50} = 0.075 m angular riprap rock. The hydraulic tests were performed on two different steep bed slopes and one steep side bank slope. However, the riprap on the bed area was fixed using an adhesive. The bed was fixed to ensure that the bed riprap was immovable so that the incipient failure conditions of riprap on the bank could be investigated.

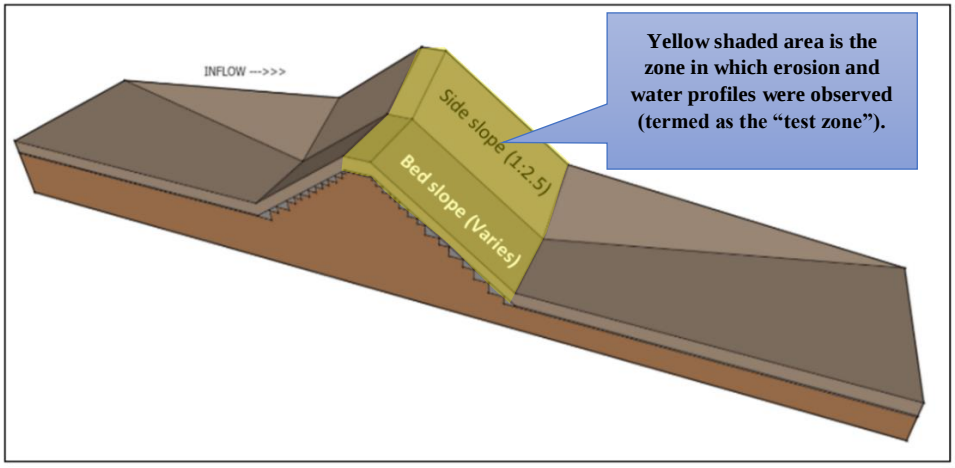

Figure 13: The general layout of the hydraulic testing model.

The main hydraulic parameters that were measured from the physical hydraulic models were the flow rate, upstream surface water elevations, the surface water elevations in the testing area and the surface water elevations at the downstream section. The measurements of the previously mentioned main hydraulic parameters allowed the riprap incipient motion analysis for this thesis. The exact steep longitudinal bed slopes and steep side bank slope tested are defined in **section 3.1** for each test.

3.1 Testing Schedule

Table 6 displays the testing schedule of all the tests and the order in which the tests were carried out. **Table 6** also shows the number of testing series undertaken at the hydraulic laboratory. Furthermore, the test numbers, and median stone size at each testing series, including the bed and side slope, are specified for each test performed. The riprap dumped over the bed was defined as either movable or immovable in each test series. Lastly, the number of successful tests performed in each test series are given in **Table 6**.

Table 6: Testing schedule of the laboratory hydraulic models

Test series	Test No.	D_{50} Size (mm)	Bed Slope	Movable Bed	Side Bank Slope	Movable Bank	Total No. of Tests
1	1-3	38	1:2	Yes	1:2.5	Yes	9
	4-6		1:2.5	Yes	1:2.5	Yes	
	7-9		1:3	Yes	1:2.5	Yes	
2	1-5	75	1:2	Yes	1:2.5	Yes	15
	6-10		1:2.5	Yes	1:2.5	Yes	
	11-15		1:3	Yes	1:2.5	Yes	
3	1-5	75	1:2	No	1:2.5	Yes	10
	6-10		1:3	No	1:2.5	Yes	

Test series one was performed with the D_{50} = 0.038m median stone size. Nine tests were carried out while changing the bed slope and keeping the riprap on the bed at a movable state. However, only seven tests were used for the analysis from Test series one. Two measured tests (in the highlighted row in **Table 6**) were not included in the analysis because there was a lack of complete survey data for the initial bed elevations and survey data which could not be found on the total station controller for these two tests.

In Test series two, tests were performed on the riprap median size of D_{50} = 0.075 m. The bed slope was changed from 0.5 to 0.4, and to 0.333. There were five tests executed on each slope. A movable bed condition represented the riprap on the bed. A total number of 15 tests were conducted so that a larger data set could be used for the analysis.

Test series three tested the same D_{50} = 0.075 m riprap size. However, tests were performed only on the bed slopes of 0.5 and 0.333. The bed was made immovable by glueing the riprap rocks on the steep bed. The main reason for glueing the bed was due to the test findings that on the previous test series one and two. The bed failed before the side bank showed any incipient movement. Ten tests were executed for Test series three, with five tests on each steep bed slope (0.333 and 0.5).

In Test series one, stability tests were performed on the D_{50} = 0.038 m riprap median stone size. The D_{50} = 0.038 m riprap median stone was tested for incipient motion failure on steep bed slopes of 0.5, 0.4 and 0.333. The side bank of the trapezoidal channel was kept at a steep slope of 0.4 for all the steep bed slopes. Test series two hydraulic tests were executed similarly to Test series one tests, except that the median stone size of the riprap was D_{50} = 0.075 m. Test series three was identical to Test series two, except that only two steep bed slopes, 0.333 and 0.5, were tested in Test series three.

3.2 Physical Hydraulic Model Design

A physical hydraulic model is a useful tool used to forecast the behaviour of a real physical phenomenon (Yalin, 1989). Yalin (1989) further stated that if the physical hydraulic model design is incorrect, then the measured results from the hydraulic model are incorrect too. Therefore, it was important for this study that the hydraulic model was designed correctly and constructed accordingly to ensure reliable data was obtained and analysed.

Hence, this section includes the details of the main physical hydraulic model design components that were accounted for, to ensure the correct design of the physical hydraulic model. This section provides the details on the following physical hydraulic design parameters: the laboratory setup (refer **Figure 14** below), the specific shape that was chosen for the hydraulic model design, hydraulic transitions, bed and side bank slopes as well as the arrestor bed length.

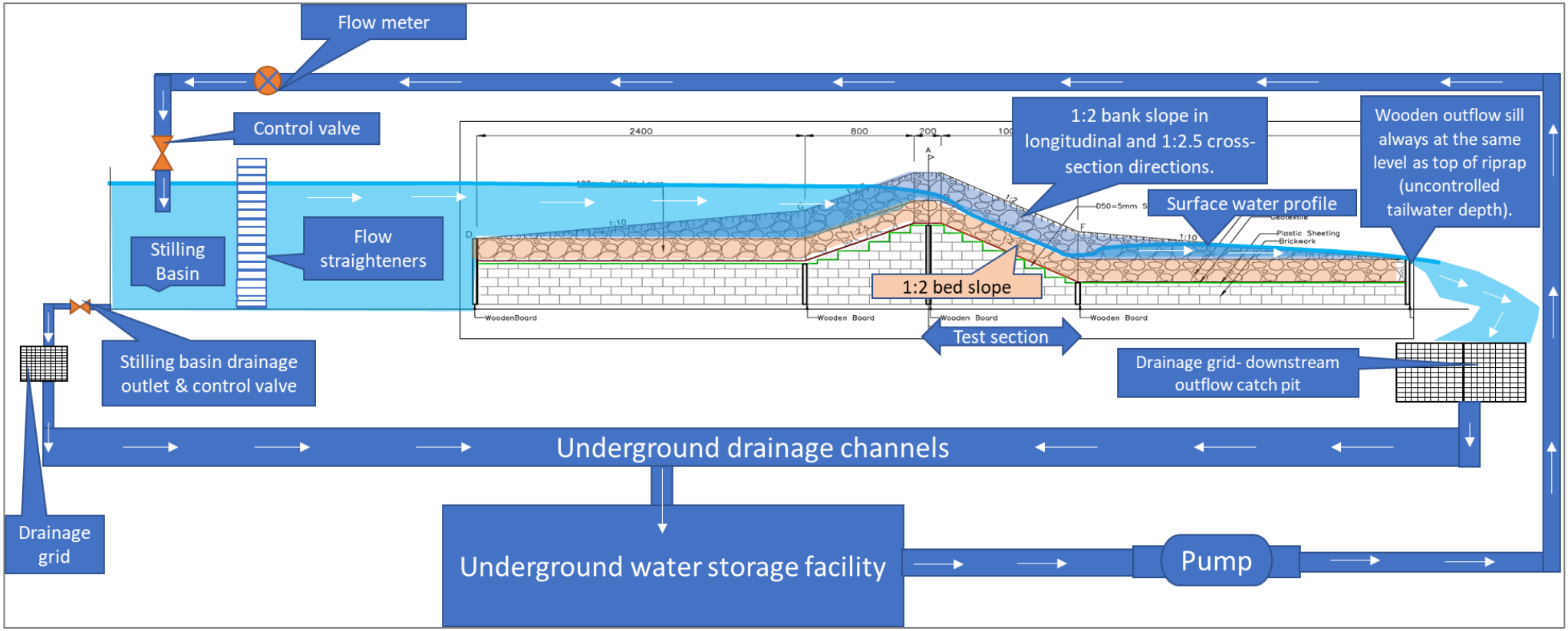

Figure 14: Overall laboratory setup of the physical hydraulic model.

The overall laboratory setup can be seen in **Figure 14**. The flow into the channel was conveyed through the hydraulic laboratory's pipelines, pumped up from the laboratory's underground water storage facility into the testing flume. The water passed through the flowmeter before entering the channel stilling basin. The control valve was used to control the flow into the stilling basin. When the water flowed into the stilling basin, air bubbles formed, turbulence and vortex were created by the water-floor impact. Thus, flow straighteners were installed to ensure that when the water reached the hydraulic model downstream, there were no major waves on the surface and the surface water level was smooth. There was no tailwater gate installed at the downstream end of the hydraulic model; water flowed freely into the laboratory drainage system downstream.

3.2.1 The General Physical Hydraulic Model Shape

The objectives of the study influenced the designed shape of the physical hydraulic model. The shape had to adhere to the following main functions:

- The testing area of the hydraulic model was designed to be a trapezoidal channel cross-section.
- The bed and bank slopes were designed to be steep.
- The upstream inflow from the flume had to be uniform with no wave at the upstream inflow section of the channel.
- The shape of the model was designed to reduce sudden contraction and expansion of the flow.
- The model had to be visible to allow accurate physical observation in the testing area.
- Adequate working space for safe movement within and around the model during the recording of measurements and observations.
- Optimised shape and size for minimal effort to change from one model setup to the next.
- Arrestor length had to be long enough to allow full development of flow.

The above considerations were afforded attention during the planning and design of the physical hydraulic model. As a result, each section of the model was designed based on the fulfilment of the required functions of the hydraulic model as well as to reduce energy losses due to a change in cross-sectional shape.

3.2.2 Design of Transitions

In open channel flow hydraulics, the change in the cross-sectional shape of a reach results in the contraction or expansion of fluid flow. Both the contraction and expansion of flow changes the fluid flow patterns in a channel. An abrupt change in the cross-sectional area of the reach can increase turbulence, velocity and instability of flow in the transitional area. However, abrupt change of cross-sectional area in this study was not a required flow characteristic.

Thus, the transitional cross-sections were designed to avoid excessive energy losses. Minimal transition effects were achieved by making the upstream and downstream cross-sectional area changes to change gradually. This was achieved by making the upstream and downstream taper to be 1:4. The tapers are shown by the thin black sloping line between area one and two in **Figure 15** as well as between area nine and ten in **Figure 15**.

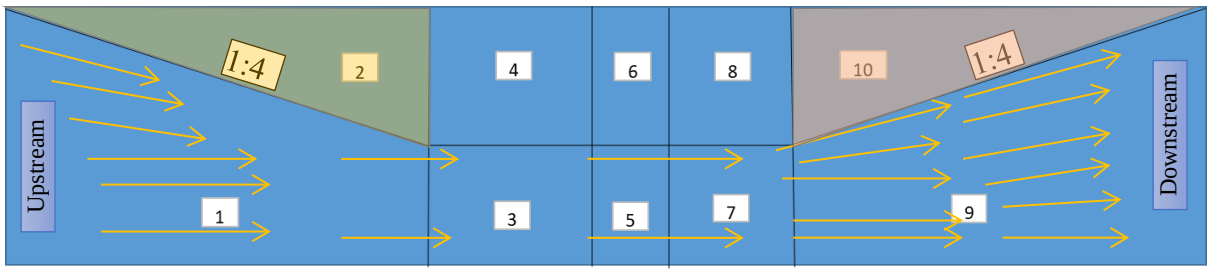

Figure 15: Plan view of the physical hydraulic model and general fluid flow lines

In the plan view, the typical flow was as shown by the flow lines (close to the bed) in **Figure 15**. The model's section two and section ten in **Figure 15** formed the transitional sections of the hydraulic model. Area two (yellow triangle upstream) of the hydraulic model reduced the cross-sectional flow area, closer to the bed. As a result, it had a contraction effect on the flow. Nonetheless, the effect of the contraction was reduced by making the horizontal taper slopes mild (1:4) and the contraction effect was also reduced by the deep incoming upstream flows.

Similarly, between area ten (orange triangle downstream) and nine (**Figure 15**), the cross-sectional flow area increased. As a result, an expansion flow was experienced in the downstream area of the model. However, the taper slopes were symmetrically designed to be gentle to reduce the expansion effect of the flow downstream. The 3D model in **Figure 13,** illustrates the upstream contraction and downstream expansion triangular areas better than the plan view in **Figure 15.**

3.2.3 Design of Longitudinal Bed and Transversal Side Bank Slopes

There were three steep longitudinal bed slopes chosen for the hydraulic model testing. The three-bed slopes were 0.5, 0.4 and 0.333. Such steep bed slopes may be possibly prevalent at the toes of mountainous regions. **Figure 16** shows a typical longitudinal section of the hydraulic model with the 0.5 (shown as 1:2 in the figure) steep longitudinal slope in the testing section.

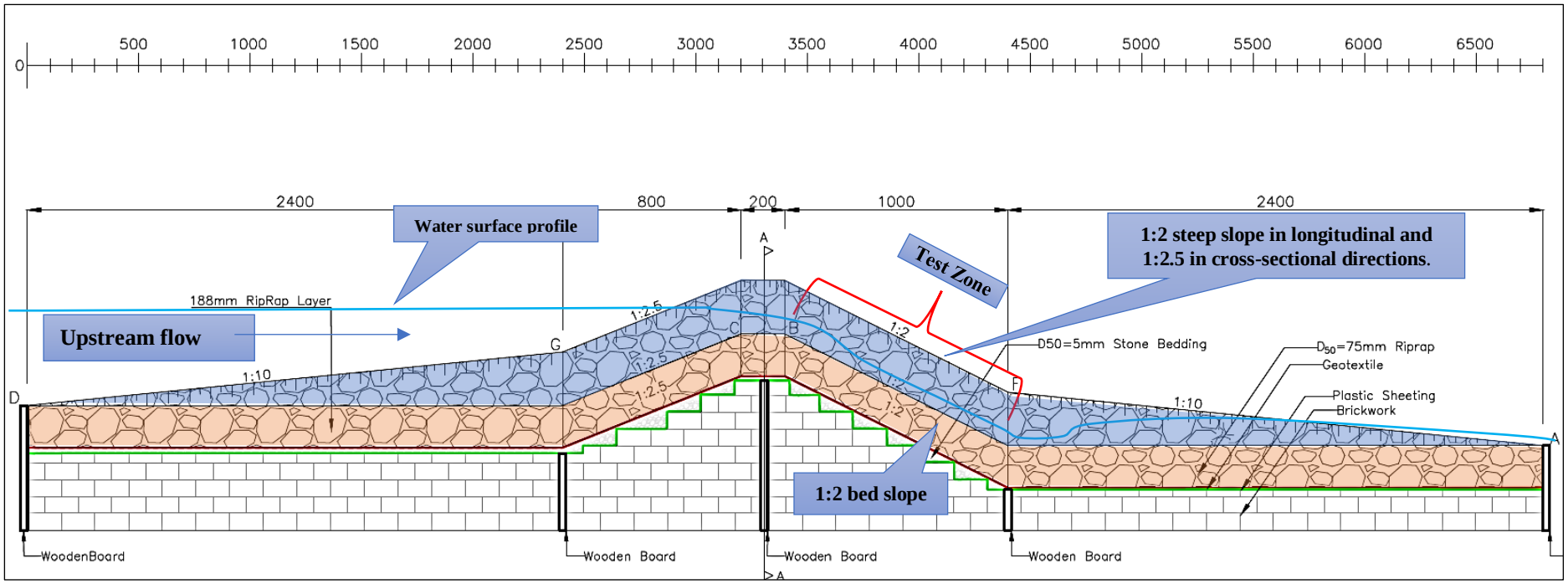

Figure 16: A typical longitudinal cross-section of a hydraulic model with steep (1:2) downstream (chute type) slope in the testing area. The model is in a 1.2 m wide flume with no tailwater control.

In **Figure 16**, the upstream section of the hydraulic model was from station 0 mm up to 3200 mm. Then from 3200 mm to 3400 mm was the weir crest area. From 3400 mm to 4400 mm was the sloped testing zone. In **Figure 16** above, the steep bed slope with a slope of 0.5, was the area of interest for this thesis, whereby the bed slope was changed (from 0.333 to 0.4 and 0.5). For the reader to have a perspective of the design model, **Figure 16** must be checked holistically with the drawings in **Appendix A. Appendix A** comprises all the physical hydraulic model design drawings for the testing Test series one and two. Test series three drawings have not been included because they were the same as Test series two, except that glue was used on the bed area.

Initially, it was planned that a 0.4 and 0.333 steep side bank slope would be tested against the three steep bed slopes. However, it was later decided that only the steepest side bank slope of 0.4 would be tested. The main reason for the decision was due to an observation made during Test series one tests. It was observed that there was no significant amount of water depth encroaching on the side banks and the steep bed slope failed before the bank. The failure of the riprap on the bed area before the side bank inferred that the measured water depth for the side bank failure would be significantly inaccurate if the test was continued (if the flow rate was increased further) on the failed bed. Thus, inaccurate measurements would not be useful for this study given that the analysis used was sensitive to the water depth. As a result, the 0.4 steep side bank slope in the testing section was maintained for all the tests. A typical cross-section is shown in **Figure 17**. However, the cross-section was taken at the top of the crest of the model at station 3300mm, but the side slope was still representative of the side slope designed in the testing section from station 3400 mm to 4400 mm.

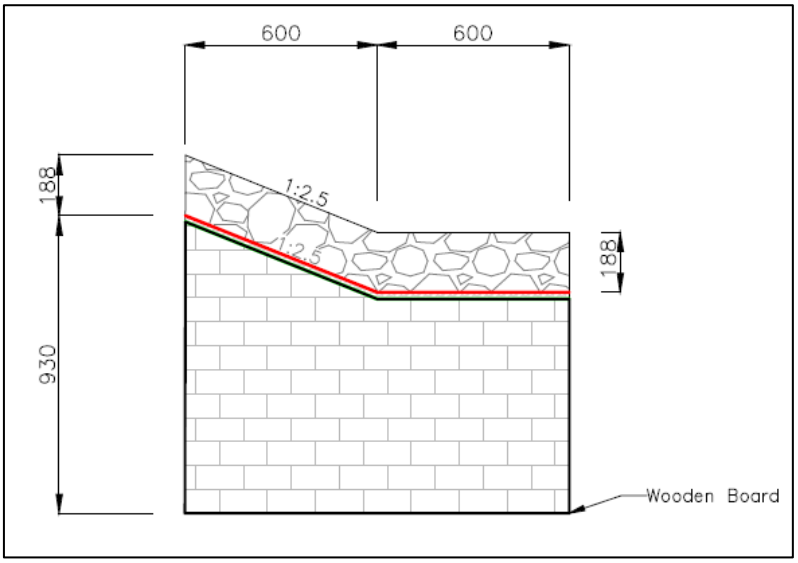

Figure 17: Typical cross-section at the top of the weir's crest (all dimensions in mm)

Taking a similar cross-section through the testing area (station 3400 mm to 4400 mm) would look like the half trapezoid section in **Figure 17.** The main hydraulic channel dimensions are the bottom width of 0.6 m and the 0.4 side slope rising over a horizontal length of 0.6 m. The channel cross-section dimensions were limited and influenced by the space available in the channel. However, the dimensions and shape of the model allowed the successful testing and measuring of the main parameters of the study.

3.2.4 Protection Length of Arrestor Bed Area

The length of the arrestor in the testing area must allow the full development of the flow over the sloped bed. The longer the steep bed slope, the better, as this would ensure the full development of the flow over a large area. However, due to the limitations in the construction of the laboratory model space, the correct length specification was required. Moreover, since material had to be bought, a long steep slope would require more material, thus cost more.

De Almeida and Martín-Vide (2009) conducted an experimental study to investigate and determine the influence of the protection length, width and protrusion of riprap. From the study, it was found that the longer the protection length, the more stable the riprap layer over the length. As a result, a recommendation that the protection length must be $L_{arr} \geq 16D_{50}$.

So, for this study the $L_{arr} = 16D_{50}(0.038\ m) = 0.608$ m and for the second stone size $L_{arr} = 16D_{50}(0.075\ m) = 1.2$ m. Therefore, the largest protection length, 1.2 m, would be enough for the two median stone sizes. However, a 1 m horizontal length was chosen as enough for all the Test series. It was noted that the protection length parallel to the bed would be longer than the chosen horizontal 1 m length for the three steep bed slopes. It was assumed that the 1 m horizontal protection length for this study was going to ensure the full development of flow during all the testing series. During the testing series, all the flows in the tests fully developed on the testing slopes before reaching the downstream expansion area. **Figure 18** shows a representative case in Test series three. The flow was uniform because of the deep flow water depth. At shallow water depths, several eddies and jets were visible over the riprap area.

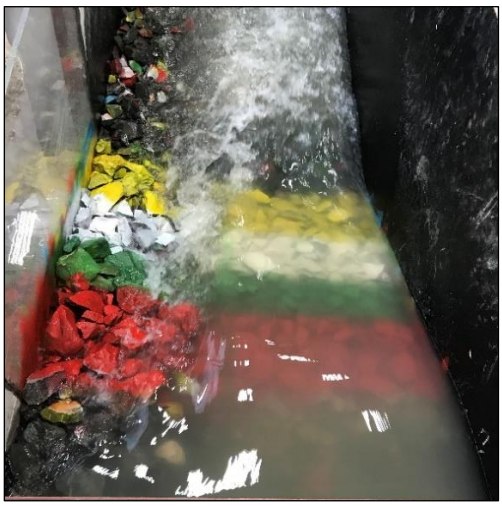

Figure 18: A typical flow condition over the testing section with deep flow conditions.

3.3 Materials and Construction of the Physical Hydraulic Model

Following the physical hydraulic model design, the building of a functional hydraulic model at the hydraulics laboratory primarily relied on choosing the appropriate materials to fulfil the pertinent structural functions of the hydraulic model. Failure to use the appropriate materials for the physical hydraulic model can lead to the catastrophic failure of the model. The upcoming section outlines the details on the construction of the physical hydraulic model.

3.3.1 Hydraulic Model Foundation Material

The hydraulic model for this study was built inside a 1.2 m width by 1.6 m deep non-tilting flume constructed from brick walls. The floor was relatively flat with slight $\pm$16 mm offset from the original 0 m reference ground elevation that was measured with a total station. This was due to the floor concrete finishing not being 100% smooth.

The non-tilting nature of the channel required that the hydraulic model foundation was built at a higher elevation to enable the construction of the steep bed slopes required for the hydraulic tests. Therefore, weir-like hydraulic models were designed and built according to the drawings in **Appendix A.**

A combination of bricks and blocks were used to build the foundation of the physical hydraulic model. It was critical that the proper material was used for the construction of the foundation to avoid any foundation settlement of the hydraulic model when testing. **Figure 19** illustrates the final built foundation with the required shape. The top part of the foundation used the gravel to shape and fill voids. The plastic and the geotextile filter, also known as the bidim, were placed after the levelling and shaping were completed as shown in **Figure 19**.

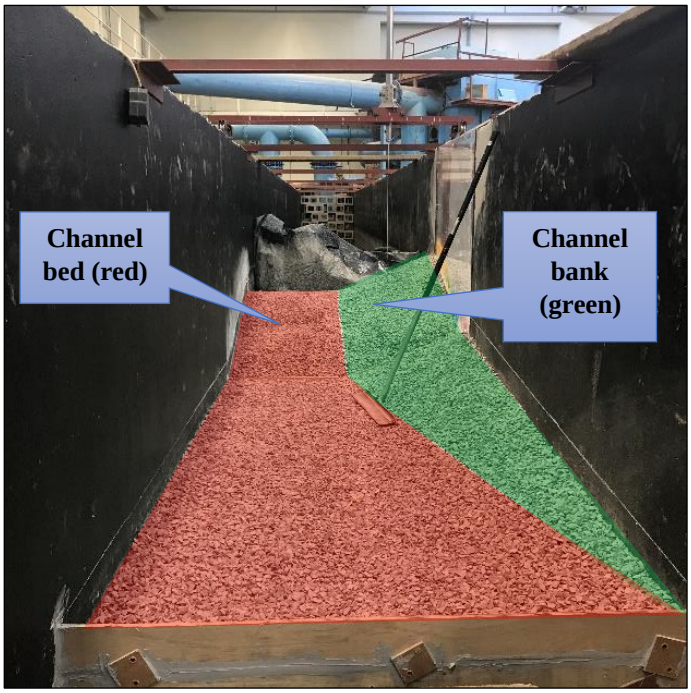

Figure 19: Finished foundation level in the upstream section of the model

Initially, a problem was experienced at the hydraulics laboratory where the 190x190x390 mm blocks (M190 blocks) with hollow openings inside were used to build the foundation. During the construction of the foundation, the blocks were filled with sand. After that, the top layer of the foundation was shaped to the desired slopes using the sand (in **Figure 19)**, the top gravel layer was initially sand).

However, during the preliminary test of the physical hydraulic model, the sand was washed away by the water. The whole testing area settled because the underlying sand was eroded. An additional contribution to the settlement was the air trapped on the foundation of the model. When the trapped air tried to escape out of the model, the air pushed the sand upwards causing the hydraulic structure to fail prematurely. As a result, the objectives of the study could not be properly investigated.

The alternative solution implemented was to fill the blocks and shape the model with larger gravel stones as shown in **Figure 19**. The D_{50} = 5 mm stone sizes were used to fill the voids in the underlying foundation. The hydraulic model performed as expected and no failure or settlement of the model was experienced afterwards.

3.2.2 Water Tightness

It was essential that the model was constructed to be impermeable. The water tightness of the hydraulic model would ensure that there was an insignificant amount of water lost in the model through seepage. It was impractical to achieve 100% water tightness at the laboratory. However, precautions were taken to try and keep the flow rates as representative as assumed.

Plastic sheeting was installed over the model underneath the bidim to reduce the amount of water seepage under the model. The plastic was placed after the foundation was built to the correct level. A clear illustration of the plastic placement can be seen in **Figure 16** above, whereby the plastic sheeting was drawn in green colour. Alternatively, the drawings in **Appendix A** display the placement position of the plastic sheeting.

The foundation blocks and bricks with the smaller gravel stones played a critical role in reducing the voids in the foundation which would require filling by seeping water. Reduction of voids spaces was achieved by ensuring a fewer void presence in the foundation.

The last precaution taken was to ensure that the model was filled with water until the whole model was saturated. In **Figure 16,** the wooden boards inside the foundation were installed to ensure damming and reduction of water loss inside the physical hydraulic model's foundation. When the model filled up, the foundation ensured that the fluid flow rates that flowed through and over the riprap were representative of the flow rate read from the flow meters.

All the above precautions ensured that the flow rate recorded from the flow meter was reliably representative of the flow conditions running over the model.

3.2.3 Filter Layer

The correct design of the underlying filter layer was key during the design of riprap for erosion protection works. The filter layer is generally designed as an underlying transitional layer with smaller sized rocks compared to the design median size riprap. For the hydraulic models in this thesis, the filter layer was laid between the riprap structure and the protected underlying soil. The filter layer inhibits the movement of smaller particles into the riprap layer.

For this study, the bidim geotextile was used as the filter layer. Bidim was favourable and more convenient to use. **Figure 20** shows the bidim laid over the weir testing area. No gravel stones invaded through the filter layer, but small sand particles were present after a test. It was easy

to replace the bidim; by cutting off a specified size replacement piece and placing over the testing zone when the Bidim was damaged.

Figure 20: The Bidim geotextile filter layer placed on top of the gravel

The main reason to favour bidim geotextile was that the hydraulic model frequently required the modification from one setup to the next. It would be time-consuming and laborious to use gravel stones as a filter layer because the gravel stone would be washed away in each test.

Moreover, using gravel as a filter layer could have interfered with the grading of the riprap after each test as the two layers might have become mixed up when the riprap layer failed. During the tests, the bidim was stable and allowed the riprap layer to be laid without sliding on the steep slopes. The bidim was only changed when it had significantly been damaged. After every test, the bidim was carefully checked. The bidim was replaced if torn or a significant amount of fine sediment (dirt from riprap stones) was washed and trapped on top of the bidim.

3.2.4 Riprap Layer Properties

After the filter layer was placed, the riprap layer was dumped on top of the hydraulic model. The riprap had to meet design specifications before it could be placed. The upcoming thesis sections provide the details of the specifications of the riprap that were laid on the top of the filter layer.

3.2.4.1 Riprap Material Type

Choosing the testing material type was dependent on the stone availability in the area in the Western Cape. The density was deemed to be the most critical determiner among other factors. It was incumbent that the most available riprap rock material be used for the incipient failure tests. Most importantly the chosen riprap had to adhere to a density close to the range 2600-2700 kg/m^3. Rocks with density in that range are generally used since they provide high stability and resilience in riprap design projects. Different stone suppliers in the Cape Town region were visited, and only two were chosen to source the required riprap. It was found that the most available angular riprap rock was the grey hornfels in **Figure 21.**

Figure 21: Pile of hornfels riprap rock

Hornfels riprap rocks are durable and dense, thus they were chosen for this specific study. The hornfels riprap rocks were sourced from the Tygerberg group of quarries. Two quarries were used to source the required riprap size for the research. The quarries that were visited were the AfriSAM Pty Ltd and Ciolli Bros Pty Ltd quarries. The quarries were located in the Durbanville area in the Western Cape.

3.2.4.2 Riprap Size

The riprap median diameter stone sizes were chosen based on scale of 1:15 model to prototype scale ratio. The tested median stone sizes were D_{50} = 0.038 m and D_{50} = 0.075 m. Initially, three stone sizes were to be tested. The middle stone size, the D_{50} = 50 mm, was no longer considered for testing due to time constraints and labour limitations, as well as the preliminary findings during the testing of Test series one. During the testing of the D_{50} = 0.038 m median stone size, the riprap on the bed area failed before the bank. Thus, for the next set of testing series, it was decided that the D_{50} = 0.05 m would not be tested, and the larger D_{50}= 0.075 m median stone size would be tested.

One of the main challenges for this research was obtaining the required stone size from a quarry, as the angular riprap stone was not readily available at the laboratory. Even when the riprap rocks were obtained from the quarries, they still required to be sorted and graded. These are typical disadvantages that would be directly encountered by engineers when opting to implement a design for riprap river revetment projects.

The following procedure was followed to obtain the required riprap size and grading:

- A large pile (more than 4.6 Tonnes) of mixed size riprap stones from the quarries were transported to the laboratory.
- The required stone sizes were determined as per the specifications to pass the specified grading (see **section 3.2.4.6 for** grading specification).
- Standard sieve diameters were used to sort and sieve the required stone sizes from the pile.
- The riprap stones were placed separately according to each size determined by sieving.
- The stones were mixed as per the grading requirements specified in **section 3.2.4.6.**

Figure 22 displays the large diameter sieves that were used to perform the sieving. The stone size was defined according to the sieve in which it was retained as opposed to the sieve that it passed through. Therefore, a stone defined as being a 26 mm stone was retained on the 26 mm square aperture sieve.

Figure 22: Standard metal sieves used for sorting the required stone sizes.

An important observation made during the sieving of the stones was that the physical stone sizes retained in each sieve were larger than the specified aperture of the sieve. This was due to the irregular shape of the stones. Thus, it was critical to reduce the use of stones that were needle-like shaped as they could go through some sieves even though they were larger than the sieve in which they were retained. This was noted, and consistency in terms of defining the stone size was used throughout the tests. This is also important for any designer who might use the findings of the thesis, to know that the stone sizes were defined according to the retaining sieve diameter aperture.

It was also important that the stone sizes were stored safely and should not mix. This was important during the grading and mixing because the correct stone size proportions were critical to obtaining the required grading. Therefore, separation of the stones by size was achieved by using blocks and wooden boards at the laboratory as shown in **Figure 23.**

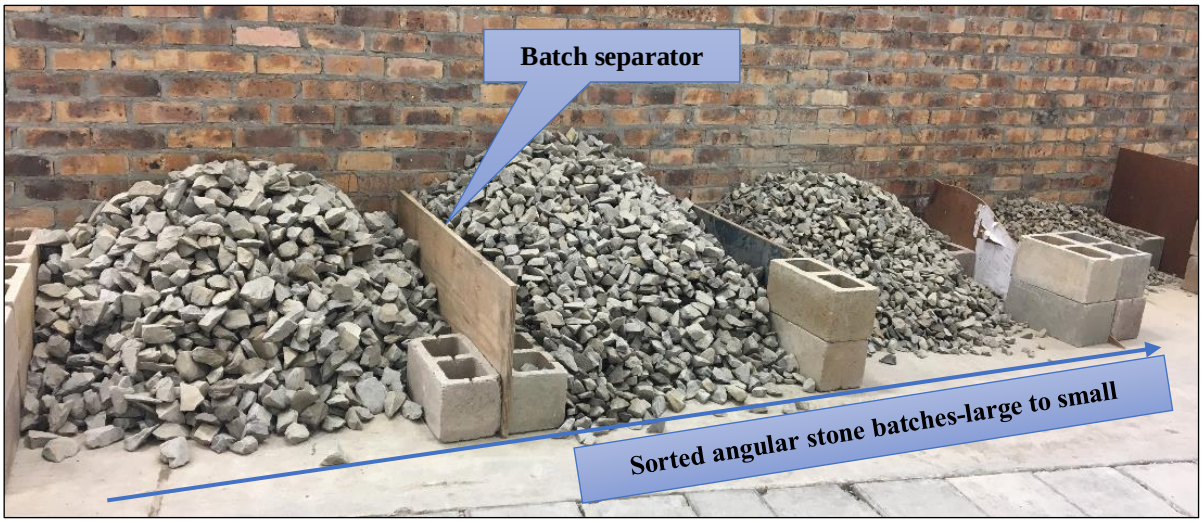

Figure 23: Stone size storage and separation.

Lastly, during Test series one, the D_{50} = 0.038 m stone was tested first. On the second testing series, the D_{50} = 0.075 m stone size was tested. In the results of the first two testing series, the riprap dumped on the bed area failed before any failure on the side bank. As a result, the challenge for Test series three was the unavailability of stones larger than D_{50} = 0.075 m. Moreover, to go to a quarry, sort and mix riprap with a larger median stone size than D_{50}= 0.075 m would be labour intensive. As a result, it was decided that the D_{50} = 0.075 m riprap on the bed area must be glued on the bed area, so that the riprap on the bed area does not fail before the riprap on the side bank. The investigator managed to test the failure conditions on the side bank of the physical hydraulic model on the downslope testing area. Thus, only the stability of the D_{50} = 0.038 m and D_{50} = 0.075 m median stone sizes were investigated.

3.2.4.3 Riprap Shape

One of the main aims of the thesis was to test angular riprap rock instead of round-shaped riprap rock. It was anticipated that the angular riprap rock provides more stability under hydraulic loads compared to rounded riprap rock of the same size. Therefore, quarried angular riprap rocks were chosen for the riprap rock layer stability investigations.

The desirable rock shapes were blocky and non-needle-like. During the sorting of the stones, all the extremely platy and needle-like riprap rocks were removed from the riprap mix. The reason for this was to ensure that the rocks used for the riprap mixture had an LT ratio less or equal to three. It was not possible to physically measure all the rocks for LT ratio, thus only the obviously extreme needle-like and platy riprap rocks were removed during the sorting.

3.2.4.4 Riprap Density

The type of rock used in riprap design provides the designer with a good indication of the rock's mass density. Both the suppliers of the hornfels riprap rocks were situated in the same geographical area. According to CIRIA *et. al.* (2007), the designer may assume a rock density of 2700 kg/m^3, however, in the case where different rock sources are used, the mass density may require re-specification. Thus, in this case, the two quarries were both in the Western Cape and were mining on the surface of the same geological rock formation known as the Tygerberg formation. Therefore, the same density of the riprap was assumed for the riprap sourced from AfriSam and Ciolli Bros (Pty) Ltd.

For the hydraulic model tests, it was critical that the same material type was used. In the study, the researcher was fortunate to obtain the same type of rock sources from the same local area in Durbanville. Thus, the rock stone type was known as the grey hornfels, and the suppliers specified the density of the rock to be approximately 2700 kg/m^3.

In Langmaak's (2013) thesis, the density of the hornfels rocks was physically confirmed to be approximately equal to 2708 kg/m^3, through physical testing of the average density of ten hornfels stones. Thus, for this research, it was justifiable to assume the same density for the hornfels rocks. A 2700 kg/m^3 hornfels rock density was assumed for this study.

3.2.4.5 Riprap Drag Coefficient

While there is a lack of universally accepted drag coefficient determination equation, the literature has numerous empirical equations, but the equations all have certain drawbacks (Wang *et al.*, 2018). The particle shapes that are significantly investigated for drag coefficients comprise sand particles and spheres at low and high Reynolds number. Moreover, regular shapes such as cubes, cylinders and prisms are generally studied as well (Wang *et al.*, 2018).

The author of this thesis could not find specific literature that attempted to determine the drag coefficient or the settling velocity of angular riprap rocks. Langmaak and Basson (2015) obtained a drag coefficient of 1.66 for large riprap rocks. However, it was not clear whether the randomly chosen riprap rocks used in the settling velocity tests were a mixture of both subangular and angular rocks or only the angular rocks were tested in the settling velocity tests. Since the shape plays a critical role in the determination of the drag coefficient, it was incumbent that a drag coefficient value was specified for pertinent riprap rock shapes.

According to (Cheng, 1997), under high particle Reynolds number, the C_D is 0.4 for spherical particles. However, for natural sediments, the C_D value is between 1 and 1.2 (Cheng, 1997). Cheng (1997) made the previously mentioned recommendations on the C_D value based on the findings of six previous studies: Sha (1956), Concharov (1962), Zhang (1989), Van Rijn (1989), Raudziki (1990), Zhu and Cheng (1993).

It is possible that no specific study has addressed the issue of the drag coefficient of angular or crushed rocks, as it could not be found from open source academic literature. As a result, Armitage (2002) recommended the determination of the drag coefficient of irregular shapes be physically tested at the hydraulics laboratory. This is important for the MN analysis approach since the results are sensitive to the drag coefficient or settling velocity.

Therefore, it was imperative that the drag coefficient of the angular stone was determined experimentally for this study. The previously mentioned drag coefficients were important as they were used as a reference to evaluate the drag coefficient and settling velocities found at the laboratory for this study.

The first step that was taken to determine the drag coefficient of the angular rocks was to determine a sample of rocks to be tested for the settling velocities. The following rock sizes were tested for the settling velocity tests:

- 0.026 m - 0.038 m
- 0.038 m - 0.053 m
- 0.053 m - 0.075 m

For each sample range, a total of 40 stones was taken from the piles in the hydraulics laboratory. The stones in the samples were measured for the three dimensions “a”, “b” and “c” as defined in the literature for use in the determination of the Corey Shape Factor. **Figure 24** displays a typical dimension measurement of the stones using a 30 cm steel ruler.

Figure 24: Measurement of the rock shape factor dimensions

After determining all the rock dimensions, each rock was dropped individually into the settling tank shown in **Figure 25**. The water from the bottom of the tank up to the top was measured and recorded for each test. A nylon fish line with a heavy material at the tip was dropped in the tank, then a mark at the top was made to mark the top surface of the water in the tank. The fish line length was measured with a measuring tape on the floor to determine the water depth of the tank.

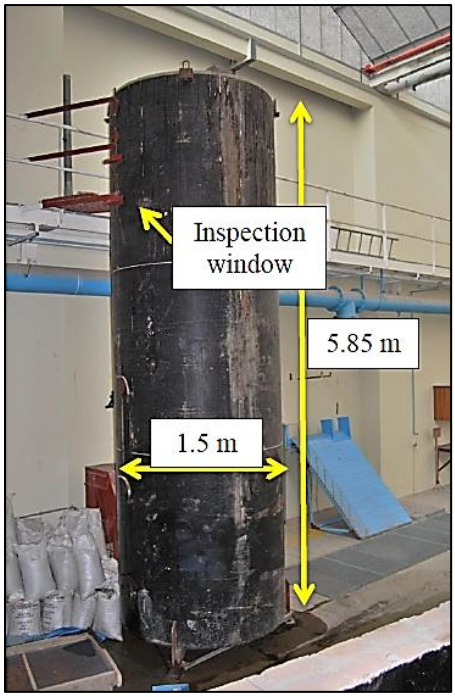

Figure 25: Settling tank used at the hydraulics laboratory (sourced from Langmaak (2013))

The time taken for a single stone to settle was recorded using a stopwatch. Langmaak (2013) used a reliable method in the determination of the settling velocities of the stones. Langmaak (2013) took advantage of the inspection windows, at the top and at the bottom of the tank. The distance travelled by the rock divided by the difference in the settling times between the two inspection windows were used to determine the settling velocities. However, in this study, the water in the tank was not sufficiently clean to take advantage of the inspection windows. As a result, only the time recorded with a stopwatch and the distance each rock travelled from the surface of the water to the bottom of the settling tank was used to determine the settling velocity, as shown below:

$$v_{ss} = \frac{Distance\ travelled\ by\ rock}{Time\ recorded\ to\ travel\ from\ top\ to\ the\ bottom\ of\ tank}$$

The 0.053-0.075 m stone size rock sample was tested on a separate day from the other rock sample sizes. The 0.026-0.038 m and 0.038-0.053 m stone sample settling velocity tests were conducted on the same day. When the 0.026-0.038 m and 0.038-0.053 m stone samples were tested, the water in the tank was refilled. Thus, the settling water depths are different in the tables in **Appendix B**. For the 0.053-0.075 m the settling water depth was 4.905 m, while for the other two samples the settling water depth was 4.960 m.

One may argue that the disadvantage with the settling velocity determination method executed for this study was the influence of human reaction time. However, the settling tank height was significantly long. Therefore, the height of the tank (thus distance travelled) significantly contributed to the reduction of the error associated with the human reaction time. Alternatively, if the rock's settling distance were shorter, then the error associated with the reaction time when pressing the stopwatch would be significant.

A summary of the rock Corey shape factors as well as the settling velocity and respective drag coefficients were tabulated in **Appendix B**. A total of 45 successful settling velocity tests were accomplished, while 120 rocks were dropped into the settling tank. The settling velocity test was deemed unsuccessful if the following occurred:

- if the rock touched a steel beam that was welded somewhere in the middle inside the settling tank; or
- if the rock touched the internal sides of the settling tank before reaching the bottom of the tank.

Using the same approach as Langmaak (2013), the Corey shape factor and drag coefficient for each of the 45 rocks was plotted in the graph as seen in **Figure 26**. A trend similar to that of Langmaak (2013) was obtained. In **Figure 26**, as the drag coefficient decreases, the Corey shape factor increases. Most of the data plotted between a drag coefficient of 1 and 3.5, with few outliers greater than C_D of 3.5. One significant observation was that the drag coefficients were all greater than one.

The drag coefficient was calculated from the measured settling velocities for each rock in the samples. **Equation 3**, $v_{ss} = \sqrt{\frac{4}{3}\frac{(\rho_r - \rho_w)}{\rho_w}\frac{gD_{50}}{C_D}}$, was used to calculate the drag coefficient for each rock in **Appendix B**. the rock density was assumed to be 2700 kg/m^3 and the density of the water was assumed to be 1000 kg/m^3. The "b" dimension of each rock was assumed to be D_{50} in **Equation 3**, since it was a logically more representative value for D_{50}. With the previously mentioned parameters known, it was possible to calculate the respective drag coefficient with **Equation 3**. The drag coefficient and the respective settling velocity were plotted onto **Figure 26**.

From **Figure 26**, a general trend was observed, whereby the decreasing drag coefficient of angular rocks relates to an increase in the settling velocities of the angular rocks. This is in correlation with the fact that drag force is a resistant force, thus more resistance from the rock

should result in smaller settling velocities, whereas smaller resistant forces should result in higher settling velocities.

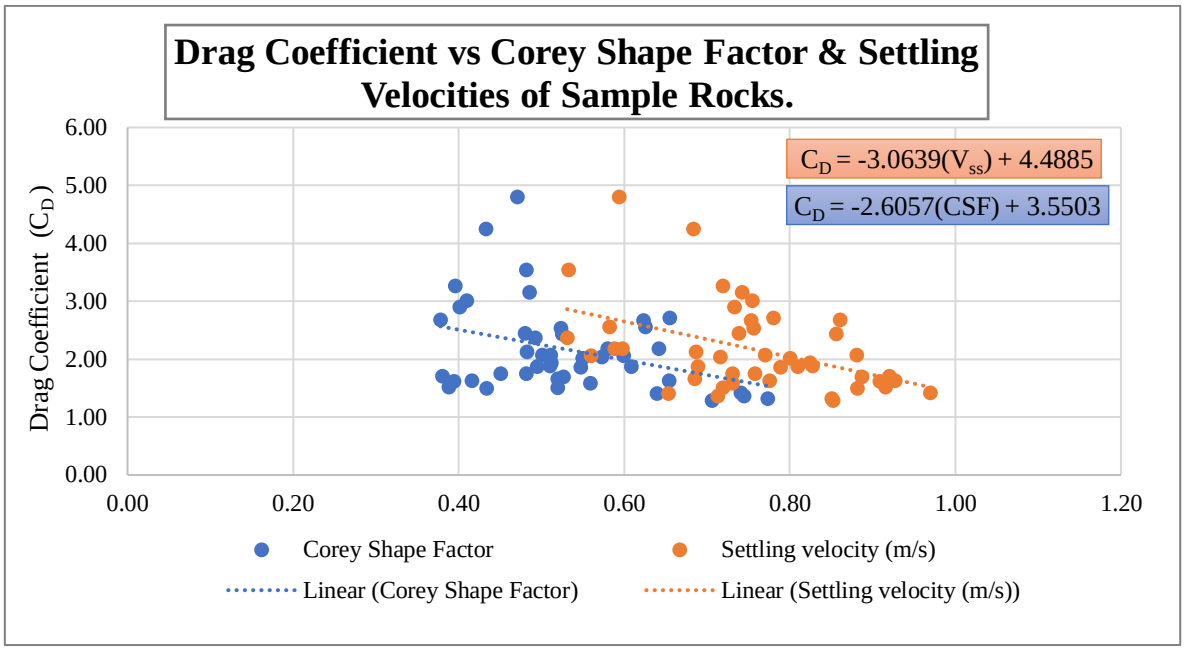

Figure 26: Graph showing the relationship between the Corey shape factor versus the drag coefficient & the settling velocities of angular riprap rock.

According to Rooseboom and Mulke (1982), the drag coefficient at high particle Reynolds number must be constant for large particles. For the 0.026-0.038 m, 0.038-0.053 m and 0.053-0.075 m stone size samples in **Appendix B**, the average drag coefficients were determined to be 2.001, 2.204 and 2.270 for each stone range. There was a slight difference due to the irregular nature of the rocks, but the results agree with the argument by Rooseboom and Mulke (1982).

The average Corey shape factor for the 45 data points was found to be 0.529, and the corresponding drag coefficient using the trendline equation was 2.17. Therefore, the assumed rock drag coefficient for angular riprap rock was determined to be 2.17. This value was acceptable since it was relatively close to the drag coefficient of 1.66 found in Langmaak's (2013) study which used similar rock shapes.

However, the discrepancy in the drag coefficients of the two studies may be attributed to the irregular nature of riprap rocks. Other reasons could be attributed to the slight difference in the methods followed by Langmaak (2013) and in this study in determining the settling time. Nonetheless, it was expected that the drag coefficient determined in this study must be greater than the 1 to 1.2 drag coefficient recommended by Cheng (1997) for natural sediment.

3.2.4.6 Riprap Grading

Riprap grading is the riprap rock size distribution for a chosen specific design. The riprap grading was important for this study due to the stability provided by the riprap of different gradings. A single study with the primary aim to investigate the best grading for riprap was not found. Literature has numerous studies that recommend different riprap rock gradings for both uniform- and non-uniform grading types. Nonetheless, it was not yet clear which was the best grading to use.

As a result, for this study, non-uniform grading was chosen for the riprap design. The decision was based on the recommendations by Stevens and Senturk (1992). The following grading criteria were implemented for both the D_{50}= 0.038 m and D_{50}= 0.075 m median stone sizes to produce riprap with the grading curves presented in **Figure 27**.

$$D_{100} \geq 2D_{50}$$

$$D_{20} \geq 0.5D_{50}$$

$$D_{min} \geq 0.2D_{50}$$

The gradation above means that the maximum (D_{100}) rock size must at least be equal to or greater than two times the median rock size. The D_{20} rock size of the grading must at least be equal to or greater than 50% of the median rock size. The minimum rock size in the grading (D_{min}) must at least be equal to or greater than 20% of the median rock size of the.

The complete sieve analysis data used to develop the grading curves in **Figure 27** were recorded in **Appendix C**.

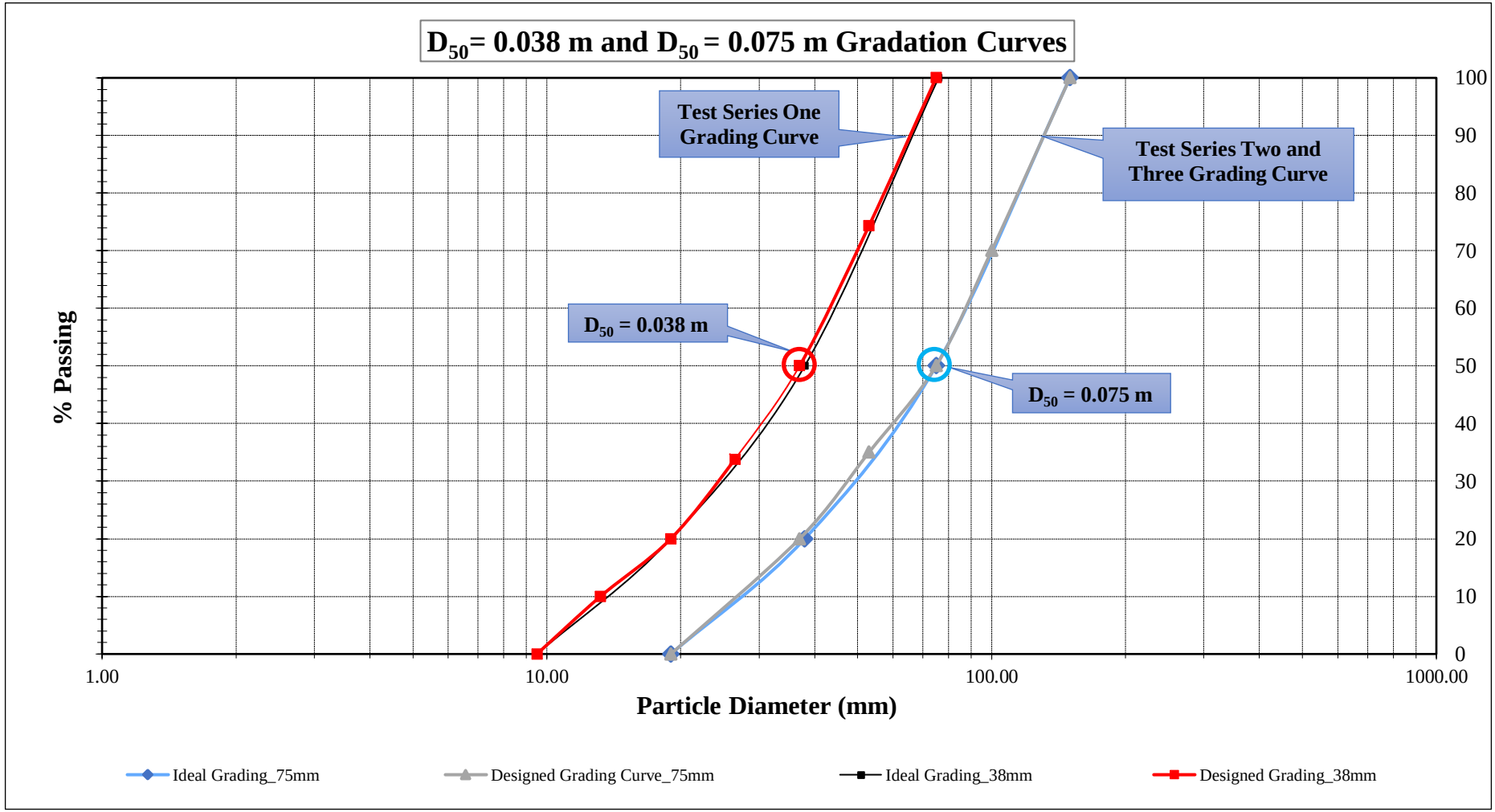

Figure 27: Riprap particle distribution curves for D_{50} = 0.038 m and D_{50} = 0.075 m riprap layer

To evaluate whether the riprap layers represented by the grading curves in **Figure 27** were well-graded, or uniform, Raudziki's (1998) uniformity criterion was used as a basis. **Equation 54** was applied to calculate the uniformity of the riprap layers.

$$\theta_g = \sqrt{\frac{D_{85}}{D_{15}}} < 1.35, \text{ for uniformity} \qquad \textbf{Eq. 54}$$

Table 7 summarises the parameters that were required to calculate the coefficient of uniformity for the two designed gradings in **Figure 26.** The D_{85} and D_{15} were read off from the two grading curves. The C_u in **Table 7** is the ratio of the D_{85} to D_{15}.

Table 7: Summary of the coefficient of uniformities for the two riprap layers

D_{50} (mm)	D_{85}:	D_{15}:	C_u:	θ_g
38	64	17	3.76	1.94
75	123	33	3.73	1.93

By applying the uniformity criteria in **Equation 54**, it was concluded that the D_{50} =0.038 m and D_{50}= 0.075 m graded riprap was non-uniform-riprap grading because both median stone sizes had θ_g that was greater than 1.35. Therefore, during the testing, the author anticipated that the uniform-riprap rock would provide a sufficiently stable riprap attack protective layer due to the following reasons:

- Presence of smaller stone sizes fill up the riprap rock voids. The filled voids reduce the number of possible jets caused by larger particles. The filling up of the voids reduced the amount of water seeping through the riprap voids, thus reducing the internal force impact on the inner layer riprap rock sizes.
- Riprap has a healing property whereby in some cases the area that failed may be stabilised by riprap rocks falling from upstream. It was observed in some tests that this specific movement occurred.
- The failure, especially on the larger riprap rock size, was generally developmental. The grading and layer thickness could be playing a significant role in this type of failure.
- The non-uniform (well-graded) nature of the riprap rock made it easy to distinguish the incipient point of failure. It was observed that the stone sizes approximately smaller and equal to the specified D_{50} defined the point of riprap incipience. The larger stone sizes only moved after the incipient failure occurred.

3.2.4.7 Riprap Angle of Repose

Depending on the shape and size of a riprap rock, the angle of repose differs accordingly. Round and smaller rocks generally comprise a smaller angle of repose compared to angular and large riprap rocks. Froehlich (2013) differentiates between two types of rock instability slopes.

The first, Froehlich (2013) defines as the particle angle of initial yield, φ. The second rock instability angle is the mass angle of repose, ϕ_r. Froehlich (2013) argues that the mass angle of repose does not necessarily provide the appropriate angle needed in the evaluation of riprap stability of a single rock.

However, the size of the single particle angle of initial yield for the median stone size of a riprap mixture is larger than the mass angle of repose of the mixture. Moreover, for the largest stone size in the riprap mixture, the mass angle of repose and the particle angle of initial yield are approximately the same. Therefore, if the two are assumed to be equal, this results in a safety factor.

Froelich (2011), studied and investigated 74 natural and crushed stockpiles of open-graded quarry rock. In the study the stockpiles were divided into three main shapes; round, subangular and angular. From a regression analysis of the stockpiles, the uncomplicated **Equation 6** in the literature review can be used to predict the mass angle of repose of the three main different stone sizes.

$$ln\ \phi_r = 3.43 + 0.0799I_1 + 0.183I_2 + 0.125 \ln\left(\frac{D_{85}}{D_{50}}\right) \qquad \textbf{Eq. 6}$$

The advantage of using **Equation 6** is that it accounts for the grading of riprap mixture by including the grading length ratio $\left(\frac{D_{85}}{D_{50}}\right)$. As a result, even if the equation is applied on different D_{50} stone sizes and grading, the grading length ratio $\left(\frac{D_{85}}{D_{50}}\right)$ accounts for this.

Therefore, it was decided that the mass angle of repose must be determined using **Equation 6** above. A summary of the calculated angle of repose can be found in **Table 8**.

Table 8: Angle of repose for the two riprap layers

Riprap D_{50} (m)	Riprap D_{85} (m)	I_1	I_2	Angle of Repose φ_r (°)
0.038	0.064	0	1	39.6
0.075	0.123	0	1	39.4

The angle of repose calculated in **Table 8** with Froelich's (2011) **Equation 6** was approximately equal. A rounded off value of 40° was assumed. From **Chapter 2** in **section 2.1.6**, the Lane (1953) curves, a 41° angle of repose specified for sediment particles that are greater than 10 mm. Van Rijn's (1993) criteria, specify a range of angle of repose between 40°-45° degree; for the sediment of an angular particle with the size 10 mm -100 mm. Thus, comparing the results obtained by using Froelich's (2011) **Equation 6**, it was accepted that 40° is a reliable value to use for the angle of repose for angular riprap design in this thesis.

3.4 Laboratory Testing Facilities

To ensure that reliable results were obtained for analysis, it was essential that the appropriate testing equipment was chosen. The value and reliability of the results of this thesis depended on the accurate measurement of the critical hydraulic parameters during the testing series. However, the measuring equipment used in the laboratory relied on the available measuring instruments. This section of the thesis describes the main equipment that was used when performing the physical model laboratory tests and how the equipment was used to measure specific data that was required to execute the analysis.

3.4.1 Video Camera

The laboratory video camera in **Figure 28** was mainly used to record videos and to capture images. Videos were recorded to assess the flow behaviour of the water over the riprap. The videos were mainly recorded at the beginning of the tests of Test series one. The author performed the tests in solitude, and as a result, the author was required to be out of the flume's sight when recording a flow meter reading or opening the valve. So, the video recordings were secured as a backup in case the researcher did not pick up a specific movement of stones or specific flow behaviour while out of sight at the testing area.

The disadvantage was that the videos required very high storage space. As a result, when the researcher performed all the tests in the first Test series and understood the flow patterns of the model, no further videos of the flow were recorded.

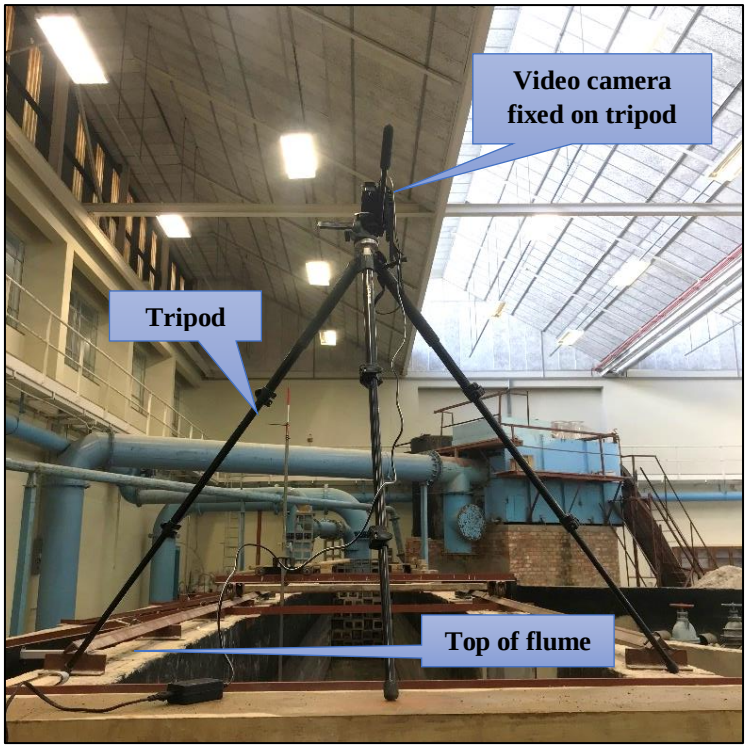

Figure 28: Video camera placed on a tripod on top of the channel

In Test series, one, two and three of the testing, the video camera was used to take pictures of the riprap testing area. The first image, in **Figure 29,** was captured when there was no riprap incipient failure; the second image, in **Figure 30,** was captured when there was an incipient failure on the riprap downslope testing zone.

Figure 29: Riprap before incipient failure motion occurred.

Figure 30: Riprap after incipient failure motion occurred.

There were some general images captured in between the two images shown. The images in between were captured to check and assess the amount of movement of rocks after a flow increase or if some movement was observed physically. Thereafter, the image comparisons would be used to assist in the decision-making process, whether the flow rate at that specific time was the incipient failure flow rate or not.

3.4.2 Flow Rate Meter

Two types of flow meters were used to measure incipient failure discharges during the testing. For Test series one, the inlet pipe that conveyed flow into the channel was a 0.1 m nominal diameter pipe. Thus, the smaller electromagnetic Proline PROMAG W flow meter was used to measure the discharge.

The smaller flow meter accurately measured flows from 0.00015 m^3/s up to approximately 0.034 m^3/s with a possible $\pm$ 0.5% error. A $\pm$ 0.5% error at 0.034 m^3/s was equivalent to $\pm$0.00017 m^3/s error. **Figure 31** shows a typical measurement with the PROMAG W discharge flow meter. The flow meters displayed the flow rate in l/s.

Figure 31: Endress + Hauser Proline PROMAG W discharge flow meter

Test series two and three was operated at flow rates larger than 0.034 m^3/s (maximum flow rate measured with the Proline PROMAG W flow meter in **Figure 31**). Consequently, a larger electromagnetic FLOWMETRIX SAFMAG flow meter was installed into a 0.3 m nominal diameter inlet pipe that conveyed flow into the flume. The SAFMAG flow meter accurately measured flow rates from 0.020 m^3/s up to approximately 210 l\s during Test series two and Test series three of the hydraulic tests. The SAFMAG also measured the flow rates at an error of +/- 0.0005 m^3/s.

Figure 32 shows the face display of the SAFMAG flow meter where the flow rate readings were recorded.

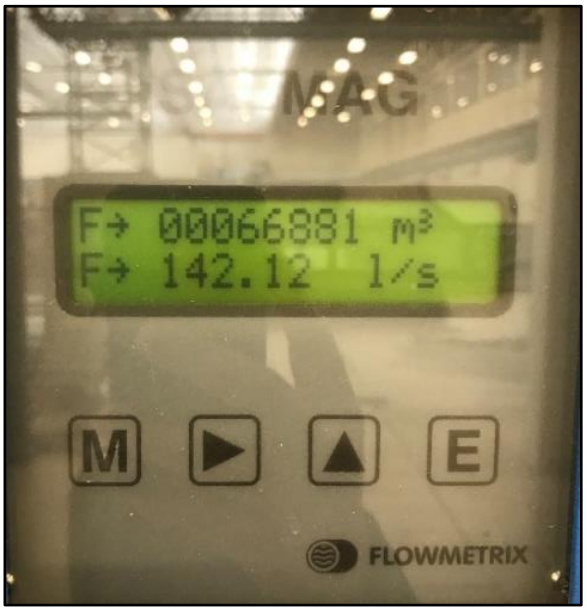

Figure 32: The FLOWMETRIX SAFMAG electromagnetic discharge flow meter

3.4.3 Point Gauge Needle

One of the main research input parameters in for this study was the average water depth over the downslope testing area. The MN was sensitive to the value of the water depth in a channel. Thus, it was critical that the water depth was determined accurately with the available measuring instruments and within the limits of the available laboratory equipment.

Generally, in hydraulic laboratory tests, the water depth can be determined from the sides of a visible flume by marking and recording the water depth on the sides. By calculating the difference between the bed and the surface water elevation marked on the visible flume sides, the water depth can be determined.

At the laboratory, it was impossible to mark the surface water from the sides of a flume. Instead, a needle was used to measure water elevations from the top of the flume. This was achieved with the aid of a trolley; the water depth gauge was clamped to the trolley. The flume wall in **Figure 33**, was opened on the side only to allow observation, but could not be used to mark water depth due to physical hydraulic model orientation and geometry.

Figure 33: Perspex glass installed on the flume sidewall opening

Since the flume walls of the channel and the hydraulic model orientation did not allow the measuring of the water depth from the sides, a trolley and needle were used to measure the water elevations from the top of the channel. Two parallel rails were built and installed on top of the two brick walls of the flume. The trolley was then placed on top of the rails, and a point gauge needle was attached to the trolley as shown in **Figure 34**.

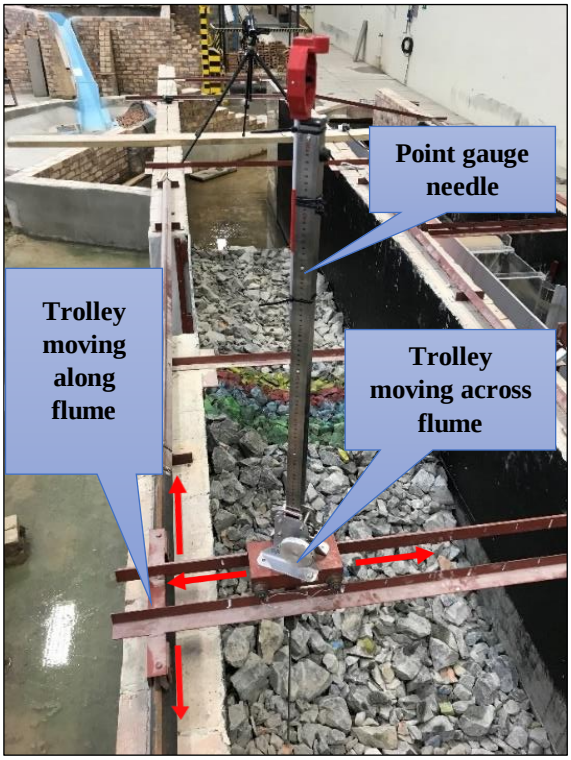

Figure 34: Trolley with attached point gauge needle

The main trolley on the rail wheels moved along the brick walls, allowing the point gauge needle to move in the longitudinal direction of the flume. The trolley that was attached to the point gauge needle allowed movement of the point gauge needle across the flume walls. Therefore, it was to manoeuvre the trolley along the flume and measure water elevations upstream and on the weir section, as well as downstream of the model.

The way in which the trolley was fitted in the testing performed on Test series one was such that the water elevations were measured from station 2700 mm to station 5200 mm as illustrated in **Figure 35**. The upstream length from the beginning of the weir was approximately 500 mm which was enough length to accurately measure the upstream water elevation without the weir head drop influencing the measurement of the upstream water elevation. In the upstream section, the water elevations were approximately at the same level.

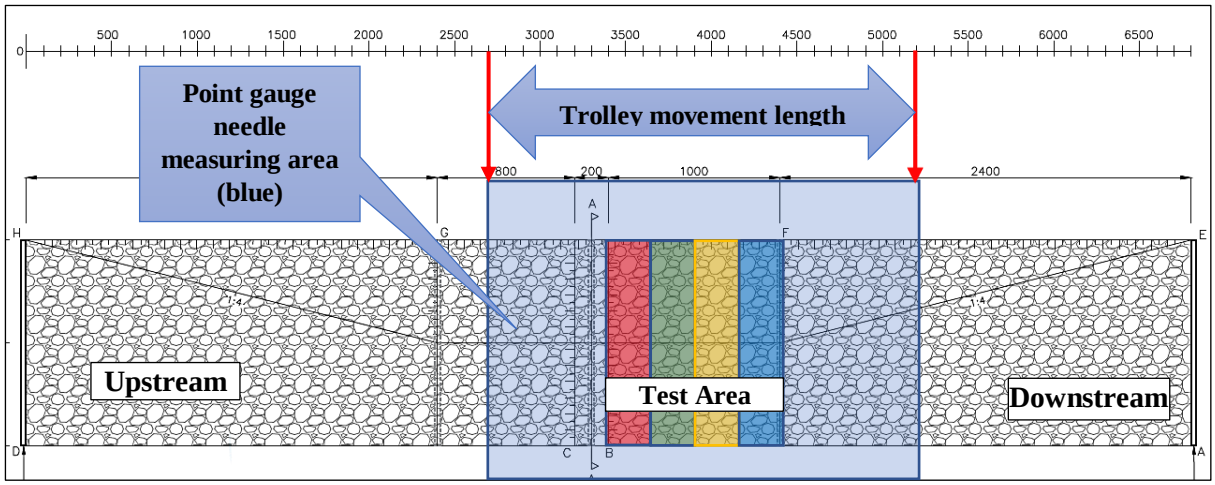

Figure 35: Area covered by point gauge needle was used for measuring water elevation in Test series one.

For the tests in Test series two and Test series three, higher incipient failure flow rates were expected. Therefore, to account for the high flow rates the main trolley rail lengths were increased in the upstream direction. This was to ensure that during the testing of high flow rates for Test series two and Test series three, the measured upstream water elevations were accurate and were not influenced by the head drop at the crest of the weir. In **Figure 36** the station where the point gauge began measuring the surface water elevation started at station 2000 mm and down to 5200 mm.

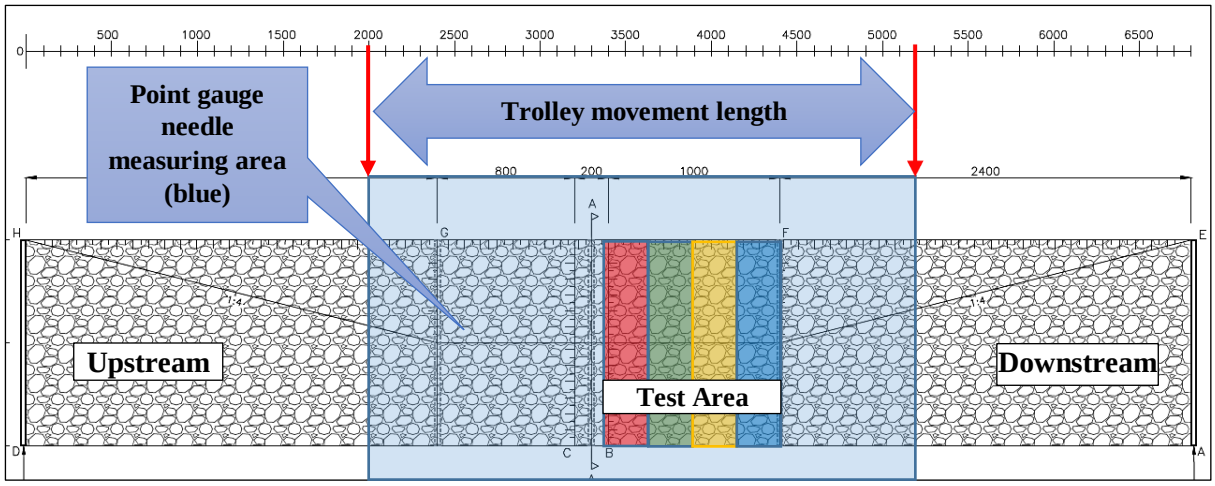

Figure 36: Test series two and Test series three point gauge needle measuring area

The measurements of the surface water elevation were conveniently obtained by using the equipment mentioned above. The trolley and needle gauge allowed the researcher to conveniently move and measure the surface water elevations along the broad area of the flume channel.

3.4.4 Total Station

The main challenge with the use of the point gauge needle to measure elevation was the manual recording and calculation of water depths. Due to the large scale of the hydraulic model, it would require a substantial amount of time and effort to manually measure water elevations for the area shown in **Figure 35** and **Figure 36**. Therefore, it was decided that the total station instrument must be used to measure the elevations and to execute the model bed surveys.

The total station was already calibrated and set to the coordinate system of the laboratory. During the use of the total station, it was essential that the total station prism was attached to the top of the point gauge needle as shown in **Figure 37**. Then, the height length from the prism centre to the most bottom point of the point gauge needle had to be measured all the time and used as an input during the total station setup.

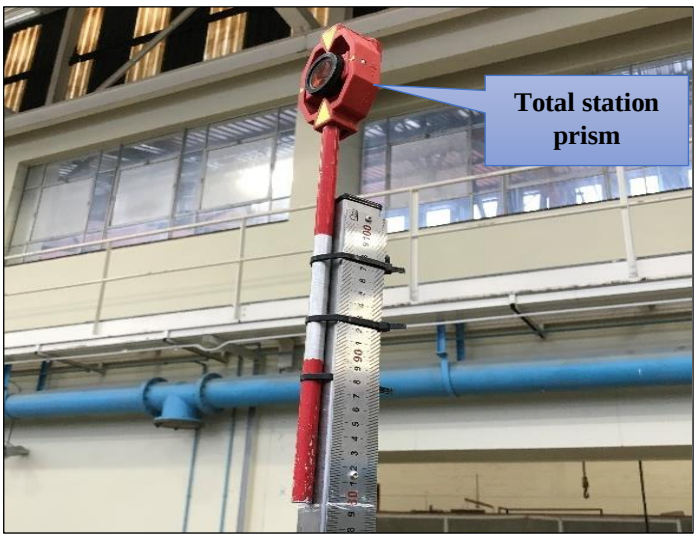

Figure 37: Prism attached to point gauge needle

The Leica total station in **Figure 38** was set up anywhere in the hydraulics laboratory where the prism-total station sight was not obstructed. Nonetheless, it was most preferential to set up the total station closer to the channel. The advantage of using the total station was that one person could successfully survey without the assistance of anyone. All that was required was the setup, and then the total station would rotate and follow the prism in whichever direction it moved for as long as the prism to total station sight is not obstructed. Another advantage of the use of the total station was that the subjectivity related to the reading of a point gauge needle elevation height was uninvolved.

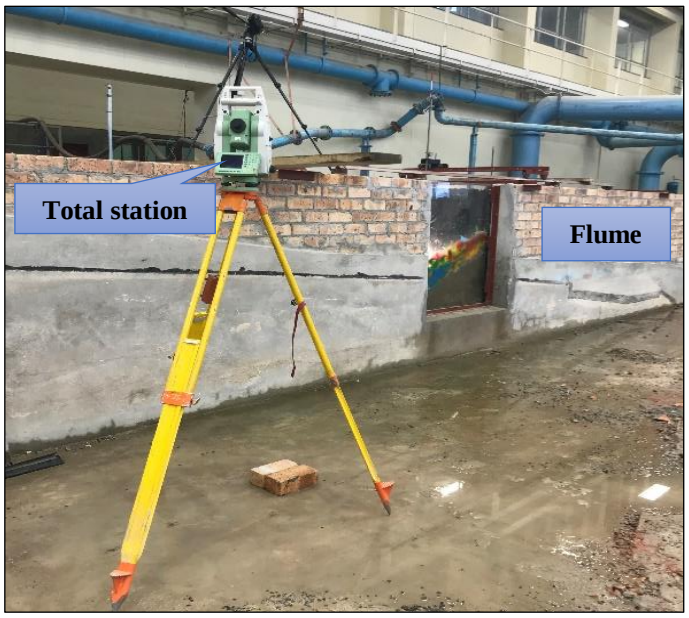

Figure 38: Leica total station set up near the hydraulic testing flume

In conclusion, the use of the total station saved a lot of time and effort in this research. The total number of tests carried out could only be possible due to the amount of time saved by the total station in measuring large amounts of data efficiently. The use of a 3D scanner was partially considered during the middle of the testing. However, it was considered unfeasible to use scanners, as there was no scanner available that could measure the surface water elevations when there was flowing water in the channel. To avoid errors and the complications attached to using two pieces of surveying equipment, the author decided to be consistent with the procedure that was already used to measure the bed elevations as well as the water elevations by using the total station.

3.5 Summary of Test Procedure Followed

The sections above in Chapter three described the testing schedule for all the test series as well as the design, construction and materials used in the construction of the hydraulic model. The main equipment used was defined in the previous section. This chapter provides a summary of the physical testing procedure that was followed to measure and record data from the physical hydraulic model. The summary of the procedure starts by describing the testing procedure at the point when the whole model was built, and when the riprap had been laid on top of the bidim. For all the 32 tests the general procedure of the hydraulic testing was according to the summary below.

3.5.1 Equipment Preparation

The first equipment that was set up was the total station. The total station was set up nearby the flume. The setup area closer to the model was favourable because the total station was not easily tampered. Also, if a total station re-setup was required, then it could be done swiftly due to a shorter model to total station distance. However, in Test series three, the total station was set up on the second floor of the laboratory due to the construction of bigger and high walled hydraulic models at the laboratory. The prism was mounted onto the needle point gauge during the total station setups (see **Figure 37**).

The next equipment that was set up was the video camera. The video camera required the setup of the tripod on top of the channel first. It was important that the tripod was placed in a stable position to ensure the stability of the video camera. After the tripod was set up and stabilised, the video camera was mounted onto the tripod, then focused on the testing area. A data transfer

cable from the laptop to the video camera was connected. This was to ensure that the image comparison could be made on site and two images could be captured and compared while running the test.

The last equipment preparation procedure was to check whether all the equipment was functioning appropriately. The total station was checked by measuring a point on the flat floor and a known fixed point on the steel bar on top of the channel, then if the coordinates corresponded it was assumed that the total station was correctly set up. The flow meter in Test series one had to be switched on all the time since it used a plug, so this was done before the test. Otherwise, in Test series two and three the flow meters were switched on by the laboratory technician when switching on the pumps. Then finally the camera was checked by taking a random image, then sending it to the laptop. However, the camera was not always checked since there were two cameras at the laboratory, and one could easily be replaced if not functioning properly.

3.5.2 Riprap Model Preparation

Three main riprap model preparation tasks were required before the actual test could commence. The first task was to survey the original bed of the riprap to get the approximate elevations of the bed level. The bed level was surveyed first, and an approximate grid of 0.075 m to 0.150 m spacing was used as a general guide for Test series two and Test series three tests. The grid was much smaller(0.05-0.1 m) for Test series one and more points were surveyed. However, since the bed surveys were done quickly, the grid structure spacing may not have been 100% within the planned limits through all the surveys. Nonetheless, this posed no significant errors in the results as the general average bed elevations were adequate. Most importantly, in the testing section, the researcher ensured that sufficient points were measured during the surveys.

A 3D elevation scanner would have been useful for surveying more accurate bed elevations. However, as explained previously in **section 3.4.4**, it was not used for the study. The average bed level was therefore used in the analysis of the results and deemed sufficient for the scope of this study. Also, this method was appropriate because in real life conditions this is how the bed elevations would be surveyed, so this method simulates the method followed by the industry when performing a river survey.

After the riprap was surveyed, the riprap testing area was sprayed with four different coloured spray paints. This was to ensure that the movement of stones would be easily visible to the naked eye, as well as to ensure that the camera depicted any movement of the rocks. An image of the sprayed riprap with the untampered riprap layer in the test section was captured with the camera. The first image was used as the reference image to track down the movement of the stones.

The last step was then to fill the model slowly with water up to the crest height. It was critical that the filling was done slowly to ensure that the air trapped under the model was released slowly. The gradual filling of the model ensured that no premature failure of the riprap was caused due to uplift pressure from the escaping air. For Test series one, the model filling and saturation stage were prepared by allowing flows at approximately 0.010 m^3/s per second to fill up the upstream section. When the flowing water was close to flowing over the crest, the flow rate was reduced to 0.005 m^3/s so that the downstream section was saturated without failing the riprap prematurely. For Test series two and Test series three, the model filling and saturation were prepared with flows between 0.015 m^3/s to 0.020 m^3/s without failure of the downslope riprap testing area.

3.5.3 Riprap Failure Test

The previous two sections outlined the general preparation of the equipment and the riprap model layer for all the tests. The preparation of the models and the equipment was a repetitive procedure in all the Test series. However, for the testing of the actual model, there were slight changes during the testing procedure.

Test series one comprised of the D_{50} = 0.038 m median size riprap while Test series two and Test series three comprised a large D_{50} = 0.075 m median size riprap. Another change between Test series two and Test series three tests was the fact that in Test series three the riprap over the bed was immovable (glued).

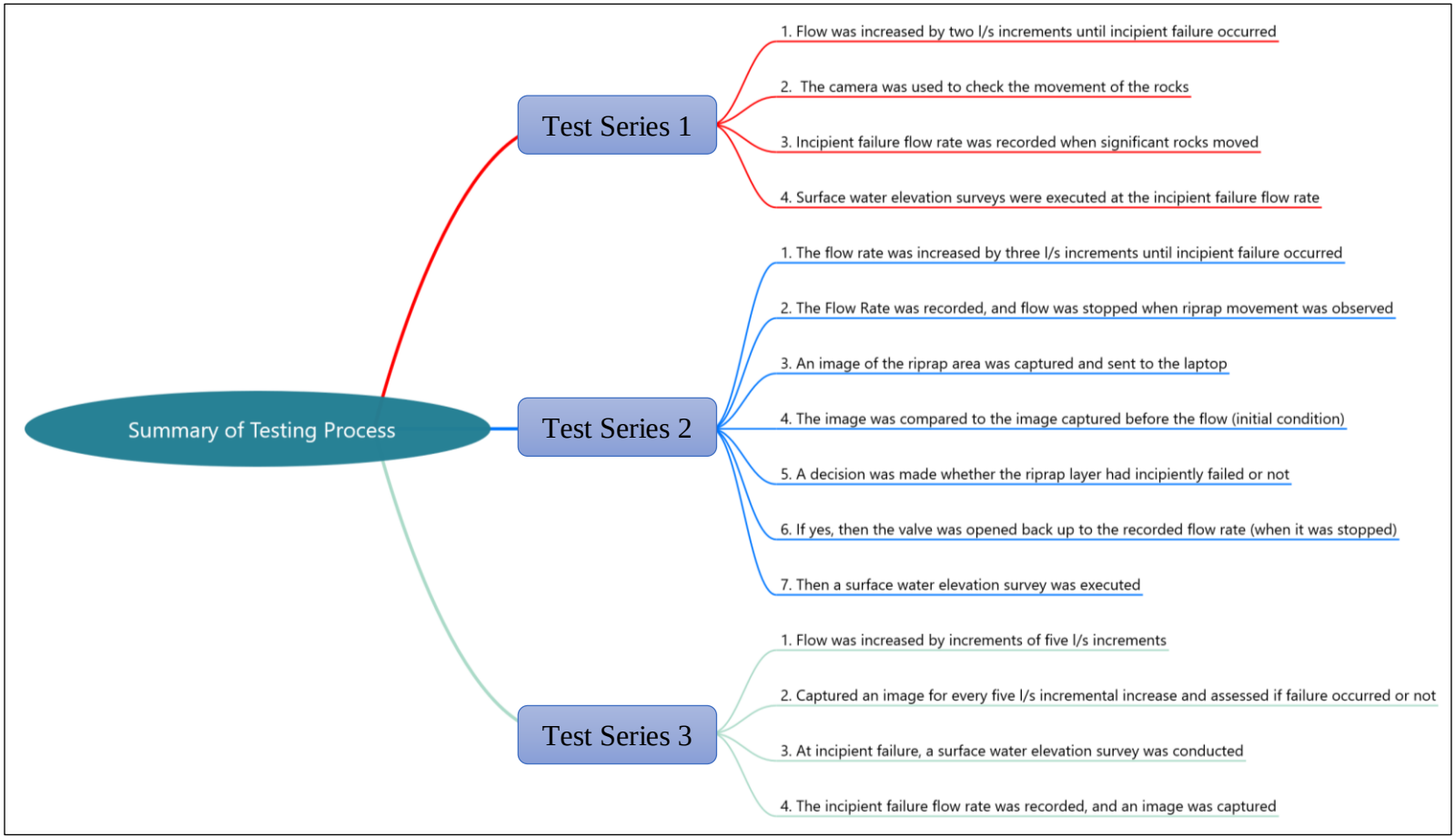

Figure 39: Mind map showing a summary of the main tasks during the testing procedure.

In Test series one, the D_{50} = 0.038 m riprap layer comprised smaller angular rock mixture compared to Test series two and Test series three. As a result, the riprap mixture in Test series one was sensitive to the incremental flowrate increases. The flow rate incremental increase for Test series one was chosen as two l/s. The incremental increase was enough to ensure that the incipient failure flow rate was accurately recorded.

Nonetheless, the incipient motion was defined as the point at which there was significant movement on the riprap slope by a combination of rocks comprising size D_{50} and less from the riprap layer. The spray-painted rocks assisted the author in determining the incipience of the riprap layer accurately. A general observation was that the stone sizes larger than the D_{50} never moved during the incipient failure conditions. The rocks larger than D_{50} only moved when the flow was increased until the whole slope failed to expose the underlying filter geotextile bidim layer.

Since Test series two was tested for the large D_{50} stone size, the incremental flow rate increase applied was three l/s for every five minutes before incipience occurred. A consistent and accurate way to check the movement of the riprap was applied by comparing the initial image captured at the beginning of the test with the image at a specific flow rate which the author was interested in knowing if there was incipient movement or not.

There were two main observations during the testing of Test series one and Test series two. The first observation was that the steeply sloped riprap beds failed at shallow depths without failing the riprap on the side banks. Thus, Test series one and Test series two did not allow the effective study of the incipient failure on the side banks. Therefore, it was decided that in Test series three the bed must be made immovable with an adhesive. This was to avoid the bed failure and to allow the flow depth to increase such that the incipient failure of the side bank would be studied. Another possible option was to increase the size of the D_{50} on the bed (larger sized riprap would allow an increase in flow depth). However, with time constraints and the effort required to find larger riprap rock, then sort, mix and lay, it would not allow time to finish the research. As a result, the bed was effectively glued, and the side banks were tested for incipient failure conditions.

The use of the camera was essential in Test series three to track the movement of the failure conditions. A consistent method to define the riprap incipient failure conditions were made possible by using the camera, especially in some cases where the movement of riprap was significant but not visible with the eye. This was evident in the cases where riprap rocks painted with same colour moved but remained in the same coloured riprap rock section.

3.6 Chapter Summary

Chapter three first described the hydraulic testing programme followed during the three-test series. The number of tests executed was highlighted. A description of the key hydraulic model design configurations and riprap stone size in each test was provided.

Thereafter, the procedure and logic followed during the design of the physical hydraulic model design parameters were described. The main hydraulic parameters that were accounted for in the design were the:

- the general shape of the model;
- the design of transitions;
- the bank and bed slopes of the trapezoidal section; and
- the riprap protection length.

Following the description of the design, the key components of the materials and construction methods during the building of the hydraulic model were outlined. This section summarised the procedure followed when constructing the foundation of the model. The method to ensure a watertight model was described including the special measure taken to ensure that the flow rate measurements read from the flow meter were representative to those flowing over the model. Then the author described the installation of the filter layer and the material used as the filter layer. All the riprap properties that were used to construct the riprap were also defined in this section.

Chapter three then provides the details of the laboratory equipment that was used to measure and obtain pertinent data required for the study. The main equipment that was described as the total station used to perform the surveys, then the flow meters that were used and the respective measuring precisions were specified. The setup and use of the video camera, which was critical in determining the incipient motion of riprap, were described. Then a brief description of the use and setup of the point gauge needle was described.

Finally, the last section of the chapter provides a summary of the testing procedure followed in each of the three riprap testing series. The section described the equipment preparation, then described how the riprap was prepared and a brief description of the actual failure test was provided on a comprehensive diagram in **Figure 39** above. Following the comprehensive diagram, a detailed description of some key information and observations during the tests was given.

Chapter 4 : Processing of Laboratory Data and Results

Chapter four provides a summary of all the data recorded during the hydraulic testing of Test series one, Test series two and Test series three. **Section 4.1** outlines the recorded flow rates at incipient failure for all the tests. Each test was given a unique test number and the respective failure flow rates were summarised in **Table 9 to Table 11**. **Section 4.2** describes the processing of the measured water elevations data from the physical hydraulic model to produce a summary of the upstream and downstream surface water elevations data. **Section 4.3** describes the use of the Surfer Golden Software version 15 (Surfer v15) and Microsoft Excel to determine the local failure water depths and slopes in the local failure regions of the riprap for each test.

4.1 Recorded Failure Flow Rates

During the testing series, the incipient failure flow rate was recorded. The incipient failure flow rate was defined as the recorded flow rate that induced significant initial riprap motion from the riprap layer. The riprap incipient failure flow rates were recorded accurately during the tests with the electromagnetic flow meters described in Chapter three.

Generally, the incipient failure flow rates from Test series one, Test series two and up to Test series three, increased from one Test series to the next, due to the increase in riprap resistance from each Test series. From Test series one to Test series two, the failure flow rates increased due to the higher resistance provided by the large D_{50} = 0.075 m (in Test series two) compared to the D_{50} = 0.038 m (in Test series one) riprap. For Test series two and Test series three the riprap size was the same. However, the side bank riprap in Test series three failed at higher flow rates because of an increased water depth showing a significant incipience-inducing effect at higher flow rates.

Table 9 to Table 11 below provides a summary of all the flow rate data recorded at each Test series for each unique test. The test numbers use a unique naming system, in which the "M_1T_1" means model one test one of that specific testing series. The M_1 was related to the 0.5 steep riprap bed slope of the model, M_2 was related to the 0.4 steep riprap bed slope of the model and the M_3 was related to the 0.333 steep riprap bed slope of the model.

Table 9: Summary of recorded physical model failure flow rates for Test series one tests

Test No.	Q_i (m^3/s)
M_1T_1	0.0121
M_1T_2	0.0120
M_1T_3	0.0118
M_2T_1	0.0120
M_2T_2	0.0120
M_2T_3	0.0120
M_3T_1	0.0158
M_3T_2	0.0159
M_3T_3	0.0169

The two encircled tests have been removed from the analysis. The bed elevation data was lost from the total station controller. Thus, elevation and water depths could not be processed for the two tests and it was decided that the two tests be discarded. So only seven tests were successfully analysed out of the nine.

Table 9 shows that there was little difference in the incipient failure flow rates (Q_i) between the 0.5 and the 0.4 steep bed slopes. Both the model one and model two steep bed slope tests failed at an average Q_i of 0.012 m^3/s. However, there was a significant difference in the Q_i for the model three tests with slightly steep 0.333 riprap bed slopes. The model three tests had a critical Q_i of 0.0158 m^3/s.

Table 10: Summary of recorded physical model failure flow rates for Test series two tests

Test No.	Q_i (m^3/s)
M_1T_1	0.0370
M_1T_2	0.0344
M_1T_3	0.0357
M_1T_4	0.0319
M_1T_5	0.0351
M_2T_1	0.0428
M_2T_2	0.0430
M_2T_3	0.0462
M_2T_4	0.0433
M_2T_5	0.0374
M_3T_1	0.0494
M_3T_2	0.0507
M_3T_3	0.0519
M_3T_4	0.0516
M_3T_5	0.0530

In **Table 10,** for Test series two, the number of tests in each model was increased to approximately five tests per model. In Test series two there was a significant variation in the observed Q_i values. The model one tests had an observed critical Q_i of 0.0319 m^3/s. The model two observed critical Q_i was 0.0374 m^3/s, which shows a slight increase compared to the model observed Q_i critical value. The slight increases could be due to the bed slope difference. The observed model three critical Q_i value was 0.0494 m^3/s. Therefore, in Test series two tests, there was a difference in the critical Q_i values, which could be mainly because of the difference in the three steep bed slopes. The 0.333 steep bed slope of model three showed the highest failure resilience.

Table 11: Summary of recorded physical model failure flow rates for Test series three tests

Test No.	Measured Flow Rates
	Q_i (m^3/s)
M_1T_1	0.1386
M_1T_2	0.1358
M_1T_3	0.1373
M_1T_4	0.0940
M_1T_5	0.0892
M_3T_1	0.0742
M_3T_2	0.1023
M_3T_3	0.1036
M_3T_4	0.1240
M_3T_5	0.0956

In **Table 11,** for Test series three, only model one and model three were tested. In model one, the critical Q_i value was 0.0892 m^3/s. However, in the model three tests, a critical Q_i value of 0.0742 m^3/s was observed during the tests. Test series three flow rates showed an opposite behaviour pattern to Test series one and two. The highest failure flow rates were observed in the steepest (0.5) bed slope while the lowest failure flow rates were observed in the slightly gentle (0.333) bed slope. However, it should be recalled that Test series three was set up in a different manner compared to Test series one and two. In Test series three, the water depth at a specific flow rate seemed to play a much greater role than the actual flow rate. In the 0.333

steep slopes, it was observed that the water depth increased much quicker than in the steep 0.5 slopes.

4.2 Upstream and Downstream Surface Water Elevations

Three main water elevations data were required during the testing series. The upstream water elevations, downstream water elevations and the surface water elevations at the downslope testing area of the riprap.

The water elevations data at the upstream area and downstream of the hydraulic model was important for use as boundary input data into the HEC-RAS numerical model simulations. The water elevations in the downslope riprap testing area were valuable in the physical determination of the water depth over the downslope riprap bed area. This section of the chapter summarises how the surface water elevations were determined, and the results obtained in each test.

4.2.1 Surveys

The total station was used to determine the required surface water elevations and the riprap bed elevations. Similar to real life river surveys, the difference between the bed survey elevations and the water surface elevations is generally regarded as the average water depth. In this thesis, the same definition was used, and the water depth was defined accordingly.

Therefore, to determine the water depths on the physical model, survey data with surface water elevations and the top of the riprap elevations was captured with the total station and stored on the controller.

4.2.2 Data Retrieval and Storage

All the data that was stored in the total station controller was retrieved with the Leica Geo Office 8.3 software and transferred to the computer. The elevation data was then exported from the Leica Geo Office 8.3 software to excel sheets as XYZ coordinate data. All the data points were stored in an orderly manner according to the testing series and test number. Good data management practice was critical in ensuring that the data was easily found and used when required because the coordinates and elevations data that were captured for the whole thesis were large and if not well managed it would cause inconvenience to find lost or misplaced data.

4.2.3 Golden Surfer v15 Software

A software to plot the coordinates and elevation data was required. Autodesk Civil 3D was the first software that was assessed to plot contour data. The major problem that was found with using Civil 3D, was that the process to create the required layers of contours took significant effort and time. In addition, the process of editing the contours or obtaining a cross-section of the data from CIVIL 3D was not user-friendly.

As an alternative, Surfer v15 was used to process elevation data. Surfer v15 saved a significant amount of time in processing the raw data into grids and then converting the grids to the required contour data. The Surfer software was chosen as the main data processing tool for this study for the following main reasons:

- good visualisation of the data;
- took less time to plot data;
- less effort input to obtain a contour;
- could easily plot stacked layers of data if they in the same coordinate system;
- less effort required for obtaining cross-sectional data;
- easy and quick to learn; and
- quick and easy to edit the layout of maps and export.

For the reasons mentioned above, Surfer software outperformed the CIVIL 3D software. Surfer v15 was found to be a useful tool for research purposes as it allows the researcher to analyse data without having to worry about the details and time to create specific plots or maps. The Surfer v15 software made it convenient for the researcher to process and analyse the elevation data.

4.2.4 Contour Generation

The first step in the determination of the required water elevations and water depths was to create layers of contours with the following datasets, for each test:

1. Bidim elevation data
2. Riprap bed elevations
3. Surface water elevation at incipient failure

The stacked contours obtained from the Surfer v15 software can be seen in **Figure 40**:

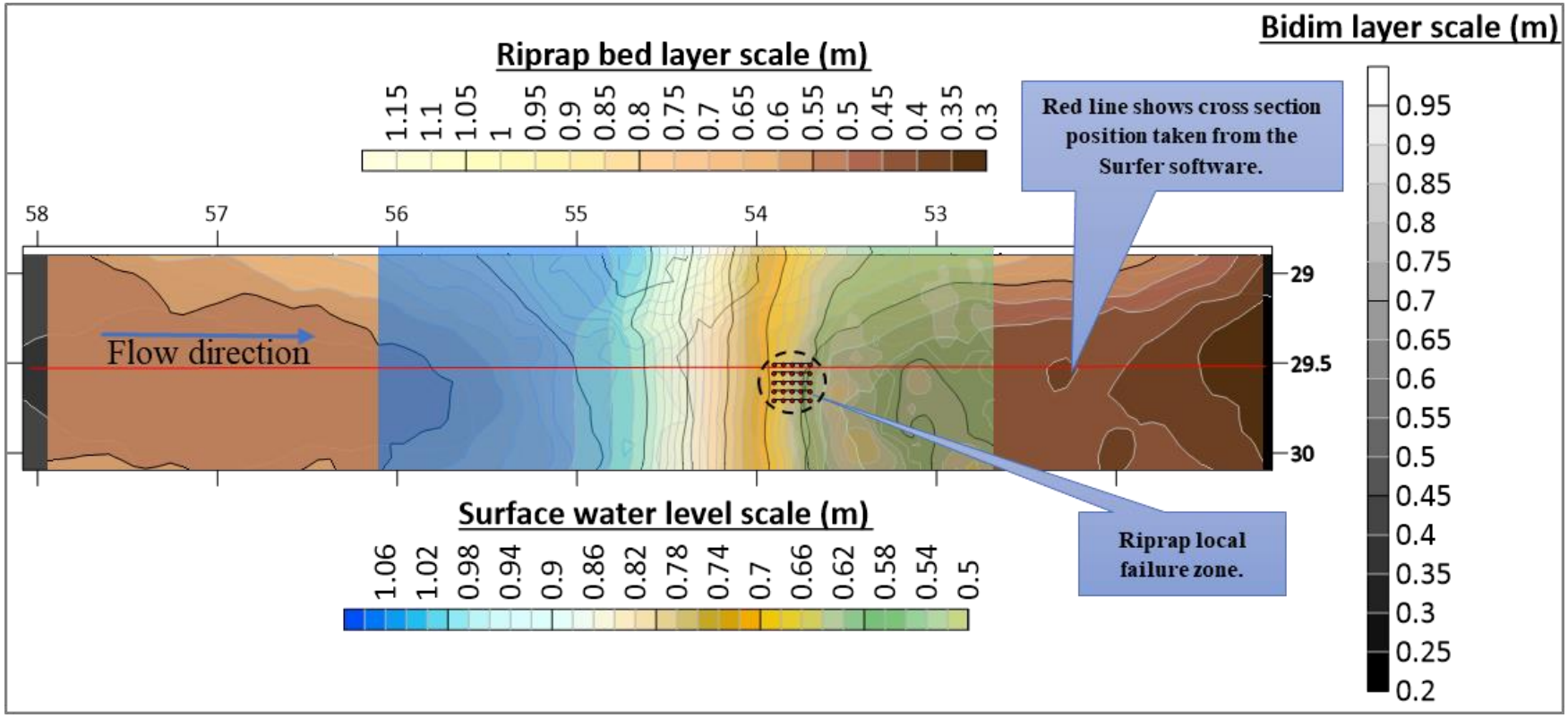

Figure 40: A sample of the bidim contour layer(black-grey), riprap bed contour layer(brown) and the surface water contour layer(blue-green) generated and stacked on top of each other with the Surfer v15 software.

Different colour schemes in **Figure 40** were used to allow the reader to realise the different layers of contours stacked on top of one another. At the bottom (the brown colour scheme) is the average top of the riprap layer. The green-yellow-white-blue colour scheme layer was the surface

water elevation layer at a specific Q_i. The bidim layer(black-grey) was not visible from the plan view because it was underneath the riprap layer (slightly visible at the far right and left ends of the contour map in **Figure 40**).

Figure 41 shows a 3D representation of the stacked data (only the surface water and riprap bed elevation are shown). The 3D layers were used to check if there were any deficiencies in the data and where they could be. For instance, in a few cases, the needle would move slowly down and capture significantly incorrect points on the surface of the water. So, the 3D model was used to check for such errors in the data.

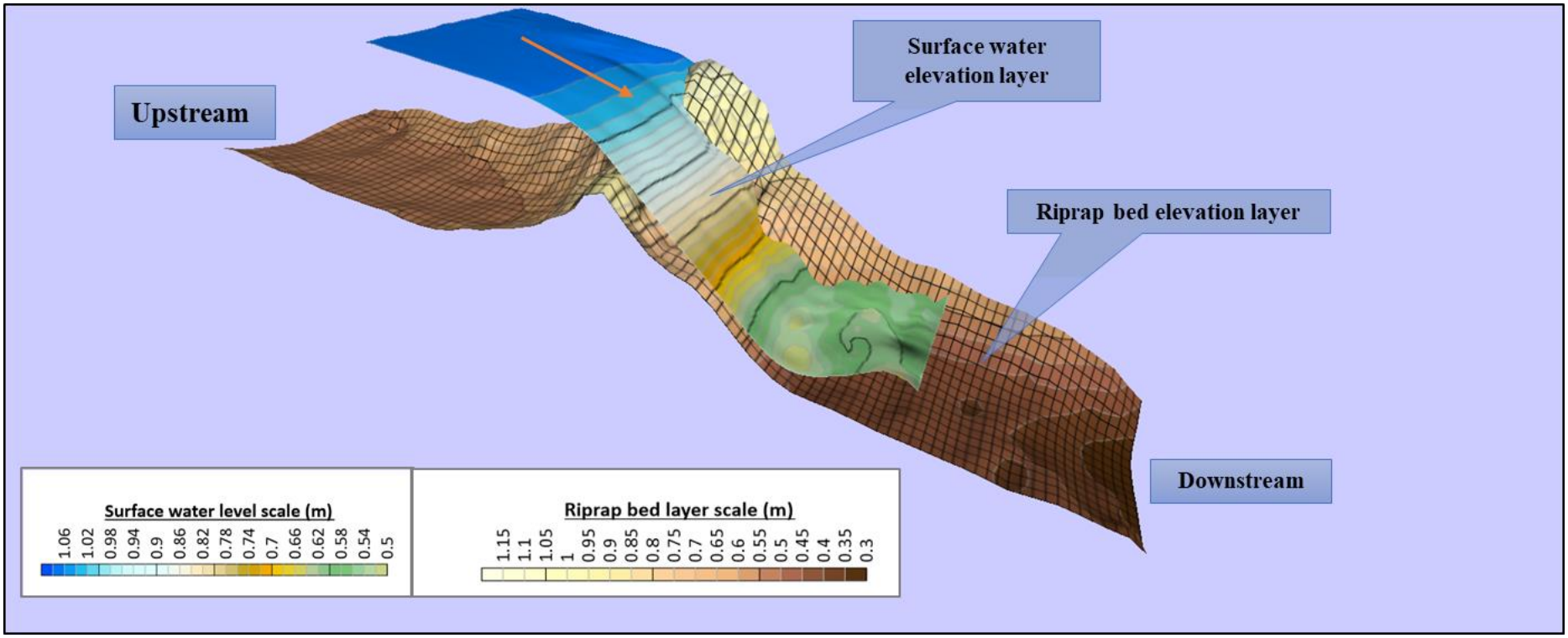

Figure 41: A 3D representation of the elevation data of the riprap bed (brown layer) and surface water level (blue-green) that was obtained using Surfer v15.

4.2.5 Cross-Sectional Data

The cross-sectional data was extracted from the contour data to obtain the upstream and downstream elevations of the model. To extract the cross-sectional data, a Surfer v15 mapping tool was used to retrieve the data. To use the tool, the software user was required to draw a line from downstream to upstream to indicate where the required cross-sectional data must be retrieved. The resulting cross-sectional profile looked like the one in **Figure 42:**

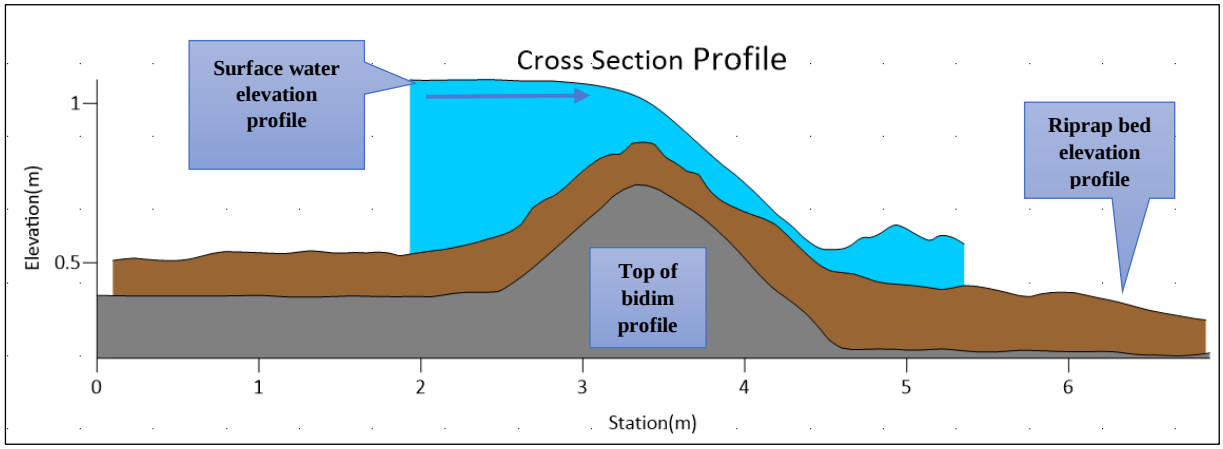

Figure 42: A typical longitudinal cross section through the three elevation data layers at Q_i.

The Surfer v15 software accurately plotted the different elevation data layers in the correct order. The grey layer was the top of the bidim, the brown layer was the riprap bed elevation and the blue layer was the surface water elevation at the pertinent Q_i.

The challenge that arose during the processing of the data was when the upstream water elevation, downstream water elevation and water depth needed to be determined from the created Surfer v15 longitudinal cross-sectional profile. The first option was to read off values manually from the diagram similar to **Figure 42**. The problem with reading off values by eye is that it would be easy to make an incorrect reading. Thus, it was decided that the cross-sectional data from Surfer v15 must be exported to Microsoft Excel. When the data was re-plotted on Excel it could be easily manipulated with the Microsoft Excel mathematical functions to determine accurate elevations at the upstream and downstream sections of the flume.

Moreover, Excel was a useful tool to use in calculating the water depth at the testing area with the exported data. **Figure 43** shows a typical Microsoft Excel-created surface water profile developed from the data imported from Surfer v15.

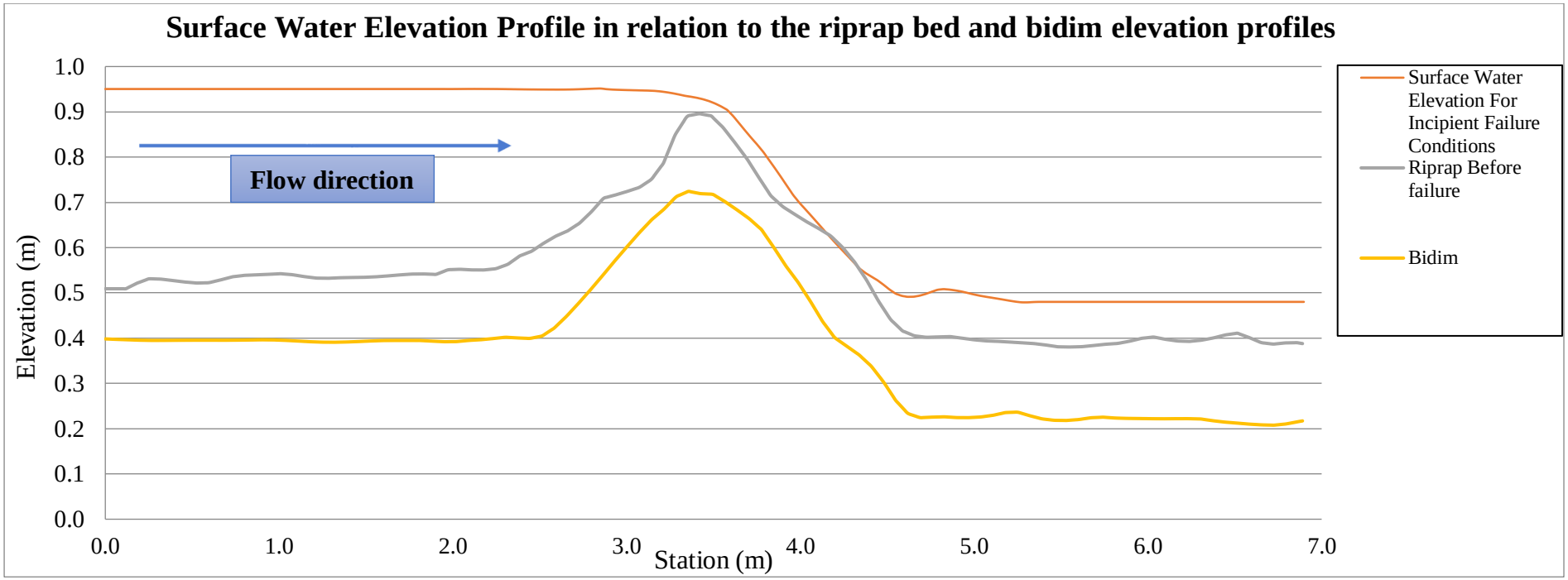

Figure 43: A typical surface water profile re-produced on Excel.

The legend in **Figure 43** shows the three sets of the elevation data that were plotted onto the profile in **Figure 43**. In **Figure 41** the surface water elevations began at station 2m, but in **Figure 43** the upstream surface water elevation was extrapolated, with the average value of the upstream surface water elevation up to station 0 m. Similar to the downstream elevations, the average downstream surface water elevation value was extrapolated and assumed to be the relevant downstream elevation. For each test, the upstream and downstream elevations were determined by creating the surface water profiles as described in this section. A summary of the measured upstream and downstream elevations can be found in **section 4.2.6.**

4.2.6 Summary of Upstream and Downstream Water Elevation Results

The upstream and downstream surface water elevations were determined using the total station elevation measurements as described in **section 4.2**. Upstream and downstream surface water elevations are generally critical as they can be used as boundary conditions for HEC-RAS numerical hydraulic modelling simulations.

The upstream surface water elevations were accurately measured, and an average of the upstream surface water elevations was used. The upstream flow was uniform, and no waves were present during the testing, as a result, constant and accurate upstream elevations were measured.

However, the downstream surface water elevations were only well recorded for Test series one and Test series two. In Test series three, at high flow rates the downstream area, in which the gauge needle measured, repeatedly formed hydraulic jumps (the orange region in **Figure 44**). The hydraulic jump conditions did not accurately represent the downstream surface water elevation conditions. Therefore, to account for this, the downstream surface water elevations with minimal water depth influence from the hydraulic jump at the toe of the riprap downslope area were measured and assumed to be the downstream elevation. For instance, further down the hydraulic jumps, the elevations dropped and were representative of the downstream conditions. Also, on the side next to the hydraulic jump (red area in **Figure 44**), the surface water elevations were relatively similar to the downstream elevations.

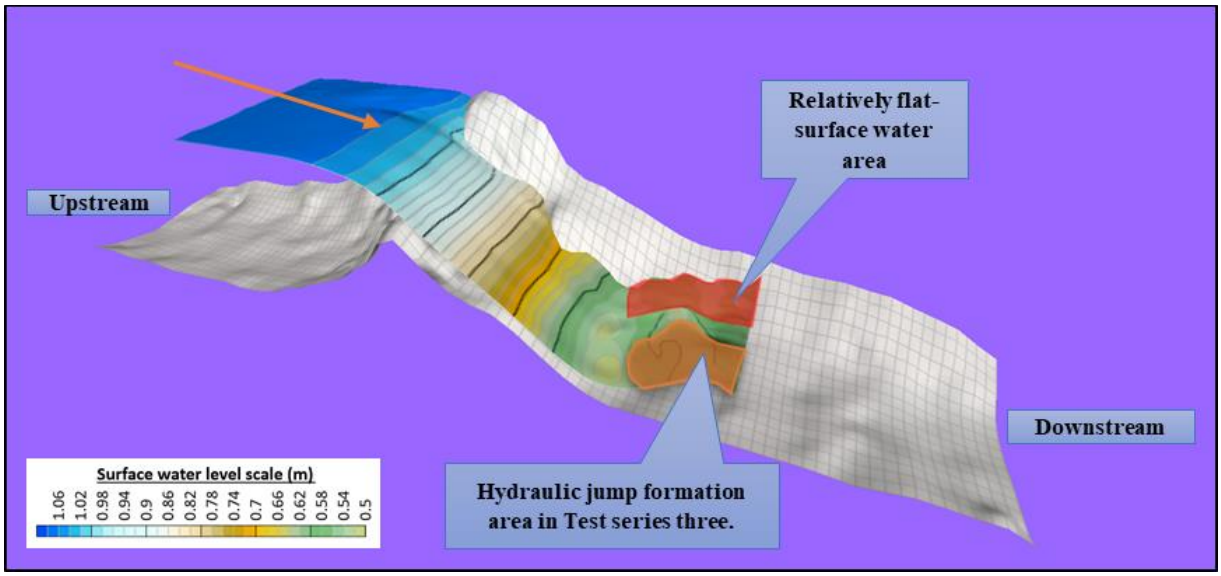

Figure 44:3D Surface of flow conditions showing the area with the hydraulic jump.

In **Figure 44,** the area shaded with an orange polygon was mainly the area where the hydraulic jump developed. Thus, the elevation in the area would be higher than the actual downstream elevation values. However, the area shaded with a red polygon in **Figure 44** comprised of flow and surface water with surface water elevations that were representative of the downstream flow surface water elevations. Therefore, the elevations in the downstream red-shaded area were used in the HEC-RAS models as the downstream water elevations when there was a hydraulic jump that changed the actual downstream surface water elevations. The limitation was that the point gauge needle could not be moved further down during the test when there was a hydraulic jump formed downstream. **Tables 12 to Table 14** below summarise the data of the upstream and downstream elevations that were measured during the model tests.

Table 12: Upstream and Downstream measured elevations at the testing of Test series one

	Model 1			Model 2			Model 3		
Test No	**Failure Condition**	**Upstream Elevation**	**Downstream Elevation**	**Failure Condition**	**Upstream Elevation**	**Downstream Elevation**	**Failure Condition**	**Upstream Elevation**	**Downstream Elevation**
1	Incipient	0.851	0.339				Incipient	0.858	0.5372
2	Incipient	0.841	0.3288				Incipient	0.8526	0.5163
3	Incipient	0.855	0.3197	Incipient	0.846	0.4353	Incipient	0.8647	0.521

Table 13: Upstream and Downstream measured elevations at the testing of Test series two

	Model 1			Model 2			Model 3		
Test No	**Failure Condition**	**Upstream Elevation**	**Downstream Elevation**	**Failure Condition**	**Upstream Elevation**	**Downstream Elevation**	**Failure Condition**	**Upstream Elevation**	**Downstream Elevation**
1	Incipient	0.950	0.471	Incipient	0.984	0.563	Incipient	1.035	0.697
2	Incipient	0.955	0.462	Incipient	0.976	0.569	Incipient	0.972	0.675
3	Incipient	0.953	0.448	Incipient	0.979	0.567	Incipient	0.987	0.678
4	Incipient	0.934	0.435	Incipient	1.005	0.573	Incipient	0.992	0.679
5	Incipient	0.952	0.479	Incipient	0.972	0.552	Incipient	0.993	0.688

Table 14: Upstream and Downstream measured elevations at the testing of Test series three

	Model 1			Model 3		
Test No	**Failure Condition**	**Upstream Elevation**	**Downstream Elevation**	**Failure Condition**	**Upstream Elevation**	**Downstream Elevation**
1	Incipient	1.0728	0.563	Incipient	1.018	0.647
2	Incipient	1.0711	0.551	Incipient	1.04	0.655
3	Incipient	1.0729	0.552	Incipient	1.039	0.668
4	Incipient	1.0259	0.539	Incipient	1.058	0.673
5	Incipient	1.0274	0.527	Incipient	1.033	0.659

From **Table 12** to **Table 14,** the upstream water elevations were accurately measured from the physical hydraulic model. The downstream elevation measurements in Test series three of the tests were influenced by turbulence, eddies and hydraulic jumps. As a result, the accuracy of the downstream elevations was not measured and recorded at high levels of confidence. However, it was still important that the elevations are recorded to the possible levels of accuracy at the laboratory.

Regardless of the fact the downstream elevations were difficult to accurately measure, the results in **Tables 12 to Table 14** were reasonable and logical measurements. In conclusion, the upstream elevations measurements comprised of high accuracy confidence and the downstream elevations comprised of reasonable measurements that can be used as boundary conditions where required.

4.3 Water Depth Determination at the Local Riprap Failure Zones

In flatbed rivers, the water depth is normally determined from the difference between the average top of riverbed elevations and the surface water elevation. This can be done by vertically determining the difference between the two surveyed elevations. To accurately determines the actual water depth flowing over steep riverbeds, the steep slope needs to be accounted for. The diagram in **Figure 45** by Novak (1999), shows how the water depth is represented on steep riprap protected slopes.

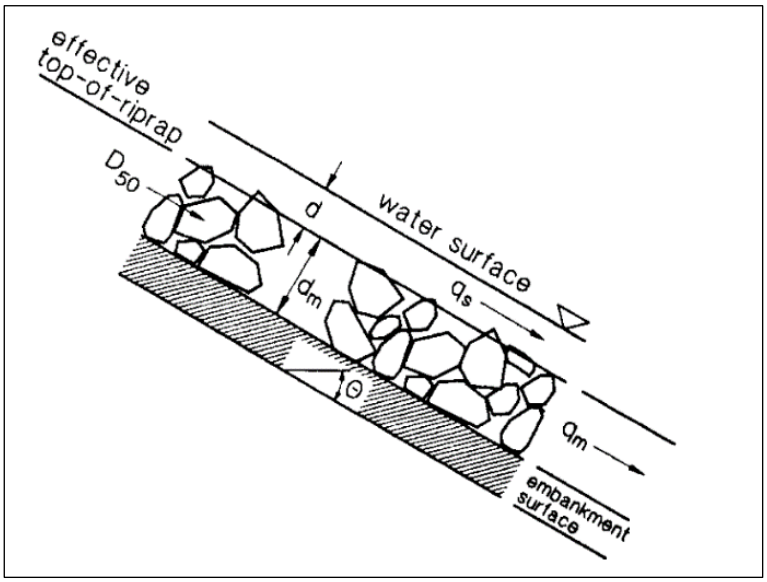

Figure 45: Water depth on steep riprap slopes (Novak, 1999).

In **Figure 45** above the "d" represents the actual water depth on top of the effective top of the riprap area. The same method was followed for this study to define and determine the water depth on the slope. The water depth on the sloped bed was the one used for the analysis in this thesis.

Initially, it was decided that the approach to determine the water depth in the riprap failure region should be based on an average water depth for one typical water surface profile cross-section (for example the average water depth in **Figure 43** would represent the water depth for the failure conditions of a specific test; the zoomed in section illustrated in **Figure 46** below). However, the problem with this approach was that it could lead to biased results as well as it was not representative of all the possible measurable conditions of the water depth in the local riprap incipient failure zone.

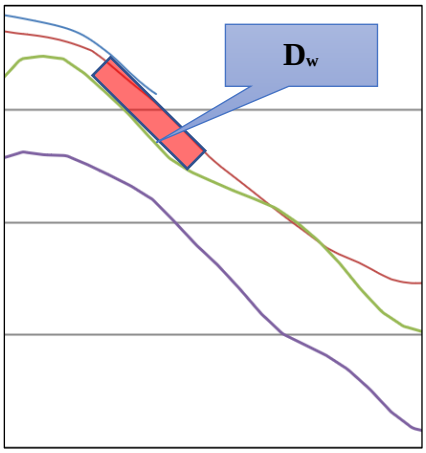

Figure 46: Physical water depth determination area on the steep slope

To further illustrate the potential bias of water depth determination by taking one cross-sectional profile from downstream to upstream, **Figure 47** shows one profile cross-section (red line) passing through the local riprap failure zone (red dots). The red line only represents one possible average water depth within the failure area. However, due to varying riprap bed levels and water elevations, the water depth in the failure zone (shown as compact red dots in **Figure 47 and Figure 48**) varies. Therefore, to account for the variation of the local water depths within the local riprap failure zones identified at the laboratory, an approach that accounts for the variations was adopted.

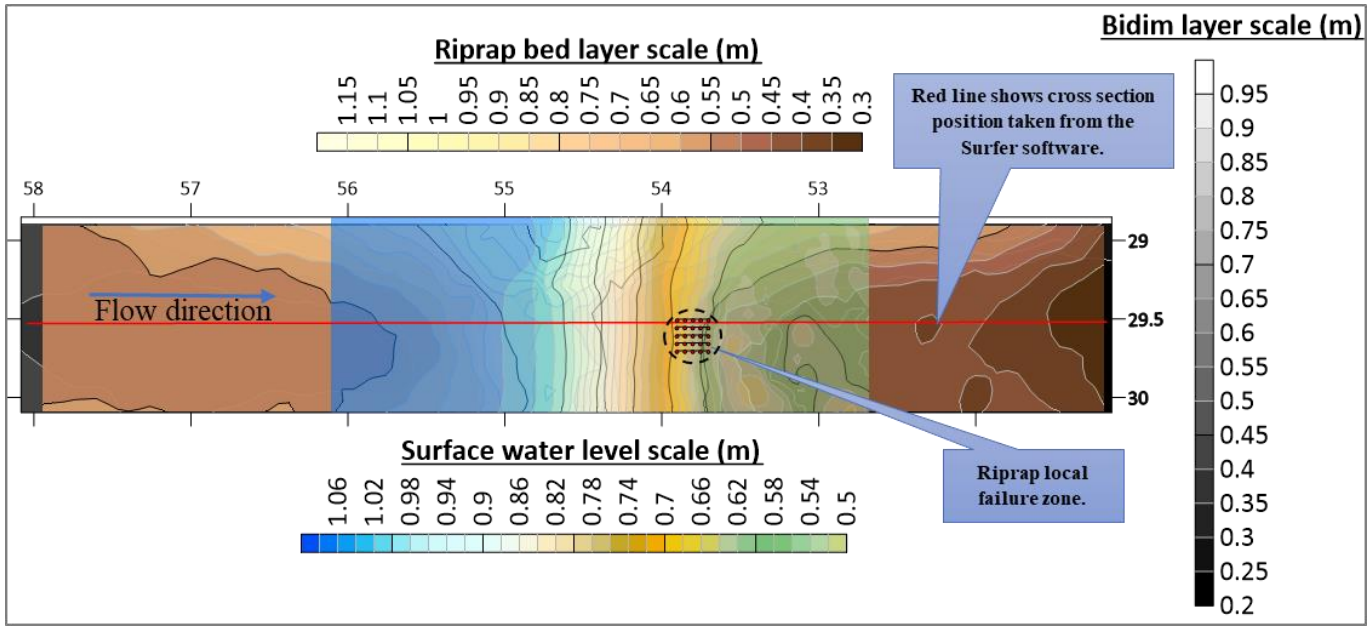

Figure 47: Typical cross-section profile position (red line) cutting through the failure area from downstream to upstream.

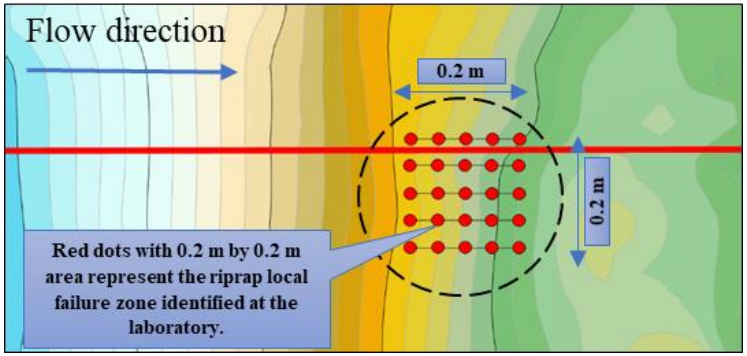

Figure 48: Exaggerated section (from Figure 47) showing the local failure zone dimensions and extent in relation to the longitudinal cross-section (red line).

Instead of using an average water depth for the analysis of a single test, the local failure area in each test was determined. A 200 mm by 200 mm (as seen in **Figure 47** and **48**) area in the failure zone was located and analysed. The local water depth and local average slopes in the riprap local failure area were determined.

Approximately 20 points (red dots) with the configuration in **Figures 48** were determined in the riprap local failure zone for each test. The red dots in **Figure 48** were placed to identify the approximate area of failure in each test. The location of the dots was based on the failure area that was observed at the laboratory. The red dots allowed the extraction of data in the local failure regions of the riprap. Cross-section data was extracted parallel in the direction of the flow. The distance from dot to dot was approximately 50 mm. The Surfer v15 tool was used to extract profile data for each of the local failure cross-section lines (the thin black lines from dot to dot in **Figure 48,** in flow direction).

It was not always possible to obtain 20 accurate water depth and slope results from the cross-sections in the local riprap failure zones. The reason was that sometimes the data in the failure region either showed measurements of very small water depths or negative water depths or slopes. The negative water depths could be due to a rock protruding through the water level or the rock being at approximately at the same elevation as the water level. So, all the local failure regions with water depths and slopes that were not logical were discarded in use for the analysis. **Figure 48** shows a zoomed in section of the local failure zone shown in **Figure 47.**

Each locally obtained cross-section profile with surface water elevations and riprap bed elevations would typically produce a profile like the one shown in **Figure 48.** The slope profiles were not as gentle as shown in **Figure 48,** the scale is distorted because the slope in the 1:1 scale was supposed to illustrate a steep slope.

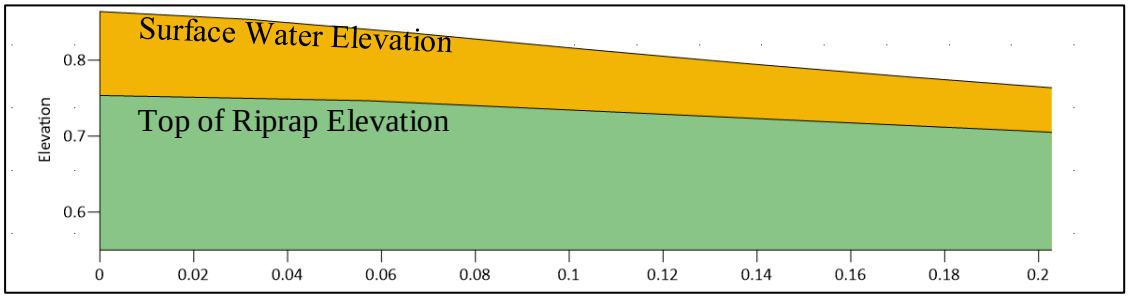

Figure 49: Top of Riprap bed level and surface water elevation profile extracted in the local riprap failure area.

In each test, five locally obtained elevation profiles similar to the one in **Figure 49** were extracted. The elevation data was then exported to Microsoft Excel. In Microsoft Excel, for each of the five cross-section profiles, the water depth and average slopes were determined for 50 mm sections (representing the distance from one dot to the next dot). For example, the profile in **Figure 49** was broken into four smaller profiles. For each of the four profiles, the average water depth and the slope were determined. The calculations were completed for all the five main cross-section profiles (black thin lines in **Figure 48**), this resulted in a maximum of 20 average water depth and slope calculation results. All the locally obtained average water depth and slopes represented 20 potential possibilities of water depth and slopes within the 200 mm by 200 mm failure zone. Therefore, the approach followed showed less bias in terms of the measured water depths in the riprap incipient failure region.

For each smaller cross-section profiles, the steep slope was accounted for and the water depth was calculated consistently in relation to the water depth definition by Novak (1999) shown in **Figure 45**. An illustration of the water depth calculation parameters is shown in **Figure 50**

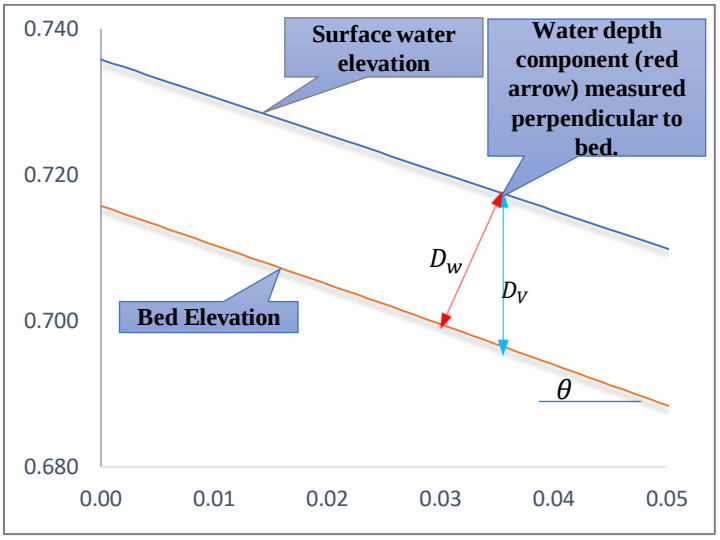

Figure 50: Local failure area water depth determination components

To physically determine the water depth for each local failure cross-section profile, uniform flow conditions were assumed. It was assumed that the water would flow on the steep slope at the same slope as the average bed level (at angle theta). The average bed slope for each local failure area was determined by applying an approximate 10%/85% slope determination method. **Figure 50** shows the vertical water depth D_v (blue line) as well as the required local failure water depth for this thesis D_w (red line) in a typical 50 mm long cross-section profile in the local failure region.

To determine D_w, the vertical water depth component D_v was calculated (as the difference between the bed and surface water elevations), represented by the blue line in **Figure 50**. Thereafter, the vertical water depth was broken down into the D_w component by multiplying the D_v with $Cos\theta$, as illustrated by **Equation 55**:

$$D_w = D_V \, Cos\theta \qquad \textbf{Eq. 55}$$

Consequently, for each local failure area, the effective top of the riprap average water depth was determined. All the calculated local slopes and the local average water depth calculations for all the tests were summarised in **Appendix D.**

It was impossible to measure 100% accurate water depth in turbulent flow conditions. The irregular nature of riprap made it very difficult to obtain water depths with high accuracy confidence.

During the elevation measurements, the eddies and jets on the steep downslope riprap area were dominant at shallow depth. The incipient failure conditions of the riprap in Test series one and two occurred at shallow flow depths. As a result, the actual physical model results of the water depth for the incipient failure conditions were measured but the confidence in the results obtained was not highly acceptable due to the irregularities and complexities in water depths measurements on rough beds. However, the investigator tried to avoid measuring in the areas with eddies and jets to obtain representable average water depths.

It was observed that the effect of the jets and numerous eddies reduced with an increase in the flow rate, thus the flow depth. A higher flow rate resulted in more uniform flow and reduced the effects of the rough bed.

In Test series three, the riprap bed was fixed, the flow rate and water depth increased such that in all the tests the jets and eddies effects reduced and uniform flow over the bed area was prevalent. Thus, the flow depth measurements at Test series three can be assumed to be more representative of the real conditions in the model.

Regardless of the limitations in determining the water depth over the riprap downslope testing area, the incipient failure flow rates, upstream surface water elevations and the downstream surface water elevations were measured with a higher level of confidence compared to the water depth measurements obtained at the failure riprap downslope slope.

Chapter 5 : Analysis of Physical Laboratory Results

Chapter five outlines the details of the approach that has been adopted to analyse and quantify the hydraulic incipient failure conditions of angular riprap dumped in wide and steep trapezoidal channels. The theoretical basis underpinning the analysis of the incipient motion of the angular riprap was based on the MN analysis.

A brief description of the critical parameters required to perform a MN analysis was described. Then the MN and the pertinent particle Reynolds number results of the physical model tests were calculated. Thereafter, the results of the analysis were discussed based on the obtained data and laboratory observations. The analysis of the local failure MN was based on the statistical approach. The probability of exceedance was used to determine the critical MN defining the incipient failure conditions of riprap dumped on steep bed slopes and steep side bank slopes.

5.1 Test Series One MN Analysis

Armitage (2010) states that Liu (1957) developed a dimensionless MN parameter in order to define the point of incipient motion of particles. Further, Liu (1957) concluded that there exists a unique relationship between the MN and the particle Reynolds number (Re_*).

Rooseboom (1992) defined the critical MN for incipient motion of a particle in turbulent flow regions as follows:

$$\frac{u_*}{v_{ss}} = \frac{\sqrt{g D_w S_o}}{v_{ss}} = Constant \qquad \textbf{Eq. 56}$$

The constant in **Equation 56** is known as the MN. The physical model analysis in this chapter uses the provided definition in **Equation 56** as a basis to calculate the local failure critical incipient MN in each test conducted at the Stellenbosch University Hydraulics laboratory.

However, it was critical for this study that the steep bed and steep side slope correction factor was accounted for. **Equation 57** was adopted and used to calculate the MN applicable to the hydraulic setup of this specific study.

$$\sqrt{k_\beta . k_\alpha} . \frac{\sqrt{g D_w S_o}}{v_{ss}} = MN \qquad \textbf{Eq. 57}$$

The $\sqrt{k_\beta . k_\alpha}$ was the correction factor for the steep bed slopes and steep side bank slope. Whereby k_β was the steep bed slope correction factor and k_α was the steep side slope

correction factor. The two correction factors were defined in Armitage (2002) literature review as follows:

$$k_\beta = Cos\beta\left(1 - \frac{Tan\beta}{Tan\varphi_r}\right) = \frac{Sin\,(\varphi_r - \beta)}{(Sin\,\varphi_r)} \qquad \textbf{Eq. 58}$$

Whereby, β = Steep bed angle

and,

$$k_\alpha = Cos\alpha\sqrt{1 - \frac{Tan^2\alpha}{Tan^2\varphi_r}} \qquad \textbf{Eq. 59}$$

Whereby, α = Steep side bank angle

To define the incipient motion in the local riprap failure regions of the physical laboratory tests, the MN was calculated using the dimensionless MN criteria as defined by **Equation 57**. Thereafter, the pertinent correction factors were applied to account for the steep bed and side bank slopes.

Table 15 provides a summary of all the critical input parameters that were required in order to calculate the MN for the Test series one physical laboratory tests.

Table 15: Hydraulic input parameters to determine MN for Test series one tests

Input Parameter	Value	Unit
D_{50}	0.038	m
ρ_r	2700	kg/m^3
ρ_w	1000	kg/m^3
v_{ss}	0.6393	m/s
$\phi_{Repose(riprap)}$	40	°
$\alpha_{Angle\ (side\ slope)}$	21.77	°
$\alpha_{Slope\ (side\ slope)}$	0.4	
$\theta_{Angle\ (bed\ slope)}$	Varies	°
$\theta_{Slope\ (bed\ slope)}$	Varies	
g	9.81	m/s^2
S_o	Varies	
D_w	Varies	m
v	1.13E-06	m^2/s at 15 °C

The average local water depth (D_w) and average local bed slopes (S_o) were measured for each test at the local failure regions (the 0.2 m by 0.2 m failure region described in **section 4.3**). The local failure region was measured for a maximum of 20 data points with the average water depths and average bed slopes where possible, and each test's measurements were summarised in **Appendix D**.

For each unique average local water depth and average local bed slope measured, there was a unique MN value calculated. For instance, a single test (e.g. test P1M3T3) with a total of 20 average local water depth and slope measurements, 20 MN results were calculated for that specific test, representing the 20 MN values in one local failure region of 0.2 m by 0.2 m.

The median stone size of 0.038 m for all the Test series one tests were used for the riprap protection. The assumed rock density (ρ_r) of 2700 kg/m^3 was chosen based on the hornfels rock material type. Langmaak (2013) experimental determined the density of hornfels rocks and obtained approximately 2700 kg/m^3. The riprap rock settling velocity was based on the experimentally observed and tested results in **Appendix B.** The settling velocity results from the laboratory were based on the 0.038 m median stone size for Test series one. The riprap angle of repose was calculated based on the Froelich (2011) method (refer to **section 3.2.4.7).**

For Test series one tests, the side slope angle was designed for 0.4. However, when calculating the MN, the side bank slope angle correction factor was not included due to the laboratory test observation made; that the steep bed area failed without the water encroaching onto the side bank slope of the riprap. Thus, it was assumed the side bank slope has no influence on the incipient failure of the riprap at shallow water depth flow and low flow rates in steep trapezoidal channels.

The density of the water (ρ_w) was assumed to be 1000 kg/m^3. Consequently, the kinematic viscosity (ν) was assumed to be 1.13E-06 m^2/s at 15 °C. There were no physical temperature measurements taken at the laboratory. The water temperature at the laboratory varied depending on the temperature differences inside the laboratory. The assumed density and kinematic viscosity were within the reasonable range which is generally assumed for design purposes. Most importantly, the MN calculations were not significantly sensitive to the minor variations (of generally assumed values) of the two water properties. Additionally, most of the tests were performed during the cold winter seasons, therefore the 15°C assumption was deemed to be reasonable.

By substituting the average local failure water depth and average local average slopes summarised in **Appendix D** and the input variables in **Table 15** into **Equation 57,** the MN values and Re_* for Test series one tests were successfully calculated. A summary of the Test series one MN values and Re_* can be obtained from **Appendix E**. About 135 MN values and Re_* results were calculated for the seven tests in Test series one.

Test series one MN and Re_* results from **Appendix E** were plotted onto the Liu diagram is shown in **Figure 51**. Two characteristic curves which were developed by Rooseboom (1992) and Armitage (2002) were plotted onto **Figure 50** to form an envelope of critical incipient motion MN and the respective Re_*.

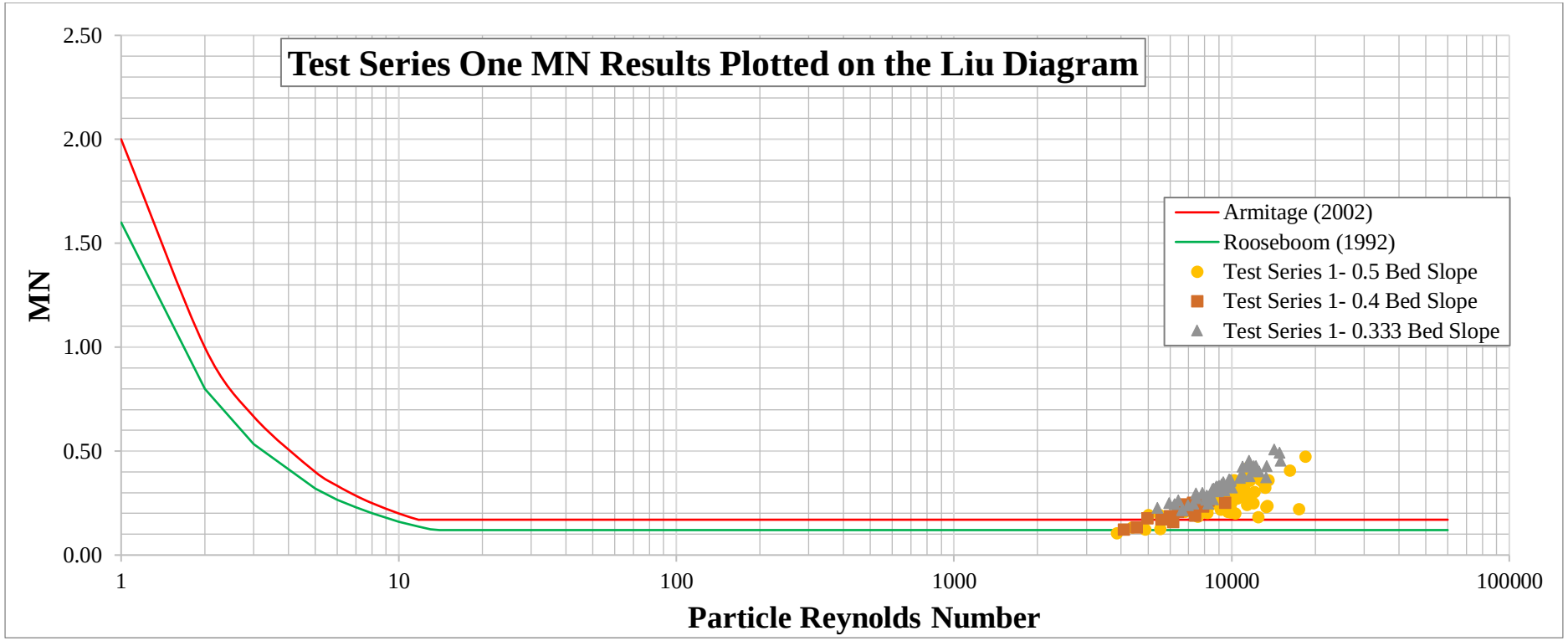

Figure 51: Test series one (incipient failure of D_{50}=0.038m riprap dumped on 0.5, 0.4 and 0.333 steep bed slopes with 0.4 steep side bank slope) MN results plotted onto the Liu diagram.

Armitage's curve was developed with the following criteria: $MN = \frac{2}{Re_*}$ for the hydraulic flow conditions falling in the laminar region ($Re_* < 11.8$) and $MN = 0.17$ for the hydraulic flow conditions in the turbulent region ($Re_* > 11.8$). However, Rooseboom's curve was developed with the criteria: $MN = \frac{1.6}{Re_*}$ for hydraulic flow in the laminar region ($Re_* < 13$) whereas the MN = 0.12 for flow in the turbulent region ($Re_* > 13$). The Test series one data was plotted on the Liu diagram in **Figure 51** to observe the relation of the results of the Test series one tests with respect to the MN criteria by Rooseboom (1992) and Armitage (2002).

Figure 52 demonstrates a closer look into the Test series one MN results lying in the high particle Reynolds number region. Test series one MN results plotted about seven points below the upper limit of the envelope MN value of 0.17. The seven points were the most critical data points with the lowest MN from the tests. Only one point plotted below the lower limit envelope MN values of the (0.12).

The remainder of the 128 MN data points plotted above the 0.17 upper limit MN. The points with MN values greater than the 0.17 showed a trend of increasing MN values with an increasing Re∗. From all the seven tests that were performed, most of the MN data points plotted above the 0.17 upper limit defined by Armitage (2002). If the 135 MN data points were perceived as 135 possible events of failure, and if the MN of 0.17 defined the local failure riprap incipient motion condition, then only 5.2 % of the data points would be below the 0.17 MN limit. The rest of the 94.8% of the MN data points obtained would be above the critical 0.17.

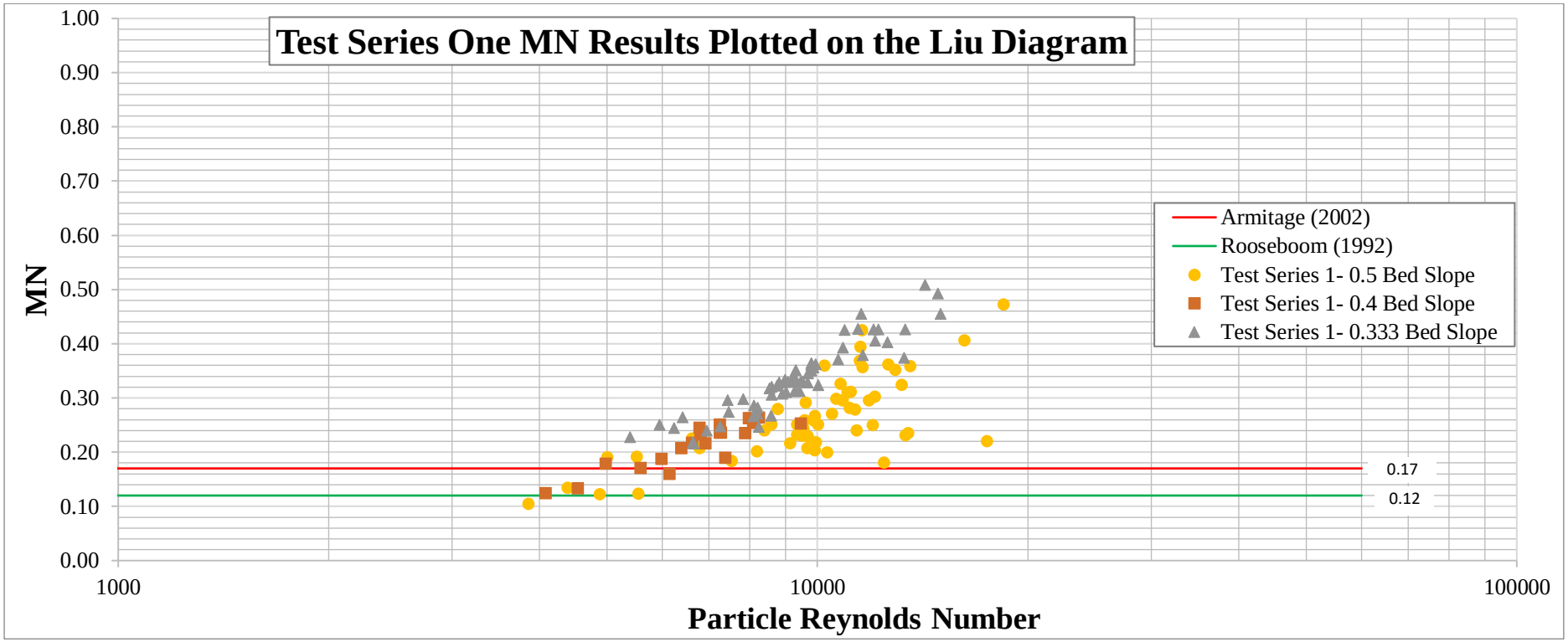

Figure 52: A Zoomed in view of the MN results of Test series one (incipient failure of D_{50}=0.038m riprap dumped on 0.5, 0.4 and 0.333 steep bed slopes with 0.4 steep side bank slopes) lying in the high particle Reynolds Region

The limitation with the MN data points plotted in **Figure 51** and **Figure 52** was the inability to show the scatter of the MN results with respect to each test performed at the laboratory in Test series one. Therefore, in order to be able to effectively demonstrate the scatter of the MN for each test the box-whisker diagram in **Figure 53** was established for each test in Test series one.

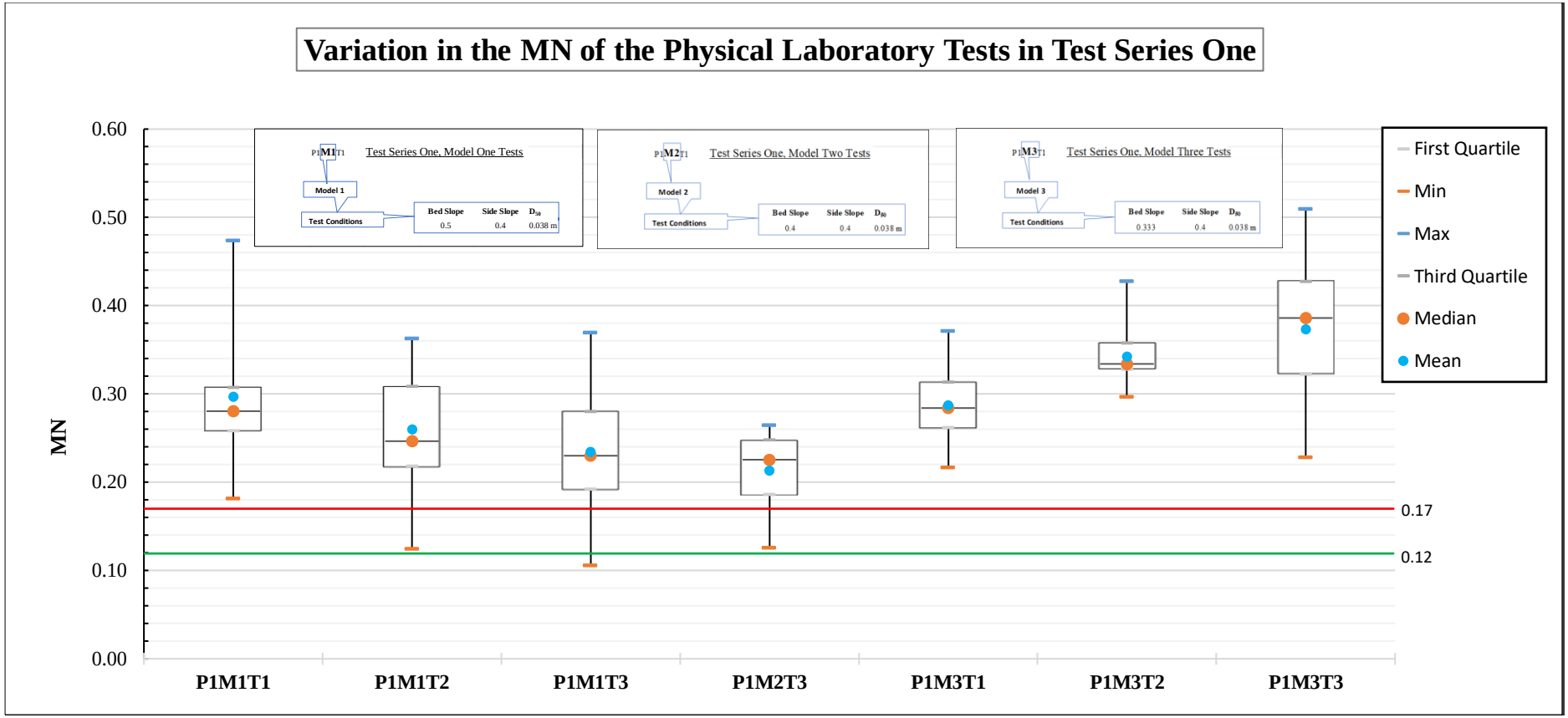

Figure 53: Box-Whisker diagram for the Test series one physical laboratory tests showing the variation in MN values per test.

It is important to understand the scatter of the calculated MN results. The scatter informs about the variation of the MN in the local failure zones. The box-whisker diagrams in **Figure 53** display the deviation of the calculated MN values for each test in Test series one. From **Appendix E** each test had a large dataset of calculated MN values. There were more than 17 MN results obtained at each failure region for each test. Therefore, the variations illustrated in all the seven tests in **Figure 53** can be deemed reliable and representative of the local failure variations of the MN values. **Appendix F** shows the standard deviations of the MN values for each test to express the variations within the local failure regions of the riprap.

The small variations in the MN values are shown by the compressed nature of the box. A compressed box illustrates the small deviations in the scatter of the MN values from the mean MN value. Test P1M3T2 has the smallest deviations in the MN values. The minimum and maximum MN values of test P1M3T2 are closer to the box. On the other hand, test P1M3T1 showed the largest variation in the calculated MN values.

It is apparent from **Figure 52** and **Figure 53** that the MN in the failure regions varies. The MN values range from a minimum of 0.105 to a maximum of 0.509 in Test series one. This is a large discrepancy in the MN values. The large variation in the obtained MN values does not facilitate the ease of determining the exact MN value to define the hydraulic incipient failure conditions of the riprap.

When a large value of the MN value is chosen to define the incipient failure condition of riprap, there is an advantage of specifying low-cost riprap median size. However, there is also a risk of specifying an undersized riprap median stone size. Moreover, if a very small MN is chosen, then a large stone size may be chosen, which can have cost implications on the overall riprap protection project. However, the advantage is that a safe riprap median stone size may be specified.

Considering the above advantages and disadvantages of choosing a MN value to define the incipient motion condition, the MN values of 0.12 and 0.17 were initially considered to be the safe region to define the MN for riprap incipient motion conditions. However, it was not clear whether to choose the 0.12 or the 0.17 since the seven critical MN tests had MN within the 0.12-0.17 MN envelope. To guide the decision, an exceedance probability statistical analysis on the critical tests with the MN values lying in the 0.12-0.17 envelop was executed.

In **Figure 53** the tests P1M1T2, P1M1T3 and P1M2T3 were the three critical tests with the minimum MN values between the 0.12 and the 0.17 MN envelope.

Therefore, an exceedance probability analysis was performed on the MN datasets of the three tests. The MN of the three critical tests P1M1T2, P1M1T3 and P1M2T3 were listed and sorted with the lowest MN value at the bottom and the highest MN for each test. Thereafter, the 5% percentile was calculated using the Microsoft Excel internal mathematical function. The resulting MN value was assumed to be the 5% of non-exceedance and 95% probability of exceedance value. **Table 16** below provides a summary of the results of the analysis.

Table 16: Summary of MN values with 95% probability of exceedance

P1M1T2 (MN)	P1M1T3 (MN)	P1M2T3 (MN)	
0.362	0.369	0.264	
0.359	0.360	0.263	
0.357	0.326	0.255	
0.352	0.310	0.254	
0.324	0.280	0.252	
0.303	0.251	0.246	
0.299	0.240	0.237	
0.251	0.235	0.237	
0.251	0.230	0.236	
0.250	0.225	0.233	
0.243	0.208	0.218	
0.240	0.202	0.217	
0.231	0.192	0.208	
0.229	0.191	0.190	
0.218	0.134	0.188	
0.217	0.123	0.179	
0.208	0.105	0.172	
0.200		0.161	
0.184		0.134	
0.124		0.125	
0.181	**0.119**	**0.134**	**5% Percentile**

From **Table 16**, it was observed that the critical MN was 0.119 obtained from test P1M1T3. Test P1M2T3 obtained a MN with a 95% probability of exceedance of 0.134 which lies between the 0.12-0.17 envelop. However, the 95% exceedance probability MN of test P1M1T2 was 0.181 which is greater than the 0.17 upper limit MN of the envelope. Therefore, the critical MN value obtained with a 95% probability of exceedance for Test series one was determined to be 0.119. The critical MN value of 0.119 was very close to the lower limit MN value of 0.12 that was determined by Rooseboom (1992).

5.2 Test Series Two MN Analysis

Similar tests to those of Test series one was conducted to perform Test series two riprap incipient failure tests. However, there were few differences in the Test series two tests performed compared to Test series one. One of the major differences was the 0.075 m median stone size tested in Test series two tests. Secondly, in testing Test series two there were more tests performed than in Test series one. About 15 tests were performed for Test series two and five tests in each designed steep bed slope were tested.

The MN in each test were calculated using the dimensionless MN criteria as defined by **Equation 57**. The relevant correction factors were applied to account for the steep bed and steep side bank slopes. However, only **Equation 58** was used to calculate the steep bed correction factor. The side slope correction factor was not applied in the calculation of the Test series two MN values. The reason for this was because the water depth inducing the incipient failure of riprap did not encroach the side slopes of the riprap. Therefore, it seemed logical to assume that the side slope correction factor did not have an influence on the final critical MN values.

Table 17 provides a summary of all the important input parameters that were required in order to calculate the MN values of Test series two physical laboratory tests.

Table 17: Hydraulic input parameters to determine MN values for Test series two tests

Input Parameter	Value	Unit
D_{50}	0.075	m
ρ_r	2700	kg/m^3
ρ_w	1000	kg/m^3
v_{ss}	0.8352	m/s
ϕ_r	40	°
$\alpha_{Angle\ (side\ slope)}$	21.77	°
$\alpha_{Slope\ (side\ slope)}$	0.4	
$\theta_{Angle\ (bed\ slope)}$	Varies	°
$\theta_{Slope\ (bed\ slope)}$	Varies	
g	9.81	m/s^2
S_o	Varies	
D_w	Varies	m
v	1.13E-06	m^2/s at 15 °C

Table 17 shows that only the median stone size and the settling velocities changed in the Test series two MN input parameters. The average local water depths and average bed slopes in the failure region varied for each test depending on the failure conditions. The average local water depths and average local slopes measured for Test series two tests are summarised in **Appendix D.**

The median stone size of 0.075 m (D_{50}) for Test series two tests were used for the riprap protection. The assumed rock density of 2700 kg/m^3 (ρ_r) was chosen based on the hornfels rock material type. The riprap rock settling velocity was based on the experimentally observed and tested results summarised in **Appendix B**. The settling velocity results from the laboratory settling velocity tests were based on the 0.075 m median stone size for Test series two tests. The rock angle of repose was 40° (ϕ_r).

The density of the water (ρ_w) was assumed to be 1000 kg/m^3 and the kinematic viscosity (ν) was assumed to be 1.13E-06 m^2/s at 15 °C. The reason for the two assumptions was explained in **section 5.2.**

By substituting the average local failure water depths and average local slopes summarised in **Appendix D** into **Equation 57** and the input variables in **Table 17,** the MN and Re_* for Test series two tests were successfully calculated. A summary of all the Test series two MN and Re_* can be obtained from **Appendix E**.

Test series two MN and Re_* results from **Appendix E** were plotted onto the Liu diagram as shown in **Figure 54**. Two characteristic curves which were developed by Rooseboom (1992) and Armitage (2002) were plotted onto **Figure 54** to form an envelope of critical incipient motion MN.

In **Figure 54** most of the measured MN results plot above the 0.17 upper limit. About ten MN points plot below the 0.17 upper limit. From the MN of 0.17, the measured MN reached up to a maximum of 0.433. The lowest MN was 0.091 read from **Figure 55**.

Figure 54 and **Figure 55** do not show the actual variations in the MN for each test in Test series two. However, all the points are plotted as a scatter. The scatter of the MN results in **Figure 54** and **Figure 55** points can be perceived as a representation of the different possibilities defining the MN values in the riprap incipient failure regions. Therefore, the box-whisker diagram in **Figure 56** was produced to display the variation in the MN values for each test in Test series two.

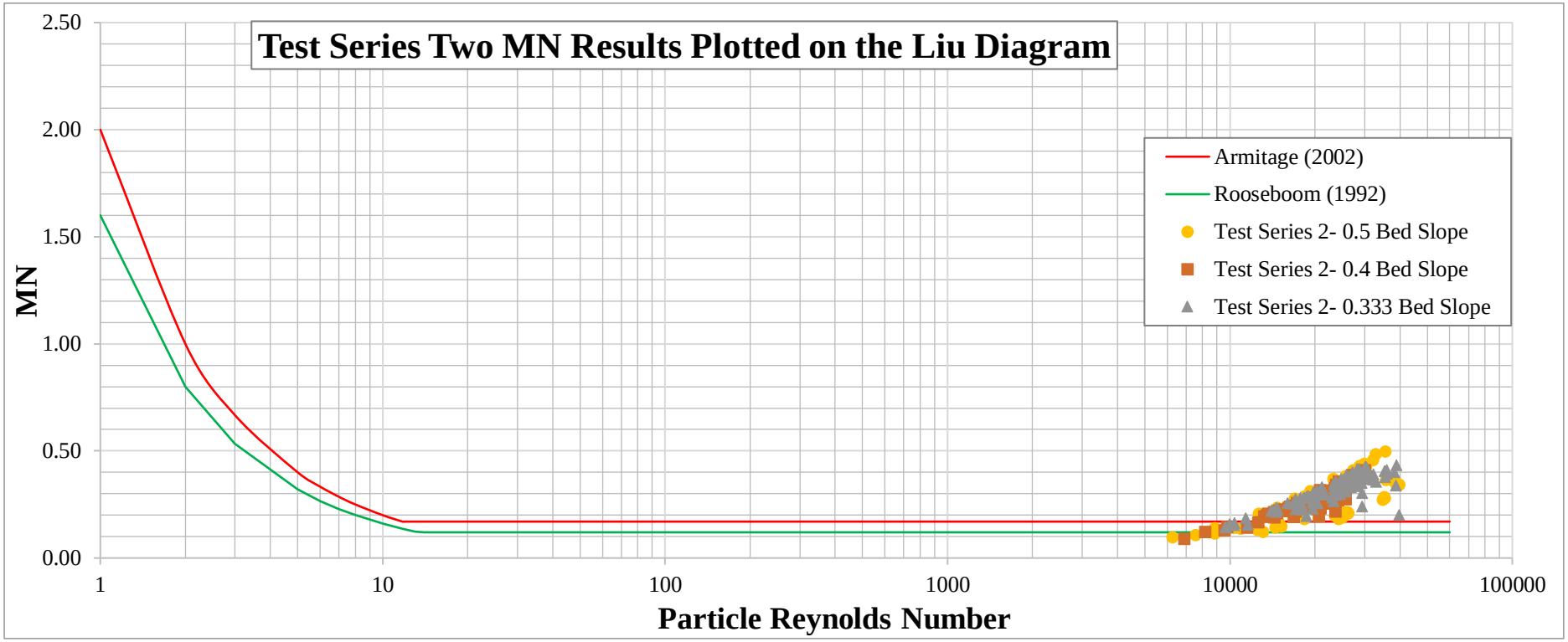

Figure 54: Test series two (incipient failure of D_{50}=0.075 m riprap dumped on 0.5, 0.4 and 0.333 steep bed slopes with 0.4 steep side bank slope) MN results plotted onto the Liu diagram.

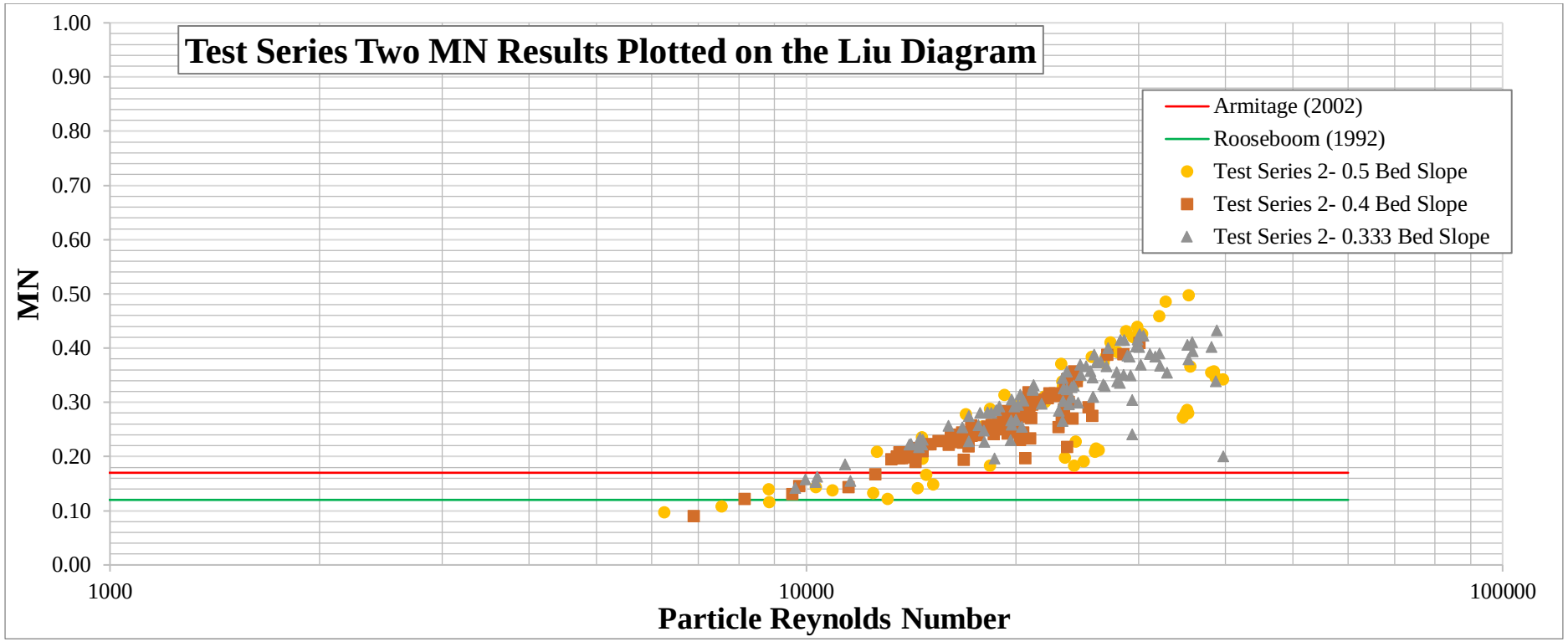

Figure 55: Zoomed in view of the MN (incipient failure of D_{50}=0.075 m riprap dumped on 0.5, 0.4 and 0.333 steep bed slopes with 0.4 steep side bank slope) results of the Test series two test results lying in the high particle Reynolds Region.

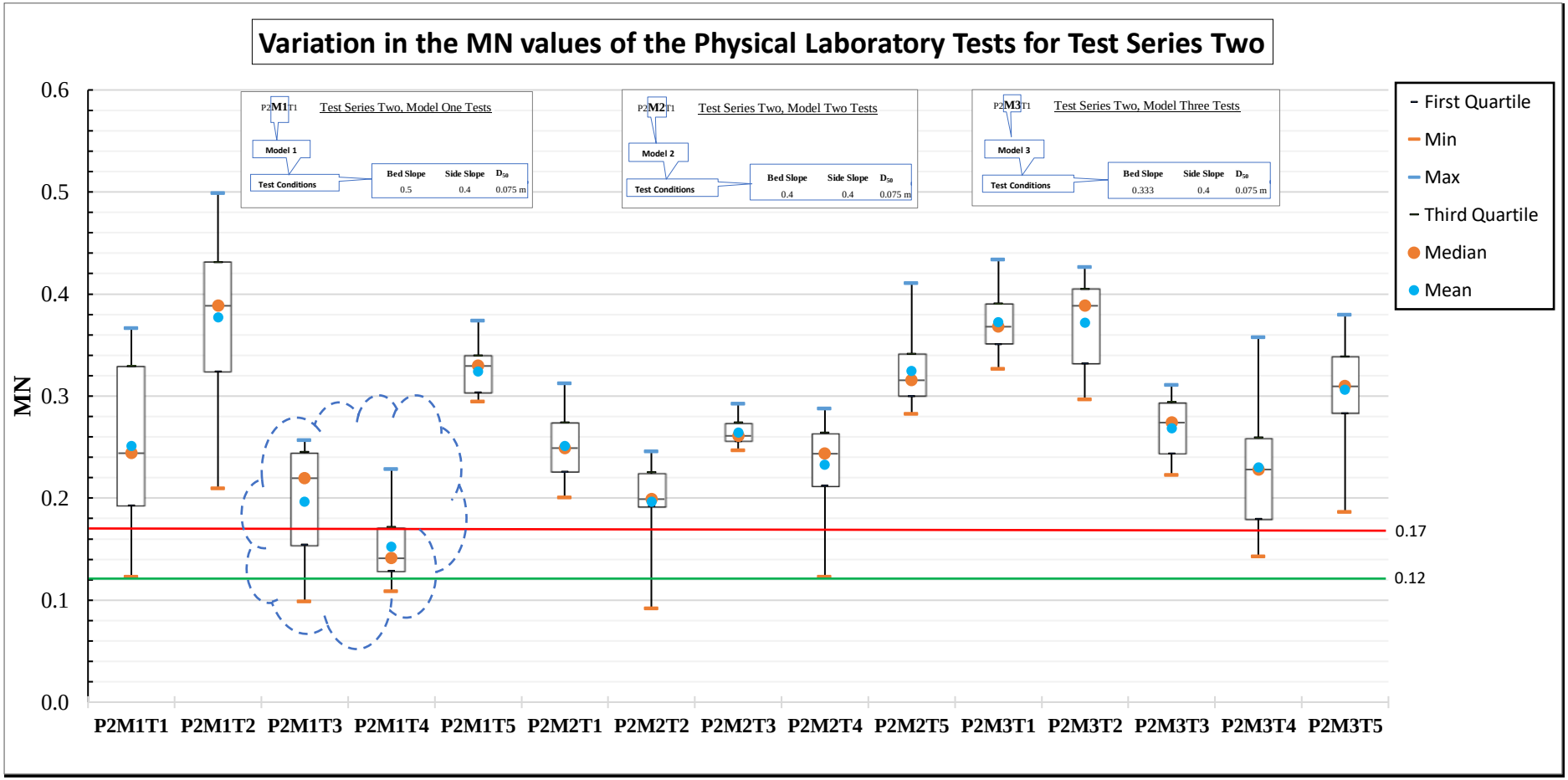

Figure 56: Box-Whisker diagram for the Test series two physical laboratory tests showing the variation in MN values per test.

Figure 56 shows the 15 successful test results of the MN analysis performed at the laboratory. The main data required to plot the box whiskers in **Figure 56** were the basic statistics shown in the legend of the graph in **Figure 55**, on the right-hand side. A summary of the basic statistics of the MN values used for plotting the box-whisker diagram of Test series two can be found in **Appendix F**.

Tests P2M1T3 and P2M1T4 were considered to produce unreliable MN box-whisker plots. This was because of the insufficient water depth and slope data measured in the failure region of the two tests. Only six and eight MN values could be obtained from the failure region of test P2M1T3 and P2M1T4, respectively. There were 20 possible measurements of water depth and slope for each test. Therefore, since the two tests only produced insufficient measurements for the analysis, no conclusions can be drawn based on the two tests. However, the tests have been included as a reference. The two tests are enclosed with a blue cloud in **Figure 56.**

Test P2M1T1 and P2M1T2 show the largest deviation of MN results. The standard deviation calculations summarised in **Appendix F** show that P2M1T2 has the largest standard deviation MN value from the mean MN value of 0.08. The P2M1T1 has the second largest standard deviation from the mean MN value of 0.079. The vertically wide boxes show a clear physical illustration of how the two tests MN results significantly vary compared to the rest of the tests in Test series two.

There were two MN test results that showed the smallest deviations from the mean value of the MN in Test Series two. The smallest value of the MN standard deviation of 0.013 was obtained from test P2M2T3. The second smallest value of the MN standard deviation was 0.021 obtained from test P2M1T5. The small deviations in the MN values are shown by the vertically squeezed nature of the boxes, illustrating the closeness of the MN values measured at the laboratory relative to the mean MN value.

Most of the box-whisker plots in **Figure 56** are positioned above the 0.17 MN upper limit value. The whole box plot including the minimum values on the box plots plotted above the 0.17 MN upper limit value except the two tests with a blue cloud.

Tests P2M1T1, P2M2T2, P2M2T4 and P2M3T4 are the only four reliable tests with the minimum MN values that are less than the 0.17 upper limit MN value. The four previously mentioned tests of Test series two were analysed by means of the probability of exceedance. The probability of exceedance analysis assisted in defining the critical MN value that has a 95% probability of exceedance with respect to the observations made at the laboratory.

Table 18 shows a summary of the sorted MN and the calculated 95% probability of exceedance MN values at the bottom of the table.

Table 18: Summary of MN with 95% probability of exceedance

P1M1T1 (MN)	P2M2T2 (MN)	P2M2T4 (MN)	P2M3T4 (MN)	
0.366	0.245	0.287	0.357	
0.358	0.237	0.276	0.332	
0.356	0.234	0.274	0.331	
0.347	0.229	0.270	0.266	
0.343	0.226	0.265	0.259	
0.286	0.223	0.258	0.258	
0.28	0.223	0.251	0.255	
0.28	0.206	0.251	0.241	
0.273	0.199	0.245	0.230	
0.215	0.199	0.242	0.228	
0.212	0.197	0.240	0.227	
0.209	0.197	0.227	0.217	
0.198	0.195	0.218	0.200	
0.191	0.194	0.210	0.196	
0.184	0.19	0.205	0.163	
0.149	0.168	0.197	0.158	
0.142	0.144	0.146	0.155	
0.122	0.131	0.122	0.153	
	0.091		0.142	
0.139	**0.127**	**0.142**	**0.152**	**5% Percentile**

The Microsoft Excel function was used to calculate the 5% percentile MN value for the tests, which also represented the 95% probability of exceedance value of the observed MN values. The four tests in **Table 18** all had 18 or more MN values measured for each test. Therefore, these were reliable tests to perform the probability of exceedance analysis.

All the 5% percentile MN values calculated above fell below Armitage's 0.17 upper limit MN value. Moreover, all the 5% percentile MN values of the four tests in **Table 18** fall above the 0.12 lower limit MN value. Therefore, all these values fall within the envelope of 0.12-0.17 MN values. The highest critical MN value with a 95% probability of exceedance was 0.152, obtained from test P2M3T4. The lowest critical MN value with a 95% probability of exceedance was 0.127. The lowest MN value of 0.127 was also very close to the lower limit of 0.12 that was obtained by Rooseboom (1992).

Test series one and Test series two tests were very similar in terms of the testing procedure followed and the behaviour of riprap failure. Therefore, similar results were expected for the critical MN value. However, Test series one tested a smaller 0.038 m median stone size while Test series two tested a larger stone size of 0.075 m, approximately two times the Test series one median stone size. So, the two critical MN value s of 0.119 and 0.127 obtained from the probability of exceedance analysis were satisfactory results. As anticipated, very similar results were obtained. The percentage difference between the two MN values for the critical incipient failure conditions for Test series one and Test series two was 6.5%.

5.3 Test Series Three MN Analysis

The main observation made in Test series one and Test series two tests was that the riprap failed in the steep bed area and did not fail on the side bank area. Therefore, in Test series one and two the side bank incipient motion conditions could not be studied. Consequently, for Test series three it was decided that the angular riprap dumped in the steep bed area must be glued with an adhesive. The glueing of the riprap over the bed area allowed the testing of the ten tests for Test series three. In Test series three, five tests were performed over the steep bed slopes of 0.5 and the remaining five tests were performed on 0.333 steep slopes.

To complete the MN value calculations based on the observed water depths and slopes for the ten tests in Test series three, the hydraulic input parameters in **Table 19** were applied into **Equation 57**. The hydraulic input parameters in **Table 19** are the same as those used in Test series two of the tests. However, the only difference was the location of the vicinity of the measured average local water depths and slopes in the incipient failure regions of the angular riprap. The incipient failure region was in the steep bed area for Test series one and two, while the local failure regions on Test series three were at or near the toe of the side bank. The observed average local hydraulic water depths and average local bed slopes at incipient failure regions for Test series three were summarised in **Appendix D.**

Table 19: Hydraulic input parameters to determine MN for Test series two tests

Input Parameter	Value	Unit
D_{50}	0.075	m
ρ_r	2700	kg/m^3
ρ_w	1000	kg/m^3
v_{ss}	0.8352	m/s
ϕ_r	40	°
$\alpha_{Angle\ (side\ slope)}$	21.77	°
$\alpha_{Slope\ (side\ slope)}$	0.4	
$\theta_{Angle\ (bed\ slope)}$	Varies	°
$\theta_{Slope\ (bed\ slope)}$	Varies	
g	9.81	m/s^2
S_o	Varies	
D_w	Varies	m
ν	1.13E-06	m^2/s at 15 °C

The MN values were calculated by applying the water and riprap hydraulic input properties in **Table 19**, plus the average local water depths and average local slopes from **Appendix D** into **Equation 57**.

Each of the calculated MN values for Test series three were summarised in **Appendix E**. The calculated MN values and Re_* from **Appendix E** were then plotted onto the Liu diagram shown in **Figure 57**. Only two data points were less than the 0.17 upper limit MN value. Most of the points plotted in abundance from an approximate MN value of 0.22 and upwards. Higher MN values for Test series three were expected, due to the high flow rates and water depths that were instigated incipient failure of riprap dumped on the 0.4 steep side bank slope. Therefore, the general overall high MN values displayed in the Liu diagram was anticipated.

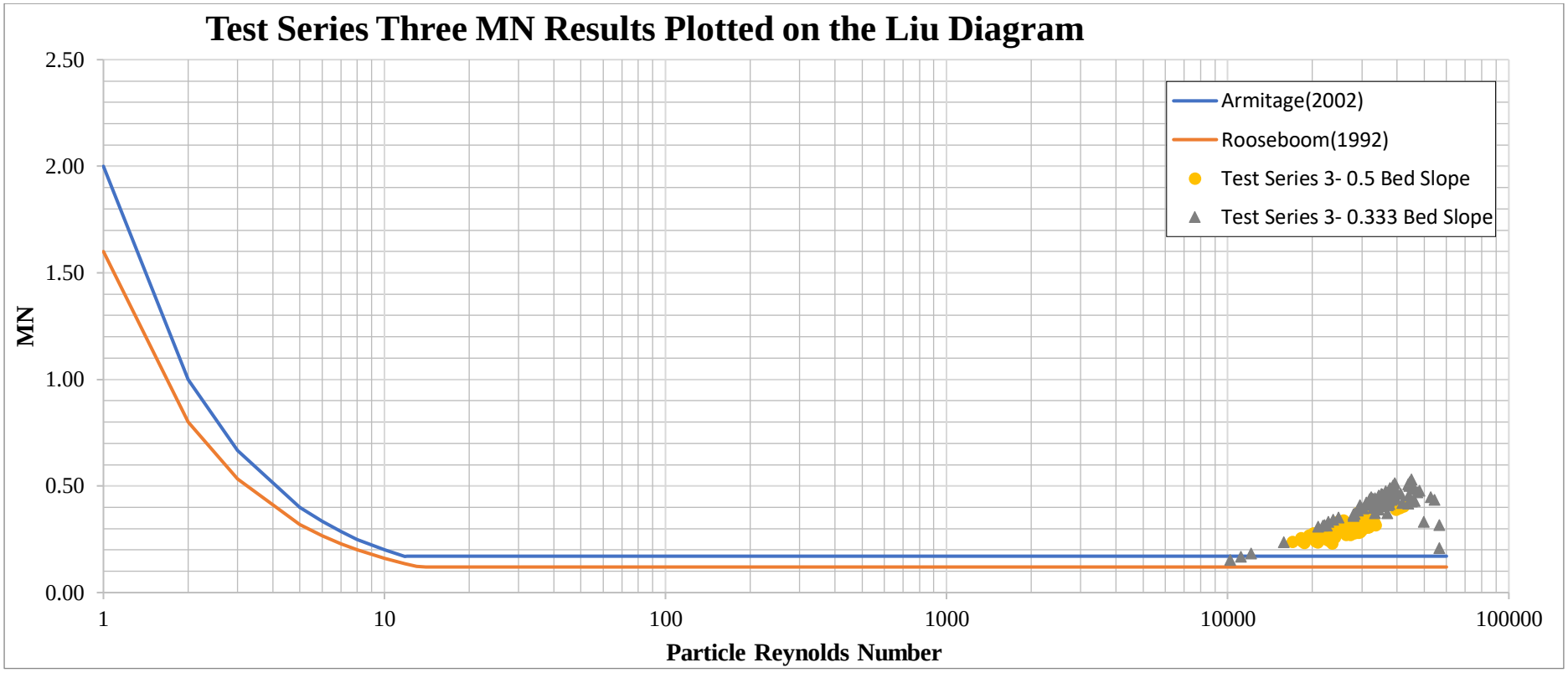

Figure 57: Test series three MN results plotted onto the Liu diagram.

Figure 58 displays a closer look at the Liu diagram for Test series three. A distinction between the tests performed on the 0.333 steep bed slope and the 0.5 steep bed slope was shown with the two differently coloured dots. The physical hydraulic model with the 0.5 steep bed slope produced MN values that were generally lower than the MN values of the models tested on the 0.333 steep bed slopes.

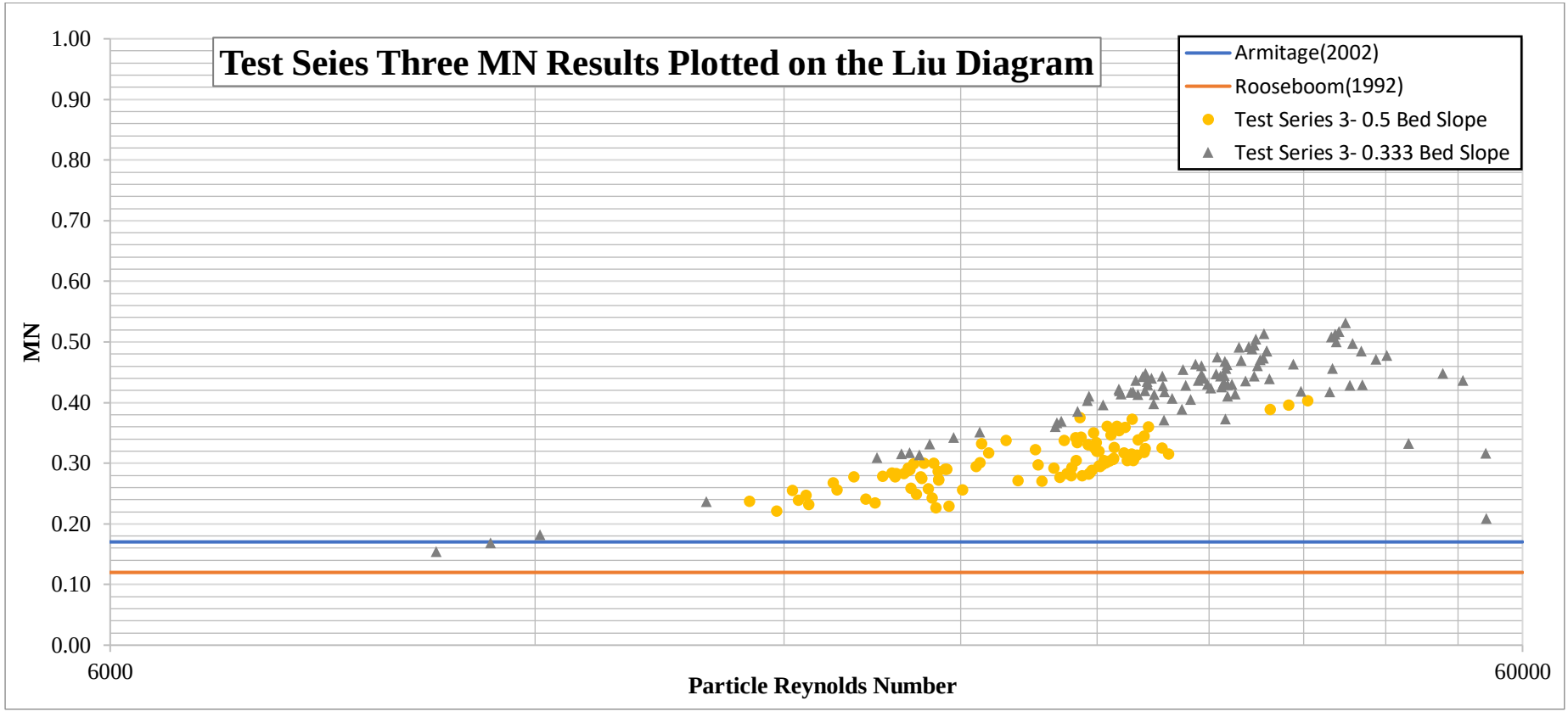

Figure 58: A Zoomed in view of the MN (incipient failure of D_{50}=0.075 m riprap dumped on 0.5 and 0.333 steep bed slopes with 0.4 steep side bank slope) results of Test series three test results lying in the high particle Reynolds Region.

The slope of the bed seems to have a significant contribution to the water depth flowing over the riprap. The Test series three tests that were performed on the 0.333 hydraulic model displayed higher water depth measurements than the models tested on the 0.5 steep slopes. However, from **section 4.1**, the high incipient failure flow rates were observed on the 0.5 steep bed slope hydraulic model. This shows that the water depth was the main contributor to high MN values plotted on the Liu diagram. Initially, the author presumed that the higher the flow rate, the higher the water depth that would be measured. From the laboratory, it seems as if the combination of the average steep bed slope and the incipient failure flow rate are important in determining the critical MN value at incipient failure conditions. It was observed at the laboratory that in steep bed slopes (e.g. 0.5 steep bed slope) a higher water depth can be produced by a higher flow rate to instigate incipient failure on the side bank slope. The 0.333 steep bed slope model configuration in Test series three failed at lower flow rates but higher water depths were observed.

The MN values observed from the 0.5 steep bed slope varied from 0.222 to 0.403 in the scatter plot shown in **Figure 58**. The variation in the MN was even greater on the hydraulic model with the 0.333 steep bed slope, whereby the MN varied from 0.154 to 0.532. However, most of the MN values obtained from the hydraulic model with the 0.333 steep bed slope, plotted above the hydraulic model with the 0.5 steep bed slope MN results.

A better representation of the variations of the MN results of each test in Test series three is represented in **Figure 59.** The box-whisker plots show that the MN values computed on the 0.5 steep bed slope showed less variation compared to the MN values computed for the 0.333 steep bed slopes. Furthermore, the calculated standard deviations of the MN values shown in **Appendix F** for all the tests prove that the model three tests exhibit larger variation compared to model one MN values. The 0.333 steep bed slope tests comprised of minimum MN values that were extremely far from the boxes. The minimum MN values could be viewed as potential outliers based on the length of the whiskers.

However, in order to avoid bias and assume that the minimum MN values on the 0.333 steep bed slope are outliers, all the MN values in the 0.333 and 0.5 steep bed slope hydraulic model setups were analysed with the exceedance probability analysis approach. Unlike Test series one and Test series two, the MN values for all the tests in Test series three were analysed for the 95% probability of exceedance, because it was not clear which tests were critical.

As a result, it was important to analyse the 95% probabilities of exceedance of the data to see where the 5% percentile MN plotted for all the tests and make a logical decision based on the results of the overall exceedance probability analysis.

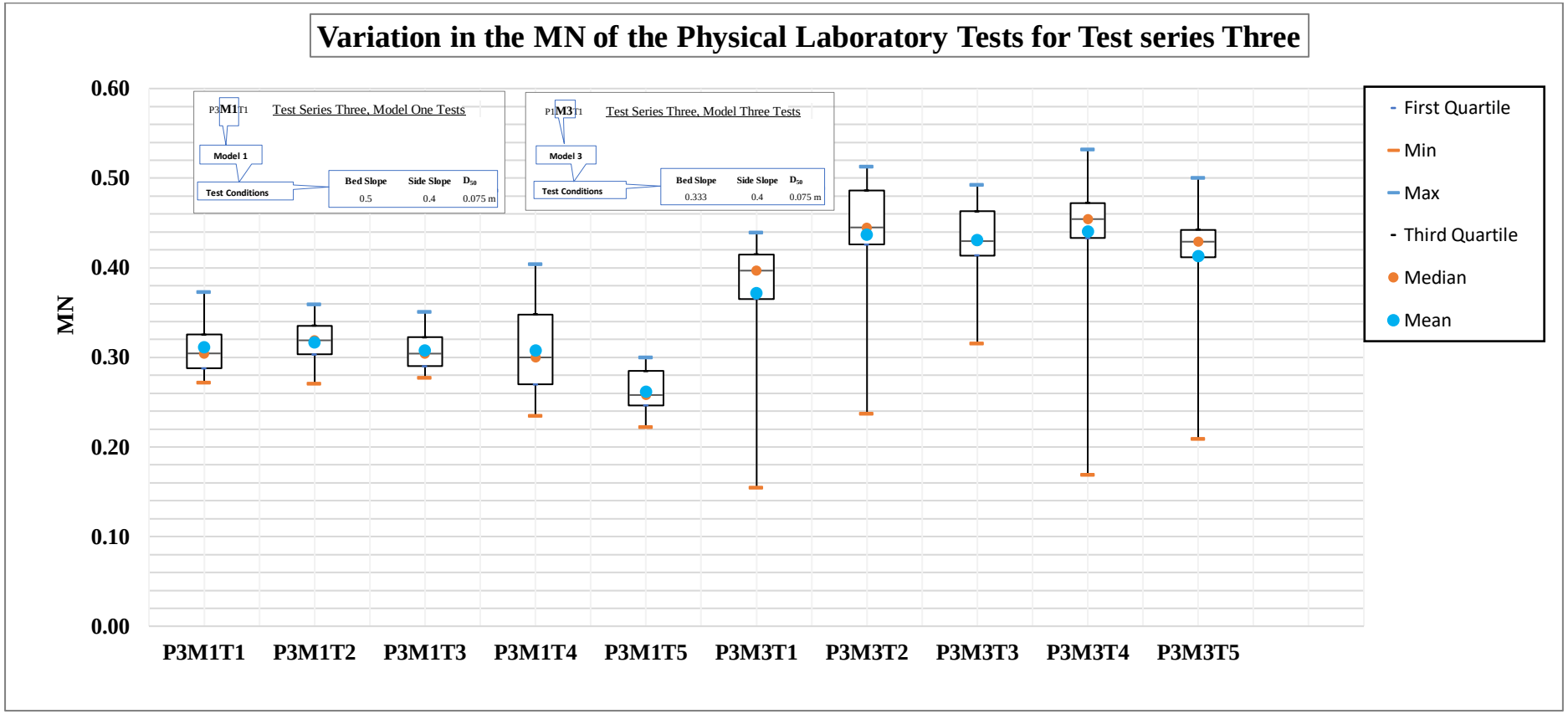

Figure 59: Box-Whisker diagram for the Test series three physical laboratory tests showing the variation in MN values per test.

Table 20 shows the summary of the MN for all the Test series three tests as well as the 95% probability of exceedance value of each test at the bottom of the table. The 95% probability of exceedance MN value was calculated as the 5% percentile of the observed MN results for each test.

Table 20: Summary of MN with 95% Probability of exceedance

P3M1T1 (MN)	P3M1T2 (MN)	P3M1T3 (MN)	P3M1T4 (MN)	P3M1T5 (MN)	P3M3T1 (MN)	P3M3T2 (MN)	P3M3T3 (MN)	P3M3T4 (MN)	P3M3T5 (MN)	
0.372	0.359	0.351	0.299	0.300	0.439	0.512	0.492	0.532	0.500	
0.361	0.352	0.347	0.403	0.295	0.430	0.508	0.488	0.517	0.473	
0.360	0.343	0.345	0.396	0.292	0.429	0.504	0.485	0.514	0.471	
0.354	0.339	0.334	0.389	0.290	0.419	0.494	0.485	0.497	0.456	
0.327	0.338	0.331	0.375	0.286	0.418	0.491	0.463	0.478	0.445	
0.325	0.335	0.320	0.361	0.284	0.414	0.485	0.463	0.470	0.440	
0.317	0.325	0.315	0.344	0.277	0.413	0.475	0.454	0.469	0.436	
0.317	0.324	0.313	0.338	0.272	0.410	0.461	0.447	0.468	0.436	
0.308	0.323	0.307	0.332	0.268	0.405	0.457	0.444	0.462	0.435	
0.305	0.320	0.305	0.302	0.259	0.398	0.446	0.430	0.461	0.429	
0.304	0.318	0.304	0.301	0.257	0.396	0.444	0.429	0.448	0.428	
0.300	0.315	0.295	0.283	0.256	0.389	0.443	0.427	0.448	0.426	
0.298	0.310	0.293	0.279	0.255	0.385	0.436	0.424	0.443	0.417	
0.297	0.307	0.292	0.278	0.249	0.371	0.433	0.414	0.440	0.417	
0.289	0.304	0.291	0.274	0.247	0.367	0.428	0.413	0.437	0.407	
0.284	0.301	0.288	0.258	0.243	0.360	0.419	0.404	0.422	0.373	
0.283	0.296	0.288	0.241	0.232	0.352	0.418	0.369	0.419	0.333	
0.280	0.282	0.283	0.239	0.229	0.314	0.331	0.342	0.410	0.316	
0.279	0.275	0.278	0.237	0.227	0.182	0.317	0.315	0.310	0.208	
0.271	0.270	0.277	0.235	0.222	0.154	0.237		0.169		
0.279	**0.275**	**0.278**	**0.237**	**0.227**	**0.181**	**0.313**	**0.339**	**0.303**	**0.305**	**5% Percentile**

Figure 59 shows that the minimum MN values of model one plotted very close to the boxes due to fewer deviations of the observed MN values to the mean value. As a result, the calculated model one 5% percentile MN in **Table 20** are MN values closer to the boxes. The lowest 5% percentile MN value of model one was 0.227 from test P3M1T5.

However, in **Figure 59** the minimum MN values of model three tests plotted significantly below the boxes. The calculated 5% percentile MN values in **Table 20** show that the minimum MN values of model three tests could be considered outliers. To logically justify the consideration of the MN as outliers, it was noted that the four tests P3M3T2, P3M3T3, P3M3T4 and P3M3T5 all had 5% percentile MN values that plotted closer to the boxes. Moreover, all the 5% percentile MN values of the four tests (in model three) were greater than 0.3. Therefore, the minimum MN values of the four tests may be considered outliers in this regard.

However, only one test in the model three tests had a minimum 5% percentile MN value of 0.181. The 0.181 MN value was determined as the 5% percentile MN. It can also be noted that the 0.181 MN value was the smallest MN value in Test series three tests.

The critical MN value for model one tests were determined to be 0.227 and the critical MN value for model three tests was found to be 0.181. There was a discrepancy because the 0.227 MN was determined from the steeper bed slope of 0.5 and it was therefore expected that the critical MN value determined from the model three must be larger than the 0.227 value. The reason for this expectation is that at the laboratory, it was observed that the riprap in the milder 0.333 steep bed slopes incipiently failed at larger water depths, thus large MN defining the critical incipient motions expected. **Table 20** also shows that only one test in model three produced a MN of 0.181 and the rest of the MN observed plotted higher up (5% percentile MN values greater than 0.3).

Based on previous research results defining the critical MN value for specifically bed slopes, a critical MN value between 0.12 (Rooseboom, 1992) to 0.17 (Armitage, 2002) or 0.18 (Langmaak and Basson, 2015) was expected to define the critical incipient motion condition of riprap in steep bed slopes. Moreover, in **section 5.1** and **5.2** of this thesis, it was found that the critical MN value defining the point of incipience of riprap in steep bed slopes (0.333-0.5) was about 0.119 with a 95% probability of exceedance.

Consequently, the investigator expected the critical MN value that defined the incipient failure conditions in Test series three to be larger than the MN values range from 0.12 to 0.18. The expectation was due to the fact that higher water depths (thus larger MN values) were observed to be the main instigator of riprap failure in the steep riprap side banks of Test series three.

Therefore, the MN of 0.181 obtained from model three with 95% probability of exceedance was very close to the 0.12-0.17 MN value range, but for the side bank riprap failure, a higher critical MN value was expected. Therefore, based on the findings of Rooseboom (1992), Armitage (2002) and Langmaak and Basson (2015) and the laboratory observations for this thesis, it made more sense to define the critical MN for Test series three tests as the 0.227 MN value obtained from the model one tests rather than the 0.181. The 0.181 MN can be assumed to be an outlier based on the above justification.

5.4 Chapter Summary

The MN for Test series one, Test series two and Test series three tests were calculated by applying MN **Equation 57.** The water depths, bed slopes in **Appendix D**, plus the riprap and water properties in **Tables 15, 17** and **19** were used as input values for **Equation 57** to compute the MN for all the tests.

Test series one, Test series two and Test series three tests were analysed individually. However, the analysis procedure was similar with minor differences regarding the median stone size and the region of failure as well as the bed state of movable/non-movable conditions. Test series one tested for the failure of 0.038 m median stone size and the incipient failure occurred only on the bed area. Test series two tested for the 0.075 m median stone size and the failure of riprap occurred in the steep bed area only. However, Test series three tested for the 0.075 m median stone size and the failure region was on the side bank.

In Test series one, it was found that the riprap critical hydraulic incipient failure condition was defined by a MN value of 0.119. In Test series two it was found that the riprap critical hydraulic incipient failure condition was defined by a MN of 0.127. As anticipated, the two critical hydraulic incipient failure MN were similar and close to Rooseboom (1992) 0.12 MN value criteria. However, in Test series three it was found that the critical hydraulic incipient failure condition for angular riprap dumped on steep side slopes of 0.4 was defined by a MN of 0.227.

Chapter 6 : Evaluation of HEC-RAS Ability to Predict Riprap Incipient Failure Conditions.

From the analysis in **Chapter 5,** it was found that there was a unique MN defining the incipient failure conditions of angular riprap dumped on steep beds as well as for angular riprap dumped on steep side bank slopes. The two critical MN were found to be 0.119 and 0.227, respectively. The two critical MN were determined with an exceedance probability of 95% with respect to the tests performed at the hydraulic laboratory.

HEC-RAS is one of the widely used hydraulic engineering design software. The software is generally used to perform hydraulic flow analysis on rivers. Based on the simulation results and the type of project, flood lines may be determined, or river protection structures may be designed using the output results from HEC-RAS.

Some of the reasons why HEC-RAS is generally favourable among river hydraulic design engineers are:

- HEC-RAS has quick computation times.
- It is relatively easy to learn to use the HEC-RAS software
- The software is based on fundamental hydraulic principles.
- The HEC-RAS is available to download for free.
- It produces reliable surface water elevations for one directional flow problems.

With respect to abovementioned reasons, some engineers may opt to use the HEC-RAS software to design stable riprap protection in steep slopes but overlooking the fact that HEC-RAS may not be able to appropriately simulate water depths its limitations in application.

Thus, it was critical that the thesis evaluates the capability of the HEC-RAS to determine the critical MN that defines the critical incipient failure conditions of angular riprap placed in steep bed slopes and steep side bank slopes.

The following limitations associated with the simulation of hydraulic flow conditions using a HEC-RAS further necessitate the evaluation of the ability of HEC-RAS to accurately determine the critical MN incipient failure conditions:

- HEC-RAS does not account for the effects of bed porosity, turbulence and wave action produced by riprap rocks.
- The bed is assumed to be fixed (immovable bed) in HEC-RAS.
- HEC-RAS models the top of the riprap as the bed level.
- Moreover, in a 1-D surface water profile simulation, only the flow in one direction is simulated. Thus, the flow behaviour and direction in a 1-D HEC-RAS modelling simulation does not simulate 3-D flow effects.

As a result of the above, the water depth may not be accurately determined when simulating open channel flows with porous bed problems.

When calculating the MN in **Chapter 5**, it was evident that the water depth was the main sensitive input parameter in **Equation 57**. Thus, the ability of the HEC-RAS software to simulate water depths that are representative of the physically determined water depths will determine its ability to simulate the riprap incipient failure conditions.

In this chapter, 1-D HEC-RAS numerical hydraulic models were prepared to simulate the hydraulic condition of the physical laboratory models that were tested.

This chapter describes the basic theory underpinning the 1-D HEC-RAS hydraulic numerical modelling software. Not all the theory was covered, but the main principles are highlighted. The main stages that were followed during the preparation of the hydraulic HEC-RAS models are described in this chapter. The stages comprise the modelling of the geometrical cross-sections of the laboratory model, the input boundary conditions, the recorded flow data for the models and the roughness coefficient determination. MN determined with the HEC-RAS model were calculated and summarised. A comparison of the HEC-RAS MN and physical model MN results was performed. Based on the comparison, correction factors were recommended for application onto HEC-RAS produced incipient motion MN analysis.

6.1 Summary of the Fundamental Theory on HEC-RAS

Surface water profiles in HEC-RAS can be calculated for steady and unsteady flows. For this thesis the assumed fluid flow behaviour was steady state gradual flow conditions. The HEC-RAS modelling software calculates the surface water profiles through an iterative procedure by solving the energy equation. HEC-RAS requires two channel cross-sections per iteration to apply the energy equation. The energy equation used by HEC-RAS to calculate the water surface profiles is as follows (Brummer, 2016):

$$Z_2 + Y_2 + \frac{\alpha_2 V_2^2}{2g} = Z_1 + Y_1 + \frac{\alpha_1 V_1^2}{2g} + h_e \qquad \textbf{Eq. 60}$$

Where Z_1 and Z_2 are the invert elevations of the

Y_1 and Y_2 are the water depths at the two cross-sections

V_1 and V_2 are the average velocities at the two cross-sections

α_1 and α_2 are the velocity weighting coefficients

g is the gravitational acceleration

h_e is the energy head loss

The terms in **Equation 60** above can be represented as shown in **Figure 59** below:

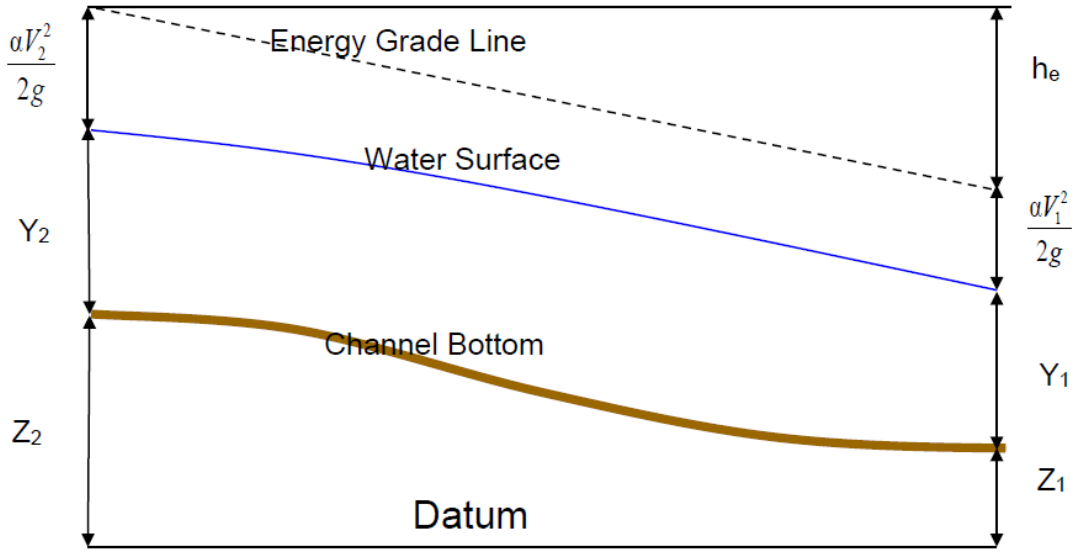

Figure 60: Diagram showing the terms in Equation 56 (Brunner, 2016)

The energy **Equation 60** represents the main open channel flow hydraulic conservation energy principle underpinning the steady state flow calculations computed with the HEC-RAS software in order to determine surface water profiles. For the detailed descriptions and actual calculations procedure for the surface water profiles, the reader is referred to chapter 2 of the HEC-RAS River Analysis System Hydraulics Reference Manual by Brunner (2016), published by the US Army Corps of Engineers.

6.2 Preparation of the HEC-RAS One-Dimensional Numerical Model

The data that was required to run a steady flow state HEC-RAS one-dimensional numerical modelling simulation (hereafter referred to as HEC-RAS) were mainly geometric and flow-related data. The most critical data required was the cross-sectional data, which provides the software with geometric information. Then, the steady state flow of data such as the flow rate and the boundary conditions were required. The main data requirements are described in the upcoming sections.

6.2.1HEC-RAS Model Geometric Cross-Sectional Data

The first step during the HEC-RAS hydraulic modelling analysis preparation was to define the reach direction and model the shape of the flume at the lab onto the HEC-RAS. The shape of the physical model was defined with cross-sectional data. To define each cross-section, the designed drawings in **APPENDIX A** were used as a reference to create cross-sectional data on HEC-RAS. **Figure 61** shows a finished model on HEC-RAS that was modelled from cross-sectional data.

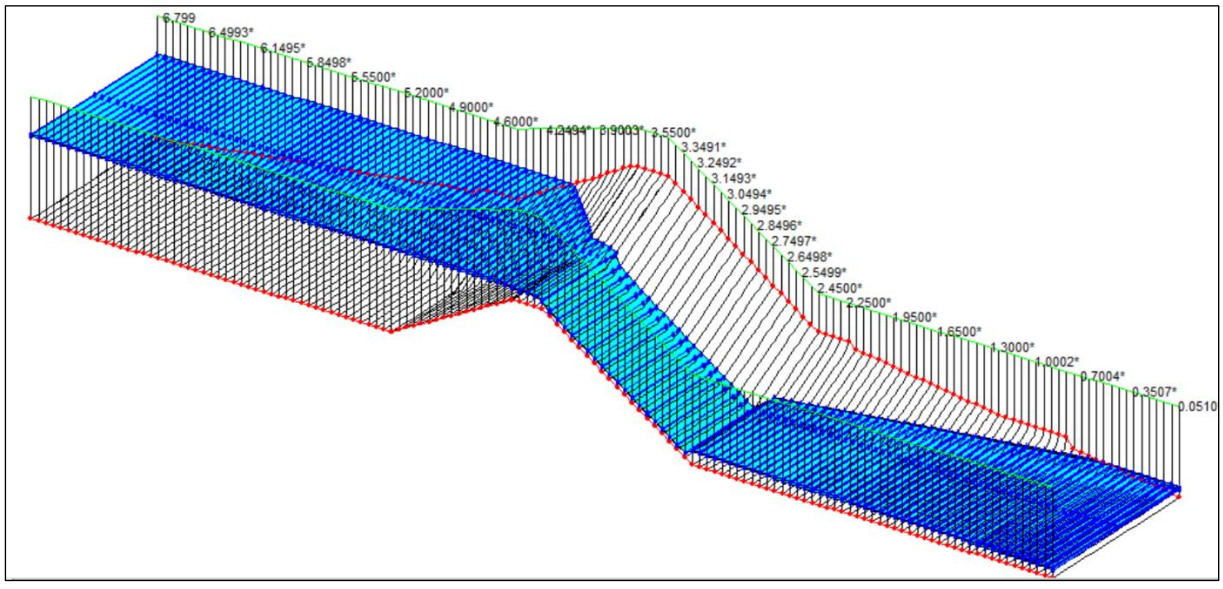

Figure 61: A perspective view of a typical model built in HEC-RAS

The numbers shown in **Figure 61** identify the station values of the cross-sections. The way in which the HEC-RAS was developed was such that station values increase from downstream to

upstream. So, the station values here are the opposite of what has been defined and designed (as in **Appendix A**) due to the limitation by HEC-RAS system of defining the station values in the opposite direction. The main cross-sections defined were at the most upstream and downstream stations, and whenever there was a change in the slope of the bed and banks. The rest of the cross-section were interpolated by 0.05 m from each other. A short interpolation distance between the cross-sections allowed an improved solution during the simulation of the surface water elevations. The HEC-RAS model was checked and refined until the accurate shape like the one at the laboratory or the designed models in **Appendix A** were achieved. After sufficient corrections and adjustments, the correct shape in **Figure 61** was achieved.

Only three unique HEC-RAS models were built. The HEC-RAS models that were prepared on HEC-RAS simulated the three physical models that were built at the laboratory. The HEC-RAS models were all geometrically similar, except the adjusted steep bed slopes whereby model one had a slope of 0.5, model two had a slope of 0.4 and the last model had a slope of 0.333. For testing Test series one and testing Test series two, the only difference between the HEC-RAS models in each testing Test series was the bed elevations. The difference in the bed elevations was due to the two different sized D_{50} median stone sizes used for testing Test series one and testing Test series two. Since testing Test series three used the same D_{50} median stone size, the same geometric HEC-RAS models were used for testing Test series three as those used in the testing Test series two. The bed elevations were at the same level. Nonetheless, in testing Test series three, only the 0.5 and 0.333 steep bed slope geometric HEC-RAS models were used.

In conclusion, most of the time was spent creating the first three geometric models in testing Test series one, but the rest of the models for testing Test series two and testing Test series three were achieved by modifying the first three geometric HEC-RAS models.

6.2.2 Reach Boundary Conditions

HEC-RAS provides the user with four main input reach boundary conditions to choose from when modelling. Depending on the type of analysis and available data, the user can choose between using the following reach boundary conditions:

- a rating curve;
- or the normal depth;
- or the critical depth

- or the known surface water elevations.

For this thesis, the author used the known upstream and downstream water surface elevations boundary conditions. The data of the known upstream and downstream water elevations were readily available because the elevations were measured during the laboratory tests. A summary of the upstream and downstream surface water elevations was tabulated in **Table 12** to **Table 14**. The known upstream and downstream surface water elevations were used as input boundary values in the HEC-RAS models for each test.

6.2.3 Channel Discharge Data at Incipient Failure

The flow rate was one of the most important parameters during the HEC-RAS simulation modelling. The main reason for its significance was that the water elevations calculated by HEC-RAS were significantly dependent on the input flow rates in the channel. Therefore, for the model to produce accurate and reliable water surface elevation calculations the flow rate input parameter needed to be a reliable input. For this thesis, the flow rates were accurately measured with the electromagnetic flow meters within +/- 0.00005 m^3/s error. All the incipient failure flow rates were recorded and summarised in **Table 9** to **Table 11** in **Chapter 4.**

6.2.4 Roughness Coefficient

The other main input parameter in the HEC-RAS geometric models were the roughness coefficient to be used on the models. There were two options that the HEC-RAS model allowed the user to choose from. The user could either choose to use the Manning n roughness coefficient or the k_s roughness coefficient.

The Manning n roughness coefficient can be determined from design manuals or literature. Using literature or design manuals as a reference for choosing Manning n roughness coefficient requires that the designer chooses a value of the Manning n for specific bed material types. The main reasoning behind the procedure is that the materials of the same type and physical roughness should comprise the same roughness, thus the same Manning n roughness coefficient. Then a calibration may be done to ensure that more accurate results are computed with the HEC-RAS numerical model.

Alternatively, the roughness element height k_s could be chosen to define the roughness of the bed. The roughness coefficient k_s is generally unique for each rough bed and is more

representative of the roughness conditions of each unique bed condition. K_s can be understood as the size of the eddies that form due to the roughness of the bed (Langmaak, 2013). It was impossible to determine one unified mathematical definition for the k_s value. Froehlich (2012) also identified the problem in the definition of the k_s value, then defined k_s in the following manner.

$$k_s = \alpha_i D_i \qquad \textbf{Eq. 61}$$

Whereby D_i is the diameter of the particle that is larger than the percentage i by mass (it could be D_{50} or D_{90}). The α_i is the constant associated with the D_i Froehlich (2012). Froelich agrees that there are different constants and D_i defined in different literature in which Bray (1982), Maynord (1991)) summarise some of the analyses which assess the value of k_s. Froelich (2012) noted that the main values that are generally used for the D_i to define k_s are D_{50}, D_{65}, D_{84} and D_{90}.

In a similar study by Langmaak (2015) the value of the constant α_i was determined for two gradings and the value of 0.81 was obtained from a calibration. The D_{90} was used, as a result, **Equation 61** was applicable in the study of large riprap in rough turbulent flow conditions:

$$k_s = 0.81\, D_{90} \qquad \textbf{Eq. 62}$$

Alternatively, the well-known Chezy (1769) equation could be used to calculate the roughness height, k_s. The Chezy equation was defined as follows (Huthoff and Augustijn, 2004)):

$$C = 18 \log\left(\frac{12R}{K_s}\right) \qquad \textbf{Eq. 63}$$

Whereby,

$$C = \frac{V}{\sqrt{RS_o}} \qquad \textbf{Eq. 64}$$

R= Hydraulic Radius

C= Chezy roughness coefficient

V= channel average flow velocity

S_o= Bed Slope

The Chezy equation was chosen as a reliable mathematical expression to use to determine the relevant k_s value for this study. However, a reliable laboratory test was needed as a reference for the calibration of the HEC-RAS model.

The most reliable test was considered as the test that showed the minimum MN standard deviation to the mean. The test with the minimum standard deviation of MN was determined from **Appendix F**. Hence, test P2M2T3 was used to calibrate the HEC-RAS model in order to determine the relevant k_s value. Test P2M2T3 had a standard deviation of 0.013 for the MN, relative to the mean.

To determine the k_s value to be used, **Table 21** was used for the calibration. The flow conditions and boundary conditions for the test P2M2T3 were modelled, as well as the geometry with the 0.4 steep bed slope. An initial guess of the k_s roughness value was applied on the steep downslope of the main testing area. The initial guess was chosen to be k_s = 0.5*0.135= 0.0675, this was based on **Equation 62** and the initial assumption made was that, $\alpha_{90} = 0.5$ and $D_{90} = 0.135$ m.

Thereafter, the HEC-RAS simulation was run and the wetted perimeter, flow area, average velocity and Froude numbers were simulated by the HEC-RAS model based on the initially assumed k_s value. For each cross-section in the downslope testing area, the hydraulic radius was calculated as the ratio of the flow area to the wetted perimeter. Then the Chezy coefficient was calculated based on the simulated results using the initially guessed k_s value. Then on the second last column in **Table 21**, the Chezy coefficient was calculated using solver (solver computed the k_s values that will produce the C value calculated based on the initially assumed k_s). Then the k_s value on the last column changed to a different value than the initially assumed. For the next iteration, the same method was followed and the k_s value converged down until the k_s values on the last column corresponded with the k_s values on the HEC-RAS model. The final calibrated results are summarised in **Table 21.**

Table 21: Final Chezy equation k_s determination value.

Cross-section no.	Wetted perimeter (m)	Flow area (m^2)	Hydraulic radius	Velocity (m/s)	Froude number	C (calculated from velocity in channel)	C (based on k_s)	k_s
1	0.74	0.02	0.0270	1.86	3.13	17.889	17.889	0.0329
2	0.74	0.02	0.0270	1.9	3.23	18.274	18.274	0.0313
3	0.73	0.02	0.0274	1.93	3.31	18.436	18.436	0.0311
4	0.73	0.02	0.0274	1.96	3.39	18.723	18.723	0.0300
5	0.73	0.02	0.0274	1.99	3.47	19.009	19.009	0.0289
6	0.73	0.02	0.0274	2.02	3.54	19.296	19.296	0.0279
7	0.73	0.02	0.0274	2.05	3.61	19.583	19.583	0.0269
8	0.73	0.02	0.0274	2.08	3.68	19.869	19.869	0.0259
9	0.73	0.02	0.0274	2.1	3.74	20.060	20.060	0.0253
10	0.72	0.02	0.0278	2.12	3.8	20.112	20.112	0.0254
11	0.72	0.02	0.0278	2.14	3.85	20.302	20.302	0.0248
12	0.72	0.02	0.0278	2.17	3.93	20.586	20.586	0.0239
13	0.72	0.02	0.0278	2.18	3.96	20.681	20.681	0.0237

The final calibrated k_s values in **Table 21,** on the last column, were not all equal. The k_s calculation was based on the cross-section position. The cross-section at the top (closer to the crest of the hydraulic model) had higher k_s values due to lower velocities at the top. The high k_s values were located at the bottom cross-sections where the velocities were high. Therefore, the k_s value at the bottom was chosen as the critical k_s and chosen as the relevant k_s value to be used for the rest of the HEC-RAS simulations. Since it was assumed that the grading and roughness of the riprap were the same for all the tests of the same median stone diameter and grading. Consequently, it was assumed that the following relationship holds $\alpha_{50} = \frac{k_S}{D_{50}} = \frac{0.0237}{0.075} = 0.316$.

So, the same k_s values were used for Test series two and Test series three HEC-RAS model tests since the D_{50} median stone size was the same. The k_s values used to simulate the Test series two and Test series three tests were 0.0237 in the downslope testing area. However, for the Test series one HEC-RAS simulations, the k_s value applied on the downslope test area was 0.012, since $\alpha_{50} = 0.316$.

Figure 62 shows a typical cross-section taken from the downslope area and the roughness k_s value applied to the bed area.

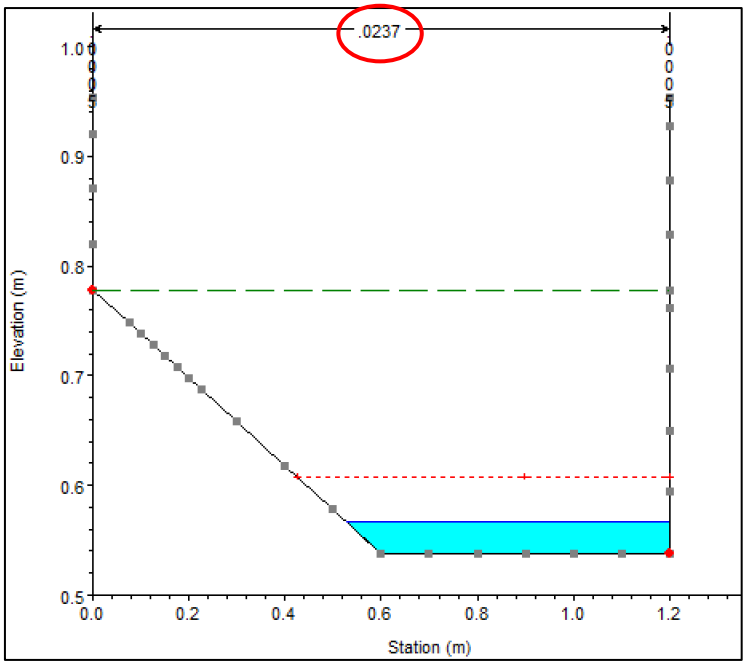

Figure 62: Typical cross-section extracted along the half trapezoidal steep downslope.

To define the k_s values for the wall and the bed area, the bank station range (0.001-1.99) were used to indicate where the k_s should be applied. The top black fine line shows the value (circled in red) and k_s value applied.

With all the geometric data, boundary conditions, flow rates at incipient failure and roughness element values available, it was possible to simulate and obtain reliable results from the 1-D HEC-RAS simulations.

6.2.5 Flow Type

HEC-RAS allowed the user to choose the flow type. There were three flow regime types to choose from:

- supercritical;
- mixed flow; or
- subcritical.

The supercritical or subcritical flow type can be chosen when the HEC-RAS user is certain that the flow in the channel section was supercritical or subcritical. Alternatively, if the user is unsure of what exactly the flow type is, then HEC-RAS can choose mixed flow type where the

HEC-RAS can iteratively find a correct solution for the water surface elevations calculations based on the input data as well as the channel geometry and bed slopes.

Since the hydraulic HEC-RAS model for this thesis comprised of a shape that changed the bed slope from upstream to downstream and the cross-section shape changed, it was decided that the mixed flow type would provide the most accurate solution for the calculations. Moreover, the supercritical flow type and subcritical flow types were chosen to check and assess the resulting surface elevations calculations. The results were not realistic for both flow types. Therefore, the author decided to choose the mixed flow type to model the flow conditions in the hydraulic model for all the tests. The results were more realistic than those provided by the two options. The mixed flow regime autonomously simulates the flow results based on the input hydraulic conditions such as the slope, flow rate, roughness and channel geometry.

6.2.6 HEC-RAS Water Depth Results

After defining the cross-sectional data, reach boundary conditions, channel flow rate data, defining the roughness element height and defining the flow type for the model, the model was run and a solution was provided by the HEC-RAS model.

HEC-RAS allows the simultaneous simulation of all the models at once if the test conditions flow data are recorded correctly. The surface water elevation profiles were then produced in one graph for all the tests, an example can be seen in **Figure 63** below.

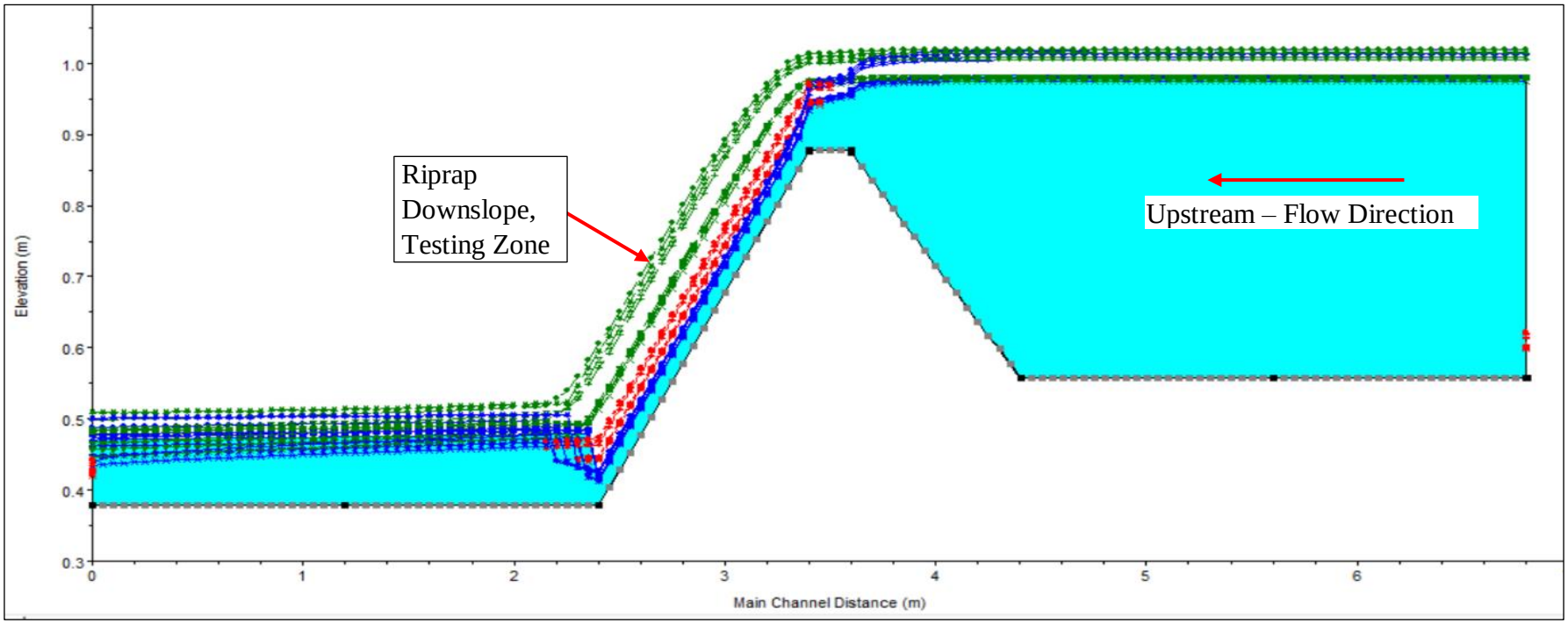

Figure 63: Typical HEC-RAS water elevation profile results of testing Test series two for model one.

The green lines in the profiles in **Figure 63** are the total energy lines, the blue lines are the water elevation lines for each test and the red dotted lines show the critical water depth at the downslope section.

The numerous water surface elevation profiles in **Figure 63** were separated and viewed one at a time to determine the water depth. The problem with the above configuration was that the water depth measurement required was in the riprap downslope testing area. The water depth could not be readily or easily read off from the HEC-RAS format shown in **Figure 63**. The steep slope effect had to be accounted for when determining the water depth in the testing area.

To accurately measure the water depth, the author had to measure the water depth perpendicular to the bed and flow direction in the riprap downslope testing area. HEC-RAS had a tool to measure distance within the model. However, the tool was unable to measure perpendicular to the bed with 100% certainty. Therefore, to measure the effective water depth, each surface water profile had to be exported undistorted (1:1, vertical to horizontal scale) to AutoCAD. Thereafter, the measuring tool and snaps were used to determine the perpendicular water depth on the downslope section in the testing area. This allowed greater confidence levels in the measurement of the simulated HEC-RAS water depth on the steep slope simulated by HEC-RAS.

For all the Test series, the same method was followed to determine the water depth at the downslope testing area in the region closer to the failure areas identified in the physical laboratory tests. A summary of the water depths measured and recorded from the HEC-RAS models and with the assistance of the AutoCAD software are tabulated in **Table 22 to Table 24**.

Table 22: Test series one HEC-RAS water depth results

Test no.	HEC-RAS model water depth results
	D_i (m)
M_1T_1	0.0122
M_1T_2	0.0122
M_1T_3	0.0120
M_2T_3	0.0135
M_3T_1	0.0168
M_3T_2	0.0168
M_3T_3	0.0168

Seven tests were simulated, and seven water depths were measured from the HEC-RAS simulations closer to the failure regions identified. The water depth increased with decreasing

bed slopes. This shows that there was a tendency of the riprap to resist incipient failure much better at the 0.333 slopes compared to the steep 0.4 and 0.5 slopes.

Table 23: Test series two HEC-RAS water depth results

Test no.	HEC-RAS model water depth results
	D_i (m)
M_1T_1	0.0253
M_1T_2	0.0242
M_1T_3	0.0247
M_1T_4	0.0231
M_1T_5	0.0244
M_2T_1	0.0316
M_2T_2	0.0309
M_2T_3	0.0324
M_2T_4	0.0309
M_2T_5	0.0279
M_3T_1	0.0387
M_3T_2	0.0394
M_3T_3	0.0402
M_3T_4	0.0413
M_3T_5	0.0408

About 15 tests were modelled in Test series two. The water depth simulated with the HEC-RAS software also showed an increase of the water depth at incipient failure conditions with a decreasing bed slope. The water depths measured on the 0.333 slopes were generally larger than those measured at the 0.5 and 0.4 steep bed slopes.

Table 24: Test series three HEC-RAS water depth results

Test no.	HEC-RAS model water depth results
	D_i (m)
M_1T_1	0.0630
M_1T_2	0.0619
M_1T_3	0.0627
M_1T_4	0.0473
M_1T_5	0.0455
M_3T_1	0.0500
M_3T_2	0.0630
M_3T_3	0.0635
M_3T_4	0.0722
M_3T_5	0.0603

In **Table 24**, the water depths determined with HEC-RAS show minor variations for the two models. During the laboratory tests, it was observed that the incipient failure flow rates required to induce incipient failure were generally higher in model one compared to model three. However, the HEC-RAS model simulated water depths in model one and model three that show minor variations. The reason could be due to the limitations of HEC-RAS in calculating the water depths at higher flow rates. The disadvantages of using HEC-RAS to model surface water elevations were described in the introduction section of this chapter. The measured physical water depths from the physical laboratory tests were higher on the 0.333 steep bed slope model. Thus, it was expected that if HEC-RAS simulated the water depths appropriately then the water depths would be higher than the values obtained for model three in HEC-RAS. However, it was also accepted that the HEC-RAS model does not fully model the conditions (exact bed roughness, porous flow through riprap, turbulence, air concentration and flow direction in 3 dimensions; to mention a few) at the laboratory given the limitations of the HEC-RAS modelling software.

6.3 MN Calculations Based on the HEC-RAS Simulated Water Depth Results

After the water depths were determined from HEC-RAS the MN values were computed for each test. The same spreadsheet used to calculate the MN values in Test series one, Test series two and Test series three of the physical laboratory results were used to determine the MN for the HEC-RAS simulated average water depths and bed slopes. The bed slopes were assumed to be the designed bed slopes 0.5, 0.4 and 0.333.

Since the HEC-RAS software is a one-dimensional hydraulic simulating software, only one MN value was calculated based on the measured water depth in the identified region closer to the failure area. So, the water depth was taken over an approximate distance of 0.2 m (along the centre of bed in HEC-RAS) in the position that was identified as the failure region. Thereafter the MN was calculated based on the water depth measurement, and the MN would be assumed to define the incipient failure conditions for that specific test. The input parameters used on the MN **Equation 57** were similar to those summarised in **Tables 15, 17** and **19** depending on the testing Test series. **Table 25** below shows a summary of the calculated MN based on the HEC-RAS simulated water depth results.

Table 25: Test series one HEC-RAS simulated MN values for each test.

Test No.	Slope	MN	Re_*
M_1T_1	0.5	0.229	8226
M_1T_2	0.5	0.229	8226
M_1T_3	0.5	0.227	8226
M_2T_3	0.4	0.248	7740
M_3T_1	0.333	0.273	7878
M_3T_2	0.333	0.273	7878
M_3T_3	0.333	0.273	7878

Table 25 shows that there was a constant MN calculated for each tested model in Test series one. The MN increased with a decreasing slope. The 0.333 model showed that the MN was high, an indication that higher flow rates (higher water depth) induced the incipient failure.

Table 26: Test series Two HEC-RAS simulated MN values for each test.

Test No.	Slope	MN	Re*
M_1T_1	0.500	0.253	23381
M_1T_2	0.500	0.247	22867
M_1T_3	0.500	0.250	23102
M_1T_4	0.500	0.242	22351
M_1T_5	0.500	0.248	22952
M_2T_1	0.400	0.291	23379
M_2T_2	0.400	0.287	73085
M_2T_3	0.400	0.294	23666
M_2T_4	0.400	0.287	23111
M_2T_5	0.400	0.273	69446
M_3T_1	0.333	0.317	23599
M_3T_2	0.333	0.320	23812
M_3T_3	0.333	0.323	24052
M_3T_4	0.333	0.327	24379
M_3T_5	0.333	0.325	24231

Table 26 shows 15 tests that were simulated with HEC-RAS in Test series two. The tests on the 0.5 and 0.4 slopes showed that the MN values were smaller comparative to model three MN values, an indication of earlier failure compared to the HEC-RAS simulated tests in the 0.333 steep bed slope hydraulic models.

Table 27: Test series three HEC-RAS simulated MN values for each test

Test No.	Slope	MN	Re*
M_1T_1	0.5	0.360	36890
M_1T_2	0.5	0.357	36572
M_1T_3	0.5	0.359	36796
M_1T_4	0.5	0.312	31969
M_1T_5	0.5	0.306	31355
M_3T_1	0.333	0.325	26824
M_3T_2	0.333	0.365	30110
M_3T_3	0.333	0.367	30239
M_3T_4	0.333	0.391	32234
M_3T_5	0.333	0.357	29463

Table 27 shows the MN values calculated for Test series three tests. Ten HEC-RAS simulations were completed. The HEC-RAS computed MN values were approximately fluctuating at the same range. There was no distinct difference in the MN values simulated

from the HEC-RAS method in Test series three. However, it was noted from **section 4.1** that there were higher flow rates that induced failure on the 0.5 steep bed slope model, compared to model three. Nonetheless, HEC-RAS seemed not to simulate the water depths well at higher flow rates. The water depths in a model with 0.5 seemed to correlate with the measured data while the water depth measured in the hydraulics laboratory showed large discrepancy with the HEC-RAS simulated water depth results.

6.4 Comparison of the Physically Determined MN With the HEC-RAS Determined MN.

In this section, the physically determined MN values found in Test series one, Test series two and Test series three were compared with the critical incipient MN values determined with the HEC-RAS modelling method described in **section 6.1** to **6.3**.

From the physical laboratory results analysis, it was found that the critical MN value for Test series one and Test series two were 0.119 and 0.227, respectively. Therefore, it made logical sense to argue that the critical MN value was 0.119. The MN value of 0.119 defined the hydraulic critical MN conditions for the incipient motion of angular riprap in steep bed slopes. However, for Test series three it was physically determined that the critical MN value that defined the incipient failure conditions of angular riprap on steep side bank slopes was 0.227.

Consequently, **Figure 64** was produced in order to demonstrate the position of the MN determined from the HEC-RAS simulations. The objective was to see how the HEC-RAS determined MN plot in relation to the physically determined MN as well as the critical MN. **Figure 64** shows the MN results for Test series one and Test series two tests of the physical and numerical methods. The green line is the 0.119 critical MN value determined from the 95% probability of exceedance for Test series one and two. The dashed blue line connects the HEC-RAS determined MN values of each test.

In **Figure 64** the HEC-RAS MN values either plotted below, close or above the mean MN values determined from the physical laboratory tests. There was no noticeable trend or relation between the physical MN results and the HEC-RAS determined MN. However, the smallest HEC-RAS determined MN value was found to be 0.227 from test P1M1T3. The highest HEC-RAS determined MN was 0.391 from test P2M3T4. It was noticed that all the HEC-RAS MN values plotted above the critical 0.119 critical MN of Test series one and Test series two.

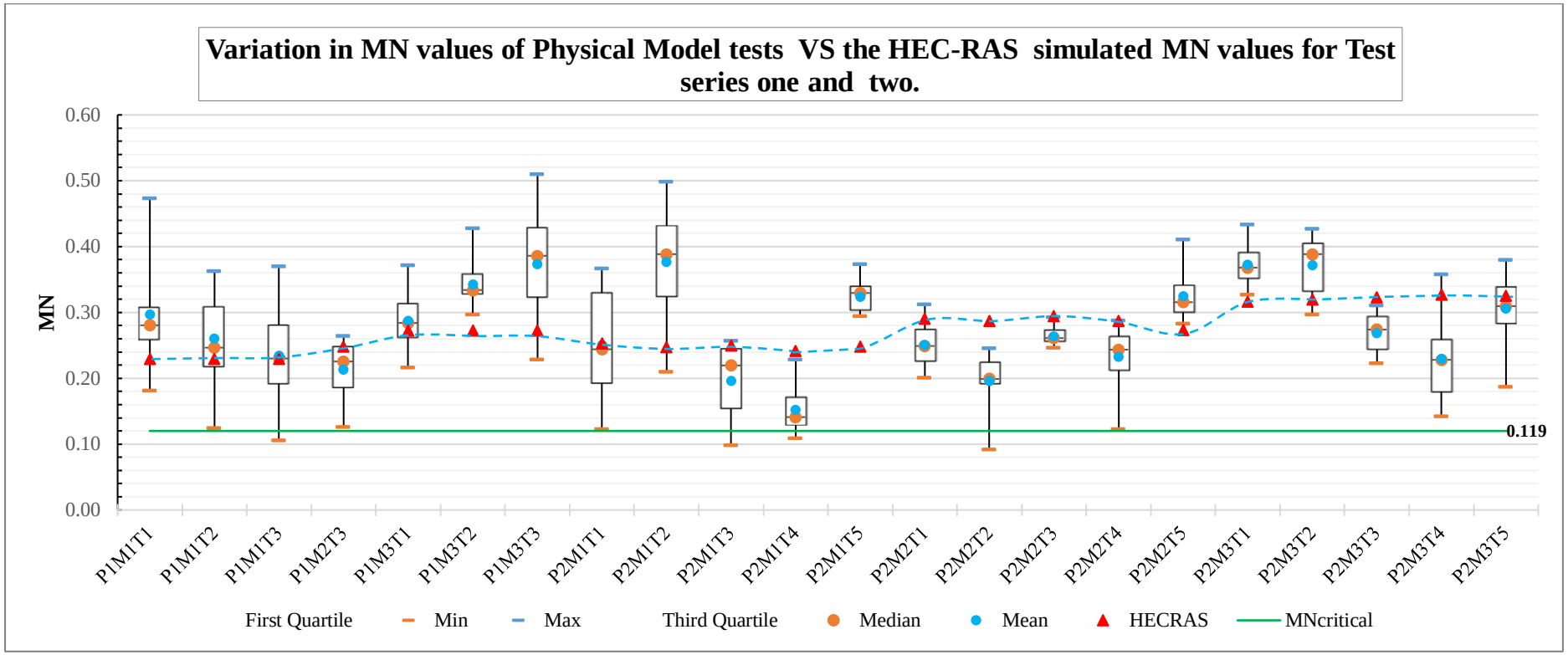

Figure 64: Comparison of HEC-RAS MN with Physically determined MN for Test series one and two.

Test series three HEC-RAS determined MN values were plotted onto the box-whisker diagram of the physically determined MN results. **Figure 65** shows the relative HEC-RAS determined MN in relation to the MN results determined from the physical laboratory results.

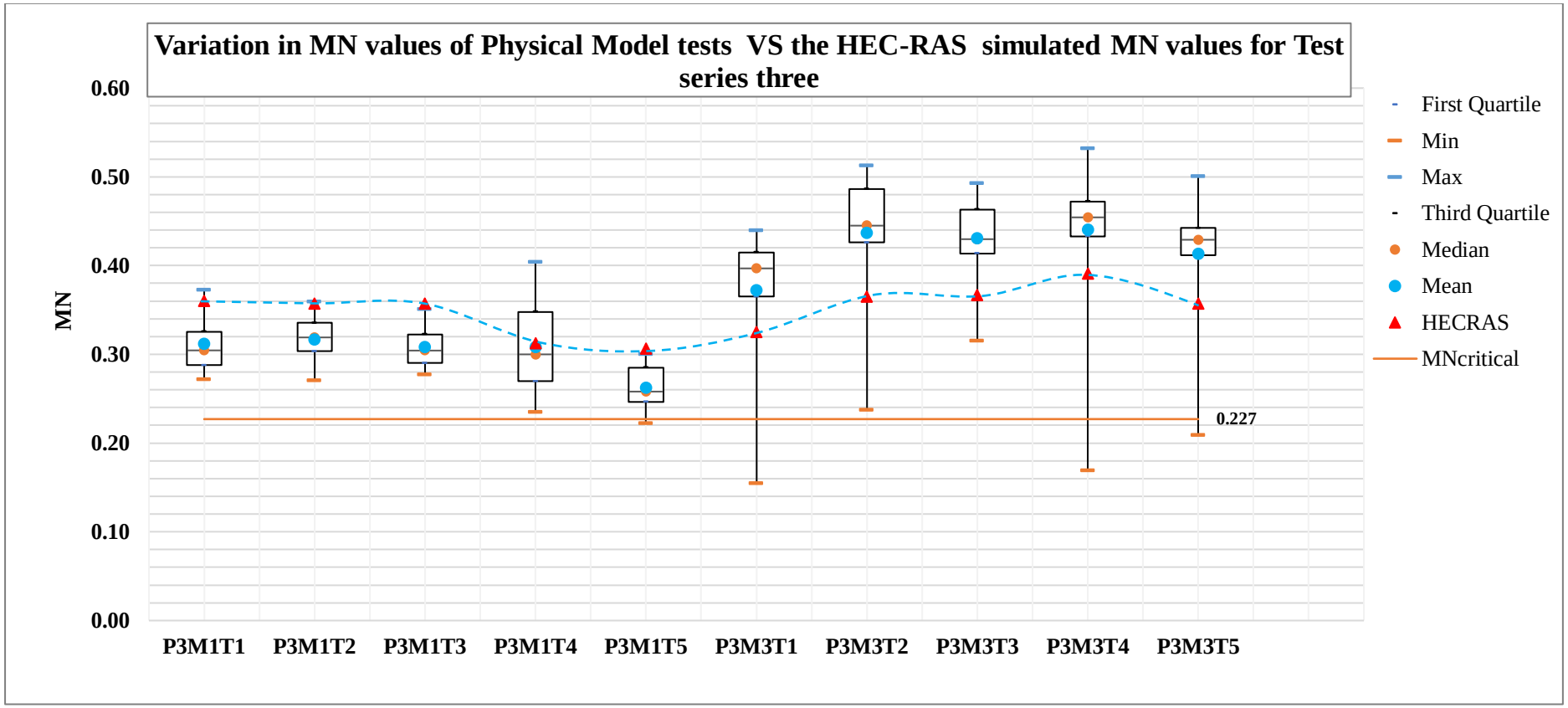

Figure 65: Comparison of HEC-RAS MN with Physically determined MN for Test series three.

The HEC-RAS simulated MN results plotted above or closer to the physical laboratory mean MN values for each test in the model one tests of Test series three. This meant that HEC-RAS generally tended to overestimate the MN for model one tests of Test series three.

However, the HEC-RAS simulated MN values all plotted below the boxes for the model three of Test series three. This meant that HEC-RAS produced MN values that were lower than the observed MN values in the physical model. The smallest MN value determined by the HEC-RAS method was 0.306 obtained from test P3M1T5. The highest HEC-RAS MN value obtained was 0.391, from test P3M3T4. All the HEC-RAS MN values plotted above the critical MN value of 0.227 in Test series three.

From the HEC-RAS analysis performed, it was evident that the HEC-RAS could not accurately produce MN results that agree with the physically determined MN results. The reasons for this may be contributed or exacerbated by the flow modelling limitations that are incorporated into the HEC-RAS modelling software. This was a very useful evaluation, as some engineers may blindly use the MN criteria and HEC-RAS surface water modelling simulations to determine the stable stone size for riprap. This could result in incorrect riprap median stone size being specified.

6.5 Determination of HEC-RAS Adjustment Factors (AF)

From the evaluation, it was important that the HEC-RAS MN results were corrected for design engineers to use the widely available HEC-RAS software modelling tool to determine the safe riprap median stone size. Therefore, it was decided that an adjustment factor (hereafter referred to as AF) must be applied to the HEC-RAS simulated MN.

The AF was determined by the ratio between the lowest MN determined from the HEC-RAS method and the critical MN obtained from Test series one and Test series two physical tests for steep bed riprap design. The ratio of the two was calculated as follows:

$$AF_{bed} = \frac{Lowest\ MN_{hecras}}{MN_{critical(physical\ model)}} = \frac{0.227}{0.119} = 1.91$$

The same procedure for calculating the AF for Test series three was followed:

$$AF_{sidebank} = \frac{Lowest\ MN_{hecras}}{MN_{critical(physical\ model)}} = \frac{0.306}{0.227} = 1.35$$

Therefore, the AF to be applied to the MN determined with HEC-RAS procedure for steep bed riprap and steep side bank riprap specification are:

- AF_{bed} (steep bed riprap) =1.91
- $AF_{sidebank}$ (steep side bank slope) =1.35

However, it must be noted that the AF listed above will only be applicable under the following design conditions:

- HEC-RAS analysis must be performed under steady-state flow conditions
- The relative roughness applied must be, $\alpha_{50} = \frac{k_s}{D_{50}} = 0.316$
- The MN criteria are only applicable to steep bed slopes of 0.5 to 0.333
- The steep side bank slope must be designed to be 0.4
- The bottom trapezoidal channel width must adhere to the bottom width to D_{50} ratio:

  $w_{ratio=}\frac{Bottom\ width}{D_{50}} = \frac{1.2\ m}{0.075\ m} = 16$ (up to 31 for the D_{50}= 0.038 m median stone size tested at the laboratory)

The application of the AF and the HEC-RAS hydraulic model design conditions listed above ensures that a safe MN value can be determined by the engineer to specify a safe D_{50} median stone for the pertinent design flow rates using HEC-RAS. To do this, the designer will have to perform a hydraulic analysis using HEC-RAS to determine the water depth and design slopes. Thereafter, the MN equation can be applied, then the pertinent AF may be applied to the calculated MN results obtained from the use of the HEC-RAS simulated water depths and bed or side bank slopes.

6.6 Guidelines for Design Application Using the MN as the Criteria for Incipient Failure of Riprap.

There are two main findings from the analysis performed in **section 6.1 to 6.5** regarding the critical MN value defining the incipient motion conditions. The first finding was that the failure of the riprap on a trapezoidal channel occurs at different hydraulic conditions for both the riprap dumped on the steep bed slopes, as well as the riprap dumped on the steep side bank slopes. The MN value defining the critical state of incipient failure of riprap on steep bed slopes was found to be 0.119. The critical MN that defined the critical incipient failure conditions of riprap dumped on steep side bank slope was found to be 0.227.

The second main finding was that the HEC-RAS steady state MN analysis method overestimates the critical MN value defining the incipient failure condition. The critical MN for the steep bed slope riprap rocks was overestimated by a minimum factor of 1.91. The HEC-RAS steady state MN analysis method defining the incipient motion of the riprap dumped on side banks was overestimated by a factor of 1.35 relative to the critical MN value determined from the physical laboratory model tests.

The main findings listed above were used to develop a method to be used by designers to specify stable riprap median stone size for specific design flow rates at steep bed slopes and steep side bank slopes using the HEC-RAS modelling software. A spreadsheet (**find design spreadsheet in the attached CD**) was developed to guide the designer through the process.

For the design of stable riprap on steep channel beds, the following design method was followed:

> **Step 1.** The recommended first step is to calculate the settling velocity using **Equation 3. Table 28** shows the material property inputs (green cells) required and recommended in the design spreadsheet to calculate the settling velocity. The spreadsheet automatically calculates the settling velocity.

Table 28: Properties required to calculate the settling velocity of D_{50}

ρ_w	1000	kg/m^3
ρ_r	2700	kg/m^3
g	9.81	m/s-2
D_{50}	0.112	m

C_D	2.17	(This is a recommended Drag Coefficient Value), A smaller drag coefficient may lead to undersized D_{50} specification

The water and rock properties in **Table 28** are recommended and typically reasonable assumptions used for riprap design (CIRIA, 2007). The D_{50} size must be determined through an iterative process, at this stage, a reasonable D_{50} size may be guessed. The designer should feel free to change any of the properties with orange coloured boxes (input cells). The Excel Design Tool is protected with a password to avoid accidental modifications of the spreadsheet.

The C_D value recommended for design purposes was based on the average C_D value determined in the laboratory. The designer may choose a C_D value of their choice but should know that if the C_D is decreased from 2.17 then D_{50} may be undersized, thus this is not highly recommended.

Step 2. Determine the steep bed slope correction factor.

To calculate the steep bed correction factor, the design steep bed slope and riprap angle of repose must be known and inserted on the spreadsheet in the green cells shown in **Table 29**. The Excel Design Tool will automatically calculate the Steep bed correction factor.

Table 29: Summary of bed slope and rock angle of repose properties

	Slope	Angle in radians	Angle in degrees
Φ_r	0.84	0.698	40
S_β	0.5	0.462	26.5

For angular riprap, the designer can use the recommended angle of repose of 40 degrees or calculate by using Froelich's (2011) **Equation 6**. The designer may feel free to determine an angle of repose based on logical engineering judgement or reliable source from the literature. The steep bed slope, S_β, needs to be specified by the designer (all green cells are input cells in **Table 29**).

Therefore, with the steep bed slope and the rock angle of repose known, the steep bed slope correction factor may be calculated by applying **Equation 58,** not forgetting to include the square root**.** The spreadsheet automatically calculates the correction factors if slope input data is provided in the green cells.

Step 3. The final step is to determine the stable D_{50} median stone size by calculating the critical MN value using **Equation 57** and applying the relevant AF.

The designer must determine the water depth using HEC-RAS steady-state flow analysis. For a specific design flow rate and geometry of the channel, HEC-RAS can compute the respective water depth on the steep bed slope. **Table 30** shows the required parameters in step three of the Excel Design tool. The AF_{bed} of 1.91 is already applied onto the MN calculated by the Excel Design Tool.

Table 30: Input data required for step three of the Excel design method

$D_{w\ (HEC\text{-}RAS)}$	0.0353	m
AF_{bed}	1.91	

The moment the designer inserts the water depth simulated with the HEC-RAS, the MN value on the Design Tool will be changed. For a safe design, the initially guessed D_{50} in step one must be changed such that the MN is 0.12 (the critical 0.119 MN value found in the analysis was rounded up to 0.12 for the design specification).

The following guidelines (stated at the end of the Excel Design Tool) may be used for the median stone size guessing iterations to achieve the required MN:

- If MN > 0.12, Increase D_{50}
- if MN = 0.12, safe
- if MN < 0.12, safe

but, if MN is significantly less than 0.12, then decrease D_{50} until MN =0.12

The designer will note that changing the D_{50} also changes the k_s value. Therefore, necessitating a repetition of the process from step one, until the water depth, k_s and D_{50} converges. When the three no longer change after running a HEC-RAS simulation then the converged D_{50} can be recommended as the safe steep bed design D_{50} for the specific design flow rate.

The same procedure (step one to step three described above) may be followed for designing the riprap dumped on the steep side banks of trapezoidal channel cross-sections. However, the only difference is the incorporation of the side bank steep slope correction factor in step two which can be calculated using **Equation 59**.

The important difference in designing the stable side bank slope is the recognition and application of the critical MN of 0.227 as well as the $AF_{sidebank}$ of 1.35.

For steep side bank slope riprap design, the following guidelines will assist the designer in guessing the correct D_{50} median stone size for the stable side bank riprap.

- If MN > 0.227, Increase D_{50}
- if MN = 0.227, safe
- if MN < 0.227, safe
- but, if MN is significantly less than 0.12, then decrease D_{50} until MN = 0.227

The attached Microsoft Excel Design Tool can be straightforwardly used by the designer to design stable riprap for steep bed slopes and the side bank channels using angular shaped riprap. Sheet one is applicable to riprap dumped on steep bed slopes. Sheet two may be used to design the riprap for the side bank channels.

The spreadsheet is easy to use, and if angular riprap rock (with the pertinent rock density used as an input parameter) will be used for the design and construction, the only parameters the designer may need to specify in the spreadsheet are the $D_{50,}$ the HEC-RAS simulated water depths and the design riprap steep bed slope. The side bank slope may be kept at a 0.4 steep slope for the designs since this study only investigated one steep side bank slope. Moreover, the application limits for the riprap prototype design in terms of the D_{50} rock size is between 0.57 m and 1.125 m (based on the 1:15 scale tested at the laboratory). Finally, a design example has been attached in **Appendix G** to illustrate how the Excel Design Tool may be used to design riprap within the applicable limits of this study.

Chapter 7 : Conclusions

Design guidelines for riprap stability studies have mainly been based on shear stress and average stream velocity theoretical frameworks and derivations. However, from Rooseboom's (1992) and Armitage's (2002) stream power-based incipient motion studies, Langmaark and Basson (2015) managed to apply the theory to define incipient motion conditions for large riprap dumped on steep bed slopes. Langmaak and Basson (2015) successfully applied Rooseboom's (1992) stream power-based MN criteria to define the critical incipient failure MN for large riprap in steep bed slopes.

To contribute towards the riprap incipient motion studies, the objectives of this thesis was to determine the critical incipient failure motion conditions of angular riprap dumped on wide and steep trapezoidal channels by means of the stream power-based MN criteria. The objectives have been met by quantifying the critical incipient failure conditions for both angular ripraps dumped in steep bed slopes and steep side bank slopes.

A physical hydraulic model study was performed in three test series. The first Test series performed seven tests on the D_{50} = 0.038 m (with a steep movable bed). The second Test series was performed on fifteen tests for the D_{50} = 0.075 m angular stone (with a steep movable bed). Finally, for Test series three, ten tests were performed on the D_{50} = 0.075 m angular riprap (with a steep immovable bed). The scale of the hydraulic physical model used in the investigation was selected relatively large i.e. 1:15 to minimize model scale effects for the D_{50} size of stone used in the model i.e. between 0.038 m and 0.075 m which represent prototype stone sizes with D_{50} between 0.57 m and 1.125 m respectively. The results of the study are therefore strictly speaking only valid for the design of prototype D_{50} size stone between stone 0.57 m and 1.125 m.

The conclusions for the study were divided into two. The first part of the conclusions was based on the literature review and the second part of the conclusions were based on the findings of the laboratory study and the analysis of the observed data.

7.1 Conclusions drawn from the literature review

The conclusions that have been drawn from the literature review assisted the investigator to successfully pursue the physical hydraulic model studies. The investigator managed to anticipate the expected behaviour of the physical hydraulic model before it was built. Thus, managed to successfully construct and perform tests on the riprap physical hydraulic model. The following main conclusions were drawn from the literature review:

- The stability of riprap in steep hydraulic channel flows was dependent on the grading of the riprap mixture, the shape of riprap and the density of the rock. There were no complete conclusions regarding the most acceptable riprap grading between uniform and non-uniform-riprap. However, the widely used non-uniform grading recommended by Simons and Senturk (1992) for riprap was used for the physical hydraulic lab. Angular shaped stones were found to provide more stability than round rocks due to the angularity that increases riprap interlocking. It was also argued that the size and mass (thus density) are important properties to account for when determining the stable riprap median rock size.
- When doing a MN-based riprap analysis, the settling velocity was found to be a critical property, implying that it must be accurately determined. It was therefore recommended that for laboratory studies the settling velocity of irregular particles must be determined physically at the laboratory.
- To design safe riprap protection, a detailed understanding of the main failure modes was required to assist the researcher to design a safe riprap armour layer for the laboratory tests. The understanding of the riprap failure modes assisted the researcher to design the laboratory riprap protection such that the objectives of the thesis were successfully achieved.
- Lastly, it was found that the shear stress-based theories for studying riprap incipient motion was well-known and currently the most reliable. Velocity-based riprap design methods were found not be widely favoured and used for design due to limitations in determining representative velocities for design purposes. Stream power-based methods were found to be useful in determining incipient failure conditions. The stream power-based MN theoretical approach was found to be valuable and useful in specifying the critical incipient failure conditions of steep riprap exposed to turbulent overtopping flows. The main critical studies in support of the stream power-based MN

theoretical approach that was found to be useful for this thesis were Rooseboom (1992), Armitage (2002) and Langmaak (2013) studies.

7.2 Conclusions deduced from the physical hydraulic model tests and analysis

The conclusions for the physical hydraulic laboratory tests and the MN analysis results may be summarised as follows:

- For riprap dumped on steep bed slopes and designed with the grading recommended by Simons and Senturk (1992) and a thickness = $2.5D_{50}$, the rocks smaller or equal to the specified D_{50} were generally the rocks that defined the critical incipient failure conditions of the riprap. The larger rock sizes of the grading did not move during incipient failure.
- In a wide trapezoidal $\left(\frac{bottom\ width}{D_{50}} = 16\ to\ 31\right)$ channel with steep bed slope (0.333-0.5) and a steep side bank slope (0.4), if the same D_{50} median stone size and grading have been dumped on the steep bed slope and side bank, the riprap on the steep bed slope area will fail before the side bank slopes fails.
- Large protruding rocks may cause premature incipient failure of riprap. The premature failure may be caused by the creation of concentrated flows and stream jets.
- The incipient failure flow conditions of riprap in wide and steep trapezoidal channels occurs under shallow hydraulic water depths. Accurate water depth measurements are almost impossible to physically measure under rough bed conditions. Thus, it was difficult to perform a MN analysis with a high level of confidence in the results obtained, due to the sensitivity of the water depth to the MN.
- Nonetheless, it was found that the critical incipient failure MN for defining the incipient failure conditions of angular riprap placed on wide steep bed slopes (0.333-0.5) was 0.119 with a probability of exceedance of 95% relative to the tests performed at the Stellenbosch University Hydraulics laboratory. The MN determined agreed with Rooseboom's (2002) criteria defining the critical 0.12 MN for a particle in the turbulent flow region.
- The first MN analysis on angular riprap dumped on a steep side slope (0.4) was performed at the University of Stellenbosch Hydraulics laboratory. It was found that critical incipient failure MN for defining the incipient failure conditions of angular

riprap dumped on a steep side bank slope of 0.4 was 0.227 with a probability of exceedance of 95% relative to the stability tests performed at the laboratory.

- Finally, the HEC-RAS one-dimensional modelling software was evaluated to assess its capability to define the physically determined critical incipient failure MN values for the physical laboratory tests. The HEC-RAS MN analysis produced average MN for each test and there was no specific relation found in each test between the HEC-RAS calculated MN and the physically determined MN. However, the HEC-RAS determined MN were found to be always greater than the two incipient motion failure criteria found in this thesis (the 0.119 and 0.227 MN values). Therefore, it was concluded that an AF of 1.91 must be applied to the MN analysis performed for the design of riprap dumped on steep beds by means of a HEC-RAS steady-state analysis. Lastly, an AF of 1.35 must be applied to the MN analysis performed for the design of riprap dumped on a steep side bank slope of 0.4 by means of a HEC-RAS steady-state analysis. A design spreadsheet has been attached for facilitating the design process when using HEC-RAS to perform an incipient failure analysis using the MN criteria.
- Riprap dumped on the 0.333 steep bed slopes was found to be more stable than the riprap on the 0.4-0.5 steep bed slopes.

Chapter 8 : Recommendations

From the physical hydraulic laboratory study and analysis, the recommendations may be divided into two. The first recommendations are based on the effective construction and design of riprap on wide and steep trapezoidal channels. The second part of the recommendations are for future research purposes:

8.1 Recommendations for riprap construction and design in wide-steep trapezoidal channels

- During construction, when dumping and levelling the riprap the large protruding riprap rocks must be removed at the top of the riprap bed. Then the area must be filled with D_{50} stone size. The reason to do this is to avoid the creation of concentrated flows and jets that will cause premature failure of the riprap armour layer.
- When following the method of design recommended in this thesis, it is critical that the riprap adheres to the grading by Simons and Senturk (1992). Angular riprap rock must be used as the riprap. Most importantly, the D_{50} rock size used must be between 0.57-1.125m (based on the physical hydraulic model scale limits tested at the laboratory).
- In case a different stone material type is available for construction (as opposed to hornfel), then the designer must account for the change in the density of a different stone type when determining the settling velocity.
- The use of bidim as a geotextile filter material is highly recommended for application. The filter is widely available and used for the benefits stated in **section 3.2.3**.
- The final recommended design MN defining the incipient failure conditions in terms of the MN criteria is as follows
    - 0.12 for riprap dumped on steep bed slopes (0.333-0.5) of trapezoidal channels,
    - and 0.227 for riprap dumped on steep (0.4) side bank slopes.
- The thickness of riprap during construction must at least be 2.5 $D_{50.}$
- The critical incipient MN values specified above, are only applicable when the bottom width to D_{50} ratio is between 16-31.
- When using HEC-RAS the recommended flow analysis method must be a steady state flow analysis, because the adjustment factors determined from the thesis are only applicable to the steady state flow analysis in HEC-RAS.

8.2 Recommendations for future research on riprap incipient motion

- A study is required to test for the best performing grading type for angular riprap in steep trapezoidal channels. The study must be able to assess the grading in terms of flow rate failure, time of failure and the nature of failure in terms of whether the grading fails instantly, or the failure is developmental. Both uniform and non-uniform gradings should be used for the compared tests.
- An optimisation study is also required regarding the effective thickness of riprap. Literature shows that generally, the thickness of riprap ranges between 2-3*$D_{50,}$ however, no specific study was found to address the optimal thickness. This is important when designing for large flow rates. The riprap protection project may be costly if the method of riprap design generally determines significantly conservative D_{50} median riprap size since the thickness depends on the D_{50} size.
- In this thesis, the steep bed and side bank failure conditions were tested separately, due to the steep bed riprap failing earlier than the side bank riprap. Therefore, the condition whereby both the steep bed riprap and the steep side bank slope riprap were both movable was not tested. It is recommended that the findings in this thesis are used to determine the stable riprap dumped on the steep bed and steep side bank at a specific flow rate where there is both significant water depth on the bed and the side bank. This is to assess the flow conditions at the toe of the riprap when there are different D_{50} defined for the steep bed and side bank riprap while both the riprap on the bed and side bank were movable.
- A three-dimensional flow analysis should be performed to evaluate the ability of the three-dimensional flow modelling software to simulate and predict incipient failure conditions. Generally, three-dimensional flow modelling software produces better simulations compared to HEC-RAS for hydraulic flow conditions in more than one direction (important for trapezoidal sections). It is understood that the riprap bed is very difficult to model due to the porous nature of the flow through the bed, turbulence, jets, rough bed and air concentrations which are usually not accounted for in a one-dimensional HEC-RAS modelling simulation. However, Suaznabar *et. al.* (2017) have shown that there exist advanced methods for assessing the riprap using computational methods, but the specific study was based on riprap stability in bridge piers. Perhaps,

the feasibility of using the method described by Suaznabar *et. al.* (2017) may be assessed and evaluated for use in riprap studies in steep trapezoidal channels.

- Lastly, further research in this field is recommended whereby sharp bends in the horizontal alignment of channels are accounted for. This study only focused on straight trapezoidal channels.

References

Abt, S. R. *et al.* 1998. Riprap Sizing at Toe of Embankment Slopes, *Journal of Hydraulic Engineering*, 124(7): 672–677.

Abt, S. R. *et al.* 2009. Round-Shaped Riprap Stabilization in Overtopping Flow, *Journal of Hydraulic Engineering*, 134(8): 1035–1041.

Abt, S. R. *et al*. 2013. Evaluation of overtopping riprap design relationships, *Journal of the American Water Resources Association*: 49(4): 923–937.

Abt, S. R. & Johnson, T. L. 1991. Riprap Design for Overtopping Flow, *Journal of Hydraulic Engineering*, 117(8): 959–972.

De Almeida, G. A. M. & Martín-Vide, J. P. 2009. Riprap Stability: Transverse and Longitudinal versus Continuous Protections, *Journal of Hydraulic Engineering*.135(6): 447–456.

Armitage, N. 2002. *A unit stream power model for the prediction of local scour in rivers by*. University of Stellenbosch.

Armitage, N. & McGahey, C. 2003. A unit stream power model for the prediction of local scour in rivers, *WRC Report No. 1098/1/03*, (1098).

Armitage, N. and Rooseboom, A. 2010. The link between Movability Number and Incipient Motion in river sediments, *Water SA*, 36(1): 89–96.

Abban, B. 2007. *Using the Movability Number to model local clear-water scour in rivers*. University of Cape Town.

Beheshti, A. A. and Ataie-Ashtiani, B. 2008. Analysis of threshold and incipient conditions for sediment movement', *Coastal Engineering*, 55(5): 423–430.

Blodgett, J. C. 1986. *Rock Riprap Design for Protection of Stream Channels Near Highway Structures*. Califonia. Available at: http://pubs.usgs.gov/wri/1986/4128/report.pdf (Accessed: 12 May 2016).

Buffington, J. M. 1999. The Legend of A. F. Shields', *Journal of Hydraulic Engineering*, 125(4): 376–387.

Buffington, J. M. and Montgomery, D. R. 1998. A systematic analysis of eight decades of

incipient motion studies, with special reference to gravel-bedded rivers', *Water Resources Research*, 33(8): 1993–2029.

CIRIA, CUR, CETMEF. 2007. The Rock Manual. *The use of rock in hydraulic engineering* (2nd edition). C683, CIRIA, London

Cheng, N.-S. 1997. Simplified settling velocity formula for sediment particle, *Journal of Hydraulic Engineering*, 123(February): 149–152.

Chiew, Y. M. and Parker, G. 1994. Incipient sediment motion on non-horizontal slopes: Début d'entraînement de sédiments sur des lits non horizontaux', *Journal of Hydraulic Research*, 32(5): 649–660.

Committee of State Road Authorities, 1994. *Guidelines for the Hydraulic Design and Maintenance of River Crossings*. Volume 3. Pretoria: Department of Transport. Available at: http://www.imesa.org.za/wp-content/uploads/2016/01/TRH25VOLIII.pdf (Accessed: 3 May 2016).

Cunninghame, M. 2005. *Numerical modelling of local scour in rivers using Fluent 6.2*. University of Cape Town.

Frizell, K. H., Ruff, J. F., and Mishra, S. 19998. Simplified design guidelines for riprap subjected to overtopping flow. Proc., Annual Association of State Dam Safety Officials (ASDSO) Conf., Las Vegas.

Froehlich, D. 2011. Mass angle of repose of open-graded rock riprap, *Journal of Irrigation and Drainage Engineering*, 50(July): 454–461

Froehlich, D. 2012. Closure to " Most Hydraulically Efficient Riprap- Lined Drainage Channels " by David C. Froehlich', *Journal of Irrigation and Drainage Engineering*, 138(November): 694–695

Froehlich, D. C. 2012. Resistance to Shallow Uniform Flow in Small, Riprap-Lined Drainage Channels, *Journal of Irrigation and Drainage Engineering*, 138(2): 203–210

Froehlich, D. C. 2012. The rap on river banks : Protecting river banks with loose rock riprap, pp. 1317–1324.

Froehlich, D. C. 2013. Sizing loose rock riprap to protect stream banks, *River Research and Applications*, 29(2). 219–235.

Gazendam, M. 2005. *Incipient Motion In Cobbleiboulder Bed Rivers*. University of Stellenbosch.

Heller, Valentin. 2011. Scale effects in physical hydraulic engineering models. *Journal of Hydraulic Research* - J HYDRAUL RES. 49. 293-306.

Hiller, P. H., Aberle, J. and Lia, L. 2018. Displacements as failure origin of placed riprap on steep slopes', *Journal of Hydraulic Research*, 56(2). 141–155.

Hiller, P. H., Lia, L. and Aberle, J. 2018. Field and model tests of riprap on steep slopes exposed to overtopping, *Journal of Applied Water Engineering and Research*. Taylor & Francis.

Hoffmans, G.J.C.M. and Verheij, H.J., 1997. Scour manual, Rotterdam, Netherlands: A.A. Balkema.

Huthoff, F., Augustijn D. 2004. Channel roughness in 1D steady uniform flow: Manning or Chezy?', *Proceedings NCR-days, The* Netherlands.

Ji, U., Yeo, W. and Kang, J. 2013. Subsidence of riprap protection without filters for different installation types of riprap around a pier in sands', *Journal of Hydro-Environment Research*, 7(1), 41–49.

Jiménez, J.A. and Madsen, O.S., 2003. A simple formula to estimate settling velocity of natural sediments. *Journal of waterway, port, coastal, and ocean engineering*, *129*(2), pp.70-78.

Khan, D. and Z., Ahmad. 2011. Stabilization of angular shaped riprap rock under overtopping flows, *World Academy of Science, Engineering and Technology*, 59.

Kobus,H. 1980. Hydraulic Modelling. German association water resources and land improvement, bulletin 7. Parey, Hamburg.

Langmaak, K. R. 2013. Incipient Motion of Riprap on Steep Slopes. University of Stellenbosch

Langmaak, K. R. and Basson, G. R. 2015. Incipient Motion of Riprap on Steep Slopes, *Journal of Hydraulic Engineering*, 141(9): 06015010:1-7

Latham, J. P., Lienhart, D. and Dupray, S. 2006. Rock quality, durability and service life prediction of armourstone, *Engineering Geology*, 87(1–2): 122–140.

Le Roux, J.P., 2014. Fall velocity of multi-shaped clasts. *Journal of Volcanology and*

Geothermal Research, *289*, pp.130-139.

Maynord, S. T. 1986. *Stable Riprap Size For Us Army Corps of Engineers, Office*. Washington DC.

Maynord, S. T., Ruff, J. F. and Abt, S. R. 1989. Riprap Design, *Journal of Hydraulic Engineering*, 115(7): 937–949.

Najafzadeh, M., Rezaie-Balf, M. and Tafarojnoruz, A. 2018. Prediction of riprap stone size under overtopping flow using data-driven models', *International Journal of River Basin Management*. Taylor & Francis: 16(4): 505-512

Novak, P. 1999. Discussion of "Roughness of Loose Rock Riprap on Steep Slopes" by C. E. Rice K. C. Kadavy, and K. M. Robinson', *Journal of Hydraulic Engineering*: 124(2), 179–185.

Oliveto, Giuseppe & Hager, Willi. 2005. Further Results to Time-Dependent Local Scour at Bridge Elements. *Journal of Hydraulic Engineering*. 131(2),97-105

Raudkivi, A.J., 1998. Loose boundary hydraulics 4th ed., Rotterdam: Balkema.

Robinson, K.M., Rice, C.E. and Kadavy, K.C., 1998. Design of rock chutes. *Transactions of the ASAE*, *41*(3), p.621.

Rooseboom, A. 1992. *Sediment Transport in Rivers and Reservoirs- A Southern African Perspective*. Report NO. 297/1/92 of the Water Research Commission of South Africa.

Rooseboom, A. and Mulke, F. J. 1982. Erosion initiation, *Recent Developments in the Explanation and Prediction of Erosion and Sediment Yield (Proceedings of the Exeter Symposium, July 1982).*, (137), pp. 59-66

Schmocker, l. hager, W.H. 2009. Modelling dike breaching due to overtopping. J. Hydraulics Res. N47(5), 585-597.

Shvidchenko, A. B., Pender, G. and Hoey, T. B. 2001. Critical shear stress for incipient motion of sand/gravel streambeds, *Water Resources Research*, 37(8): 2273–2283.

Simons, D. B., & Şentürk, F. 1992. *Sediment transport technology: water and sediment dynamics*. Littleton, Colo., USA, Water Resources Publications.

Stevens, M. A., Simons, D. B. and Richardson, E. V. 1979. Riprap Stability Analysis, *Transportation Research Record 950*, (June).

Stoffberg, F. 2005. *Evaluation of the incipient motion criteria for rock in reno mattress and*

Rip Rap. The University of Stellenbosch.

Suaznabar, O., Bojanowski, C., Lottes, S., Shen, J., Kerenyi, K. and Kilgore, R. (2018). *Advanced Methodology to Assess Riprap Rock Stability at Bridge Piers and Abutments*- Federal Highway Administration's (FHWA) Report NO. *FHWA-HRT-17-054*.

Thornton, C. I. *et al.* 2014. Enhanced Stone Sizing for Overtopping Flow. *Journal of Hydraulic Engineering*, 140(4):

Wang, Yuhai & Jiang, W.-G. 2013. Scale effects in scour physical-model tests: Cause and alleviation. Journal of Marine Science and Technology (Taiwan). 21. 532-537.

Yang, C.T. 1973. Incipient motion and sediment transport. *Journal of the Hydraulics Division*, 99(10): 1679-1704. 06014005:1-4

Yang, C. T. and Stall, J. B. (1974) *Unit Stream Power for Sediment Transport in Natural Rivers*.

Appendices

Appendix A: Test series One and Test series Two Model Design Drawings

The drawings are enclosed in the CD, the drawing resolution and size is too large to fit into A4 page, thus refer to drawings in CD.

Appendix B: Rock Sample Settling Velocities and Drag Coefficient

Settling velocities of rock sample 0.026-0.038 m

Stone number	a (mm)	b (mm)	c (mm)	Settling time (s)	Water depth (m)	Settling velocity (m/s)	D (dimension b in (m))	C_D	Corey shape factor
1	60	45	25	9.32	4.960	0.5322	0.045	3.533	0.48
2	55	30	20	9.34	4.960	0.5310	0.03	2.365	0.49
3	56	35	23	7.24	4.960	0.6851	0.035	1.658	0.52
4	49	31	29	6.96	4.960	0.7126	0.031	1.357	0.74
5	53	40	28	7.2	4.960	0.6889	0.04	1.874	0.61
6	60	29	25	8.86	4.960	0.5598	0.029	2.058	0.60
7	45	35	23	8.3	4.960	0.5976	0.035	2.179	0.58
8	48	27	23	7.59	4.960	0.6535	0.027	1.406	0.64
9	62	42	23	6.79	4.960	0.7305	0.042	1.750	0.45
10	56	35	23	6.9	4.960	0.7188	0.035	1.506	0.52
11	56	34	28	8.43	4.960	0.5884	0.034	2.184	0.64
12	41	39	25	8.52	4.960	0.5822	0.039	2.559	0.63
13	57	38	26	6.79	4.960	0.7305	0.038	1.583	0.56
						Average V_{ss}= 0.6393	**Average C_D =**	**2.001**	

Settling velocities of rock sample 0.038-0.053 m

Stone number	a (mm)	b (mm)	c (mm)	Settling time (s)	Water depth (mm)	Settling velocity (m/s)	D (dimension b in (m))	C_D	Corey shape factor
1	90	65	40	6.56	4.960	0.7561	0.065	2.528	0.52
2	70	68	43	6.59	4.960	0.7527	0.068	2.669	0.62
3	95	76	40	8.36	4.960	0.5933	0.076	4.801	0.47
4	72	43	43	5.83	4.960	0.8508	0.043	1.321	0.77
5	74	60	32	6.72	4.960	0.7381	0.06	2.449	0.48
6	70	52	33	6.29	4.960	0.7886	0.052	1.860	0.55
7	70	45	27	6.55	4.960	0.7573	0.045	1.745	0.48
8	80	70	30	6.77	4.960	0.7326	0.07	2.900	0.40
9	62	42	36	5.82	4.960	0.8522	0.042	1.286	0.71
10	75	45	28	7.23	4.960	0.6860	0.045	2.126	0.48
11	92	52	30	5.63	4.960	0.8810	0.052	1.490	0.43
12	70	58	35	6.2	4.960	0.8000	0.058	2.015	0.55
13	85	44	40	6.4	4.960	0.7750	0.044	1.629	0.65
14	75	47	34	6.93	4.960	0.7157	0.047	2.040	0.57
						Average V_{ss}=0.7628	**Average C_D =**	**2.204**	

Settling velocities of rock sample 0.053-0.075 m

Stone number	a (mm)	b (mm)	c (mm)	Settling time (s)	Water depth (mm)	Settling velocity (m/s)	D (dimension b in (m))	C_D	Corey shape factor
1	94	55	36	6.37	4.905	0.7700	0.055	2.063	0.501
2	96	65	30	5.33	4.905	0.9203	0.065	1.707	0.380
3	94	63	32	5.29	4.905	0.9272	0.063	1.629	0.416
4	86	55	34	6.06	4.905	0.8094	0.055	1.867	0.494
5	84	59	36	5.95	4.905	0.8244	0.059	1.930	0.511
6	109	80	49	5.73	4.905	0.8560	0.08	2.428	0.525
7	86	58	36	5.93	4.905	0.8272	0.058	1.885	0.510
8	76	60	50	5.06	4.905	0.9694	0.06	1.420	0.740
9	82	74	51	6.29	4.905	0.7798	0.074	2.706	0.655
10	110	60	32	5.4	4.905	0.9083	0.06	1.617	0.394
11	105	57	30	5.36	4.905	0.9151	0.057	1.514	0.388
12	111	89	43	7.18	4.905	0.6831	0.089	4.241	0.433
13	87	78	40	6.61	4.905	0.7421	0.078	3.150	0.486
14	87	60	38	5.53	4.905	0.8870	0.06	1.696	0.526
15	86	76	32	6.82	4.905	0.7192	0.076	3.267	0.396
16	102	89	36	5.7	4.905	0.8605	0.089	2.673	0.378
17	103	72	44	5.57	4.905	0.8806	0.072	2.065	0.511
18	112	77	38	6.5	4.905	0.7546	0.077	3.007	0.409
						Average V_{ss}= 0.8352	**Average C_D =**	**2.270**	

Appendix C: Grading Curve Data and Coefficients of Uniformity

Sieve Analysis Data Sheet 1 (D_{50}= 0.038 m)

Project name:	**Determination of the Critical Incipient Failure Conditions of Angular Riprap Dumped on Wide & Steep Trapezoidal Channels**	**Tested By:**	M.Appolus
Location:	Stellenbosch University	**Checked By:**	M.Appolus
Riprap Layer Depth:	95mm	**D_{50}**	0.038 m

Ideal Grading		**Designed Grading**	
Diameter (mm)	**Soil Passing (%)**	**Soil Passing (%)**	**Sieve Aperture (mm)**
76.00	100.0	100	75.00
38.00	50.0	74	53.00
19.00	20.0	50	37.00
9.50	0.0	34	26.50
		20	19.000
		10	13.2
		0	9.5

D_{10}:	13.2	$(\frac{D_{85}}{D_{15}})$ =**C_u:**	3.33	The coefficient of Uniformity (C_u)in terms of D_{10} and D_{60}
D_{30}:	25	$(\frac{D_{85}}{D_{30}})$ = **C_c:**	1.76	
D_{60}:	44			
D_{15}:	17	$(\frac{D_{85}}{D_{15}})$ =**C_u:**	3.76	The coefficient of Uniformity (C_u)in terms of D_{15} and D_{85}
D_{50}:	38	$(\frac{D_{85}}{D_{50}})$ = **C_c:**	1.68	
D_{85}:	64			

C_u =Coefficient of Uniformity &

C_c =Grading Length Ratio

Sieve Analysis Data Sheet 2 (D_{50}= 0.075 m)

Project name:	**Determination of the Critical Incipient Failure Conditions of Angular Riprap Dumped on Wide & Steep Trapezoidal Channels**	**Tested By:**	M.Appolus
Location:	Stellenbosch University	**Checked By:**	M.Appolus
Riprap Layer Depth:	185mm	**D_{50}**	0.075 m

Ideal Grading		**Designed Grading**	
Sieve Aperture (mm)	**Soil Passing (%)**	**Sieve Aperture (mm)**	**Soil Passing (%)**
150.00	100.0	150.00	100
75.00	50.0	100.00	70
38	20.0	75.00	50
19.00	0	53.00	35
		37.00	20
		19.000	0

D_{10}:	28	$(\frac{D_{85}}{D_{15}})$ =**C_u:**	3.14	The coefficient of Uniformity (C_u) in terms of D_{10} and D_{60}
D_{30}:	49	$(\frac{D_{85}}{D_{50}})$ = **C_c:**	1.796	
D_{60}:	88			
D_{15}:	33	$(\frac{D_{85}}{D_{15}})$ =**C_u:**	3.73	The (C_u) in terms of D_{15} and D_{85}
D_{50}:	75	$(\frac{D_{85}}{D_{50}})$ = **C_c:**	1.64	
D_{85}:	123			

C_u = Coefficient of Uniformity &
C_c = Grading Length Ratio

Appendix D: Average Water Depth and Slope in the riprap local failure regions

Test series One | Model One

Test 1			Test 2			Test 3		
Profile	**Average Bed Slope**	**Average Water Depth (m)**	**Profile**	**Average Bed Slope**	**Average Water Depth (m)**	**Profile**	**Average Bed Slope**	**Average Water Depth (m)**
1	0.545	0.0182	1	0.614	0.005	1	0.706	0.023
2	0.562	0.0225	2	0.672	0.014	2	0.398	0.030
3	0.499	0.0227	3	0.591	0.024	3	0.315	0.020
4	0.442	0.0188	4	0.514	0.029	4	0.469	0.014
5	0.566	0.0139	5	0.575	0.009	5	0.579	0.014
6	0.522	0.0170	6	0.640	0.018	6	0.231	0.010
7	0.539	0.0164	7	0.572	0.027	7	0.514	0.003
8	0.519	0.0160	8	0.481	0.030	8	0.559	0.004
9	0.649	0.0136	9	0.589	0.013	9	0.570	0.011
10	0.555	0.0201	10	0.707	0.023	10	0.326	0.008
11	0.570	0.0203	11	0.531	0.031	11	0.485	0.013
12	0.513	0.0207	12	0.431	0.028	12	0.346	0.011
13	0.750	0.0186	13	0.633	0.013	13	0.440	0.004
14	0.777	0.0355	14	0.645	0.020	14	0.496	0.022
15	0.562	0.0422	15	0.560	0.023	15	0.445	0.024
16	0.343	0.0349	16	0.495	0.021	16	0.404	0.017
17	0.550	0.0559	17	0.625	0.014	17	0.435	0.010
18	0.273	0.0442	18	0.561	0.016			
			19	0.554	0.015			
			20	0.524	0.015			

Test Series One | Model Two

Test 3		
Profile	**Average Bed Slope**	**Average Water Depth (m)**
1	0.415	0.010
2	0.401	0.015
3	0.376	0.015
4	0.342	0.012
5	0.536	0.006
6	0.451	0.012
7	0.414	0.014
8	0.384	0.012
9	0.545	0.009
10	0.523	0.015
11	0.329	0.014
12	0.385	0.010
13	0.385	0.012
14	0.376	0.010
15	0.414	0.008
16	0.432	0.006
17	0.284	0.015
18	0.293	0.008
19	0.434	0.003
20	0.460	0.004

Test Series One | Model Three

Test 1			Test 2			Test 3		
Profile	**Average Bed Slope**	**Average Water Depth (m)**	**Profile**	**Average Bed Slope**	**Average Water Depth**	**Profile**	**Average Bed Slope**	**Average Water Depth**
1	0.274	0.018	1	0.171	0.029	1	0.258	0.028
2	0.378	0.016	2	0.268	0.027	2	0.264	0.026
3	0.424	0.013	3	0.288	0.029	3	0.286	0.023
4	0.390	0.010	4	0.292	0.030	4	0.334	0.013
5	0.337	0.022	5	0.244	0.032	5	0.387	0.031
6	0.314	0.019	6	0.270	0.032	6	0.361	0.036
7	0.344	0.014	7	0.302	0.028	7	0.290	0.037
8	0.380	0.010	8	0.304	0.026	8	0.255	0.026
9	0.357	0.022	9	0.281	0.032	9	0.495	0.032
10	0.336	0.021	10	0.258	0.034	10	0.442	0.046
11	0.340	0.018	11	0.326	0.025	11	0.250	0.047
12	0.376	0.016	12	0.394	0.023	12	0.119	0.031
13	0.350	0.024	13	0.254	0.028	13	0.402	0.040
14	0.330	0.025	14	0.255	0.026	14	0.372	0.054
15	0.370	0.022	15	0.326	0.025	15	0.200	0.054
16	0.358	0.022	16	0.401	0.036	16	0.074	0.036
17	0.331	0.031	17	0.232	0.024	17	0.306	0.043
18	0.268	0.029	18	0.305	0.022	18	0.301	0.061
19	0.191	0.018	19	0.300	0.029	19	0.187	0.064
20	0.452	0.014	20	0.324	0.042	20	0.076	0.042

Test Series Two | Model One

Test 1			Test 2			Test 3			Test 4			Test 5		
Profile	**Average Bed Slope**	**Average Water Depth (m)**	**Profile**	**Average Bed Slope**	**Average Water Depth (m)**	**Profile**	**Average Bed Slope**	**Average Water Depth (m)**	**Profile**	**Average Bed Slope**	**Average Water Depth (m)**	**Profile**	**Average Bed Slope**	**Average Water Depth (m)**
1	0.668	0.020	1	0.225	0.111	1	0.268	0.028	1	0.296	0.008	1	0.294	0.056
2	0.630	0.041	4	0.100	0.050	2	0.267	0.025	2	0.387	0.007	2	0.250	0.050
3	0.531	0.055	5	0.286	0.101	3	0.275	0.019	3	0.507	0.013	3	0.274	0.044
4	0.666	0.022	6	0.071	0.093	4	0.337	0.015	4	0.581	0.024	4	0.279	0.040
5	0.655	0.043	7	0.051	0.073	5	0.128	0.014	5	0.267	0.005	5	0.293	0.047
6	0.582	0.058	8	0.144	0.054	9	0.147	0.006	6	0.354	0.005	6	0.292	0.047
7	0.582	0.007	9	0.209	0.092				7	0.475	0.011	7	0.281	0.047
8	0.646	0.025	10	0.207	0.084				8	0.544	0.014	8	0.287	0.045
9	0.652	0.044	11	0.213	0.072							9	0.307	0.043
10	0.617	0.059	12	0.231	0.057							10	0.305	0.045
11	0.557	0.009	13	0.082	0.105							11	0.284	0.044
12	0.637	0.025	14	0.231	0.089							12	0.302	0.043
13	0.649	0.044	15	0.267	0.075							13	0.297	0.037
14	0.600	0.058	16	0.269	0.062							14	0.297	0.036
15	0.556	0.010	17	0.120	0.104							15	0.295	0.035
16	0.646	0.024	18	0.268	0.089							16	0.316	0.035
17	0.643	0.045	19	0.284	0.075							17	0.262	0.049
18	0.583	0.059	20	0.285	0.063							18	0.238	0.044
												19	0.236	0.040
												20	0.275	0.036

Test Series Two | Model Two

Test 1			Test 2			Test 3			Test 4			Test 5		
Profile	**Average Bed Slope**	**Average Water Depth (m)**	**Profile**	**Average Bed Slope**	**Average Water Depth (m)**	**Profile**	**Average Bed Slope**	**Average Water Depth (m)**	**Profile**	**Average Bed Slope**	**Average Water Depth (m)**	**Profile**	**Average Bed Slope**	**Average Water Depth (m)**
1	0.319	0.038	1	0.225	0.023	1	0.293	0.032	1	0.213	0.007	1	0.319	0.066
2	0.212	0.032	2	0.228	0.020	2	0.288	0.033	2	0.589	0.022	2	0.229	0.059
3	0.270	0.026	3	0.330	0.018	3	0.266	0.032	3	0.267	0.018	3	0.316	0.052
4	0.302	0.023	4	0.480	0.021	4	0.282	0.027	4	0.217	0.010	4	0.296	0.047
5	0.339	0.030	5	0.214	0.024	5	0.288	0.025	5	0.570	0.017	5	0.264	0.064
6	0.202	0.023	6	0.230	0.018	6	0.293	0.027	6	0.504	0.030	6	0.185	0.054
7	0.302	0.020	7	0.345	0.014	7	0.296	0.028	7	0.322	0.022	7	0.294	0.043
8	0.338	0.020	8	0.456	0.014	8	0.302	0.026	8	0.264	0.019	8	0.293	0.036
9	0.371	0.024	9	0.229	0.024	9	0.286	0.025	9	0.430	0.023	9	0.254	0.051
10	0.220	0.019	10	0.253	0.017	10	0.299	0.026	10	0.411	0.031	10	0.228	0.044
11	0.375	0.018	11	0.336	0.011	11	0.324	0.027	11	0.360	0.022	11	0.287	0.036
12	0.396	0.022	12	0.392	0.008	12	0.334	0.025	12	0.299	0.021	12	0.326	0.031
13	0.447	0.028	13	0.233	0.026	13	0.285	0.028	13	0.339	0.024	13	0.277	0.042
14	0.186	0.023	14	0.258	0.017	14	0.304	0.028	14	0.333	0.029	14	0.270	0.039
15	0.465	0.020	15	0.258	0.017	15	0.342	0.029	15	0.338	0.026	15	0.304	0.036
16	0.474	0.028	16	0.345	0.003	16	0.364	0.028	16	0.312	0.025	16	0.288	0.033
17	0.385	0.034	17	0.240	0.027	17	0.291	0.035	17	0.319	0.028	17	0.293	0.041
18	0.226	0.027	18	0.261	0.017	18	0.307	0.029	18	0.283	0.030	18	0.300	0.038
19	0.483	0.025	19	0.307	0.007	19	0.347	0.025				19	0.342	0.038
20	0.461	0.032	20	0.317	0.001	20	0.394	0.023				20	0.244	0.036

Test Series Two | Model Three

Test 1			Test 2			Test 3			Test 4			Test 5		
Profile	**Average Bed Slope**	**Average Water Depth (m)**	**Profile**	**Average Bed Slope**	**Average Water Depth (m)**	**Profile**	**Average Bed Slope**	**Average Water Depth (m)**	**Profile**	**Average Bed Slope**	**Average Water Depth (m)**	**Profile**	**Average Bed Slope**	**Average Water Depth (m)**
1	0.409	0.041	1	0.401	0.033	1	0.238	0.038	1	0.334	0.009	1	0.229	0.042
2	0.409	0.046	2	0.313	0.041	2	0.144	0.035	2	0.388	0.019	2	0.435	0.047
3	0.334	0.045	3	0.398	0.048	3	0.316	0.028	4	0.148	0.070	3	0.073	0.041
4	0.297	0.043	4	0.397	0.057	4	0.406	0.030	5	0.354	0.025	4	0.109	0.062
5	0.420	0.043	5	0.370	0.036	5	0.194	0.042	6	0.243	0.030	5	0.109	0.054
6	0.414	0.051	6	0.379	0.048	6	0.138	0.033	7	0.772	0.047	6	0.109	0.045
7	0.324	0.052	7	0.348	0.056	7	0.324	0.028	8	0.205	0.063	7	0.241	0.039
8	0.292	0.052	8	0.338	0.062	8	0.418	0.033	9	0.339	0.020	8	0.165	0.058
9	0.429	0.046	9	0.316	0.042	9	0.174	0.044	10	0.216	0.023	9	0.168	0.053
10	0.421	0.055	10	0.420	0.057	10	0.140	0.033	11	0.638	0.031	10	0.171	0.048
11	0.337	0.057	11	0.296	0.070	11	0.336	0.028	12	0.315	0.043	11	0.612	0.057
12	0.279	0.058	12	0.281	0.075	12	0.426	0.036	13	0.232	0.009	12	0.227	0.056
13	0.466	0.052	13	0.526	0.038	13	0.193	0.041	14	0.222	0.011	13	0.185	0.056
14	0.458	0.063	14	0.490	0.061	14	0.163	0.030	15	0.516	0.016	14	0.142	0.051
15	0.324	0.063	15	0.252	0.075	15	0.336	0.028	16	0.395	0.024	15	0.506	0.057
16	0.251	0.059	16	0.238	0.078	16	0.426	0.036	17	0.133	0.017	16	0.267	0.059
17	0.517	0.065	17	0.501	0.050	17	0.196	0.033	18	0.148	0.017	17	0.175	0.059
18	0.481	0.073	18	0.462	0.064	18	0.202	0.025	19	0.447	0.020	18	0.277	0.051
19	0.300	0.072	19	0.231	0.074	19	0.307	0.024	20	0.465	0.027			
20	0.218	0.065	20	0.211	0.073	20	0.367	0.035						

Test Series Three | Model One

Test 1			Test 2			Test 3			Test 4			Test 5		
Profile	**Average Bed Slope**	**Average Water Depth (m)**	**Profile**	**Average Bed Slope**	**Average Water Depth (m)**	**Profile**	**Average Bed Slope**	**Average Water Depth (m)**	**Profile**	**Average Bed Slope**	**Average Water Depth (m)**	**Profile**	**Average Bed Slope**	**Average Water Depth (m)**
1	0.294	0.050	1	0.351	0.053	1	0.361	0.057	1	0.219	0.052	1	0.256	0.048
2	0.484	0.045	2	0.405	0.051	2	0.395	0.055	2	0.250	0.043	2	0.313	0.041
3	0.506	0.043	3	0.501	0.048	3	0.440	0.049	3	0.329	0.034	3	0.345	0.034
4	0.511	0.040	4	0.526	0.050	4	0.498	0.048	4	0.364	0.027	4	0.406	0.028
5	0.265	0.042	5	0.385	0.059	5	0.379	0.051	5	0.227	0.063	5	0.239	0.045
6	0.465	0.035	6	0.382	0.057	6	0.402	0.050	6	0.254	0.061	6	0.316	0.037
7	0.502	0.038	7	0.484	0.050	7	0.442	0.047	7	0.355	0.060	7	0.364	0.031
8	0.514	0.039	8	0.497	0.049	8	0.488	0.048	8	0.361	0.055	8	0.444	0.027
9	0.254	0.045	9	0.356	0.055	9	0.309	0.041	9	0.235	0.050	9	0.237	0.047
10	0.423	0.041	10	0.447	0.053	10	0.490	0.039	10	0.245	0.042	10	0.313	0.040
11	0.451	0.043	11	0.496	0.046	11	0.498	0.042	11	0.357	0.035	11	0.361	0.034
12	0.476	0.048	12	0.491	0.044	12	0.507	0.046	12	0.392	0.031	12	0.440	0.030
13	0.369	0.060	13	0.349	0.049	13	0.271	0.040	13	0.272	0.072	13	0.189	0.046
14	0.388	0.058	14	0.439	0.047	14	0.497	0.037	14	0.499	0.073	14	0.254	0.035
15	0.425	0.049	15	0.487	0.045	15	0.504	0.041	15	0.506	0.077	15	0.312	0.026
16	0.494	0.043	16	0.482	0.044	16	0.512	0.046	16	0.514	0.080	16	0.502	0.026
17	0.363	0.064	17	0.326	0.036	17	0.254	0.044	17	0.190	0.050	17	0.167	0.046
18	0.414	0.059	18	0.494	0.035	18	0.455	0.040	18	0.170	0.039	18	0.237	0.034
19	0.445	0.049	19	0.514	0.039	19	0.473	0.040	19	0.263	0.030	19	0.305	0.024
20	0.492	0.043	20	0.496	0.042	20	0.489	0.044	20	0.400	0.025	20	0.494	0.025

Test Series Three | Model Three

Test 1			Test 2			Test 3			Test 4			Test 5		
Profile	**Average Bed Slope**	**Average Water Depth (m)**	**Profile**	**Average Bed Slope**	**Average Water Depth (m)**	**Profile**	**Average Bed Slope**	**Average Water Depth (m)**	**Profile**	**Average Bed Slope**	**Average Water Depth (m)**	**Profile**	**Average Bed Slope**	**Average Water Depth (m)**
1	0.412	0.077	1	0.335	0.093	1	0.345	0.086	1	0.313	0.106	1	0.480	0.066
2	0.484	0.084	2	0.317	0.091	2	0.530	0.093	2	0.489	0.109	2	0.678	0.085
3	0.254	0.079	3	0.520	0.093	3	0.118	0.088	3	0.288	0.107	3	0.306	0.089
4	0.169	0.069	4	0.128	0.088	4	0.258	0.072	4	0.032	0.089	4	0.374	0.083
5	0.416	0.079	5	0.355	0.099	5	0.321	0.096	5	0.223	0.111	5	0.884	0.077
6	0.515	0.086	6	0.298	0.098	6	0.402	0.098	6	0.578	0.111	6	0.317	0.100
7	0.238	0.082	7	0.460	0.097	7	0.278	0.093	7	0.422	0.113	7	0.339	0.093
8	0.255	0.072	8	0.267	0.091	8	0.322	0.112	8	0.217	0.103	8	0.388	0.087
9	0.380	0.085	9	0.451	0.109	9	0.322	0.112	9	0.371	0.123	9	0.343	0.078
10	0.413	0.088	10	0.376	0.119	10	0.384	0.090	10	0.196	0.123	10	0.802	0.092
11	0.300	0.084	11	0.056	0.104	11	0.363	0.083	11	0.264	0.111	11	0.247	0.094
12	0.336	0.074	12	0.363	0.087	12	0.247	0.116	12	0.341	0.104	12	0.376	0.085
13	0.245	0.100	13	0.374	0.121	13	0.122	0.107	13	0.357	0.131	13	0.314	0.088
14	0.040	0.085	14	0.282	0.123	14	0.236	0.095	14	0.079	0.129	14	0.729	0.101
15	0.373	0.076	15	0.110	0.110	15	0.270	0.088	15	0.180	0.113	15	0.341	0.105
16	0.395	0.069	16	0.249	0.094	16	0.276	0.123	16	0.305	0.104	16	0.317	0.093
17	0.145	0.098	17	0.262	0.133	17	0.291	0.118	17	0.257	0.140	17	0.487	0.106
18	0.031	0.077	18	0.262	0.126	18	0.247	0.112	18	0.187	0.130	18	0.606	0.113
19	0.274	0.066	19	0.259	0.119	19	0.199	0.101	19	0.199	0.119	19	0.396	0.115
20	0.410	0.063	20	0.235	0.110				20	0.208	0.107	20	0.228	0.108

Appendix E: MN Analysis for Physical Model

The Spreadsheet Used to Calculate MN for Test Series One

Input Values				
D_{50}	0.038	m		
ρ_r	2700	kg/m3		
ρ_w	1000	kg/m3		
V_{ss}	0.6393	m/s		
$\phi_{Repose\ (riprap)}$	40	°	0.698	Radians
$\alpha_{Angle\ (side)}$		°	0.380	Radians
$\alpha_{Slope\ (side)}$	0.4			
$\beta_{Angle\ (bed)}$		°	0.462	Radians
$\beta_{Slope\ (bed)}$	0.500			
g	9.81	m/s^2		
S_o	0.50			
$D_{water\ depth}$	0.026	m		
v	0.00000113	m^2/s at 15 °		

$$\sqrt{k_\beta . k_\alpha} . \frac{\sqrt{gDS_o}}{V_{ss}} = MN$$

k_β = Steep angle correction factor

k_α = Side Slope Correction factor

K_β	K_α	Correction factor	$\sqrt{(gD_wS_o)}$	V_{ss}	MN	$(V*D_{50})/v$
0.359	1.000	0.599	0.354	0.639	0.331	11893

The spreadsheet above was used to individually calculate the MN for each water depth and slope data point from **Appendix E**, Test series one tests. The MN with the side correction factor of one was taken to be the correct MN for Test series one tests. The strikethrough values were not used as inputs in the calculation

Summary of MN and Re* Results For Test Series One Tests

P1M1T1		P1M1T2		P1M1T3		P1M2T3		P1M3T1		P1M3T2		P1M3T3	
MN	**Re***	**MN**	**Re***	**MN**	**Re***	**MN**	**Re***	**MN**	**Re***	**MN**	**Re***	**MN**	**Re***
0.271	10487	0.124	5544	0.235	13476	0.217	6908	0.274	7468	0.296	7436	0.334	8983
0.296	11846	0.2	10326	0.369	11493	0.264	8239	0.266	8097	0.33	8958	0.323	8747
0.311	11160	0.229	9688	0.36	10225	0.263	7974	0.267	8577	0.336	9292	0.33	9089
0.292	9611	0.352	12925	0.251	8587	0.233	6794	0.216	6655	0.356	9870	0.24	6943
0.232	9348	0.184	7540	0.23	9517	0.161	6142	0.311	9020	0.351	9317	0.379	11620
0.267	9915	0.24	11371	0.191	5008	0.236	7869	0.286	8111	0.361	9805	0.406	12090
0.258	9899	0.324	13198	0.105	3861	0.255	8085	0.248	7260	0.346	9693	0.393	10880
0.259	9593	0.362	12622	0.123	4887	0.237	7249	0.218	6633	0.332	9317	0.321	8599
0.204	9914	0.217	9139	0.202	8197	0.19	7376	0.313	9281	0.362	9943	0.374	13297
0.282	11122	0.231	13356	0.192	5514	0.254	9461	0.308	8914	0.364	9794	0.455	14988
0.279	11316	0.359	13570	0.24	8401	0.252	7240	0.282	8218	0.33	9458	0.428	11426
0.296	10860	0.357	11600	0.225	6610	0.208	6385	0.271	8203	0.324	10021	0.264	6410
0.181	12454	0.208	9678	0.134	4389	0.237	7269	0.329	9671	0.329	8816	0.427	13354
0.22	17487	0.25	11997	0.31	11045	0.218	6609	0.33	9511	0.318	8538	0.493	14875
0.406	16225	0.303	12071	0.326	10796	0.188	5978	0.313	9422	0.331	9506	0.426	10924
0.394	11512	0.299	10647	0.28	8769	0.172	5576	0.313	9299	0.403	12589	0.228	5395
0.473	18457	0.218	9947	0.208	6785	0.246	6770	0.371	10704	0.298	7836	0.427	12024
0.425	11576	0.251	10013			0.179	4973	0.34	9223	0.306	8600	0.509	14255
		0.243	9547			0.125	4083	0.245	6234	0.35	9795	0.455	11555
		0.251	9350			0.134	4536	0.247	8246	0.427	12229	0.251	5944

The Spreadsheet Used to Calculate MN for Test Series Two

Input Values				
D_{50}	0.075	m		
ρ_r	2700	kg/m3		
ρ_w	1000	kg/m3		
V_{ss}	0.8352	m/s		
$\phi_{Repose\ (riprap)}$	40	°	0.698	Radians
$\alpha_{Angle\ (side)}$		°	0.380	Radians
$\alpha_{Slope\ (side)}$	0.4			
$\beta_{Angle\ (bed)}$		°	0.462	Radians
$\beta_{Slope\ (bed)}$	0.500			
g	9.81	m/s^2		
S_o	0.50			
$D_{water\ depth}$	0.056	m		
v	0.00000113	m^2/s at 15 °		

k_β Steep angle correction factor

k_α Side Slope Correction factor

$$\sqrt{k_\beta . k_\alpha} . \frac{\sqrt{g D_w S_0}}{V_{ss}} = MN$$

k_β	k_α	Correction factor	$\sqrt{(gD_wS_o)}$	V_{ss}	MN	$(V*D_{50})/v$
0.359	1.000	0.599	0.524	0.835	0.376	34785

For Test series two, a similar MN calculating spreadsheet was used to calculate the movability MN and respective Re_* ($(V*D_{50})/v$). Similarly, with Test series one test results, the MN with no side slope effect was used to define the incipient motion of riprap in Test series two. Test series two used large riprap median stone size

Summary of MN and Re* Results for Test Series Two Tests

P2M1T1		P2M1T2		P2M1T3		P2M1T4		P2M1T5	
MN	Re*	MN	Re*	MN	Re*	MN	Re*	MN	Re*
0.184	24240	0.486	32812	0.256	17904	0.144	10313	0.373	26697
0.198	23523	0.236	14633	0.243	16987	0.138	10897	0.339	23307
0.366	35601	0.498	35401	0.245	17236	0.133	12471	0.347	24396
0.191	25017	0.278	16943	0.196	14661	0.228	24341	0.311	21970
0.273	34686	0.209	12624	0.14	8821	0.108	7545	0.342	24481
0.356	38150	0.288	18324	0.098	6248	0.116	8832	0.34	24352
0.122	13067	0.432	28749			0.167	14850	0.336	23760
0.212	26275	0.411	27316			0.184	18330	0.331	23566
0.28	35348	0.384	25682					0.327	23751
0.343	39669	0.353	23908					0.334	24237
0.142	14450	0.314	19249					0.329	23339
0.215	26048	0.44	29861					0.33	23834
0.28	34982	0.421	29447					0.304	21868
0.347	38691	0.384	26869					0.298	21404
0.149	15195	0.371	23233					0.296	21210
0.209	25965	0.459	32115					0.301	22001
0.286	35229	0.427	30324					0.34	23622
0.358	38454	0.393	27936					0.31	21167
								0.296	20156
								0.294	20685

P2M2T1		P2M2T2		P2M2T3		P2M2T4		P2M2T5	
MN	Re*	MN	Re*	MN	Re*	MN	Re*	MN	Re*
0.312	22934	0.223	15053	0.283	20232	0.122	8150	0.41	30077
0.258	17232	0.206	13944	0.283	20189	0.218	23662	0.358	24233
0.278	19471	0.226	16786	0.278	19376	0.205	14343	0.389	28488
0.239	17282	0.234	20931	0.256	18174	0.146	9760	0.34	24446
0.278	20832	0.223	14921	0.246	17545	0.197	20629	0.388	27024
0.216	14295	0.195	13229	0.259	18530	0.276	25709	0.319	20834
0.222	16006	0.19	14331	0.263	18883	0.24	17682	0.328	23510
0.227	17029	0.194	16826	0.253	18243	0.21	14665	0.3	21489
0.255	19797	0.229	15476	0.246	17463	0.245	20453	0.343	23670
0.2	13467	0.197	13605	0.255	18388	0.287	23421	0.308	20848
0.219	17093	0.168	12563	0.264	19485	0.242	18581	0.296	21084
0.243	19438	0.144	11488	0.257	19188	0.227	16355	0.282	20890
0.272	23270	0.237	16102	0.259	18422	0.251	18863	0.317	22345
0.208	13589	0.199	13800	0.265	19159	0.274	20419	0.305	21354
0.231	20240	0.199	13800	0.277	20865	0.258	19319	0.299	21641
0.271	24107	0.091	6891	0.272	21010	0.251	18278	0.282	20124
0.301	23802	0.245	16727	0.292	20868	0.265	19492	0.317	22717
0.241	16271	0.197	13725	0.271	19685	0.27	19144	0.308	22210
0.255	23001	0.131	9532	0.256	19369			0.314	23613
0.291	25402			0.246	19673			0.284	19461

P2M3T1		P2M3T2		P2M3T3		P2M3T4		P2M3T5	
MN	Re*	MN	Re*	MN	Re*	MN	Re*	MN	Re*
0.33	26820	0.296	23854	0.292	19894	0.155	11575	0.303	20501
0.351	28540	0.324	23663	0.231	14710	0.227	18011	0.336	28232
0.346	25778	0.333	26691	0.297	21771	0.332	21194	0.186	11361
0.326	23431	0.389	31131	0.284	23035	0.259	19709	0.275	17110
0.339	27976	0.309	24016	0.285	18737	0.258	17675	0.257	15996
0.369	30225	0.356	27904	0.223	14125	0.2	39690	0.234	14572
0.366	26991	0.384	29096	0.267	19687	0.357	23681	0.295	20157
0.358	25602	0.402	30079	0.299	24564	0.228	17121	0.314	20273
0.35	29214	0.328	24037	0.281	18210	0.217	14521	0.305	19714
0.384	31726	0.39	32169	0.222	14052	0.241	29389	0.292	18931
0.386	28900	0.416	29891	0.268	20004	0.331	24219	0.339	38716
0.375	26473	0.426	30124	0.31	25796	0.142	9644	0.345	23321
0.367	32231	0.304	29365	0.28	18444	0.153	10319	0.323	21151
0.406	35288	0.394	35905	0.225	14466	0.196	18648	0.28	17755
0.403	29753	0.415	28614	0.268	20004	0.255	20409	0.379	35394
0.366	25221	0.415	28271	0.31	25796	0.158	9968	0.373	26069
0.402	38218	0.355	32961	0.254	16766	0.163	10365	0.326	21146
0.433	38888	0.411	35853	0.222	14668	0.23	19662	0.351	24775
0.423	30495	0.4	27112	0.248	17995	0.266	23320		
0.369	24757	0.388	25892	0.302	23384				

Summary of MN and Re$_*$ results for Test series Three Tests

The same Excel spreadsheet in Test series two tests are shown above was used to determine the MN and respective Re$_*$ for Test series three Tests. However, the MN number of results obtained from the spreadsheet accounted for the side slope correction factor.

Input Values				
D_{50}	0.075	m		
ρ_r	2700	kg/m3		
ρ_w	1000	kg/m3		
V_{ss}	0.8352	m/s		
$\phi_{Repose\ (riprap)}$	40	°	0.698	Radians
$\alpha_{Angle\ (side)}$		°	0.380	Radians
$\alpha_{Slope\ (side)}$	0.4			
$\beta_{Angle\ (bed)}$		°	0.462	Radians
$\beta_{Slope\ (bed)}$	0.500			
g	9.81	m/s^2		
S_o	0.50			
$D_{water\ depth}$	0.056	m		
v	0.00000113	m^2/s at 15 °		

k_β Steep angle correction factor

k_α Side Slope Correction factor

$$\sqrt{k_\beta . k_\alpha} . \frac{\sqrt{g D_w S_0}}{V_{ss}} = MN$$

k_β	k_α	Correction factor	$\sqrt{(gD_wS_o)}$	V_{ss}	MN	$(V*D_{50})/v$
0.359	0.817	0.541	0.524	0.835	0.340	34785

P3M1T1		P3M1T2		P3M1T3		P3M1T4		P3M1T5	
MN	Re*	MN	Re*	MN	Re*	MN	Re*	MN	Re*
0.317	25128	0.338	28405	0.351	29800	0.299	22228	0.300	22966
0.308	30788	0.335	29943	0.347	30646	0.283	21600	0.290	23456
0.305	31497	0.325	33337	0.345	32366	0.302	24773	0.295	24611
0.284	29605	0.315	33674	0.313	31991	0.241	20567	0.249	22321
0.283	21865	0.359	31371	0.334	29014	0.332	24826	0.284	21461
0.271	26350	0.352	30710	0.331	29530	0.338	25844	0.277	22474
0.280	28747	0.324	32418	0.320	30068	0.361	30461	0.259	22120
0.279	29240	0.318	32362	0.315	31704	0.344	29193	0.243	22912
0.289	22092	0.343	28953	0.291	23388	0.301	22608	0.292	22020
0.297	27231	0.339	32054	0.283	28540	0.279	21135	0.286	23135
0.304	28974	0.310	31524	0.295	30108	0.274	23145	0.272	23160
0.317	31311	0.301	30407	0.307	31823	0.258	22769	0.257	24071
0.361	30965	0.323	27100	0.278	21572	0.375	29156	0.268	19486
0.354	31082	0.320	29970	0.277	28218	0.389	39741	0.256	19613
0.325	29865	0.307	30758	0.288	29733	0.396	40953	0.232	18738
0.298	30258	0.304	30308	0.305	31807	0.403	42251	0.229	23553
0.372	31739	0.275	22524	0.288	22006	0.278	20168	0.255	18235
0.360	32580	0.270	27396	0.292	27938	0.237	17002	0.247	18653
0.327	30819	0.282	29566	0.293	28766	0.239	18411	0.222	17770
0.300	30297	0.296	30070	0.304	30591	0.235	20874	0.227	23042

P3M3T1		P3M3T2		P3M3T3		P3M3T4		P3M3T5	
MN	**Re***	**MN**	**Re***	**MN**	**Re***	**MN**	**Re***	**MN**	**Re***
0.410	37091	0.444	36674	0.430	35896	0.469	37909	0.373	36974
0.419	41801	0.436	35359	0.429	46196	0.478	48073	0.333	49843
0.396	30275	0.428	45270	0.315	21804	0.468	36925	0.417	33471
0.314	22447	0.317	22093	0.369	28289	0.169	11155	0.426	36739
0.414	37566	0.461	38938	0.447	36426	0.440	32758	0.456	37004
0.418	43820	0.446	35541	0.463	41289	0.448	52686	0.445	36881
0.385	29035	0.457	43994	0.427	33372	0.497	45484	0.436	38206
0.367	28075	0.419	32429	0.485	39521	0.419	31099	0.407	33897
0.430	37360	0.485	46136	0.485	39521	0.517	44487	0.208	56553
0.439	39707	0.508	43932	0.444	38754	0.443	32313	0.417	31686
0.413	32914	0.237	15851	0.424	36085	0.461	35541	0.429	37101
0.398	32890	0.433	36861	0.463	35192	0.470	39128	0.428	34640
0.429	32558	0.512	44192	0.342	23732	0.532	44972	0.316	56497
0.182	12093	0.494	38750	0.414	31176	0.310	20950	0.473	39335
0.405	34913	0.331	22816	0.413	32038	0.410	29583	0.440	35675
0.389	34435	0.418	31780	0.492	38393	0.462	37060	0.471	47263
0.352	24761	0.504	38838	0.488	38597	0.514	39370	0.436	54444
0.154	10205	0.491	37802	0.454	34497	0.448	32451	0.500	44297
0.360	28010	0.475	36462	0.404	29511	0.437	31929	0.435	32532
0.371	33446	0.443	33347			0.422	31065		

Appendix F: Basic Statistics for MN of Laboratory Tests

Test Series One

	P1M1T1	P1M1T2	P1M1T3	P1M2T3	P1M3T1	P1M3T2	P1M3T3
First Quartile	0.258	0.218	0.192	0.186	0.262	0.328	0.323
Min	0.181	0.124	0.105	0.125	0.216	0.296	0.228
Median	0.281	0.247	0.230	0.226	0.284	0.334	0.386
Mean	0.297	0.260	0.234	0.213	0.287	0.343	0.373
Max	0.473	0.362	0.369	0.264	0.371	0.427	0.509
Third Quartile	0.307	0.308	0.280	0.248	0.313	0.357	0.427
Standard Dev	0.077	0.064	0.075	0.041	0.040	0.031	0.082

Test Series Two

	P2M1T1	P2M1T2	P2M1T3	P2M1T4	P2M1T5	P2M2T1	P2M2T2	P2M2T3
First Quartile	0.193	0.324	0.154	0.129	0.303	0.226	0.192	0.256
Min	0.122	0.209	0.098	0.108	0.294	0.200	0.091	0.246
Median	0.244	0.389	0.220	0.141	0.330	0.249	0.199	0.261
Mean	0.251	0.377	0.196	0.152	0.324	0.251	0.196	0.264
Max	0.366	0.498	0.256	0.228	0.373	0.312	0.245	0.292
Third Quartile	0.329	0.431	0.245	0.171	0.339	0.274	0.225	0.273
Standard Dev	0.079	0.080	0.059	0.037	0.021	0.031	0.038	0.013

	P2M2T4	P2M2T5	P2M3T1	P2M3T2	P2M3T3	P2M3T4	P2M3T5
First Quartile	0.212	0.300	0.351	0.332	0.244	0.180	0.283
Min	0.122	0.282	0.326	0.296	0.222	0.142	0.186
Median	0.244	0.316	0.368	0.389	0.274	0.228	0.310
Mean	0.232	0.324	0.372	0.372	0.268	0.230	0.306
Max	0.287	0.410	0.433	0.426	0.310	0.357	0.379
Third Quartile	0.263	0.341	0.390	0.404	0.293	0.259	0.338
Standard Dev	0.043	0.036	0.029	0.041	0.030	0.061	0.047

Test Series Three

	P3M1T1	P3M1T2	P3M1T3	P3M1T4	P3M1T5	P3M3T1	P3M3T2	P3M3T3	P3M3T4	P3M3T5
First Quartile	0.288	0.303	0.290	0.270	0.246	0.365	0.426	0.414	0.433	0.412
Min	0.271	0.270	0.277	0.235	0.222	0.154	0.237	0.315	0.169	0.208
Median	0.304	0.319	0.304	0.300	0.258	0.397	0.445	0.430	0.454	0.429
Mean	0.312	0.317	0.308	0.308	0.262	0.372	0.437	0.431	0.441	0.413
Max	0.372	0.359	0.351	0.403	0.300	0.439	0.512	0.492	0.532	0.500
Third Quartile	0.326	0.335	0.323	0.348	0.285	0.415	0.486	0.463	0.472	0.442
Standard Dev	0.029	0.024	0.023	0.054	0.024	0.074	0.068	0.047	0.078	0.065

Appendix G: Design Example using the Riprap Excel Design Tool

Riprap Design Example

The following design scenario was used as an example to illustrate how to design riprap dumped in steep bed and side bank slopes of trapezoidal cross-sectional channels using the Excel Design Tool with interface shown in **Appendix H**.

For this riprap design example, the following material properties assumptions apply:

- Angular riprap rock used ($C_D = 2.17$)
- Hornfels material used for the riprap ($\rho_r = 2700$ kg/m^3)
- Water at room temperature flowing through the channel ($\rho_w = 1000$ kg/m^3)

1. Channel Geometry of the HEC-RAS model

The main geometric components of the straight trapezoidal channel for the design example was as shown in **Figure F1:**

Longitudinal Profile:

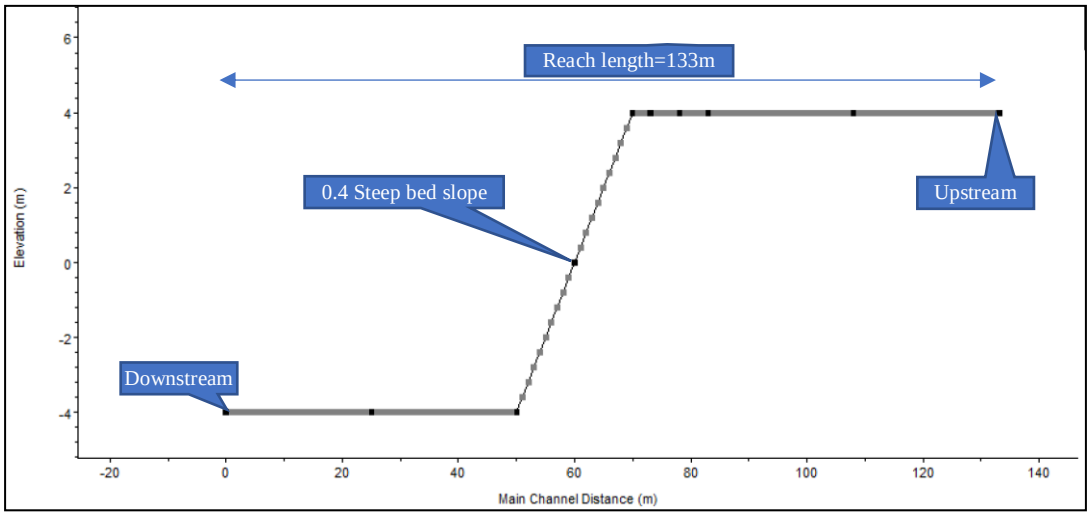

Figure F1: Longitudinal profile of the channel

The downstream 0% slope channel section was 50 m long, the 40% (0.4) steep bed slope section was 20 m long and the upstream 0.0001% slope was 63 m long. Thus, making a total channel length of 133 m.

Cross-Sectional Profile:

A similar geometric cross-sectional profile was used throughout the length (133 m) of the channel, from upstream to downstream. The cross-sectional profile dimensions can be found in **Figure F2**:

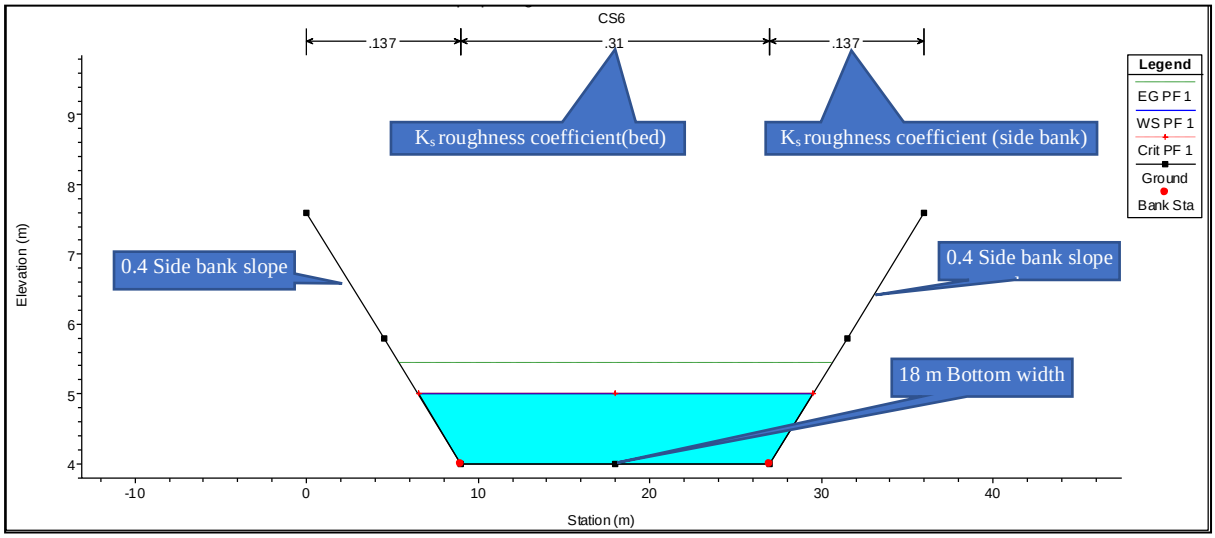

Figure F2: Showing the channel cross-sectional components and main dimensions

Perspective view of the channel

The finished HEC-RAS model geometry of the channel looked like the one shown in **Figure F3.** With the longitudinal and cross-sectional profiles as shown in **Figure F1** and **Figure F2** above:

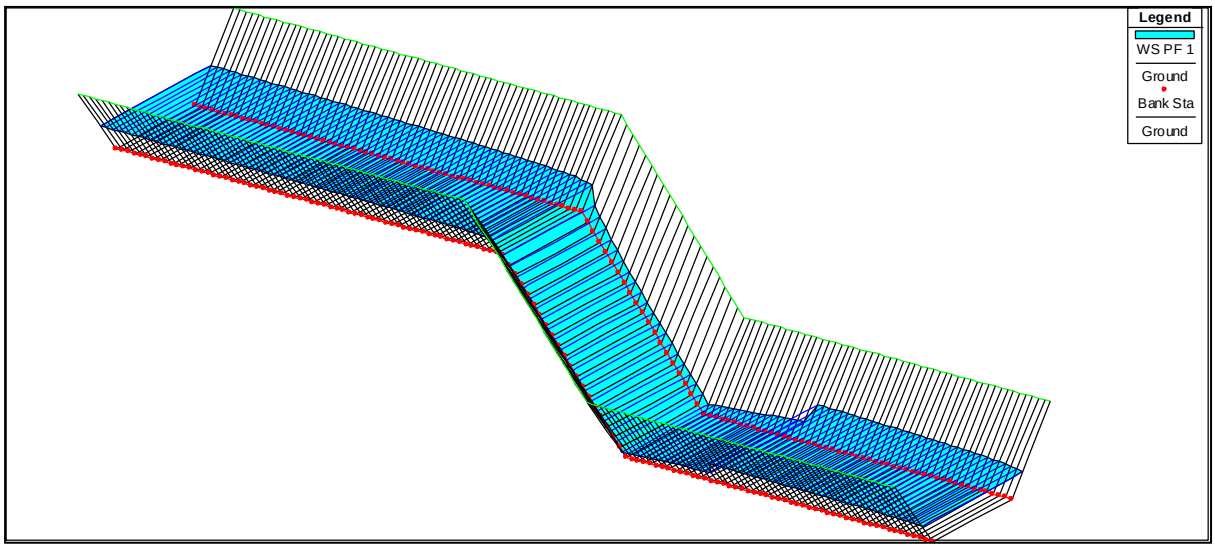

Figure F3: Perspective view of the complete channel geometric model from HEC-RA

2. Steady state data for HEC-RAS model

After modelling the HEC-RAS geometric model, the steady-state input data was required. There were two main data required for the steady state flow analysis; the first one was the design flow rate and the second was the reach boundary conditions. For this example, three design flow rate data were considered, the design flow rates were:

- 40 m^3/s
- 30 m^3/s
- 20 m^3/s

For the boundary conditions, there were four possible choices to choose from HEC-RAS. However, the designer's choice was limited to the available boundary conditions data. For this example, since there were no known surface water elevations or flow rate curves available, the designer chose to use the normal depth boundary condition for the upstream section (assumed a slope of 0.0001, since HEC-RAS does not allow 0% input slope for this boundary condition). Thereafter, the boundary condition chosen for the downstream section was the critical depth.

3. HEC-RAS model Results

For each of the three design flow rates, simulations were computed individually. For example, in the 40 m^3/s case; the D_{50} median riprap for the bed and side banks were assumed and inserted on the Excel Riprap Design Tool in the green coloured input cells shown in **Appendix H**. The Excel Design Tool automatically calculates the k_s roughness coefficient based on the assumed D_{50}. The initial roughness coefficient was applied on the bed and on the side bank of the HEC-RAS geometric model. After the roughness coefficients for the bed and the side bank were applied, then a simulation for the water depth was run on HEC-RAS. The typical HECRAS longitudinal profile output was as shown in **Figure F4**:

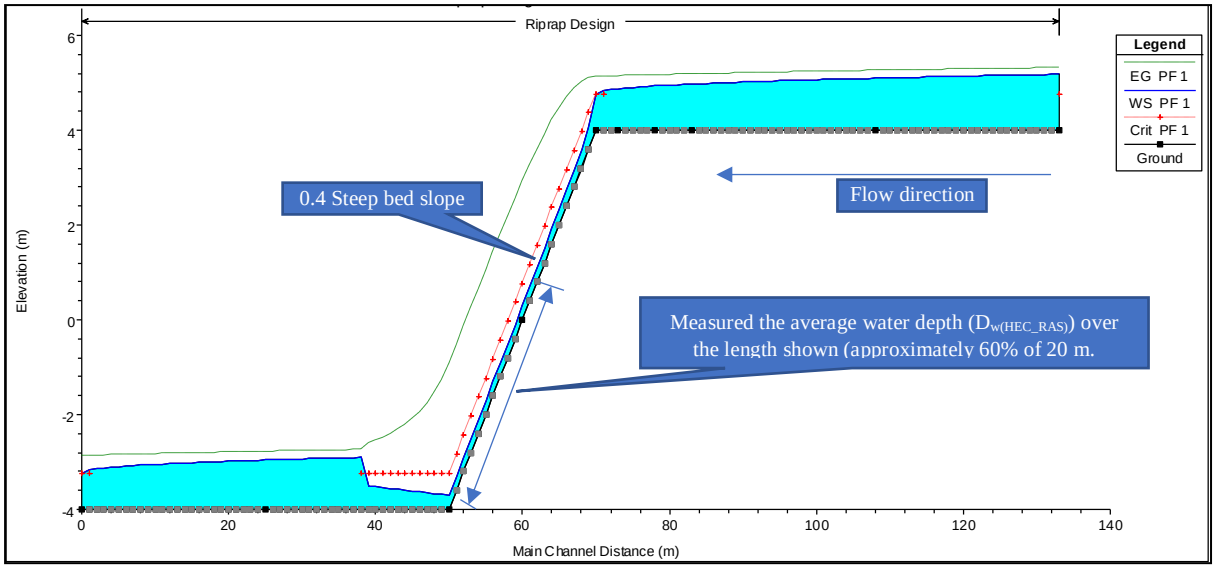

Figure F4: Typical HEC-RAS model simulation longitudinal profile output.

4. Excel Design Tool Results

After the HECRAS model was run once, the designer exported the HEC-RAS longitudinal profile to AUTOCAD (ensure that the export to AUTOCAD scale ratio is 1:1). The average water depth on the steep slope was measured perpendicular to the steep bed slope. The average water depth was measured over a 60% length of the steep bed slope (0.4), from the bottom (toe) of the steep bed slope. The average water depth was then used as an input variable (green cells in **Appendix H**, in **step 3**) into the Excel Design Tool for both the steep bed riprap design and the side bank riprap design. The solver function of the excel sheet was then applied to determine the actual D_{50} for both the bed and side bank slope. After applying the solver function, the Excel Design Tool calculates the new D_{50} (which will be very close to the required design D_{50}). With the new D_{50} provided by the solver function, then a new iteration is required, since the roughness coefficient changes. Repeating the process by changing the k_s roughness coefficient on HEC-RAS until the water depth simulated by HEC-RAS does no longer change. When the water depth and k_s does not change, then the D_{50} for the bed was regarded as the final solution. The D_{50} may be determined manually by guessing D_{50} (green cells shown in **Appendix H**, in **step 1**) and using the SAFE MN value guidelines stipulated at the bottom of the spreadsheet in **step 3** of **Appendix H**).

Following the above procedure for all the three flow rates (40 m^3/s, 30 m^3/s, 20 m^3/s), the following summary of results was produced from the design example after all the simulations and iterations:

Table F1: A summary of the main Excel Design Tool and HEC-RAS results.

Q (flow rate)	(m^3/s)	40		30		20	
Riprap Position		**Bed**	**Side bank**	**Bed**	**Side bank**	**Bed**	**Side Bank**
$D_{w(HEC-RAS)}$	(m)	0.297	0.297	0.245	0.245	0.188	0.188
B_s or T_s	(m)	2.570	1.170	2.120	0.970	1.630	0.740
D_{50}	(m)	1.028	0.470	0.848	0.390	0.651	0.300
K_s		0.325	0.148	0.268	0.122	0.206	0.094
$D_{50(Bed)}/D_{50(sidebank)}$		2.19		2.17		2.17	

The results in the table above were based on the riprap Excel Design Tool calculations, therefore the main symbols used were defined in the Excel Design Tool in **Appendix H**. From the results above, applying the Excel Design Tool for the flow rate of 40 m^3/s in the channel geometry described (in section **1.** of this design example**)** produced a design D_{50} of 1.028m for the steep bed region. The D_{50} of 1.028m was very close to the maximum D_{50} limit of application of 1.125m (described in the Excel Design Tool in **Appendix H**). In the case that D_{50} was greater than the 1.125 m limit, then the reliability of the results of the Excel Design Tool may not be guaranteed. Similarly, if the designed D_{50} rock size was less than 0.57 m, then the Excel Design Tool results, in that case, cannot be guaranteed to be reliable.

It can be seen from the results in the table above that the ratio of the designed bed D_{50} to the designed side bank D_{50} riprap was a constant of about 2.18 on average. In simple terms, the designed D_{50} riprap dumped on the steep bed was about two time the designed side bank D_{50} riprap.

5. Excel Design Tool Applicability Checks

5.1 The designed D_{50} median riprap sizes were within the acceptable prototype D_{50} median riprap sizes. All the D_{50} median riprap sizes were within the 0.57 m-1.125 m range.

5.2 Bottom width to D_{50} ratio checks, appropriate if (bottom width/D_{50}) = 16-31. The ratios were as follows for the design flow rates; 40 m^3/s, 30 m^3/s and 20 m^3/s, respectively:

- $\frac{Bottom\ width}{D_{50}} = \frac{18\ m}{1.028\ m} = 17.51$
- $\frac{Bottom\ width}{D_{50}} = \frac{18\ m}{0.848\ m} = 21.23$
- $\frac{Bottom\ width}{D_{50}} = \frac{18\ m}{0.651\ m} = 27.65$

Therefore, it can be concluded that all the three design D_{50} median riprap sizes were within the acceptable limit of the required bottom width and D_{50} ratio. The steep bed slope (0.4 in this design example) was within the applicable range of slopes 0.333-0.4. The steep side bank slope was also 0.4 as per requirement for the For the Excel Design Tool in **Appendix H**.

Therefore, it can be concluded that the results obtained were within the acceptable application limits specified in the riprap Excel Design Tool in **Appendix H**.

6. Recommended Cross Section Drawing

Figure F5 shows the recommended cross section design layout for the 40 m^3/s design flow rate, only. Similar layouts of cross-sections may be drawn for the 30 m^3/s and 20 m^3/s design flow rates scenarios but should be drawn according to the dimensions of the design results pertinent to those conditions. **Figure F5** illustrates how riprap may be designed and constructed to provide the required protection.

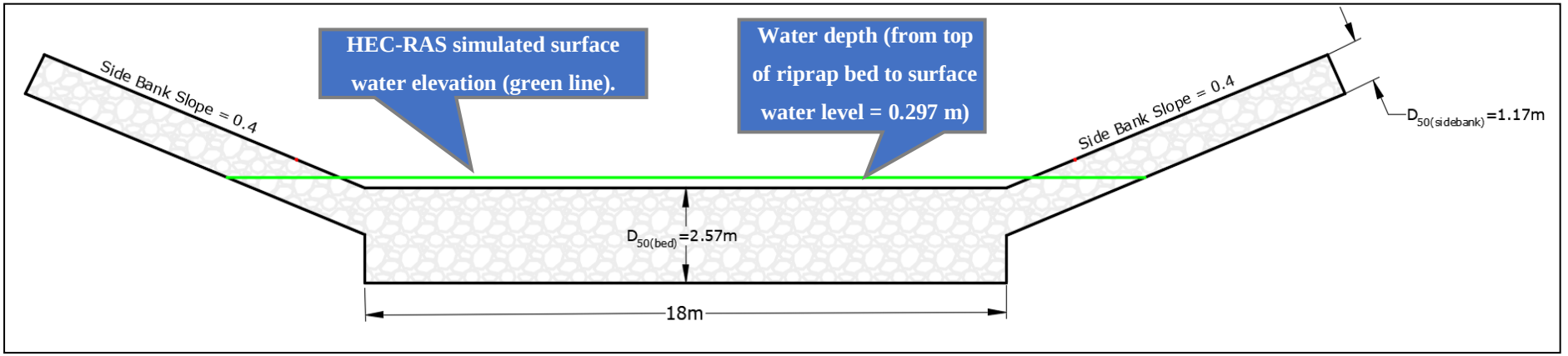

Figure F5: Typical cross section design drawing based on the calculated D_{50} sizes of the bed and side bank riprap for the cross-section.

For all the design results; shallow water depth flow is always anticipated over the steep bed area, for as long as; the riprap Excel Design Tool is applied within the specified applicable limits and the riprap over the steep bed area is designed for movable conditions. Higher water depth (higher resistance) may be achieved if the Engineer can design for a rough immovable riprap bed (if there is a method applied to ensure the riprap on the bed area will be fixed).

The Excel Design Tool has been linked to the word "Appendix H " above in this design example ,alternatively the Design Tool may be downloaded on the following website: https://16729870.wixsite.com/riprapdesign

Appendix H: Excel Spreadsheet Design Tool Interface

Design of Riprap Dumped on Steep Bed Slope: Worksheet 1

Project :

Designer : **Checked by:**

Date : **Date :**

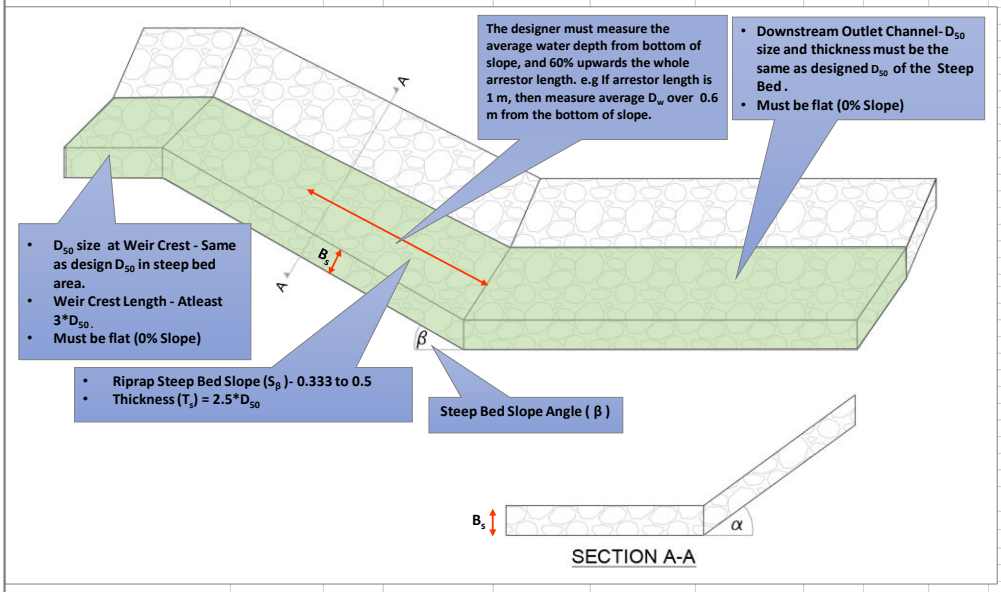

Note: Application limits

1. The applicability of the Excel Design Tool is limited to riprap dumped in straight trapezoidal cross sectional channels with steep beds ranging from 0.333 to 0.5, and with side bank slopes of 0.4. The results of this design tool are only valid for the design of prototype D_{50} stone size between stone 0.57 m and 1.125 m.

2. The designer must ensure that the bed bottom width to D_{50} (bed) ratio is between 16-31, since this was the range tested at the laboratory.

Legend

Input cells

Constant

Calculated parameter

1. Settling Velocity

$$V_{ss} = \sqrt{\frac{4}{3}\frac{(\rho_r - \rho_w)}{\rho_w} g D_{50} \frac{1}{C_D}}$$

= 2.583 m/s

ρ_w	1000	kg/m^3	ρ_w= Density of water
ρ_r	2700	kg/m^3	ρ_r= Density of riprap rock
g	9.81	m/s-2	C_D= Drag coefficient
D_{50}	0.651	m	D_{50}= Riprap median stone size (bed)
C_D	2.17	(This is a recommended Drag Coeffecient Value) , A smaller drag coeffecient may lead to underesized D_{50} specification	
B_s	1.63	m	B_s= Bed Riprap Thickness
K_s=	0.206		K_s= HEC-RAS roughness coefficient on the (bed)

2. Steep Bed Slope Correction Factor

$$k_\beta = \frac{Sin(\varphi_r - \beta)}{(Sin\ \varphi_r)}$$

= 0.475

$$\sqrt{k_\beta}$$

= 0.689

	Slope	Angle in radians	Angle in degrees	
ϕ_r	0.84	0.698	40	ϕ_r= Rock angle of repose
S_β	0.4	0.380	21.8	S_β = Bed Slope
				K_β= Steep Bed Slope Correction Factor

3. Determination of D_{50} from Critical MN (Bed)

$$\sqrt{K_\beta} \cdot \frac{\sqrt{g D_{w(HECRAS)} S_\beta}}{V_{ss}} = 0.12 * AF_{bed}$$

MN = 0.120

$D_{w(HECRAS)}$	0.188	m	Water Depth Calculated with HECRAS Steady flow analysis, Use K_s/D_{50}=0.316 for roughness coeffecient)
AF_{bed}	1.91		(HECRAS MN Adjustment Factor)

If MN > 0.12	Increase D_{50}
if MN = 0.12	SAFE
if MN < 0.12	SAFE
but, if MN significantly < 0.12	Decrease D_{50} until MN = 0.12

Design of Riprap Dumped on Steep Side Bank Slope: Worksheet 2

Project : _____

Designer : _____ **Checked by:** _____

Date : _____ **Date :** _____

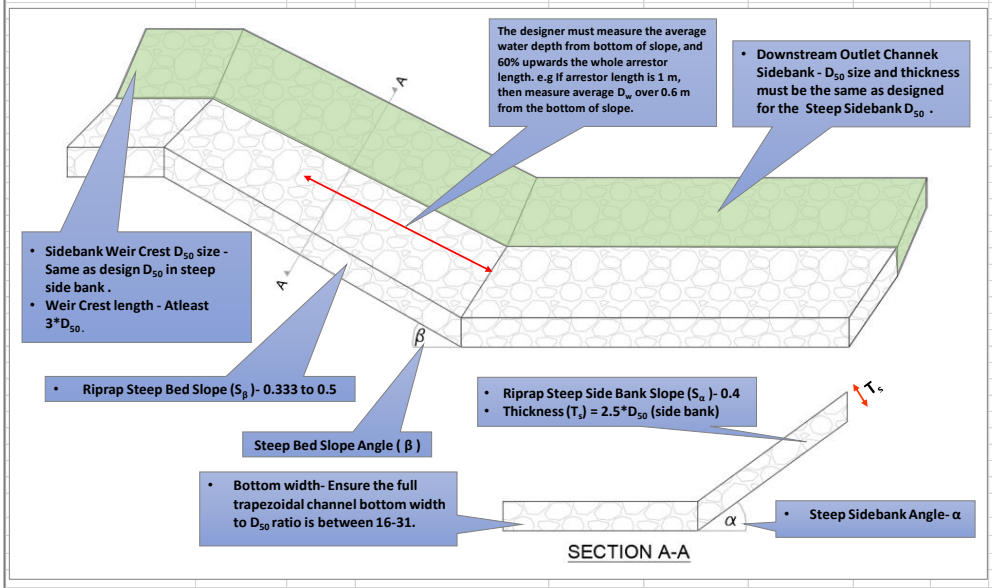

Note: Application limits

1. The applicability of the Excel Design Tool is limited to riprap dumped in straight trapezoidal cross sectional channels with steep beds ranging from 0.333 to 0.5, and with side bank slopes of 0.4. The results of this design tool are only valid for the design of prototype D_{50} stone size between stone 0.57 m and 1.125 m.

2. The designer must ensure that the bed bottom width to D_{50} (bed) ratio is between 16-31, since this was the range tested at the laboratory.

Legend

Input cells
Constant
Calculated parameter

1. Settling Velocity

$$V_{ss} = \sqrt{\frac{4}{3}\frac{(\rho_r-\rho_w)}{\rho_w}\frac{gD_{50}}{C_D}}$$ = 1.746 m/s

ρ_w	1000	kg/m^3	ρ_w= Density of water
ρ_r	2700	kg/m^3	ρ_r= Density of riprap rock
g	9.81	m/s^{-2}	C_D= Drag coefficient
D_{50}	0.30	m	D_{50}= Riprap median stone size (side bank)
C_D	2.17	(This is a recommended Drag Coeffecient Value) , A smaller drag coeffecient may lead to underesized D_{50} specification	
Side Bank Riprap Thickness T_s	0.74	m	T_s= Sidebank Riprap Thickness
HECRAS K_s=	0.094		K_s= HEC-RAS roughness coefficient on the (SIDEBANK)

2. Steep Bed and Sidebank Slope Correction Factors

$$k_\beta = \frac{Sin(\varphi_r-\beta)}{(Sin\,\varphi_r)}$$ = 0.475

$$k_\alpha = Cos\alpha\sqrt{1-\frac{Tan^2\alpha}{Tan^2\varphi}}$$ = 0.817

Therefore, $\sqrt{K_\beta . K_\alpha}$ = 0.623

	Slope	Angle In radians	Angle In degrees	
ϕ_r	0.84	0.698	40	ϕ_r = Rock angle of repose
S_α	0.4	0.380	21.8	S_α = Side Bank Slope
S_β	0.4	0.380	21.8	S_β = Bed Slope
				K_α = Steep Sidebank Slope Correction Factor
				K_β = Steep Bed Slope Correction Factor

3. Determination of D_{50} from Critical MN (sidebank)

$$\sqrt{K_\beta . K_\alpha}\,.\,\frac{\sqrt{gD_{w(HECRAS)}S_\beta}}{V_{ss}} = 0.227 * AF_{sidebank}$$

$D_{w(HECRAS)}$	0.188	m	Water Depth Calculated with HECRAS Steady flow analysis, Use K_s/D_{50}=0.316 for roughness coefficient)
$AF_{sidebank}$	1.35		(HECRAS Adjustment factor)

MN = 0.227

If MN >/= 0.227	Increase D_{50}
if MN = 0.227	SAFE
if MN < 0.227	SAFE
if MN significantly < 0.227	Decrease D_{50} until MN = 0.227